Solution-processing of $Cu(In,Ga)(S,Se)_2$ solar cells from metal chalcogenides – aspects of absorber crystallisation and interface formation

by

Soňa Uličná

Doctoral Thesis

submitted in partial fulfilment of the requirements for the award of Doctor of Philosophy of Loughborough University

May 2019

Contents

Abstract

Photovoltaic (PV) solar cells provide a simple and smart way for direct conversion of sunlight into electricity, which is a clean alternative to conventional fossil fuel-based energy conversion methods. As a result of ongoing research, photovoltaic technologies are becoming both more efficient and cheaper. Thin film solar cells, particularly chalcogenides, are a promising area of research as they offer substantial cost savings as a consequence of reduced material usage and cheaper atmospheric fabrication processes.

$Cu(In,Ga)(S,Se)_2$ (CIGS) solar cells are currently the best performing commercially deployed thin film PV technology. However the best performing CIGS devices are fabricated using sophisticated vacuum-based co-evaporation or co-sputtering systems requiring high capital costs and high energy budgets. Lower costs are achievable using alternative atmospheric deposition methods. These typically involve two step processes consisting of electrodeposition, nanoparticle or molecular solution coatings followed by high temperature annealing in a chalcogen containing atmosphere. A wide range of these methodologies have been investigated in recent years. A number of different precursor materials and solvents are available which offers a variety of different advantages. The solution-processed absorbers still lag behind the vacuum-based materials in terms of material quality however, due to presence of voids, impurities and the large number of grain boundaries. The most efficient solution-based methodologies also involve the use of highly toxic and in some cases explosive reagents, reducing the potential for commercial exploitation.

The work presented in this thesis describes development of a novel, environmentally-friendly and potentially scalable solution deposition method for fabrication of CIGS absorber layers. This method uses a molecular precursor solution consisting of metal chalcogenides (copper and indium sulphides, gallium and selenium) and alkahest binary solvents (1,2-ethylenediamine and 1,2-ethanedithiol). Metal chalcogenides have the advantage of being free from detrimental impurities and the amine-thiol solvent system is able to break their

strong covalent bonds. This way the use of highly toxic and explosive hydrazine to prepare pure, single-phase CIGS absorbers can be circumvented. The precursor solutions are deposited onto Mo-coated substrates by a scalable deposition method such as spray-coating, and are subsequently converted into a single-phase CIGS absorber upon high temperature selenisation.

CIGS absorbers prepared using this methodology were found to suffer from poor crystallinity with large numbers of voids and grain boundaries limiting solar cell performance. Three separate approaches were investigated in this thesis in order to overcome these limitations. The first approach aimed to improve the absorber crystallisation and increase the grain size by modifying the selenisation configuration and conditions. Larger grains were obtained by tuning the selenisation process; however full absorber recrystallisation was not achieved. A fine-grained CIGS layer which formed near the back contact was found to be Cu and In deficient relative to the large grains at the absorber surface. The second attempt involved adjustment of the [Cu]/[Ga+In] (CGI) ratio across the absorber depth, again with the aim of improving crystallinity. This was attempted by depositing the CIGS precursor in the form of a Cu-rich/Cu-poor bilayer rather than as a single-layer. This resulted in some improvement in the absorber grain size and smoothness, but only at the absorber surface.

The third approach focused on the external doping of the absorber with sodium. Sodium is known to boost the electronic properties of CIGS solar cells, and also to enhance CIGS grain growth. A novel strategy for controlled grain growth involving thermal evaporation of a thin NaCl layer onto the as-deposited CIGS absorber is presented here. A significant improvement in the absorber crystallisation was observed after the selenisation. However the solar cell performance was very dependent on the NaCl layer thickness and the resulting amount of this impurity introduced into the absorber rather than on the grain size. The optimum amount of Na caused a significant increase in device open-circuit voltage (V_{OC}) and fill factor (FF). Understanding the mechanism of action of Na on these solution-processed absorbers is complex due to very different absorber morphologies obtained for different doping amounts, and the presence of voids and rough surfaces. It would also require deeper characterisation involving more comprehensive study of defects and compositional quantification.

Other aspects of device processing examined in this work are the Mo back contact and the heterojunction formed with CdS. Excessive $MoSe_2$ formation at the back contact is often observed in solution-processed solar cells due to absorber porosity providing little protection to the underlying Mo from Se vapours. In this work $MoSe_2$ was effectively controlled by incorporation of a Mo-N diffusion barrier layer. Mo-N was inserted in between two Mo layers forming a Mo/Mo-N/Mo structure. Control of $MoSe_2$ layer thickness prevented delamination, allowed for better compositional control and improved grain growth due to increased Cu and Se availability for absorber recrystallisation. The importance of covering the CIGS absorber surface with CdS as quickly as possible after selenisation was demonstrated using time-resolved photoluminescence (TRPL) measurements. The minority carrier lifetime decayed faster in uncoated CIGS as compared to CIGS/CdS after exposure to air. Moreover air-annealing of the CIGS/CdS was shown to be beneficial for solar cell performance, reducing interface recombination and adjusting the field profile in the space charge region (SCR).

Careful adjustment of the selenisation environment, absorber composition, alkali doping and improvement of both back contact and heterojunction properties paved the way for CIGS solar cells with efficiencies up to 12% using an amine-thiol solution-processing approach. Simplicity, low toxicity, straightforward compositional control and the possibility of extrinsic doping are very promising attributes of this methodology, and has a significant potential for large-scale industrial CIGS solar cell fabrication. Further investigations of automated spraying, alkali treatments, gallium grading and absorber porosity reduction are suggested as potential routes to further efficiency improvements.

Acknowledgements

The journey through my PhD was the most extraordinary and enriching experience I had a chance to live so far. I would like to express an immense and sincere gratitude to various people that were directly or indirectly involved in it, and from whom I have received a great amount of support. Without their help, this work would not have been possible.

First of all, I would like to thank my principal supervisor, Dr. Jake Bowers for accepting me as a PhD student as a part of the Photovoltaic Materials and Devices (PVMAD) group in Centre for Renewable Energy Systems and Technology (CREST). I am particularly grateful for his guidance, helpful discussions, practical input, encouragement, confidence in my capabilities and opportunities he has provided me throughout my entire PhD. I would equally like to thank my second supervisor, Prof. Mike Walls for his kind support, thoughtful advice and ideas. Further I would like to thank Dr. Tom Betts and Professor Bart Vermang for agreeing to examine my work presented in this thesis.

Apart from my supervisors and examiners, I would like to thank a number of people I had a chance to meet and work with in CREST laboratories. During my years at CREST I have been sharing my research related but also not-related troubles, living wonderful experiences at conferences, doing sports and enjoying after work activities in our small town of Loughborough with a number of wonderful people. Among them, a special thanks goes to Dr. Nayia Arnou, who has introduced me to solution-processing of CIGS and taught me all the processing steps. In addition, she provided me with a valuable support and advice when I was starting this journey and became a very good friend of mine. Further I would like to thank Rachael Greenhalgh, Dr. Patrick Isherwood, Christos Potamialis, Dr. Fabiana Lisco, Liam Welch, Jamie Lowe and Lewis Wright for being great people to work with and for always creating a friendly and open atmosphere in the lab. I am deeply grateful to Dr. Kevin Bass for his immense technical help in the lab and for looking after our safety.

For specific measurements, my thanks go to Dr. Ali Abbas for performing valuable TEM measurements, Vincent Tsai for building PL and TRPL measurement system and measuring my CIGS samples. I wish to thank Mustafa Togay for his patience and sense for detail while performing the capacitance profiling and temperature dependent J-V and admittance spectroscopy. Additionally I would like to thank Alex Smith for measuring my best cell using the accredited solar simulator. I would like to acknowledge Loughborough Materials Characterisation Centre (LMCC) for the use of their facilities for material characterisation. Especially my thanks go to Dr. Keith Yendall who has helped me with every problem I encountered during my frequent use of the scanning electron microscope and Dr. Patricia Cropper for assisting with the XPS measurements. I also acknowledge the Loughborough Surface Analysis (LSA) Ltd., specifically Dr. Ben Grew for SIMS and Falk Reinhardt from Bruker Nano Berlin for XRF measurements on my CIGS absorbers.

I would also like to express my immense gratitude to my supervisors for the opportunity of three months long research secondment in the National Renewable Energy Laboratory and the Supergen SuperSolar Hub for funding it. This research visit broadened my horizons and I am thankful to all people I have met in Colorado and who made this experience even more extraordinary. Special thanks go to Dr. Maikel van Hest who has introduced me to, for me a completely new area of research, perovskite solar cells. He has given me an excellent supervision during my visit, full of helpful discussions, ideas as well as practical support in the lab. Further thanks to Dr. Benjia Dou (Dak) who has guided me through all the practical laboratory processes, assisted me with the measurements and was very patient and helpful. Thanks go also to Rachael, Sean and all the people who helped me to discover natural beauties of Colorado, and joined me not only for countless hiking trips but also for a nice meal, a pint in a local brewery and the fantastic concert of Muse in the Red Rocks Amphitheatre.

Finally, I wish to thank my beloved family who has always believed in my capabilities and provided me with unconditional support and love. Last but not least I would like to thank Tasos for lightening up my days, preparing wonderful holidays for me and bearing with me even in less motivating phases of my time as a PhD student.

List of publications

1. **S. Uličná**, P. J. M. Isherwood, P. M. Kaminski, J. M. Walls, J. Li, and C. A. Wolden, “Development of ZnTe as a back contact material for thin film cadmium telluride solar cells,” *Vacuum*, 139, 159–163, 2017.

2. **S. Uličná**, B. Dou, D. H. Kim, K. Zhu, J. M. Walls, J. W. Bowers, and M. F. A. M. van Hest, “Scalable Deposition of High-Efficiency Perovskite Solar Cells by Spray-Coating,” *ACS Appl. Energy Mater.*, 1, 1853–1857, 2018.

3. **S. Uličná**, P. Arnou, A. Abbas, M. Togay, L. M. Welch, M. Bliss, A. V. Malkov, J. M. Walls, and J. W. Bowers, “Deposition and application of a Mo–N back contact diffusion barrier yielding a 12.0% efficiency solution-processed CIGS solar cell using an amine–thiol solvent system,” *J. Mater. Chem. A*, 7, 7042–7052, 2019.

4. P. Arnou, C. S. Cooper, **S. Uličná**, A. Abbas, A. Eeles, L. D. Wright, A. V. Malkov, J. M. Walls, and J. W. Bowers, “Solution processing of $CuIn(S,Se)_2$ and $Cu(In,Ga)(S,Se)_2$ thin film solar cells using metal chalcogenide precursors,” *Thin Solid Films*, 633, 76–80, 2017.

5. C. S. Cooper, P. Arnou, L. D. Wright, **S. Uličná**, J. M. Walls, A. V Malkov, and J. W. Bowers, “An innovative approach for fabrication of $Cu_2ZnSnSe_4$ absorber layers using solutions of elemental metal powders,” *Thin Solid Films*, 633, 151–155, 2017.

Conference proceedings:

1. **S. Uličná**, P. Arnou, C. S. Cooper, L. D. Wright, A. V Malkov, J. M. Walls, J. W. Bowers, “Hydrazine-free metal chalcogenide precursor solutions for sprayed $CuIn(S,Se)_2$ thin film solar cells,” in *Proceedings of the 12th Photovolt. Science and Technol. Conf.,* Liverpool, UK, 2016.

2. **S. Uličná**, P. Arnou, C. S. Cooper, L. D. Wright, A. V. Malkov, J. M. Walls, and J. W. Bowers, “A comparison of different selenisation approaches for solution-processed $Cu(In,Ga)(S,Se)_2$ solar cells,” in *Proceedings of the 13th Photovolt. Science and Technol. Conf.,* Bangor, UK, 2017.

3. **S. Uličná**, P. Arnou, A. Eeles, M. Togay, L. D. Wright, A. Abbas, V. Malkov, J. M. Walls, and J. W. Bowers, “Control of $MoSe_2$ formation in hydrazine-free solution-processed CIS/CIGS thin film solar cells,” in *Proceedings of the 44th IEEE Photovolt. Spec. Conf.,* Washington, DC., USA, 186-191, 2017.

4. **S. Uličná**, M. Togay, M. Bliss, V. Tsai, L. D. Wright, J. Lowe, A. V. Malkov, J. M. Walls, and J. W. Bowers, “Electronic properties of solution-processed Cu(In,Ga)(S,Se)$_2$ solar cells using metal chalcogenides and amine-thiol solvent mixtures,” *in Proceedings of the 7th World Conf. Photovolt. Energy Conversion, WCPEC - A Jt. Conf. 45th IEEE PVSC, 28th PVSEC 34th EU PVSEC*, Waikoloa, HI, USA, 859–864, 2018.

5. P. Arnou, **S. Uličná**, A. Eeles, M. Togay, L. D. Wright, A. V. Malkov, J. M. Walls, and J. W. Bowers, “Variation of Cu Content of Sprayed Cu(In,Ga)(S,Se)$_2$ Solar Cells Based on a Thiol-Amine Solvent Mixture,” in *Proceedings of the 44th IEEE Photovolt. Spec. Conf.,* Washington, DC., USA, 146–150, 2017.

6. M. Togay, **S. Uličná**, S. Bukhari, F. Lisco, M. Bliss, A. Eeles, J. M. Walls, and J. W. Bowers, “Exploring metastable defect behavior in solution-processed antimony doped CIGS thin film solar cells,” *in Proceedings of the 7th World Conf. Photovolt. Energy Conversion, WCPEC - A Jt. Conf. 45th IEEE PVSC, 28th PVSEC 34th EU PVSEC*, Waikoloa, HI, USA 1960–1965, 2018.

7. V. Tsai, C. Potamialis, **S. Uličná**, M. Bliss, T. R. Betts, and R. Gottschalg, “Quantifying minority carrier lifetime and collection efficiency of solar cells by combined optical and electrical characterisation techniques,” in *Proceedings of the 35th European Photovolt. Solar Energy Conf.and Exhib.*, Brussels, Belgium, 114-121, 2018.

Abbreviations

α	Absorption coefficient
AC	Alternating current
AM	Air Mass
AR	Anti-reflection
a-Si	Amorphous silicon
AS	Admittance spectroscopy
AZO	Aluminium-doped zinc oxide
BF33	Borofloat glass
CBD	Chemical bath deposition
CGI	[Cu]/[Ga+In] ratio
CIS	Copper indium diselenide
CIGS	Copper indium gallium diselenide
c-Si	Crystalline silicon
CSS	Close space sublimation
CTE	Coefficient of thermal expansion
C-V	Capacitance-voltage
CZTS	Copper zinc tin sulfide
DC	Direct current
DI	Deionised
DLCP	Drive-level capacitance profiling
DMSO	Dimethyl sulfoxide
E_A	Activation energy
EA	Ethyl acetate
E_C	Conduction band energy
ED	Electrodeposition
EDA	1,2-ethylenediamine
EDT	1,2-ethanedithiol
EDX	Energy-dispersive X-ray spectroscopy
E_F	Fermi level energy
E_g	Bandgap energy
EL	Electroluminescence
EQE	External quantum efficiency
E_V	Valence band energy
FF	Fill factor
FWHM	Full width half maximum
GB	Grain boundary
GGI	[Ga]/[Ga+In] ratio
ICDD	International Centre for Diffraction Data
i-ZnO	Intrinsic ZnO
J_0	Dark saturation current density

JCPDS	Joint committee on powder diffraction standards
J_{MPP}	Current density at maximum power point
J_{SC}	Short-circuit current density
J-V	Current density-voltage
J-V-T	Temperature dependent current density-voltage
L_D	Minority carrier diffusion length
MPP	Maximum power point
NP	Nanoparticle
ODC	Ordered defect compound
PCE	Power conversion efficiency
PE	Partial electrolyte
PDT	Post-deposition treatment
PID	Proportional integral derivative
P_{in}	Incident power
PL	Photoluminescence
PTFE	Polytetrafluoroethylene
PV	Photovoltaics
QNR	Quasi-neutral region
RF	Radio frequency
R_S	Series resistance
R_{SH}	Shunt resistance
RT	Room temperature
RTP	Rapid thermal processing
SCR	Space charge region
SEM	Scanning electron microscope
SIMS	Secondary ion mass spectrometry
SLG	Soda-lime glass
STC	Standard test conditions
τ	Minority carrier lifetime
TCO	Transparent conductive oxide
TEM	Transmission electron microscope
TFSC	Thin film solar cells
TGA	Thermogravimetric analysis
TRPL	Time-resolved photoluminescence
TU	Thiourea
V_{bi}	Built-in voltage
vdW	van der Waals
V_{MPP}	Voltage at maximum power point
V_{OC}	Open-circuit voltage
v/v	Volume-to-volume ratio
W	Depletion region width
XPS	X-ray photoelectron spectroscopy
XRD	X-ray diffraction
XRF	X-ray fluorescence

CHAPTER 1

Introduction to CIGS solar cells

1.1 Photovoltaics

1.1.1 Solar as a renewable energy source

Extensive dependence of the global population on fossil fuels such as coal, oil and gas coupled with a constantly increasing energy demand have led to considerable environmental concerns regarding global warming [1][2]. These conventional energy sources have a negative impact on the environment not only during their extraction and production, but also resulting from their use through the release of large amounts of carbon dioxide (CO_2) to the atmosphere [1][2][3]. Increasing amounts of CO_2 in the atmosphere block part of the solar radiation from being re-emitted back into space and instead reflect it back to the earth resulting in gradual warming of the planet surface [2]. Consequently it is of high interest for the modern society to raise public awareness and progressively replace the greenhouse gas emitting energy sources with climate neutral ones.

Photovoltaic (PV) energy is a clean and environmentally sustainable alternative to conventional energy sources such as fossil fuels. The conversion of solar radiation into electricity is a simple and smart way of producing renewable energy. Solar radiation - free, abundant and available daily - is collected by a solar panel, which is simply left standing outside. Only 90 minutes of sunlight could provide enough energy to satisfy the energy needs of the whole planet for the entire year [4]. However solar energy forms only a small fraction in the current energy electricity production, meeting only 1.9% of the global electricity production with over 400 GW of installed capacity (end of 2017) [5].

Thanks to ongoing research, PV technology is constantly improving to achieve more efficient energy conversion combined with reduced cost. Therefore, thin film solar cells and especially the chalcogenides are a promising area of research as they present a potential cost saving in terms of materials and fabrication processes. The

PV market is dominated by silicon wafer-based technology. Approximately 92% of all solar panels are made from silicon [6]. Thin film technologies, which account for the remaining 8% of the PV market, find it very hard to compete with Si technology due to the abundance of silicon in the Earth's crust, its low toxicity, high material purity and the maturity of the technology resulting from the microelectronics industry [7]. The main issues of crystalline silicon (c-Si) are the high production costs associated with high wafer cost (50% of the total production cost) and complicated manufacturing process requiring a high thermal budget (~1100°C) [8]. The c-Si technology is currently reaching lab cell efficiencies of 26.7% and lab module efficiencies of 24.4% [9].

1.1.2 PV operating principles

The sun is an energy source with a radiation spectrum similar to black body near 5800 K. The total radiant energy flux over the whole surface is approximately 3.8 x 10^{26} W, but only a small fraction is intercepted by the Earth. The mean solar irradiance reaching the outside of the Earth's atmosphere is 1367 W/m^2, a value also known as the Solar Constant [10]. Absorption and reflection in the Earth's atmosphere lead to further reduction of the irradiation reaching the ground to approximately 1 kW/m^2. However this value only serves as a reference as the net value depends on factors such as geographical location, time of the day/year, weather conditions and the presence of physical obstacles [11].

Solar cells are semiconductor devices with a suitable absorber material allowing for absorption of photons from the incident sunlight and creating mobile carriers, electrons and holes, that are effectively separated at the terminals of the device [12]. This interaction of light particles (photons) with the solid matter leading to ejection of electrons to a higher energy level is the basis for the photovoltaic effect discovered by French scientist Edmond Becquerel [13]. Three main conditions have to be fulfilled to achieve efficient PV energy conversion: 1) a suitable material to absorb as many photons as possible, generating electron-hole pairs; 2) existence of a p-n junction to effectively separate the charges before they naturally recombine; and 3) effective electron transport to the external circuit.

Sunlight contains photons of wide range of energy levels E:

$$E = h\upsilon \qquad [1.1]$$

where h is the Planck's constant and υ is the frequency of radiation. When the energy exceeds a certain threshold (the bandgap energy), a weakly bound electron is promoted from the semiconductor valence band (E_V) to the conduction band (E_C), where it is "free" to move and conduct electricity [12]. The bandgap (E_g) of the photovoltaic absorber is therefore the fundamental parameter defining how many charge carriers will be generated as it determines the part of the spectrum that can be absorbed by the semiconductor ($E>E_g$). The bandgap separates valence band states, which are full of electrons, from conduction band states, which are empty at equilibrium. The promoted electrons leave behind vacancies in the valence band called holes, which behave like virtual charge carriers. When created charge carriers are not separated and collected fast enough, the electrons and holes will relax back to their equilibrium state through the process called recombination. The excited electrons will quickly thermalise to the conduction band edge and then decay across the bandgap to the vacant space in the valence band [12]. The electron-hole pair generation, thermalisation and recombination are illustrated in Figure 1.1.

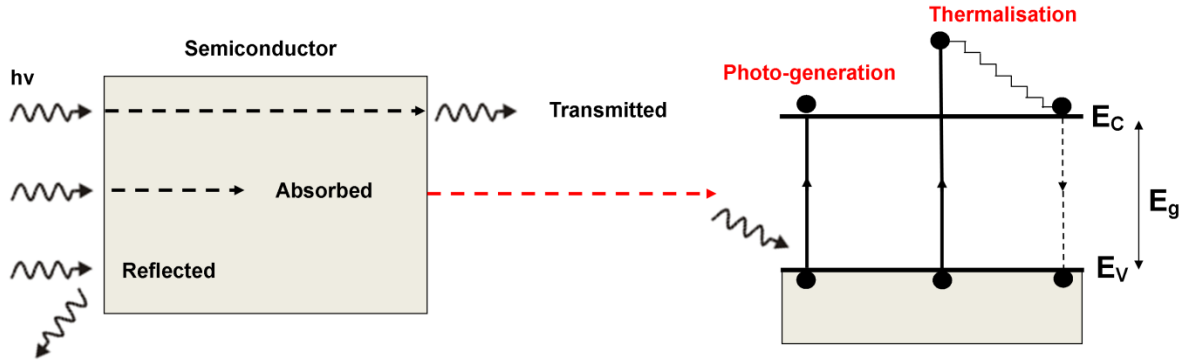

Figure 1.1 Schematic diagram of the path of light reaching the semiconductor. Only some of the photons with suitable energy are absorbed, others are transmitted through or reflected from the surface (left). Not all absorbed photons participate in photo-generation. Thermalisation and recombination occur when the charges are not effectively separated (right).

Doping is a way of increasing the population of mobile electrons or holes in the semiconductor by intentionally introducing impurities. Donor atoms provide electrons available for conduction. These electrons are not needed for bonding and therefore less energy is required to promote them to the conduction band. Semiconductors doped with donor atoms are called n-type as they have excess negative over

positive carriers, whereas acceptors are atoms with fewer electrons which dope the semiconductor p-type. The dopants can be seen as states in the bandgap, visualised in the band diagram by the position of the Fermi energy (E_F) in regards to E_C and E_V. In an intrinsic material, E_F lies in the middle between E_V and E_C. When the material is doped n-type or p-type, E_F shifts closer to E_C or E_V respectively [14].

A p-n junction is formed by intimately joining two semiconductor regions with different electronic properties (doping types) together. The p-n junction provides an electrostatic force driving the photo-generated charges to be swept across the junction, away from their point of creation. The created space charge results in a built-in electric field blocking further migration across the junction. The region near the junction is called the 'space charge region' (SCR) or 'depletion region' as it exhibits localised carrier depletion. The regions on either side of the SCR are charge neutral, also called the 'quasi-neutral region' (QNR). The electrostatic potential difference created by the positive and negative space charge exposure in the SCR is called the 'built-in voltage' (V_{bi}). Due to the built-in electric field, the electrons within the diffusion length region are pushed away from the p-type absorber to the n-type buffer and are collected by the n-type electrode. Similarly holes are pushed away from the n-type buffer to the p-type layer and collected by the p-type electrode. Figure 1.2 a) schematically illustrates the mechanism of PV energy conversion [15]. A schematic representation of the CIGS band structure under zero bias conditions is presented in Figure 1.2 b) [16].

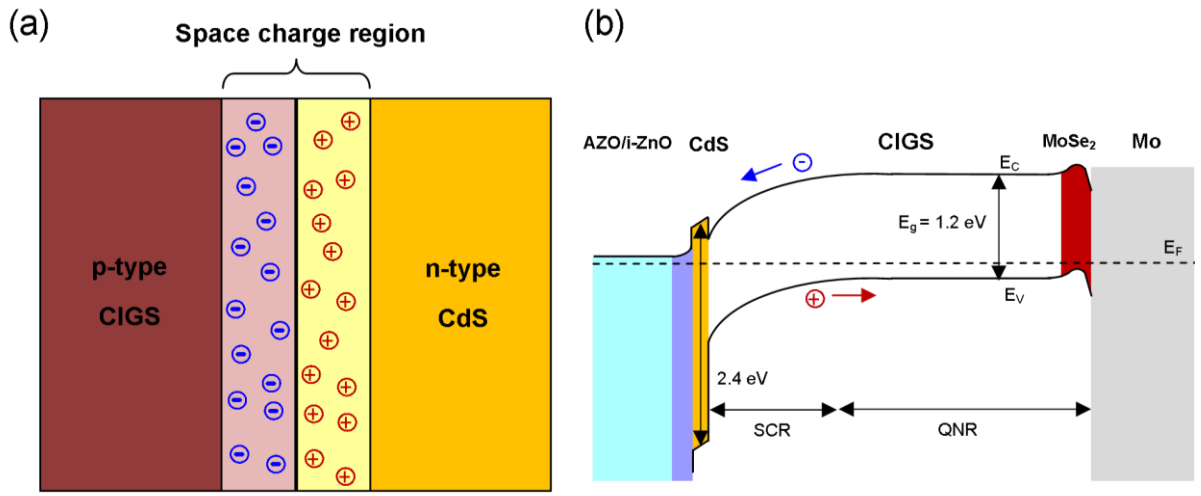

Figure 1.2 Diagram of the p-n junction showing the formation of a SCR (a) and band diagram of a CIGS solar cell under 0 V bias conditions (b).

1.2 Thin film PV

The solar cell is a device carefully designed to efficiently absorb and convert sun light to electrical energy. A number of semiconductor materials can be used to fabricate a solar cell. The choice of a suitable material is based on how well its optical characteristics match the solar spectrum as well as its electrical capabilities. These characteristics include an appropriate bandgap, absorption coefficient (α), minority carrier lifetime (τ), diffusion length (L_D) and surface recombination velocity (S) [17]. Anti-reflection coatings (AR) are typically used for high efficiency solar cells to minimise reflection from the module or cell front surface. The p-n junction is the heart of a solar cell. Efficient charge separation requires a high built-in voltage which can be achieved by sufficient doping of the n- and p-type materials. Finally, efficient carrier transport requires good quality material with few defects to limit non-radiative recombination (through localised energy states within the bandgap, caused by material defects) [18].

Unlike silicon (E_g = 1.1 eV) which is a weak optical absorber, hence requiring cell thicknesses of 180 µm, thin film solar cells have the advantage of a direct bandgap. This means that the E_C minimum is directly above the E_V maximum, and an absorber thickness of only a few microns (1-3 µm) is sufficient to achieve effective absorption of sunlight [12]. The benefits of thin film solar cells (TFSC) as opposed to the market leader silicon arise from the potential cost savings (lower thickness, higher throughput, scale-up production), diversity of processing and device options, better control of the doping profile, and high power-to-weight ratio important for space applications [19][20]. Despite the many advantages and achievements of TFSC PV, the remaining challenge is to make them cheaper and more price competitive compared to c-Si.

The main thin film PV technologies and their characteristics are summarised in Table 1.1. Amorphous silicon (a-Si) is the most mature of the TFSC technologies. The drawbacks of the technology include low power conversion efficiencies (PCEs), performance degradation during the first hours of light exposure and seasonal variations of the performance [19]. Cadmium Telluride (CdTe) has the highest market share of thin film technologies owing to module manufacturer First Solar fabricating CdTe by close space sublimation (CSS) [21]. Gallium Arsenide (GaAs) is

the most efficient among the TFSC, however this technology is too expensive for large-scale terrestrial application [22]. Kesterite-based thin film $Cu_2ZnSn(Se,S)_4$ (CZTS) has similar structure and electronic properties to CIGS, with the benefit of using non-toxic, earth abundant materials. Despite the similarities, the highest efficiencies achieved are far below those of CIGS due to losses associated with poor CZTS material quality [23].

Table 1.1 Comparison of different thin film single-junction technologies, efficiencies from [9][24][25][26]**. Only the first three are commercialised.**

Technology	Bandgap	Best research cell efficiency	Module efficiency
a-Si	1.7 eV	14.0%	9.8% (Solarex)
CdTe	1.45 eV	22.1%	18.6% (First Solar)
CI(G)S	1.0-1.7 eV	23.35%	19.2% (Solar Frontier)
CZTS	1.0-1.5 eV	12.6%	N/A
GaAs	1.42 eV	29.1%	25.1% (Alta Devices)

1.3 CIGS solar cells

1.3.1 General aspects of the technology

The $Cu(In,Ga)(Se,S)_2$ (CIGS) chalcopyrite-structured semiconductor is a promising material for thin film solar cells. CIGS is currently the best performing, commercially deployed polycrystalline thin film solar cell technology with a record efficiency of 23.35% achieved by Solar Frontier in 2019 [26]. Historically, a $CuInSe_2$ (CIS) material with a bandgap of 1.04 eV was first synthesised by Hahn *et al*. in 1953 [27]. The first CIS device with a measured efficiency was reported in 1975 by the evaporation of CdS onto CIS single-crystal, achieving 12% PCE [28]. Since then, the laboratory efficiencies and fabrication techniques have dramatically improved. Today, the most efficient CIGS solar cells are fabricated by vacuum processes such as co-evaporation or co-sputtering. The three-stage co-evaporation process invented by the US National Renewable Energy Laboratory (NREL) in 1994 set the milestone of efficiencies beyond 20% [29]. Commercial module efficiencies of 16.1% have been achieved in industry [8]. The ultimate goal of this promising PV technology is to increase the efficiencies of the modules while reducing the costs. According to a model proposed by Kapur *et al.,* the projected cost for 1000 MW/yr production with a module efficiency of 15% should be as low as 0.34 $/W [30].

Generally, CIGS soar cells are grown in substrate configuration, which also gives the highest performances. In this configuration the light enters the cell through the transparent conductive oxide (TCO) on the top of the device, and the back contact is deposited on the substrate (Figure 1.3). Superstrate configuration, typically used to grow CdTe solar cells, is unfavourable due to undesirable inter-diffusion of Cd from CdS into the CIGS absorber during the high temperature processing of the absorber layer (often above 500°C) [31].

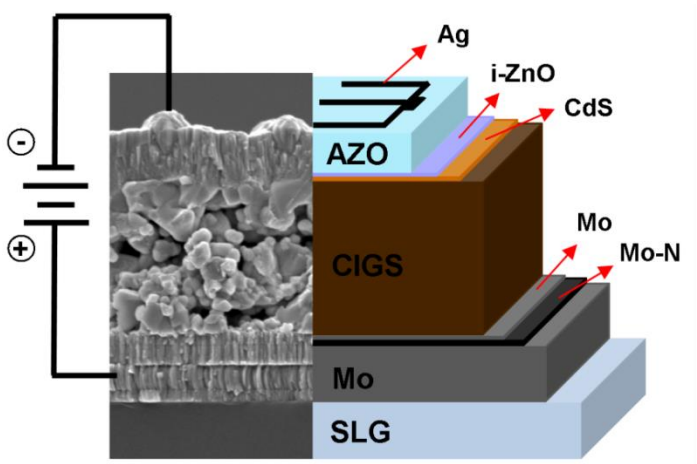

Figure 1.3 Schematic diagram and SEM cross-section through the CIGS stack typically fabricated for this thesis.

The solar cell is typically built on soda-lime glass (SLG) substrate, but various alternatives such as flexible metal and polyimide foils are being explored. Molybdenum grown by sputtering is the most commonly used back contact. A thin intermediate layer of $MoSe_2$ forms at the Mo/CIGS interface forming an ohmic contact. Subsequently, the CIGS absorber is deposited by a wide range of vacuum and non-vacuum techniques. As for CdTe, CdS grown by chemical bath deposition (CBD) is the most commonly used buffer layer for CIGS. For the window layer and top electrode, a combination of intrinsic and Al-doped ZnO (i-ZnO/AZO) is typically used [32][33].

1.3.2 Material and solar cell properties

The absorber material is the chalcopyrite-structured semiconductor $Cu(In,Ga)(S,Se)_2$ (CIGS), belonging to the I-III-VI_2 family of alloys. It has a direct and tunable bandgap, typically selected in the range of 1.0 – 1.5 eV for PV applications. Moreover a very high optical absorption coefficient (10^5 cm^{-1}), tolerance for trace impurities and sufficiently passive grain boundaries make this material an excellent choice for

photovoltaic applications [34]. The bandgap can easily be tailored by substituting In atoms by smaller Ga and/or Se atoms with S and vice versa. Slightly wider bandgap devices are desirable as they provide a better match to the solar spectrum, resulting in increased voltages [8]. The optimum Ga content for minimal bulk defects was found to be [Ga]/[Ga+In] ~0.3 [35]. In addition, it was shown that bandgap grading through the absorber with higher Ga towards the back would create a back surface field reflecting electrons towards the front junction. This results in improved collection of charge carriers, especially at long wavelengths [36]. Sulphur addition acts mainly on the valence band maximum and partial sulphurisation leads to very high device efficiencies with reduced interface recombination and increased carrier collection. Such devices are fabricated by Solar Frontier with a S-rich surface and Ga-rich back [37]. However if the S content is too high ([S]/[S+Se] > 0.61), the fill factor (FF) of the device deteriorates severely due to increase in series resistance (R_S) [38].

The tetragonal chalcopyrite crystal structure is a complex variant of the cubic II-VI zinc blende structure of ZnS with doubled periodicity along the c-axis. The Zn (II) cation is substituted by chalcogenide compounds Cu (I) and In (III)/Ga (III) having Se or S as their anion. Cu-Se and In-Se bonds are not of the same strength resulting in a tetragonal distortion (lattice parameter ratio c/a ≠ 2) [39]. The crystal structure of the tetragonal chalcopyrite CIGS unit cell is presented in Figure 1.4.

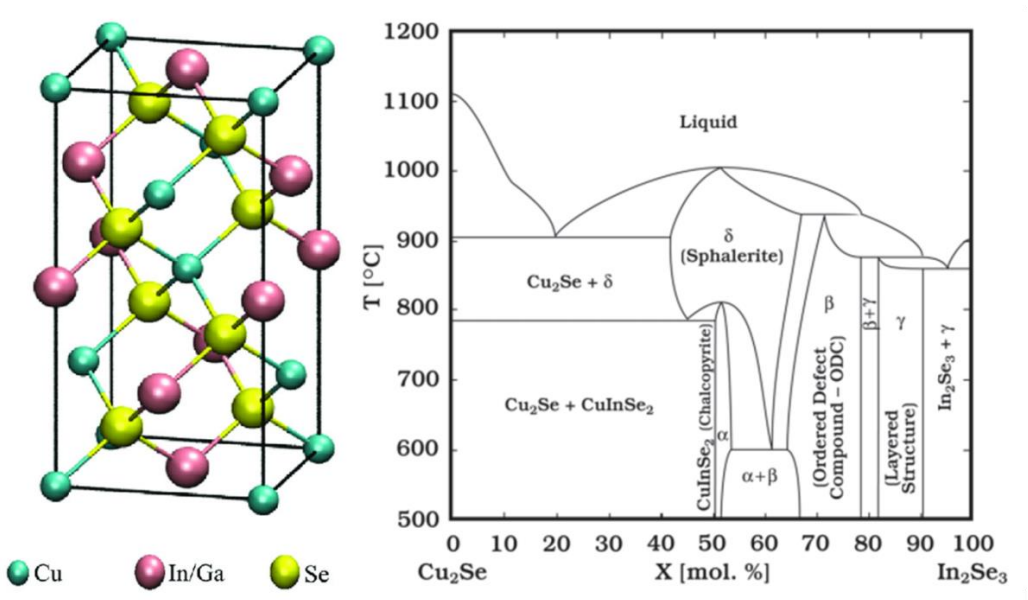

Figure 1.4 Schematic diagram of the tetragonal chalcopyrite crystal structure (left) and the binary phase diagram along the Cu_2Se and In_2Se_3 section of the Cu-In-Se ternary phase diagram, adapted from [39][40]**.**

The Cu-In-Se ternary diagram has been studied by a number of authors and their understanding is crucial to design a fabrication process of a single-phase absorber material [41][40][42]. The ternary phase $CuInSe_2$ lies along the Cu_2Se and In_2Se_3 pseudobinary tie-line (line of two-phase equilibria) of the ternary diagram. A simplified version of this diagram is presented in Figure 1.4. The ternary $CuInSe_2$ phase is denoted α-CIS. Along this tie-line, other ternary phases exist, namely β-$CuIn_3Se_5$, γ-$CuIn_5Se_8$ and δ which is a sphalerite-structured phase (high temperature modification of α and β phases with no cation ordering). The β-phase is often referred to as ordered defect compound (ODC) formed from the α-phase having $2V_{Cu}$-In_{Cu} defects. In equilibrium, the required α-CIS phase has a small existence range, represented by a narrow zone with x (mol% of In_2Se_3 in In_2S_3+Cu_2S) ~50-52%, corresponding to a slightly Cu-poor content of 24.0-24.5 at% ($0.94 < [Cu]/[In] < 0.97$). Higher Cu contents result in the formation of a secondary phase Cu_2Se in addition to the single-phase α-CIS. However, more Cu-deficient compositions can be accommodated owing to an extraordinary stability of the $2V_{Cu}$-In_{Cu} defect complex. Increasing temperature, alloying with Ga and adding a small quantity (~ 0.1 at%) of Na impurity further widens the α-CIS phase window [41].

Grain boundaries (GBs) play an important role in the CIGS absorbers, dictating the current-voltage characteristics of the cell. They define an interruption of the long-range order in the crystal. GBs adversely influence the majority carrier mobility and reduce minority carrier lifetime. Moreover GBs can become charged and induce band bending. However GBs in chalcopyrite devices have more benign effects compared to the other semiconductors, owing to inherently low recombination at GBs, beneficial effects of GBs passivation by Na or O and downshift of the E_V that repels holes from the GB region [16].

Due to a number of different atoms present in this complex semiconductor, many types of defects can form. However many of these defects can be seen as benign or even beneficial [16]. This inherent stability and large tolerance for deviations from stoichiometric composition are one of the significant benefits of CIGS as a thin film technology. Defects may appear as single-defect states with energy levels within the bandgap or as multiple defect states or distribution with a continuous state density in the bandgap. In CIGS, the indium-on-copper-antisites (In_{Cu}) and the copper vacancy (V_{Cu}) are the dominant donor and acceptor defects respectively [16]. At Cu-poor

compositions, the V_{Cu} defect is the shallowest intrinsic acceptor responsible for the p-type doping of the absorber. Due to energetically favourable donor-acceptor compensation, the $2V_{Cu}$ + In_{Cu} defect complex has a high probability of formation. However this defect does not produce a significant crystal distortion and no transition level of this defect complex is present within the bandgap hence it does not result in any detrimental electronic states. The majority of donor V_{Se} defects are bound in the defect complex V_{Se} + V_{Cu} having negative binding energy. The $(V_{Se} + V_{Cu})^-$ introduces an antibonding level at 0.85 eV above the E_V [41].

For Cu-poor CIGS films, alkali doping was found to be essential to achieve high performances, leading primarily to increases in the open-circuit voltage (V_{OC}) and fill factor (FF). Many studies report structural and electronic changes to the absorber upon Na doping, however the exact mechanism and whether the Na acts at GBs or in grain interiors is not yet explained with any certainty [43]. Alkali PDTs (post-deposition treatments) were found to be the most efficient ways of intentional alkali doping. Whereas NaF PDT mainly modifies the bulk electronic properties, KF leads to significant alteration of the CIGS surface composition creating a Cu and Ga depleted surface [44].

1.3.3 Fabrication processes

Even though the CIGS thin film technology has many beneficial features, the fabrication of a high-quality absorber layer is a very complex process often requiring expensive vacuum-based technologies. The most successful fabrication technique for CIGS absorber layers achieving the highest efficiencies is 3-stage co-evaporation of the constituent elements from multiple sources under excess Se conditions. The advantage of this method is the possibility to vary the Cu-flux during the deposition which is critical as it strongly affects the film growth. Overall Cu-poor composition is necessary to form CI(G)S phase, avoiding formation of highly conductive Cu_2Se secondary phases lowering device performance. However, all electronic properties including defect density, bulk recombination and transport are better when CIGS is grown under Cu-rich conditions [8]. The process first introduced by NREL starts with the deposition of In, Ga in excess Se (1^{st} stage), followed by co-deposition of Cu and Se (2^{nd} stage). Finally the Cu composition is readjusted during the 3^{d} stage to achieve an overall Cu-poor composition by deposition of In, Ga and Se [41].

Moreover, the variation of the Ga/In flux ratio allows for bandgap grading in the absorber. However the precise control of the large area uniformity is challenging because the elemental fluxes are sensitive to very small temperature differences [32].

Among other fabrication methods, sequential processes consisting in deposition of the absorber, followed by thermal annealing in reactive or inert atmosphere are an alternative to the co-evaporation. This method is suitable for large area deposition providing good control over the film composition and thickness. Precursor materials of various types can be deposited by sputtering, thermal evaporation, electrodeposition, nanoparticle- or solution-processing. The small-grained precursor is converted into a polycrystalline layer of the desired composition typically via chalcogenide reaction using S and Se or H_2S and H_2Se vapours [8]. The hydride gasses are toxic, however they have the advantage of being more reactive and easier to control [45]. The largest commercial manufacturer of CIGS modules uses sputtering followed by 'sulphurisation after selenisation' (SAS) [37].

Recently, research attention has focused on CIGS deposition onto flexible substrates, where efficiencies over 20% are also achievable. To transfer the fabrication process onto substrates such as metal or polyimide foils, several aspects such as process temperatures and external alkali doping need to be addressed. EMPA has developed a low temperature (350°C) CIGS growth process achieving efficiencies of 20.4% on polyimide films. At the end of the process, NaF and KF PDT provide the alkali doping of the absorber [46].

Despite the promising CIGS material properties, practicalities of the technology (low weight, flexibility, suitability for monolithic integration and high radiation tolerance if the final product is intended for space applications) and its accomplishments, CIGS commercial module production accounts for only 2% of the total market [6]. CIGS industrial production is carried out by companies such as Solar Frontier, AVANCIS, Solibro and Manz [33]. As opposed to lab-scale, where the efficiency is the primary focus, in large-area industrial production, low-cost, reproducibility, high-throughput and process tolerance are of much greater importance [8]. The limitations and current challenges in the commercialisation of CIGS can be summarised in the following points [8][33]:

- Compositional uniformity between runs (CIGS is a quaternary compound and the uniformity and reproducibility over large-area influences the film electrical and optical properties and consequently the production yield. In-situ non-destructive detection tools are required.)
- Standardisation of equipment (Several fabrication steps require different tools with different throughputs. Substrate handling in-between the processes can be an issue. An in-line process would be the most suitable solution.)
- Scaling-up (Large gap between small-area cell efficiencies (~23%) and commercial module efficiencies (~16%).)
- Indium supply and production (Indium is a by-product of zinc and is therefore dependent on zinc production. As many as 31 tons of In are required to produce 1 GW PV.)
- In large-scale production, a dynamic deposition process (substrate in motion) will likely affect the growth kinetics as compared to the static small area processes typical of laboratory synthesis. Consequently the high efficiency of small-area devices might not be reproducible over the large area.

Significant research is still required to transfer the processes from expensive vacuum-based to low-cost large-are atmospheric processes whilst keeping the material quality and solar cell performance at a high level.

1.4 Non-vacuum processing of CIGS solar cells

Non-vacuum processing of CIGS possesses significant advantages over the vacuum-based techniques which has led to a considerable research interest in this field in recent years. The general benefits of non-vacuum processing are summarised in few points below [32][47][48]:

- Lower capital cost of the equipment (simplified equipment with no vacuum parts, chambers, pumps)
- High throughput (no pumping-down time, fast and large-area deposition)
- High material utilisation efficiency (Sputtering and evaporation are very material inefficient through unintentional deposition on the vacuum chamber walls. Liquid coating methods on the other hand can have nearly 100% precursor utilisation.)

- Large area uniformity and straightforward compositional control (the final film composition is closely related to the composition of the precursor material)
- Lower energy budget (less energy intensive processes, depositions at lower temperatures followed by short heat treatment such as rapid thermal processing (RTP))

Despite this significant potential and the ongoing high levels of research into atmospheric deposition of CIGS absorbers, some challenges still remain. The performance of such devices is lagging significantly behind the performance of co-evaporated cells. This is mostly caused by the inferior material quality of atmospherically-processed absorbers, which typically contain more defects related to the presence of impurities, voids and material inhomogeneities [8]. Non-vacuum absorbers are usually fabricated in two-step processes, where a precursor is first deposited at low temperature and then converted into the CIGS phase by high temperature annealing in a chalcogen atmosphere. Deposition methods can be divided into several categories depending on the precursor material used. These include [47]:

- Coating or printing of molecular precursor solutions
- Coating or printing of nanoparticle-based inks (suspensions)
- Electrochemical and chemical bath-based techniques such as electrodeposition

Electrodeposition (ED) is a well-established electrochemical technique widely used in the electronics industry. This technique is however difficult to apply to CIGS technology, as different constituent elements have different redox potentials and reduction kinetics. This results in limited control over the stoichiometry and phase homogeneity. Moreover, the electrochemical behaviour of Se is very complex, exhibiting several oxidation states (+6, +4, 0, -2). To overcome the associated thermodynamic and chemical difficulties, strategies such as co-electrodeposition or electrodeposition of stacked layers have been adopted [49]. However the deposited precursor layers have to be subjected to high temperature annealing steps often in the presence of chalcogen vapours. The most successful ED technique up to date was developed by Nexcis, using successive ED of elemental Cu, In and Ga, and

which was further annealed in Se/S atmosphere to form a 17.3% efficient $Cu(In,Ga)(S,Se)_2$ solar cell [50].

The following sub-sections will focus on the direct-coating methods of molecular solution and nanoparticle-based inks discussing the strong and weak points of each method and the particular device performances achieved. The choice of the precursor, deposition route and conditions used are crucial as they greatly influence the reaction kinetics, resulting in different absorber morphologies and phases formed. Unwanted elements from solvents, additives or precursors such as carbon and oxygen can remain in the film after imperfect removal during annealing and impede grain growth or cause film deterioration. The molecular or nanoparticle precursors can be coated or printed onto the substrate by various deposition techniques including spin-coating, spray pyrolysis, blade-coating and inkjet printing.

Spin-coating consists of flooding the substrate surface with the precursor solution and spinning off the excess. It is currently one of the most important research techniques due to high reproducibility, uniformity and suitability over wide viscosity range of solutions. However this technique is not applicable for large area depositions. The principle of blade-coating is to distribute the solution by moving a sharp blade parallel to the substrate surface. The coating thickness is controlled by the distance between the blade and the substrate. It is a simple, low-cost, large-area compatible technique with high material utilisation. However this method requires a relatively viscous ink formulation. Inkjet printing, sometimes defined as high definition spray-coating is a direct coating or patterning of the ink at low temperatures and atmospheric conditions. The requirement is to develop an ink with suitable viscosity and long-term air stability. Dip-coating involves substrate immersion and withdrawal in the solution at a constant speed. Spray-coating consists of forming an aerosol of the precursor solution and delivering it onto a heated substrate. The aerosol formation can be achieved by means of pressurised gas or by forcing a liquid through an ultrasonic nozzle. During spraying, solvent evaporation upon contact with the hot surface and film growth are taking place. This technique can achieve high-uniformity, high throughput, large-area coatings with high material utilisation efficiency and is compatible with roll-to-roll processing [32].

1.4.1 Nanoparticle route

The advantage of the nanoparticle (NP) inks over the molecular solutions lies in the properties of the pre-formed nanoparticles, including well-defined structure, high phase purity and stoichiometry, offering a range of tunable optical and electrical properties [51]. In this approach, the nanoparticles are first synthesised, then dispersed in common solvents to form a stable colloid and finally deposited onto the substrate to form a uniform coating. To synthesise the chalcopyrite NPs, methods such as hot-injection, solvothermal reaction or chemical welding are most commonly used [23][48]. The stable NP ink can be then coated onto the substrate at ambient conditions by any of the above described deposition techniques. A selenisation treatment of the as-deposited nanocrystals provides nanoparticle sintering and consequent densification of the absorber film. The drawback of the method is the use of organic ligands to control the kinetics, inter-particle sintering and nucleation growth and avoid agglomeration and consequent stoichiometry deviations [47]. The fluxing agents typically used are long-chain alkyl ligands (trioctylphosphite or oleylamine). Having insulating properties, these ligands impede the efficient transport between the NPs whilst their bulkiness causes the formation of cracks upon their removal from the film. Their removal can also leave undesired carbon impurities. Additional actions, such as heat, chemical treatment or ligand-exchange are often necessary to overcome these issues [51]. Moreover, nanoparticle synthesis methods are generally complicated low yield procedures requiring particular conditions (pressure, temperature, inertness) and tedious purification steps [48].

Direct use of single-phase ternary or quaternary NPs (CIS, CISe, CIGS and CIGSe) is very limited due to higher melting point compared to their binary phase particles, hindering effective NP sintering [51]. The most successful attempt involved a quaternary CIGS NPs suspended in a hexanedithiol ink developed by Guo *et al*., which was doctor-bladed onto the substrate. After the NaCl treatment and selenisation, this approach yielded 12% efficient CIGSSe solar cell [52]. Lower melting point and higher reactivity of particles containing phases other than the desired absorber phase offer the advantage of easier phase transformation and film densification. Currently the most successful multi-phase NP technique uses selenide NPs and a single-stage annealing process. This method was developed by Nanosolar reporting efficiency of 17.1% [53].

An alternative approach involving a hybrid nanoparticle/solution-based ink was found to present a promising compromise, keeping the benefits of NPs whilst reducing the drawbacks of the method. The molecular solution would act as a medium to improve binding between NPs whilst the NPs would act as nucleation sites and consequently improve the grain growth. Using this approach, the addition of CuS and In_2S_3 NPs to a molecular solution of metal chlorides resulted in improved grain growth and an increase of efficiency by 85% to 6.2% as compared to the NP-free solution [54].

1.4.2 Molecular solution-based methods

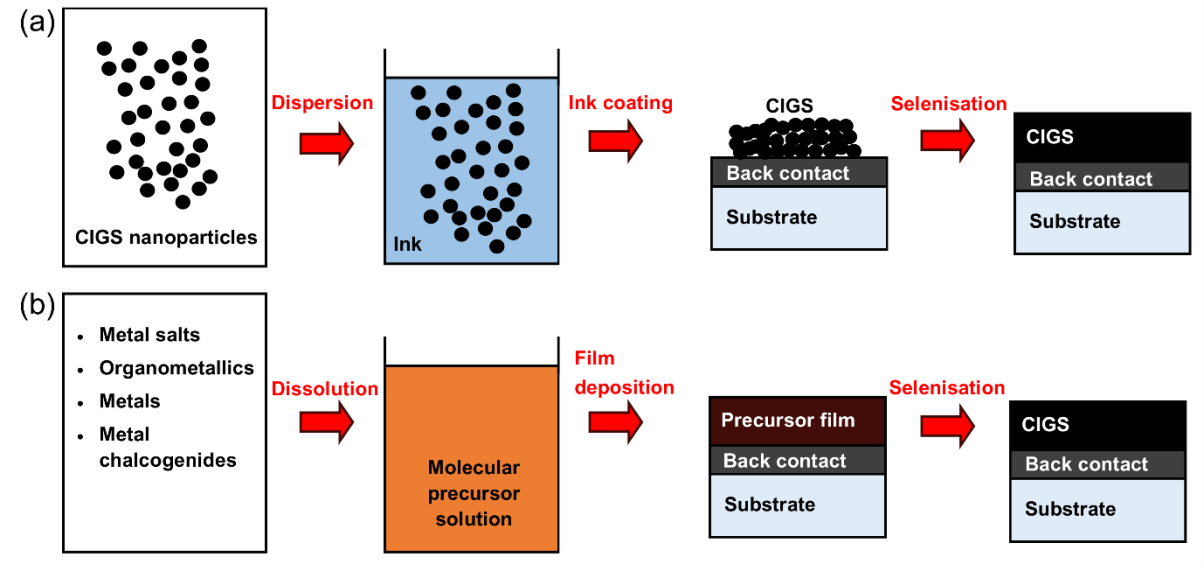

Figure 1.5 Schematic diagram comparing the nanoparticle (a) and molecular solution (b) CIGS deposition approach [48]**.**

Unlike the nanoparticle approaches described above, true solution techniques involve micron to nanometre-scaled entities (precursors) mixed at molecular level in a solvent. This approach allows deposition of films with the desired stoichiometry, high crystallinity and good uniformity. The stoichiometry of the solution is reflected in the film composition. A stable solution is then directly coated on the substrate using an appropriate technique and subsequently annealed to convert the precursors into a chalcopyrite phase. True solutions overcome the need for particle preparation and stabilisation and therefore present a more up-scalable and straight-forward option [55]. Moreover, the precursor homogeneity at the molecular scale may result in superior film uniformity. Widely used precursor materials for the solution-deposition of CIGS include metal oxides, metal salts, organometallics, metals and metal

chalcogenides. Both nanoparticle and molecular solution routes are illustrated in Figure 1.5. Table 1.2 summarises the advantages and drawbacks of different precursor materials for direct liquid coating.

Table 1.2 Comparison of precursor materials for direct liquid coating methods [32]

Material	***Advantages***	***Disadvantages***	***Reported efficiency***
Oxides	*Air-anneal to burn out residual carbon*	*Difficulty to remove oxygen from the final film*	*10.1%* [56]
Salts	*Off-the-shelf chemicals, high solubility and multiple options*	*Impurities from salts, difficulties of crystallisation*	*14.7%* [57]
Organometallics	*Formation of metallic layers or reactive amorphous oxides*	*Carbon or oxygen contamination in the final film, low thickness*	*13.3%* [58]
Metals	*Ideal precursor, no impurities*	*Tendency to alloy and aggregate, phase segregation*	*9.5%* [59]
Chalcogenides	*Readily reactive, contamination free*	*Strong covalent bonds, solvent toxicity*	*17.3%* [60]

1.4.2.1 Metal salts, oxides and organometallic precursors

Metal salts (chlorides, nitrates), oxides and metal-organics are the most convenient precursors to use because of their good solubility in wide range of solvents (including water and alcohol) which allows for safe and simple processing. Moreover they are cheap, readily available and can be stored long-term. The main problem limiting the efficiencies achieved by this route is the incorporation of unwanted impurities from the salts and the atmosphere (i.e. C, Cl, O) that remain in the film in unacceptably high quantities when deposition is performed below 300°C. Above 400°C a loss of S and Se results in the formation of oxide phases. A residual carbon layer is often found between the Mo back contact layer and the CIGS absorber causing poor adhesion and creating high series resistance. The use of binders to stabilise the solution and enhance its viscosity, thereby reducing the required number of coating cycles, is the major source of impurities. Moreover the bulkiness of the sacrificial ligands may cause cracks and film disruption upon their removal from the film [32][47].

In terms of efficiencies, Pan *et al*. formed metal-organic solutions of metal oxides in a combination of butyldithiocarbamic (BDCA) acid and ethanol. The BDCA was synthesised from butylamine with carbon disulphide. After spin-coating this stable and non-toxic solution followed by selenisation, over 10% efficient CIGSe solar cells

were achieved [56]. Uhl *et al.* reported 13.0% efficient $CuIn(S,Se)_2$ and 14.7% $Cu(In,Ga)(S,Se)_2$ by spin-coating and subsequent selenisation of a dimethyl sulfoxide (DMSO)- and thiourea (TU)-based ink containing metal chlorides. The absorber layers appeared to be free of both binary phases and a carbon rich layer. TU and DMSO were shown to coordinate with Cu(I) and In(III) oxidation states respectively, resulting in stable molecular inks [57]. From the scalable deposition techniques, 10.5% efficient CIGSSe was achieved by spray-coating of halide-based aqueous solutions, while 10.7% Se-rich CIGSSe was reported from a nitrate-based aqueous precursor solution [61][62]. Berner *et al.* prepared a Cu-In-Ga solution by dissolving metal carboxylates in a nitrogen containing base. Blade-coating of the precursor solution resulted in CIGSe devices with 11% efficiency, which was further improved to 13.3% after intentional Na doping [58]. The inkjet printing route was taken by Lin *et al.* dissolving Cu, In and Ga nitrates in alcohol-based solvents, yielding over 11% efficient CIGSSe devices after annealing in Se/H_2S atmosphere [63].

1.4.2.2 Metal chalcogenides in hydrazine

Metal chalcogenides form the ideal precursor materials as they only contain the required elements (Cu, In, Se, S). Consequently no undesired impurities will be introduced into the solution by the precursor materials. However, the solubility of metal chalcogenides is very poor in most common solvents due to strong covalent bonds, hence limiting their use as precursors for CIGS solar cells. Mitzi *et al*. demonstrated that using hydrazine as a solvent helps to overcome this problem. In the reaction referred to as ‘dimensional reduction’, the metal-chalcogenide framework is broken and chalcogenide anions are separated by small hydrazinium cations ($N_2H_5^+$). Upon annealing, the small, weakly coordinating hydrazine species leave the film without affecting its properties and without leaving any undesired impurities behind. CIGS precursor solutions are prepared by separately dissolving In_2Se_3 with additional Se, Cu_2S with additional S and Ga with added Se, followed by mixing, spin-coating and crystallisation on a hot plate at 540°C. This approach developed at IBM’s T.J.Watson Research Centre, yielded CIGS efficiencies of 15.2% with a grain size close to the film thickness [64]. Since then, the efficiencies using the hydrazine method were further increased to 17.3% [60]. This method is so far the most successful solution-based approach. Despite efficiencies getting closer to those

of vacuum-based devices, the cells still suffer from a larger open-circuit voltage deficit.

The benefits hydrazine offers as a weakly coordinating, strongly reducing, polar and clean solvent are clear. However, the drawback of this method is the toxic, highly reactive and carcinogenic nature of hydrazine. This raises a number of safety and environmental concerns. Consequently the hydrazine-based approach is unsuitable for the large-scale industrial application [23]. An alternative method using Cu-In hydrazinium precursors in non-hydrazine solvents (ethanolamine/DMSO) was developed by Yang Yang *et al*. [65]. They found that DMSO coordinates with metal cores, Cu and In, breaking Cu-S and In-Se bonds of Cu_2S and In_2Se_3 pre-prepared in hydrazine. Ethanolamine provides strong intramolecular interaction and reducing capability, and stabilises the obtained metal chalcogenide. Uniform and controllable CIGS films were obtained, however low film thickness due to non-optimised solution viscosity for spin-coating resulted in a device efficiency of only 3.8%. This efficiency is however comparable to the hydrazine method with CIGS solar cells of a similar thickness (300 nm) [65]. Despite the potential of this method, the use of hydrazine is not eliminated completely; therefore other less-hazardous methods have to be considered for industrial application.

1.4.2.3 Amine-thiol solvent system to dissolve metal chalcogenides

To avoid the use of hydrazine, while keeping the benefits of metal chalcogenide precursors, more environmentally-friendly solvents were explored to dissolve indium and copper species. Webber *et al*. came with a novel, relatively non-hazardous binary solvent mixture of 1,2-ethanedithiol (EDT) and 1,2-ethylenediamine (EDA) that can readily dissolve a series of nine bulk V_2VI_3 (V = As, Sb, Bi; VI = S, Se, Te) chalcogenides at room temperature (RT) and atmospheric pressure leading to good quality, highly crystalline semiconductor films with negligible organic content. The mechanism of this reaction is not yet fully understood but the hypothesis suggests the formation of EDA-ligated thiolatochalcogenometallate anions stabilised by EDA-H^+ cations [66].

Table 1.3 Solar cell parameters of devices produced by various deposition methods

Method	PCE %	V_{OC} mV	J_{SC} mA/cm^2	FF %	Deposition	Post-treatment	Ref
Vacuum-based techniques							
3-stage co-evaporation	22.6	741	37.8	80.6	3-stage co-evaporation	PDT	ZSW [67]
Co-sputtering	22.9*	746	38.5	79.7	Sputtering from metallic targets	Sulfurisation after selenisation (SAS)	Solar Frontier [37]
Non-vacuum techniques							
Electrodeposition	17.3	621	37.3	74.7	ED of metallic precursors	Annealed in Se/S	Nexcis [50]
Nanoparticles	17.1	651	34.6	75.9	Printing of a slurry containing selenides and metal oxides	Single-stage annealing	Nanosolar [53]
Molecular solution	17.3	660	35.8	73.4	Metal chalcogenides in hydrazine, spin-coating	Annealing at 500-600°C	Suzhou Raysoll Nanotech [60]
Molecular solution approach							
Metal chalcogenides in hydrazine	17.3	660	35.8	73.4	Spin-coating	Annealing at 500-600°C	[60]
Metal chalcogenides in amine/thiol	12.0	622	28.7	67.5	Spray-coating	Selenisation at 540°C	This work [68]
Metals in amine/thiol	9.5	528	26.6	67.5	Spin-coating of pure metals	Selenisation at 550°C	[59]
Metal salts in DMSO/TU	14.7	661	31.2	71.5	Spin-coating	Selenisation <550°C	[57]
Metal oxides in BDCA and ethanol	10.1	561	27.6	65.0	Spin-coating	Selenization at 540°C	[56]
Metal carboxylates in methanol and N-containing base	13.3	532	36.5	68.5	Blade-coating	Selenisation at 600°C	[58]

*This efficiency record was recently broken and the new record is now 23.35% still held by Solar Frontier. Details about this cell are not yet published.

Since then, several groups have used this amine-thiol solvent system for application in CIGS solar cells. Among them, one of the first was our CREST laboratory, where Arnou *et al*. developed the CIGS solution-processing approach using metal chalcogenides and progressively reached stable efficiencies of up to 10% [69][70]. Wu *et al*. successfully dissolved pure metals (Cu, In, Ga) in EDA/EDT forming a

molecular solution. After spin-coating several layers, intermediate annealing on a hot plate at 350°C and selenisation at 550°C, solar cells with an efficiency of 9.5% were achieved [59]. Agrawal *et al*. use a similar solvent structure, monoamine-dithiol, resulting in pure selenide 12.2% efficient CIGSSe. This was achieved in the controlled environment of a nitrogen-filled glovebox and using spin-coating [71].

In this work, a diamine-dithiol solvent mixture is used to dissolve Cu_2S, In_2S_3 and Ga with additional Se at room temperature and without the need for an inert atmosphere in a glovebox. A single-phase $Cu(InGa)(S,Se)_2$ with efficiencies up to 12.0% can be obtained after deposition and selenisation. The devices are fabricated by spray-coating of the precursor solution and subsequent selenisation in the tube furnace or RTP. Similar efficiencies to the two previous groups can be achieved with the advantage of a scalable deposition technique and atmospheric conditions employed here. A brief summary of different CIGS fabrication processes and research efficiencies achieved are summarised in Table 1.3.

1.5 Scope of the thesis

1.5.1 Motivation for this work

Development of a scalable, non-toxic, reproducible and relatively low-cost deposition method for fabrication of efficient CIGS solar cells is the motivation behind this thesis. The loss mechanisms in the solution-processed CIGS are related to smaller grain sizes, impurities from the precursors and imperfect phase transformation. They are specific for each precursor/deposition/post-treatment strategy and differ from the loss mechanisms in the conventional vacuum-based techniques. There have been limited studies providing deep understanding of the properties and loss mechanisms in solution-based chalcopyrite-structured solar cells.

The objectives of this thesis are:

- Further develop the amine-thiol based molecular solution approach involving dissolution of metal chalcogenides and precursor deposition by spray-coating.
- Reduction of $MoSe_2$ interface layer thickness at the back contact and improvement of the heterojunction quality.
- Identification of the absorber layer limitations and formation of a large-grained absorber with suitable thickness, composition and doping properties.

- Ultimately achieving improved device efficiencies.

1.5.2 Structure of the thesis

After the introduction of this thesis providing a broad context and state-of-art of the solution-processing of CIGS solar cells, the experimental Chapter 2 will follow. This chapter will describe the deposition procedures involved in fabrication of each constituting layer of the solar cell and the characterisation tools employed to study the electronic and morphological properties. Four result chapters will follow. Chapter 3 focuses on the CIGS back contact engineering and necessity of the $MoSe_2$ thickness control in solution-processed CIGS solar cells. Chapter 4 studies the properties of the CIGS/CdS interface through experiments with air-annealing of the junction. The two remaining chapters deal with the CIGS absorber quality, more specifically looking at the paths for improvement of absorber crystallinity. Chapter 5 describes a development and optimisation of a suitable selenisation process to produce crystalline CIGS absorber films and the effects of varying Cu content through the absorber depth. Chapter 6 develops an efficient way of intentional Na-doping of the absorber, in theory producing improved grain growth and GBs passivation enhancing electronic properties of the device. The last chapter provides concluding remarks and an outlook.

CHAPTER 2

Vacuum-free CIGS thin films: solar cell fabrication and characterisation

2.1 Scope

The first part of this chapter outlines the solution-based CIGS solar cell fabrication process, from substrate to front contacts. The CIGS solar cells presented here are prepared in substrate configuration, starting with Mo deposition onto the glass substrate, followed by the light-absorbing layer, buffer layer and front contact. The light is coming to the absorber through the front contact TCO.

Table 2.1 Chemicals involved in the CIGS solar cell fabrication process

Chemicals	State	Purity (%)	Supplier	Purpose
In_2S_3	powder	99.98	Alfa Aesar	CIGS precursor
Cu_2S	powder	99.5	Alfa Aesar	CIGS precursor
Ga	metal pieces	99.9999	Acros Organics	CIGS precursor
Se	powder	99.999	Alfa Aesar	CIGS precursor
1,2-ethanedithiol	liquid	≥ 98.0	Sigma-Aldrich	CIGS precursor
1,2-ethylenediamine	liquid	≥ 99.5	Sigma-Aldrich	CIGS precursor
Ethyl acetate	liquid	≥ 99.5	Alfa Aesar	CIGS diluent
Se	pellets	99.999	Alfa Aesar	Selenisation
NaCl	powder	≥ 99.5	Fisher Scientific	Dopant
Thiourea	powder	≥ 99.0	Sigma-Aldrich	CdS buffer layer
$CdSO_4$	powder	≥ 99.0	Sigma-Aldrich	CdS buffer layer
NH_4OH	liquid	28-30%	Acros Organics	CdS buffer layer
Mo	sputtering target	99.95	Testboune	Back contact
ZnO	sputtering target	99.99	Plasmaterials	Window layer
AZO 98 wt%	sputtering target	99.99	Plasmaterials	Window layer
Ag	pellets	99.99	Kurt Lesker	Front contact grid

Much of this work is dedicated to the structural, compositional and electrical characterisation of CIGS absorbers and solar cells. A combination of various

measurement techniques provides valuable insight into the material morphology and electronic properties. This can be used to better understand the solar cell performance. The characterisation techniques employed in this work are presented in the second part of this chapter. Table 2.1 summarises the chemicals used in the CIGS solar cell fabrication.

2.2 CIGS solar cell processing steps

2.2.1 Mo back contact and Mo-N diffusion barrier

CIGS solar cells were fabricated in substrate configuration on 1 mm thick SLG or Corning Eagle XG glass substrates. SLG is the most commonly used substrate for CIGS thanks to its low-cost, microscopically smooth surface, stability at elevated processing temperatures and high sodium content which provides beneficial doping to the CIGS absorber [32]. For the purpose of studying intentional alkali doping of the CIGS absorber, alternative alkali-free Corning Eagle XG glass substrates were used [72].

Mo as an electrical back contact is a typical choice for CIGS solar cells and offers relatively low sheet resistance, chemical and thermal inertness and mechanical hardness necessary for cell scribing [32][48]. For this work, Mo was deposited by DC sputtering using a Nordiko magnetron sputtering system. Two separate layers were deposited to encourage good adhesion and conductivity with a final combined thickness of ~900 nm and sheet resistance of ~0.4 Ω/sq. The sputtering setup consisted of a Mo target (30 cm x 10 cm) placed at a working distance of approximately 10 cm from a rotating drum carrying 5 cm x 5 cm glass substrates. The deposition parameters are described in detail in Chapter 3. As an alternative for certain experiments, Mo-coated SLG substrates of ~600 nm with a sheet resistance of ~0.2 Ω/sq provided by M-Solv Ltd. were employed.

The reaction of Mo and Se during thermal processes involved in CIGS absorber preparation results in the formation of a $MoSe_2$ interlayer between Mo and CIGS. The $MoSe_2$ creates an adequate ohmic contact to the p-type absorber if sufficiently thin [73][74]. However solution-processed CIGS absorbers often suffer from excessively thick $MoSe_2$ layer formation which causes adhesion problems and high series resistances [75][76]. Various diffusion barriers including metal oxides and

nitrides have been studied in order to prevent Se diffusion to the device back contact [77][78][79]. In this work, a Mo-N/Mo bilayer was deposited by DC sputtering on top of the initial Mo layer to effectively control the $MoSe_2$ thickness. In this bilayer, Mo-N acts as a barrier against Se diffusion whilst the overlying Mo is converted into $MoSe_2$ to ensure an ohmic contact to the absorber. This is discussed in greater detail in Chapter 3.

2.2.2 CIGS absorber layer

The CIGS solution-based absorber formation involves three steps: molecular precursor solution preparation, deposition via spray-coating and precursor film annealing in selenium atmosphere (selenisation). The entire precursor film preparation is carried out in air inside a fume hood. Selenisation is subsequently performed in an enclosed furnace using nitrogen as a carrier gas. The general processing steps are schematically illustrated in Figure 2.1.

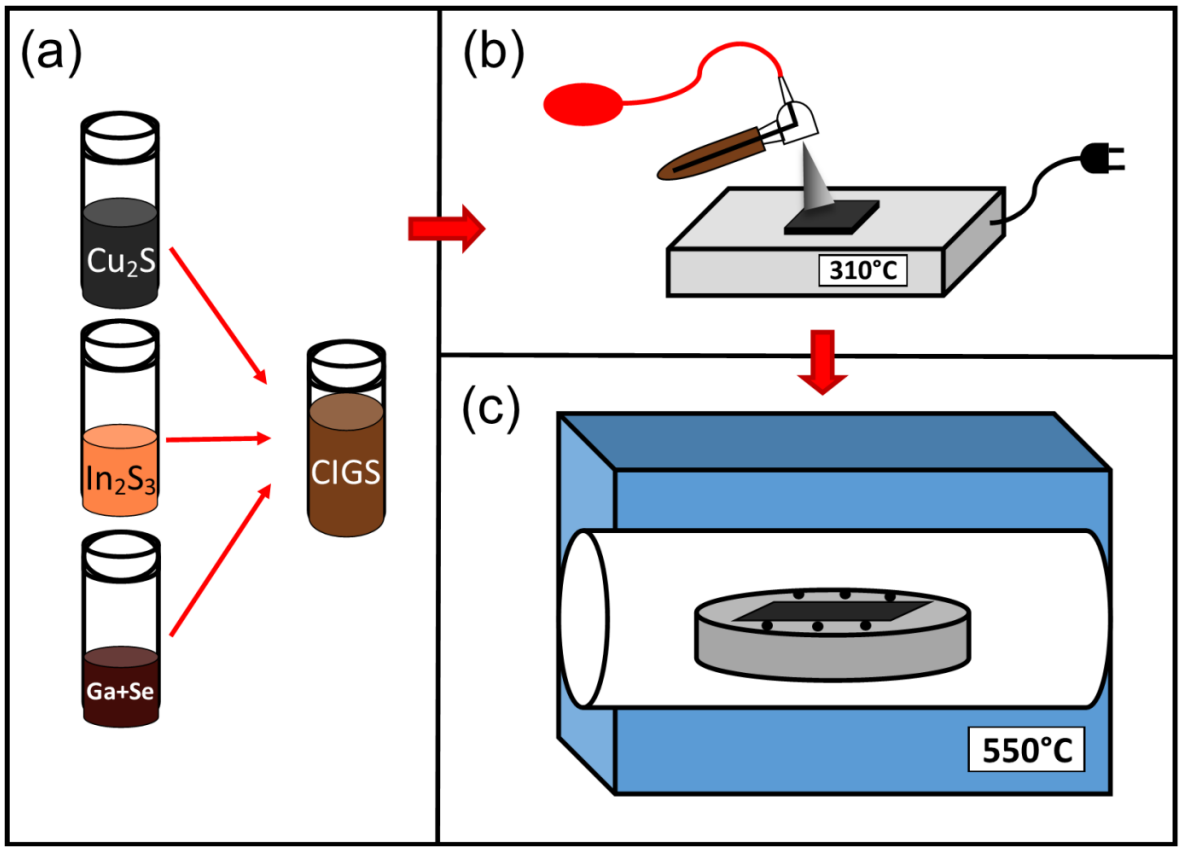

Figure 2.1 Schematic diagram of CIGS absorber fabrication consisting of three stages: (a) CIGS molecular precursor solution preparation from individual chalcogenide precursors, (b) CIGS solution deposition onto Mo-coated substrates via spray-coating on a hot plate preheated at 310°C and (c) post-deposition precursor film annealing in selenium atmosphere using tube furnace or RTP at 550°C.

2.2.2.1 Molecular precursor solution preparation

CIGS precursor solution was prepared using the relatively non-hazardous binary solvent mixture of 1,2-ethanedithiol (EDT) and 1,2-ethylenediamine (EDA). As previously shown by Webber *et al.*, this 'alkahest' solvent mixture in volume ratio of 1:10 EDT:EDA readily dissolves a number of chalcogenides at room temperature (RT) and atmospheric pressure and can be used for preparation of solution-processed solar cell absorbers [66][80]. Metal chalcogenides are used as a starting material as they are free of detrimental impurities such as carbon, oxygen and halogens, which can cause deterioration of device electronic properties or impede grain growth [81][82]. Their low solubility in common benign solvents makes them a rare choice of a starting material however. They are typically used in combination with hydrazine as a solvent, which provides a highly effective but also extremely hazardous approach [83]. In this work, the EDA/EDT solvent system was employed to dissolve metal chalcogenide precursor powders of In_2S_3, Cu_2S and metallic Ga with excess Se to form precursor solutions with a target concentration of 0.2 M.

Prior to the material dissolution step, the vials were purged with nitrogen using nitrogen-filled balloons and the solvents were introduced through a septum in the lid using syringes to minimise the solution's exposure to air. Mild heating (~50°C) of the Ga precursor solution in an ultrasonic bath was required for several minutes in order to melt the Ga metal pieces to allow its dissolution in presence of excess chalcogen. The solutions were left stirring overnight at RT. The coloured suspensions formed initially are converted over time into clear, optically transparent solutions. The three individual precursor solutions were then combined in predetermined ratios to achieve the desired film composition. In this work, $Cu_{0.9}In_{0.7}Ga_{0.3}(S,Se)_2$ was selected as the 'base-line' composition. [Cu]/[Ga+In] (CGI) and [Ga]/[Ga+In] (GGI) ratios of 0.88-0.95 and ~0.3 respectively were found to lead to best performing CIGS solar cells with bandgaps in the range of 1.1-1.3 eV [42].

4.5 mL of Cu_2S, 3.5 mL of In_2S_3 and 3 mL of Ga+Se solutions were taken from each respective 0.2 M stock solution and combined in an empty vial. The resulting CIGS solution was then left stirring for approximately 3 hours prior the deposition. The stirring time of individual or mixed precursor solutions was not found to have a significant effect on the deposition or film properties so long as the solutions were

fully dissolved and optically transparent. It should be noted that the approach is identical to prepare CIS precursor solutions. In_2S_3 and Cu_2S stock solutions are combined targeting Cu-poor composition (Cu/In = 0.8) in order to avoid formation of undesired secondary Cu_xSe phases [42]. Unlike the hydrazine method, excess chalcogen is only required for dissolution of the Ga precursor. For 1 mmol of Ga, adding 2 mmol of Se led to complete dissolution when assisted by mild heating [64]. Figure 2.2 shows a photograph of the individual and mixed precursor solutions.

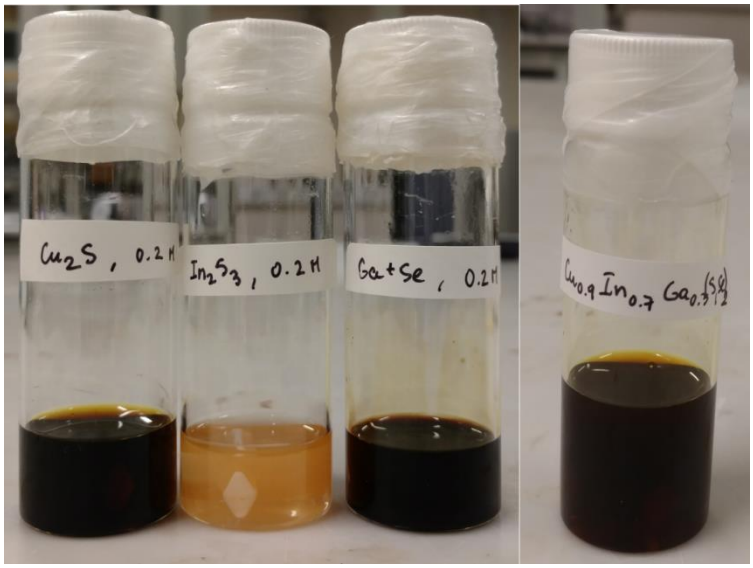

Figure 2.2 Photograph of the dissolved individual precursor solutions (Cu_2S, In_2S_3 and Ga+Se) with concentration of 0.2 M. The CIGS solution on the right-hand side of the picture was prepared mixing the three stock solutions with the ratio to target a $Cu_{0.9}In_{0.7}Ga_{0.3}(S,Se)_2$ composition.

2.2.2.2 Precursor solution deposition via spray-coating

Prior to deposition, the mixed CIGS precursor solution was further diluted with ethyl acetate (EA) (CIGS: EA 2:1 v/v). The dilution was found to be beneficial for the precursor film smoothness and appropriate thickness. A number of common solvents including acetone, methyl ethyl ketone (MEK) and DMSO were also tested as potential diluents. These solvents were selected based on their physical properties such as boiling point, viscosity, polarity, dielectric constant and surface tension. Among the studied solvents, ethyl acetate was found to be the most suitable choice, causing no interaction with the complexes already formed, with suitable wetting properties on the substrate and creating a densely packed, smooth absorber layers. Further details about the diluting solvent optimisation can be found in [84]. Figure 2.3 shows SEM surface images of selenised CIS films prepared with and without dilution.

The final absorber film from non-diluted precursor solution was thicker and its surface was significantly rougher, containing a number of cracks. Such a rough absorber surface may cause problems at the interfaces with buffer and window layers as their thicknesses might not be sufficient to provide full surface coverage [85].

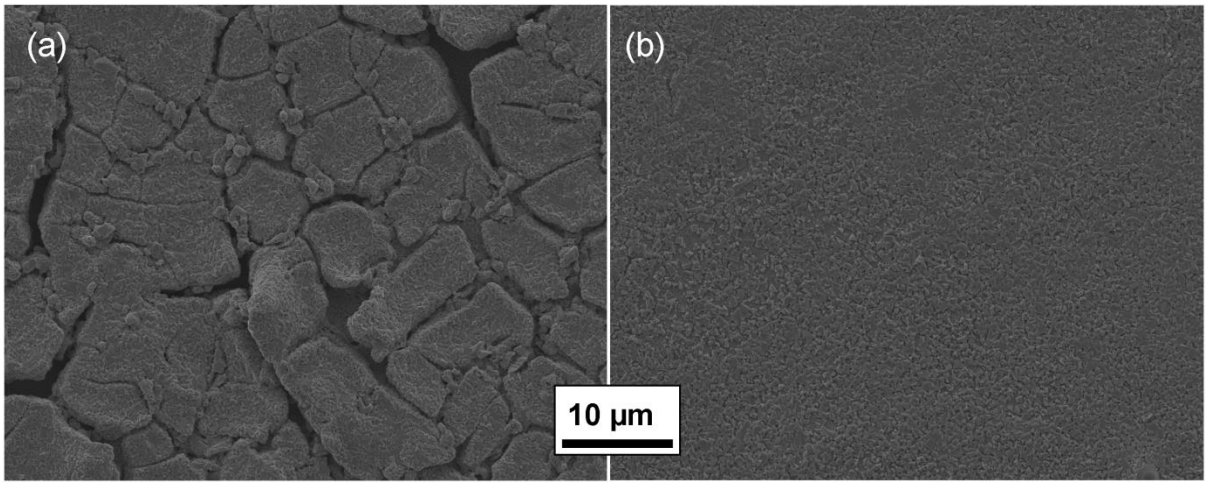

Figure 2.3 SEM surface images of selenised CIS thin films deposited via spray-coating of precursor solution without any dilution (a) and CIS solution being diluted using ethyl acetate (2:1 CIGS:EA v/v) (b).

After combining ethyl acetate with the CIGS solution, the mixture was initially immiscible, but became clear after stirring for approximately 30 min at RT. At this point, the solution was filtered (0.45 µm PTFE) and transferred into an enclosed test-tube using a syringe. Finally, the septum stopper covering the test-tube was replaced with a glass chromatography atomiser. Spraying was carried out in ambient air inside a fume cupboard. To atomise the solution, a rubber bulb connected to the atomiser is compressed. The incoming air forces the liquid to rise from the test-tube reservoir through the capillary. At the top, the solution meets the stream of air where it forms an aerosol and is carried to the substrate. The spraying procedure was performed manually, while keeping the spraying distance and angle roughly the same (~15 cm and ~45° respectively).

Prior to spraying, the Mo-coated substrates were placed on a hot plate preheated at 310°C. Up to three 5 cm x 5 cm substrates were sprayed at time. To achieve a suitable absorber thickness, spraying was repeated several times. Typically, six layers form a suitable CIGS absorber thickness (1.5-2 µm) after selenisation. Between individual spray steps, the film was dried for 150 s to evaporate residual

solvents from the film. The deposition and drying temperature of 310°C was selected based on thermogravimetric analysis (TGA) of CIS precursor solutions [69]. Low drying temperature results in solvent trapped in the film and its evaporation during selenisation creates extensive pinholes. Too elevated drying temperature causes Mo oxidation and the rapid evaporation of the solvent leaves voids and cracks in the film. After the final layer was deposited, the precursor film was dried for 240 s, then allowed to cool naturally. The as-deposited precursor films were stored in ambient air inside a dessicator between the deposition and selenisation stages. When properly stored, the as-deposited films were found to be stable for several months.

2.2.2.3 Post-deposition annealing in Se atmosphere: selenisation

In the final absorber preparation step, the precursor films were annealed at high temperature in the presence of selenium vapour to form a crystalline CIGS phase. Selenisation is a critical step in the absorber formation and defines the properties of the final thin film (phase purity, compositional uniformity, film density and surface roughness). It therefore needs precise optimisation in order to obtain acceptable film morphology, and to prevent delamination, cracks and voids resulting in reduced device performance [86][87][88]. The obtained film depends strongly on the selenisation reactor design and conditions used (temperatures, pressures and duration) [75][86].

Various selenisation approaches were employed during the course of this work to achieve acceptable absorber morphology and electronic properties. Chapter 5 is devoted to optimisation of the selenisation process and processing conditions for alkahest-based CIGS solar cells. For most of the experiments described in this work, selenisation was performed using either a two-temperature-zone tube furnace or an RTP oven. The sample (2.5 cm x 5 cm) was placed inside a graphite box filled with Se pellets (typically 300-800 mg). The selenisation tube containing the graphite box was first purged with nitrogen several times to remove all the air. The tube was then sealed creating a closed system favourable to obtain a high Se partial pressure. The starting pressure was chosen depending on the reactor type and size. Too low a pressure causes the Se to evaporate too early in the process resulting in poorly crystalline absorber. Higher pressure delays the Se evaporation; however the increase in pressure with temperature ramping has to be taken into account so that

the final pressure in the tube does not exceed atmospheric pressure. The dwell temperature was set to 540-550°C for up to 90 min. Temperatures above 500°C are often necessary to transform the deposited elements into the crystalline CIGS phase and the higher the temperature, the greater the degree of crystallinity of the resulting film [87]. During selenisation, the Se pellets melt and evaporate, creating a high partial pressure over the sample. Since the graphite box is not hermetically sealed, some Se vapour escapes from the box. The overpressure inside the box raises the lid and some Se vapour flows out to establish an equilibrium between internal and external gas pressure [86].

2.2.3 CdS buffer layer

CdS is the most appropriate buffer layer choice used in the highest efficiency CIGS solar cells. Its beneficial effects include increased carrier lifetime, optimum band alignment, and improved lattice matching at the heterojunction interface. Moreover, the CdS layer provides a protection of the junction against sputter damage during the window layer TCO deposition steps [89]. CdS deposition by chemical bath (CBD) has been shown to provide good coverage of a rough CIGS surface while having benign or even beneficial effects with respect to the absorber surface [90]. CBD helps to remove surface metal oxides and acts as a medium for Cd incorporation to the CIGS surface [91][92]. Cd incorporation during a partial electrolyte (PE) pre-treatment, most likely into V_{Cu} surface defects led to surface n-type doping and was shown to improve device V_{OC} and FF [93].

In the devices fabricated for this work, CdS buffer layers with an approximate thickness of 80 nm were grown on the top of the CIGS absorbers using CBD. The CdS CBD recipe was based on the optimisation study for high efficiency CIGS solar cells carried out by Contreras *et al.* [89]. The chemical bath, held at a temperature of 70°C consisted of 183 mL of DI water, 25 mL of $CdSO_4$ (0.015 M), 12.5 mL of thiourea (1.5 M) and 32.6 mL of NH_4OH (28-30%). $CdSO_4$ and thiourea provide Cd and S precursors and NH_4OH acts as a complexing agent. The process started with a 5 min Cd^{2+} and NH_3^+ PE treatment of the immersed samples using all the bath constituents except thiourea. Thiourea was then added and CdS deposition was allowed to proceed for ten minutes under constant stirring of the bath using a magnetic stirrer. At the end of the process, samples were taken out, immediately

rinsed with DI water, and dried under compressed air. Air-annealing of the junction subsequent to the CBD was found to be beneficial for the solar cell performance increasing the V_{OC} of the device by promoting the Cd interdiffusion into the absorber surface [94]. The conditions used and the effects of air-annealing are presented in detail in Chapter 4.

2.2.4 Window layer and metal grid

The window layer is formed of a bilayer consisting of a thin (~50 nm) high-resistivity intrinsic zinc oxide (i-ZnO) layer followed by a thick (~500 nm) highly conductive Al-doped ZnO (AZO) layer. Both layers were deposited directly onto the CdS layer by RF magnetron sputtering from single ceramic targets.

The incorporation of an i-ZnO layer between CdS and AZO has been routinely used in combination with CBD CdS to produce high efficiency CIGS solar cells. The i-ZnO layer is thought to protect the underlying CdS from sputter damage from highly energetic particles during AZO deposition and serves as a seed layer to enhance the grain growth of the AZO [95]. Moreover, it was shown by Rau *et al.* that the i-ZnO's beneficial role also consists in preventing spatial inhomogeneities (local recombination sites) from dominating the device V_{OC} [96]. Finally, it is generally recognised that i-ZnO can supress leakage currents between the absorber and the TCO due to its high resistivity. Its presence is therefore especially important for devices with rough absorber surfaces [85][97].

TCOs are wide-bandgap degenerately-doped n-type metal oxide semiconductors. The purpose of the TCO layer is to admit as much sunlight to the junction region and absorber layer as possible while forming a low-resistive contact to the device. A suitable TCO should exhibit both, high transmission (> 80% in the visible range) and low resistivity (< $1x10^{-3}$ Ω.cm.) [98]. AZO provides a suitable trade-off between conductivity and transparency for application in CIGS solar cells and therefore it is also the most common choice for this technology. In this work, AZO was RF sputtered at RT from a 2 wt% Al_2O_3-doped ZnO target. Prior the deposition, the chamber base pressure is in the 10^{-7} Torr range and the sputtering was carried out at working pressure of 1 mTorr in presence of 7 sccm of Ar. The typical sheet resistance of the AZO thin film after 1h of deposition is approximately 15 Ω/sq.

Finally, a metallic grid was deposited on top of the window layer to effectively collect the current from the entire active area of the cell. Approximately 500 nm of silver was thermally evaporated through a shadow mask onto the TCO. Individual cells of an area of 0.25 cm^2 were mechanically scribed. No AR-coating was performed on any of the presented devices. Figure 2.4 shows a photograph of the various thin films which make up the finished device.

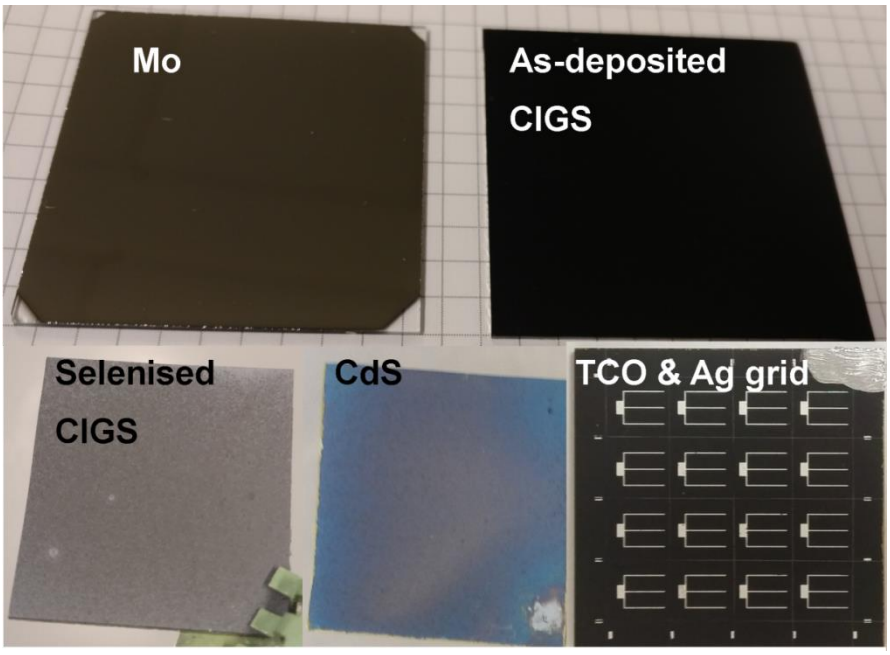

Figure 2.4 Photograph showing visual aspect of the Mo, as-deposited and selenised CIGS, CdS and AZO thin films with Ag grid.

2.3 Material characterisation techniques

2.3.1 Electron microscopy (SEM, TEM) and Energy dispersive X-ray spectroscopy (EDX)

Use of a scanning electron microscope (SEM) allows for detailed film imaging and identification of structural features and defects at the nanometre length scale. The technique provides information about film thickness and allows for qualitative assessment of film morphology, crystallinity and surface roughness. To form the image, an emitted beam of accelerated electrons interacts with the studied specimen. Secondary electrons (electrons ejected from the sample after collision with higher energy beam electrons) and backscattered electrons (beam electrons reflected from atomic nuclei) are collected by the detector [99]. Prior to imaging, the samples were coated with a thin (~10 nm), conductive layer of Au/Pd to reduce the dielectric charging effects of the glass substrate. SEM surface and cross-section images of the

CIGS solar cells were acquired using JEOL 7800F field emission gun scanning electron microscope (FEG-SEM) with acceleration voltage of 5 kV and electron-beam current of 8 A.

Transmission electron microscopes (TEM) use a similar principle except that electrons are transmitted through much thinner samples prior to collection rather than being reflected from the sample surface. As a result, TEM images have even higher magnification than those from other electron microscopes, and can provide detail down to angstrom scales. Consequently very small features, thin layers, interfaces and grain boundaries often invisible by SEM can be studied in greater depth using TEM [100]. To prepare TEM cross-section samples through the device and into the glass substrate, a standard in-situ lift out method was performed by Focused Ion Beam (FIB) milling using a dual beam FEI Nova 600 Nanolab [101]. The prepared specimen was coated with a thin Au/Pd alloy layer prior to analysis using an FEI Tecnai F20 scanning TEM (STEM) in bright or dark field imaging mode as well as in high angle annular dark field (HAADF) mode as appropriate. The system is equipped with a silicon drift detector (SDD) and has an operating voltage of 200 kV.

Both types of microscopes are equipped with an Oxford Instruments EDX detector for elemental quantification of the films. Along with the secondary and backscattered electrons, X-rays are also emitted from the specimen upon bombardment with electron beam during SEM/TEM imaging. These are captured by the EDX detector which identifies different elements based on their X-ray energy. EDX elemental mapping is more accurate in combination with TEM however, due to lower sample thickness and consequent lower interaction volume [102]. The interaction volume is visualised in Figure 2.5 a) [103]. When analysing the elemental spectrum of the $MoSe_2$ layer using EDX/SEM (Spectrum 3 in Figure 2.5 b)) acquired with a 20 kV acceleration voltage, elements from other layers are detected along with Mo and Se. Consequently the evaluation of impurities in this layer is inaccurate. Moreover, for non-homogeneous, bulk samples, the poor detection limit for light elements such as C and Na and peak overlapping of some elements of interest, such as Mo and S is a significant drawback (Figure 2.5 c)) [104]. Hence in this work EDX in combination with SEM was used solely for relative comparison of similar samples.

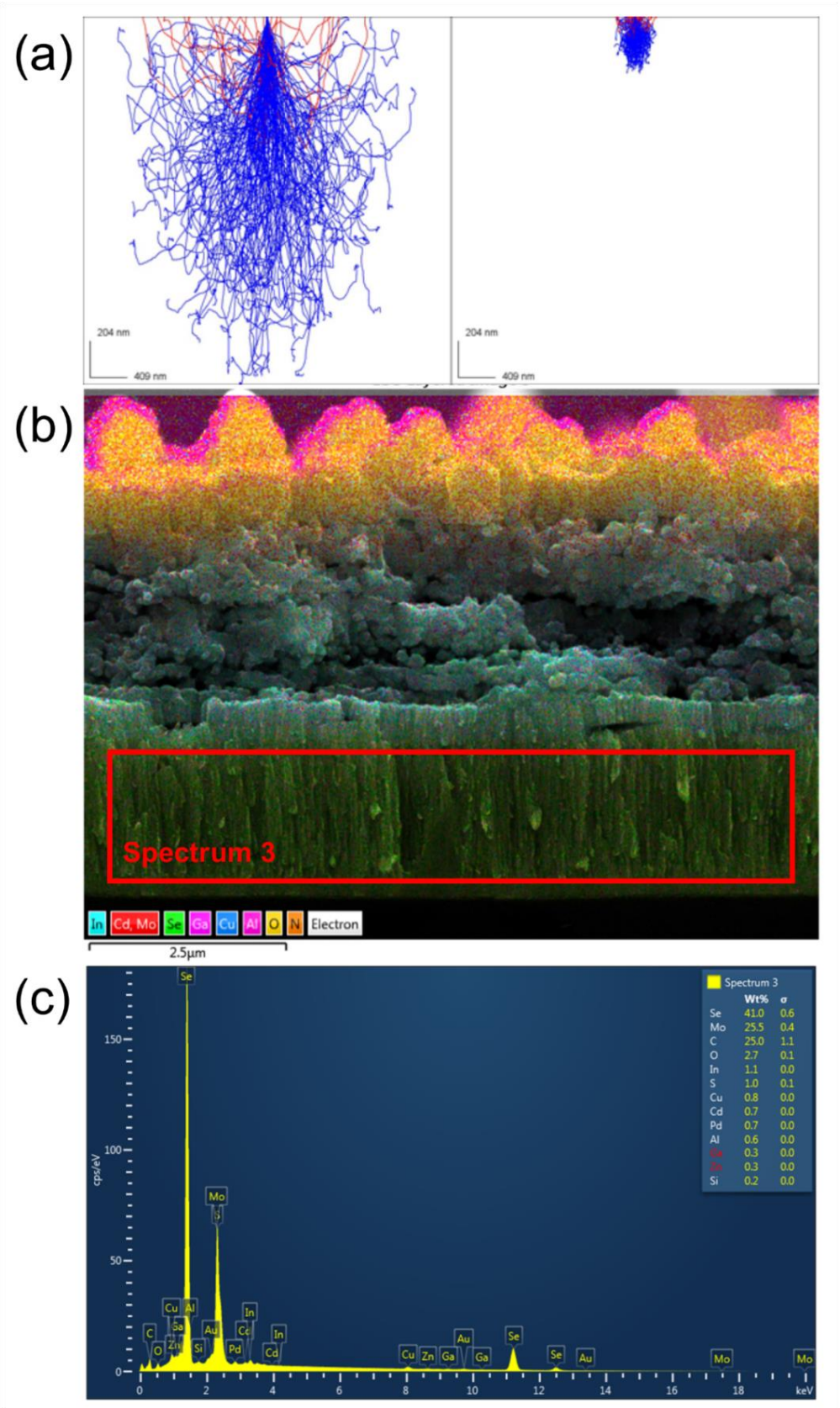

Figure 2.5 Interaction volume visualised by Monte Carlo simulation of Al sample at 15 kV (left) and 5 kV (right) interpreted from [103] **(a), SEM image at 20 kV with EDX mapping of CIGS cross-section (b) and elemental spectra of the $MoSe_2$ layer (Spectrum 3) showing detection of elements from all layers (c).**

2.3.2 X-ray diffraction (XRD)

XRD analysis was used to identify the crystal structure and provide an indicative assessment of the crystal quality of the following materials: Mo, Mo-N, CIGS and NaCl. XRD patterns were collected using Bruker D2 Phaser benchtop diffractometer. The system is equipped with Cu-K_α radiation source (λ = 1.5418°) and Lynexeye^{TM} detector. The divergence slit and antiscatter plate were set to 1 and 3 mm respectively. During the acquisition, the sample was rotating at 15 rpm. The data were recorded between 2θ = 20-90° with step size of 0.02°.

In this measurement technique, the incident X-ray beam interacts with the crystal lattice of the studied material. Constructive interference resulting in peak formation happens when conditions satisfy Bragg's law [105]:

$$n\lambda = 2d\sin\theta \qquad [2.1]$$

where λ is the incident wavelength, d is the atomic layer spacing in crystal lattice and θ is the diffraction angle. The obtained XRD pattern can then be compared with those in the standard crystallographic databases, such as the International Centre for Diffraction Data (ICDD).

2.3.3 Raman spectroscopy

Raman spectroscopy is a non-destructive optical technique allowing for identification of peaks and bands characteristic of different phases and structural defects such as secondary phases and defective chalcopyrite layer often referred to as an order defect compound phase (ODC), which are not detectable using XRD. The Raman technique comprises inelastic scattering of laser-excited radiation with molecular vibrations in the material. The inelastically scattered photon loses part of its energy. The Raman scattering signal shows a frequency shift relative to the frequency of the excitation light, providing information about which atoms vibrate in the crystalline lattice [102].

Micro-Raman spectra were measured using a Jobin-Yvon LabRam HR system equipped with an x50 objective lens and an He-Ne laser (λ = 632.817 nm) in backscattering configuration. The estimated laser spot size is 1.5 µm. All spectra were calibrated with respect to the silicon Raman mode at 520.7 cm^{-1}. The

crystalline structure and chemical composition of the sample determines the shape, frequency and intensity of Raman peaks and bands.

2.3.4 X-ray fluorescence (XRF)

XRF is a non-destructive and relatively fast analysis method allowing the evaluation of thickness and composition of multi-layered structures. The technique uses Rh-L X-rays to irradiate the sample and excite the electrons within the material. An electron is ejected from a lower electron shell of a given atom leaving a vacancy behind. An electron from a higher shell then drops to fill the vacancy, emitting an X-ray photon. These photons are collected by the detector and used to characterise the elements within the sample. Due to lower attenuation of X-rays than electrons, XRF has larger penetration depth than techniques such as XPS. It cannot however detect light-weight elements below Na due to increased likelihood of ejecting an auger electron from the outer shell of the atom [106].

The XRF measurements were performed by Bruker Nano in Berlin, using a benchtop M1 Mistral micro XRF. The device was calibrated using a homogeneous reference ZSW co-evaporated CIGS sample with a known composition. The samples were measured using a 10 x 10 point pattern across the whole sample area. The dwell time for each spot was 30 s. The measurement was performed at 50 kV using a 0.7 mm collimator.

2.3.5 X-ray photoelectron spectroscopy (XPS)

XPS was used to analyse the elemental composition of both the surface and bulk of the material. The technique consists in illuminating the surface with monochromated X-rays. This causes emission of electrons from the surface which then pass through the analyser characterising their kinetic energies, to the detection plate. The binding energy of the electrons is obtained by subtracting the kinetic energy of the emitted electrons and the detector work function from the energy of the incident X-rays. Using the binding energies, emission spectra of peaks corresponding to energy levels within the atomic structure of the material are obtained. Binding energy shifts give an indication of oxidation states or shared electrons in covalent bonds. The XPS is often equipped with an Ar ion source to etch off the surface material, which is used for tracking the elemental composition and molecular bonding through different layers of the material [107].

To perform the analysis, a Thermo Scientific K-Alpha^{TM} XPS surface analysis tool with Snapshot acquisition for depth profiling was used. An electron flood gun was employed to reduce charging to avoid peak shifting. The charge was corrected to the reference C1s peak at a binding energy of 284.8 eV. The machine was equipped with an EX06 ion source, a 180° double focusing hemispherical 128 channel analyser and an Al-K_α X-ray source with an X-ray photon energy of 1.48 keV and a beam width of 400 µm. The survey scan range was between -10 and 1350 eV with step size of 1 eV and dwell time of 0.1 ns/step. For high resolution scans the step size was reduced to 0.1 eV. For depth profile acquisitions an Ar^+ ion etch at 3 keV for 30 s was used for each measurement step. Peak fitting was carried out with the Thermo Advantage analysis suite, using Smart (a Shirley variant) background subtraction.

2.3.6 Secondary ion mass spectrometry (SIMS)

SIMS is typically used to analyse the material's elemental composition by sputtering the specimen surface with a focused primary ion beam, whilst detecting positive secondary ions. The mass/charge ratios of these secondary ions are analysed with a mass spectrometer. Unlike any other composition detection technique, this method has a good sensitivity to group 1-13 elements and detection limits are extremely low (below ppm). Due to a large variation in ionisation probabilities, SIMS is a qualitative measurement technique; however quantification is possible with a reference sample [108][109].

In this work, the analysis of CIGS absorbers was performed at Loughborough Surface Analysis (LSA) Ltd in order to determine the presence of sodium in the absorber. A Cameca IMS 3f SIMS instrument was used, with a 150 µm transfer lens, 175 µm raster size and mass resolution (m/Δm) of 300. To eliminate potential charging effects, the samples were coated with a thin layer of gold. No quantification of the data was performed as no appropriate reference sample was available.

2.4 Device characterisation techniques

2.4.1 Current density-voltage (J-V)

The measurement of J-V curves under dark and light conditions is one of the key characterisation methods for determining the efficiency of the opto-electrical energy

conversion process taking place within the device. The solar cell being tested is held under standard test conditions (25°C and AM1.5G) and its current is measured as a function of applied voltage. The primary performance indicators, open-circuit voltage (V_{OC}), short-circuit current density (J_{SC}), fill factor (FF) and power conversion efficiency (PCE), can be extracted from the J-V curve (Figure 2.6).

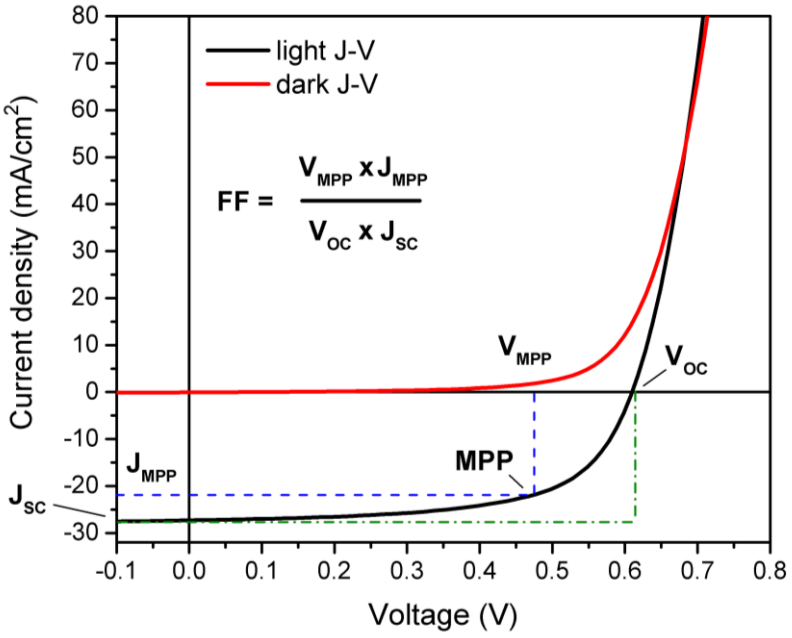

Figure 2.6 Light and dark J-V curves of a CIGS device. The light J-V curve allows extraction of the main performance indicators such as V_{OC}, J_{SC}, FF and PCE.

The V_{OC} is the voltage at zero current density, whilst the J_{SC} is the current density at zero voltage. The FF can be calculated as a ratio between the rectangular area determined by voltage and current density at the maximum power point (MPP) and that determined by J_{SC} and V_{OC} (blue and green rectangles in Figure 2.6 respectively). The PCE is calculated using the formula:

$$\mathrm{PCE}\ (\%) = \frac{\mathrm{FF} \times V_{OC} \times J_{SC}}{P_{in}} \qquad [2.2]$$

where P_{in} is the power of the incident light. Finally, the series resistance (R_S) of the solar cell can be obtained from the slope of the quasi-vertical part of the J-V curve and the shunt resistance (R_{SH}) from the slope of the quasi-horizontal part [15].

J-V characterisation of the majority of solar cells presented in this work was carried out using an ABET solar simulator under standard test conditions (STC). Illumination of 1000 W/m^2 was achieved with a Xe light source calibrated using a reference Si

diode. A substrate temperature of 25°C was maintained by a heating-cooling measurement stage equipped with a PID controller. Finally the AM1.5G spectrum was matched using a series of filters inside the simulator. All devices had an area of 0.25 cm^2 and were contacted using a Keithley in 4-wire configuration. Electrical contacts were maintained on the top Ag grid and uncovered Mo back layer respectively using probes.

2.4.2 External Quantum Efficiency (EQE)

EQE can be defined as the number of electrons collected by the external circuit per photon incident on the solar cell. Whilst measurement of J-V gives an absolute value for the J_{SC}, EQE enables monitoring solar cell photocurrent behaviour at different wavelengths, thus giving information about the origin of the losses (i.e. optical, recombination). To perform the measurement, light from a halogen bulb is chopped using a filter wheel and passes through a monochromator before being used to illuminate the cell. EQE is a localised measurement, with an illumination spot size typically in the millimetre range. The photocurrent spectrum is detected and compared to spectra from calibrated reference cells. The solar cell bandgap can be extrapolated from the long wavelength cut-off of the EQE curve [102].

EQE spectra were collected using a Bentham PVE300 QE system with a chopped xenon/halogen dual light source. Calibration was performed using Si and Ge reference diodes. For CIGS solar cells, the measurements were performed at 0 V bias in the 300 - 1200 nm wavelength range with 5 nm step size.

2.4.3 Capacitance-voltage (C-V), Drive-level capacitance profiling (DLCP) and Admittance spectroscopy (AS)

Capacitance profiling measurement techniques such as C-V, DLCP and AS provide useful information about the bulk and interface properties of solar cells through examination of the sub-bandgap electronic states associated with defects and impurities. The capacitance signal is defined as a function of charge response to a small change in voltage, $C = \delta Q/\delta V$, and is sensitive to carrier capture and emission from trap states. The electronic states are divided into ‘shallow’ and ‘deep’ states. The techniques discussed here detect non-radiative transitions associated with deep states which act as recombination centres, reducing the minority carrier mobility and in some cases causing Fermi energy pinning [102].

C-V measurement can provide a profile of the doping density of the absorber as a function of distance from the junction. The relatively large density of deep states in thin film devices such as CIGS may not give very accurate results, but can be useful for sample comparison. Arguably, the method assumes that the depletion region is precisely defined, ends abruptly and is fully depleted of free carriers. The depletion width is assumed to vary with applied voltage and the charge density within the depletion region remains constant, while the remainder of the bulk is neutral. The capacitance response originates from the depletion edge only, measured as a function of voltage using the following equation [110]:

$$C^{-2} = \frac{2(V_{bi} - V_{dc})}{q\varepsilon\varepsilon_0 N_A A^2} \quad [2.3]$$

where C is the capacitance, V_{bi} is the built in voltage, V_{dc} is the DC bias voltage, q is the charge of an electron, ε_0 is the permittivity of the free space, ε is the relative permittivity of the absorber material, A is the cell area and N_A is the doping concentration on the lightly doped side of the junction. By plotting C^{-2} vs. V_{dc}, the gradient yields the C-V density N_{CV} and the intercept gives V_{bi}:

$$N_{CV} = -\frac{C^3}{q\varepsilon\varepsilon_0 A^2} \left(\frac{dC}{dV_{dc}}\right)^{-1} \quad [2.4]$$

DLCP is used to determine the density of states which respond dynamically to an AC excitation bias. This is large enough so that the capacitance is no longer constant with voltage. DLCP yields the density of states within the bandgap analogue to C-V, without requiring knowledge of material parameters other than its dielectric constant. High-frequency DLCP can therefore give a more accurate estimation of the free carrier density in the samples with deep traps. This technique is relatively insensitive to the presence of interface or near-interface states, hence a comparison with C-V profile can separate interface from bulk defects [111].

AS measures the sample capacitance as a function of small-signal AC frequency and temperature. This technique is used to determine the defect energy levels and density of states. As in DLCP, trap states in the device respond to the applied AC bias, adding to the capacitance. Applied bias shifts the Fermi level such that trap levels at different depth in the bandgap can be measured. At low temperature or high

frequency, the trap states freeze-out as the conductivity is too low to respond fast enough to the excitation. The capacitance response will be limited to that of a bulk dielectric. Increasing the temperature or decreasing the frequency will be accompanied with a characteristic step in the capacitance curves at a particular transition frequency where the traps start to respond. The frequency (f_i) and temperature (T_i) of the inflection point of the step are used to calculate the energy of the trap level E_T:

$$\ln\left(\frac{2\pi f_i}{T_i^2}\right) = -\frac{E_T}{kT_i} + \ln(\sigma\gamma) \qquad [2.5]$$

where k is Boltzmann's constant, σ is the capture cross-section for the trap and γ is a constant associated with the effective band edge density of states [112].

C-V and DLCP measurements were performed using a Keysight E4990A impedance analyser. The voltage was swept from -1 V to 1 V at a frequency of 100 kHz at RT. Temperature dependent electrical measurements such as AS were conducted using an evacuated closed-cycle helium cryostat. The temperature was controlled in the range from 105 – 315 K using a LakeShore 335 temperature controller. Prior to the measurements, the samples were kept in the dark for 1 h to ensure a relaxed state. AS data were acquired using the Keysight E4990A impedance analyser operating at frequencies from 100 Hz to 1 MHz at zero bias conditions. In addition to these techniques, temperature dependent current density-voltage (J-V-T) measurements were performed using the cryostat, a Keysight B2902A measurement unit and a halogen light source.

2.4.4 Photoluminescence (PL)

Photoluminescence is the emission of light from a material resulting from its excitation through absorption of light of sufficient energy. PL radiation is a result of a transition of electrons from higher occupied states to lower vacant states. PL measurements provide information about material bandgaps and minority carrier lifetimes [102].

Spectrally-resolved PL and time-resolved PL (TRPL) measurements were conducted using an in-house constructed measurement system equipped with a single excitation laser source [113]. In the measurement setup, a selection of carefully

arranged optics was used to focus a pulsed picosecond laser with a wavelength of 640 nm on the sample. The luminescence emitted by the laser-excited sample was collected, collimated and sent through a monochromator prior being passed to the detectors. The detector for PL measurements is an amplified InGaAs photodiode with an extended wavelength range (500-1700 nm). For TRPL, a photomultiplier tube in the NIR (950-1700 nm) allows measurement of CIGS cells.

To conduct the measurements of CIGS solar cells, the laser excitation was pulsed at 40 MHz to measure a detectable PL signal. The wavelength was scanned from 900 to 1200 nm with a 1 nm step size. CIGS PL spectra have one main broad emission peak corresponding to the material bandgap, which is the primary source of radiative band-to-band recombination. TRPL was conducted on the same measurement spot, with the wavelength selected based on the material bandgap (~1055 nm) with a laser pulse frequency of 20 MHz. TRPL measures minority carrier lifetime through luminescence decay caused by radiative recombination.

2.4.5 Electroluminescence (EL) imaging

EL describes a reciprocal action to the normal operating of a solar cell as a light absorbing diode converting incident light into electricity. Electroluminescent emission of light is a consequence of the application of a forward electric bias to the diode. This leads to radiative recombination and consequent emission of photons with energies close to the material bandgap. EL emission is recorded using a charge-coupled device (CCD) camera. The signal reflects recombination, optical and resistive losses in the device [102].

EL device mapping was carried out using an Apogee Alta F800 camera equipped with a Quioptiq Inspec X IR lens with an aperture f-stop of 2.8. Each cell was placed in forward bias, with a current injection approximately equal to the J_{SC}. Image acquisition time was 10 minutes.

2.5 Preliminary analysis of the as-deposited and selenised absorber films and conclusions

Typical morphologies of the as-deposited and selenised CIGS absorbers fabricated using the experimental procedures described above are shown in SEM cross-sections (Figure 2.7). The absorber was prepared using the base-line (CGI = 0.9,

GGI = 0.3) composition and on an alkali-free glass substrate. No intentional doping of the absorber was performed.

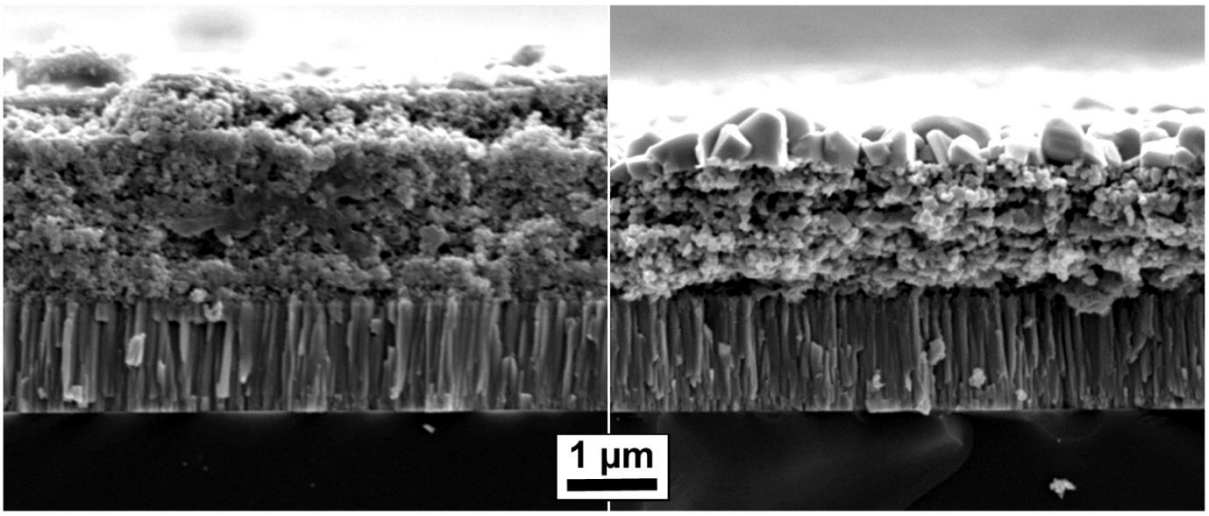

Figure 2.7 SEM cross-sections of the as-deposited (left) and selenised (right) absorbers with intended base-line composition ($Cu_{0.9}In_{0.7}Ga_{0.3}Se_2$).

The images in Figure 2.7 clearly show the porous nature of the sprayed absorbers. The selenisation process failed to fully crystallise the absorber, resulting in relatively porous CIGS with a bilayer morphology consisting of larger surface grains overlying poorly crystalline material. The compositional and thickness variation across the entire device was investigated using XRF (Figure 2.8).

XRF clearly shows a significant variation in absorber layer thickness across the device, thought to be a consequence of the deposition method employed. The absorber thickness estimated using XRF is typically lower than the thickness obtained from the SEM images in Figure 2.7. On average XRF gave a thickness of 0.78 µm for the as-deposited absorber (averaged area: top right corner) as opposed to 2.3 µm obtained from the SEM image for the same sample region. The selenised sample gave similar results, with XRF showing an average of 1.83 µm absorber layer thickness as opposed to 1.95 µm obtained from the SEM cross-section. This large deviation in thickness estimation, especially in the as-deposited sample, may be a consequence of the scale of the sample porosity. Moreover, the measurement was calibrated using a reference ZSW co-evaporated CIGS solar cell with known composition and thickness. Due to the fundamentally different absorber morphology of co-evaporated and solution-processed absorbers, this calibration sample was arguably not the ideal choice for thickness evaluation.

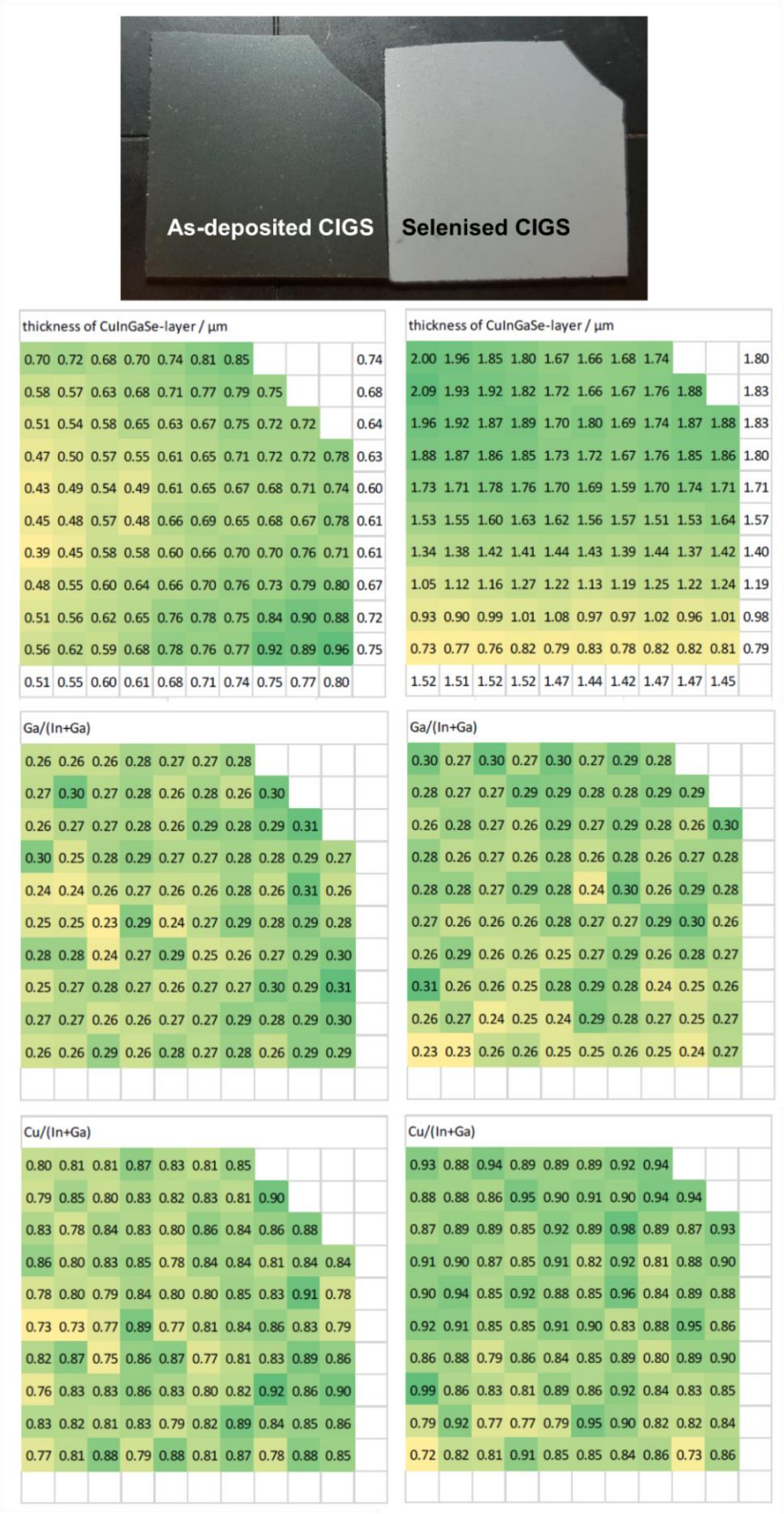

Figure 2.8 XRF thickness and compositional analysis across the sample area after manual spraying (left) and selenisation (right) of the precursor film using base-line CIGS precursor solution. The cross-section SEM images in Figure 2.7 were taken from the missing corner of the samples.

Regarding the film composition measured by XRF, this is close to the intended composition from the precursor solutions with GGI and CGI values of 0.3 and 0.9 respectively. The observed spatial compositional deviations can also relate to the thickness variations, as thinner areas are often the furthest from the intended CGI and GGI values. Thinner films may end up with slightly different overall composition from the thicker films due to different reaction kinetics during selenisation and different thickness ratio between the large- and fine-grained layers. Absorber film composition and morphology will be studied in the following chapters. It will be shown that absorber composition and doping have a significant effect on the absorber morphology and consequently on the device performance.

CHAPTER 3

Substrate and back contact for CIGS solar cells

3.1 Scope

Prior to introducing the content of this chapter, it is important to highlight how significant a role the glass substrate and Mo back contact play in solution-processed CIGS solar cells. The amount of sodium supplied and a quality ohmic contact to the absorber are the obvious requirements. In atmospheric processing physical delamination can be a serious issue. Variation of the glass substrates from batch to batch, fast oxidation of Mo during absorber deposition in air and the very porous nature of the absorber material providing little protection to the underlying Mo against Se vapour are the primary factors responsible for delamination observed during this work. Consequently it is particularly important for the development of solution-processed CIGS to fully understand the behaviour of the glass and back contact to achieve good quality solar cells.

This chapter describes the choice of an appropriate substrate and the optimisation of the Mo back contact for solution-processed CIGS solar cells. Glass substrates differ from each other in chemical composition and thermal expansion. Some glass substrates, namely the most frequently used soda-lime glass, contain alkaline elements such as sodium or potassium which are beneficial for CIGS solar cell absorbers [67]. During the fabrication process, CIGS solar cells undergo various annealing stages with temperatures reaching as high as 550°C. Thermal and chemical stability and inertness of the glass and Mo back contact during these processes are crucial for achieving efficient devices. Mo deposition conditions have to be carefully optimised for good adhesion and conductivity of the back contact. Delamination due to excessive $MoSe_2$ formation at the Mo/CIGS interface during selenisation is often seen in solution processed CIGS and CZTS solar cells and regularly proved problematic in this work [73]. The application of the back contact

diffusion barrier provided control over the $MoSe_2$ growth and allowed for improved CIGS back contact properties and adhesion.

3.2 Glass substrate

All the glass substrates employed in this work were 1 mm thick, cut into 5 cm x 5 cm squares. They were cleaned in three successive ultrasonic baths at temperature of ~50°C for 15 min each. The first bath consisted of de-ionised (DI) water with soap, the second bath contained acetone and the third isopropanol. The residual solvent was removed using a compressed air gun. Three different types of glass were considered for the use as substrates in the solution-based CIGS solar cells studied in this thesis: soda-lime glass (SLG), Schott borofloat glass (BF33) and Corning Eagle XG glass (Eagle). The choice of substrate was found to have an effect on the degree of delamination and overall device efficiency. In order to understand these effects, chemical and thermal assessment of the different substrates was performed.

3.2.1 Chemical composition

Chemical composition of the three glass substrates was measured on both sides of the glass slide using XPS surface analysis and the results are summarised in Table 3.1. Prior to the XPS measurement, the surface was ion etched for 30 s to remove any surface contaminants such as carbon related to the sample preparation and handling.

Table 3.1 Chemical composition of the glass substrate surface (front and back) measured using XPS

At%	SLG		BF33		Eagle	
	Front	*Back*	*Front*	*Back*	*Front*	*Back*
Si	33.0	31.8	31.8	33.2	26.5	27.6
O	57.9	56.9	58.8	57.8	56.9	57.4
Sn	-	-	0.6	-	-	-
Na	2.8	2.5	-	0.7	-	-
K	-	-	0.5	-	-	-
Mg	3.4	3.1			0.3	0.5
Al	-	1.0	1.4	1.2	8.1	7.4
B	-	-	5.5	5.6	5.7	4.4
Ca	2.9	2.7	0.6	-	2.5	2.7
C	-	2.0	0.8	1.5	-	-

The most important compositional difference between the three glass substrates is their alkaline element content, such as sodium and potassium. From this study SLG, the conventional substrate for CIGS solar cells, has over 2.5 at% of Na. In contrast, the Eagle glass shows no presence of alkaline elements at all. This is in agreement with the manufacturer specification sheet reporting a typical alkali content lower than 0.05 wt% [72]. The BF33 substrate has low but measurable content in alkaline elements and is the only substrate containing potassium. There are a large number of studies discussing the beneficial effects of alkali elements on CIGS absorber opto-electronic and morphological properties and hence device performance [43][44] [114][115]. It is widely accepted that at temperatures close to the strain point of SLG alkali elements become mobile enough to diffuse into the Mo and CIGS layers. The mechanism proposed is Na^+/H^+ ion exchange where H^+ is stored in Mo during air-exposure and Na source is Na_2O from the glass [116]. The Na diffusion proceeds through oxygenated columnar Mo GBs and it was also shown that oxidised Mo supplies higher amounts of Na to the absorber [117][118]. Using SLG does not allow for a precise control over the Na diffusion however, as substrates are never identical, the out-diffusion process is rather complex and it depends strongly on the oxidation state and properties of the Mo film [118][119]. For this reason alkali barrier layers such as SiO_2 and Al_2O_3 are often deposited between the SLG substrate and the Mo layer and the alkali doping is supplied externally [120][121]. In this work an alkali-free substrate (Corning Eagle XG) was used to study Na doping of solution-processed CIGS solar cells (Chapter 6).

3.2.2 Thermal expansion

A glass substrate with a suitable thermal coefficient is necessary in order to avoid any delamination caused by the stress at the interface between glass and Mo during high temperature annealing. Thermal expansion is caused by the asymmetry of the amplitude of thermal vibrations related to the chemical bonding and composition in the glass and the thermal history of the glass [122][123][124]. The thermal expansion coefficient of the three glass substrates was measured using a TA Instruments Thermomechanical Analyzer (TMA Q400EM). A flat-tipped standard expansion probe was placed in contact with the sample positioned on a flat stage and a small static force of 0.01 N was applied. In order to simulate the selenisation conditions where temperatures as high as 550°C are applied for up to one hour, an equivalent

heating regime was used. The programme consisted of first bringing the temperature to a constant 50°C, ramping the temperature at 5°C/min to 550°C followed by a 60 min dwell time, and finally naturally cooling down to 50°C. The probe movement recorded sample expansion or contraction. Generally, it is difficult to obtain quality expansion data from the first run due to stress relaxation or change of morphology of the sample [125]. The push rod or the sample can also change their position slightly during the first heating cycle. Therefore three cycles of heating (5°C /min ramp rate) and cooling the sample were performed without touching the dilatometer or the sample. The thermal expansion profile of the three glass substrates at a heat rate of 5°C/min is shown in Figure 3.1.

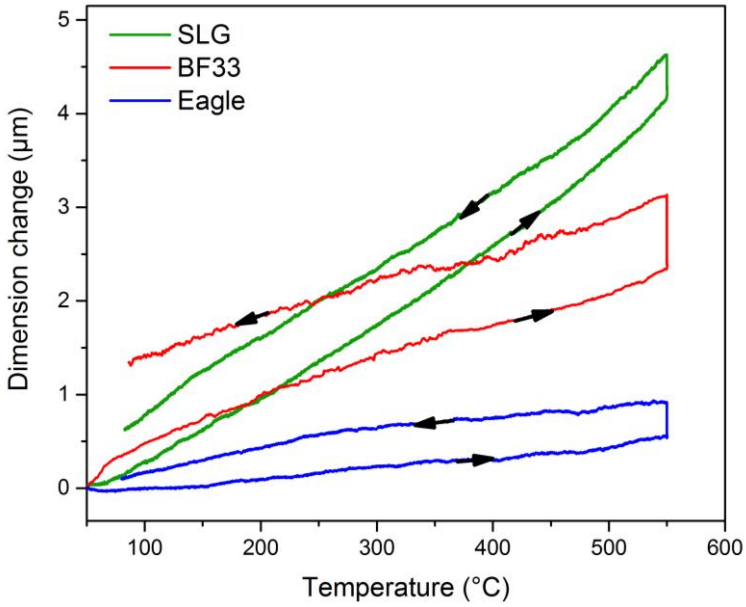

Figure 3.1 Thermal expansion profile of SLG, BF33 and Eagle glass with heat rate of 5°C/min.

The coefficient of linear thermal expansion (CTE) is the mean slope of the $\Delta L/L_0$ = f(T) curve within the temperature interval ΔT [126]. The $\Delta L/L_0$ = f(T) curve for the heating part of the thermal cycles shown in Figure 3.1 is plotted in Figure 3.2 a). Most glass expansion data in literature state the CTE for temperature ranges up to 300°C. In order to compare the CTE obtained experimentally with the values for glass expansion found in the literature, the curves were replotted in Figure 3.2 b) with shortened temperature range. The linear extrapolation of the part of the $\Delta L/L_0$ curves corresponding to the temperature range of 100-300°C was performed in order to obtain the experimental values for CTEs. The experimental and theoretical CTEs are summarised in Table 3.2.

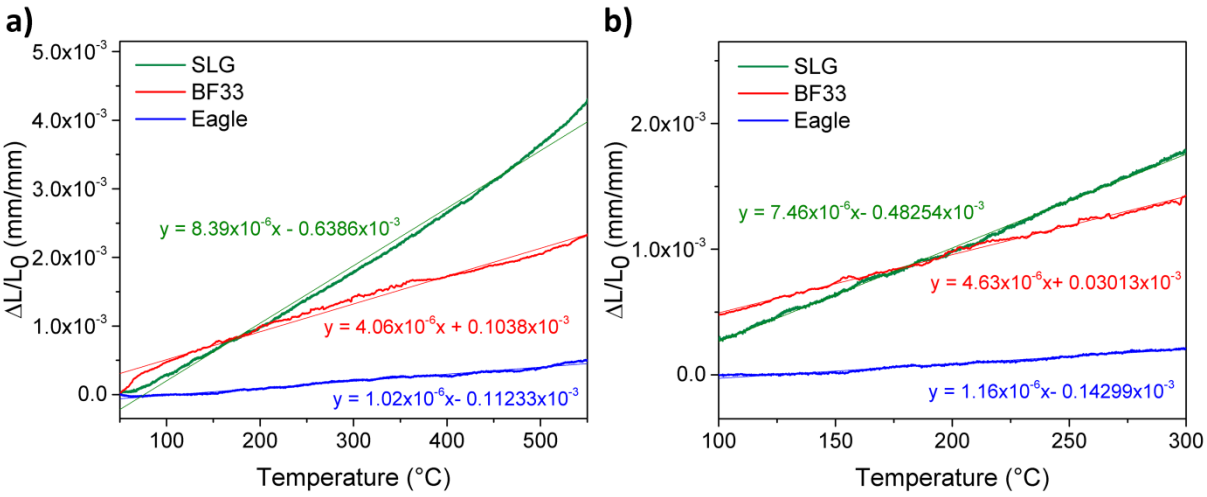

Figure 3.2 CTE extrapolation by linear regression of the slope of $\Delta L/L_0 = f(T)$ curve for full temperature range T = 50-550°C (a) and T = 100-300°C (b).

Table 3.2 CTEs for SLG, BF33 and Eagle glass obtained experimentally (CTE_{exp}) and from literature (CTE_{th})

($°C^{-1}$)	SLG	BF33	Eagle
CTE_{exp} *(50-550°C)*	$8.39x10^{-6}$	$4.06x10^{-6}$	$1.02x10^{-6}$
CTE_{exp} *(100-300°C)*	$7.46x10^{-6}$	$4.63x10^{-6}$	$1.16x10^{-6}$
CTE_{th}	~$8.3x10^{-6}$ [127]	$3.25x10^{-6}$ (20-300°C) [128]	$3.17x10^{-6}$ (0-300°C) [72]

The expansion coefficients measured experimentally (CTE_{exp}) differ slightly from those found in the literature (CTE_{th}). The possible source of error or deviation from the theoretical values may result from different sample sizes, heating rates, measurement setup and the experimental procedure. The sample size and heating rate have an influence on the CTE values. The heating rate of 5°C/min and sample size of 10 x 10 x 1 mm were in agreement with the specification of the TA instrument and the ISO 7991 standard [126]. The CTE was obtained from the heating profile as controlled cooling would require a supply of liquid nitrogen. The glass manufacturer most likely used slightly different experimental methods and instruments, causing the variation between the experimental and theoretical values compared in Table 3.2. Most importantly, the samples are internally comparable as identical temperature cycles were applied to all samples and the measurement instrument has good temperature and measurement precisions (+/- 1°C and +/- 0.1% respectively).

Experimentally and from the literature, the Na-free Eagle glass substrate has the lowest expansion coefficient among the studied substrates, followed by the low-Na

BF33 glass with an experimental CTE approximately four times greater. Finally the SLG was found to be the most thermally expansive glass substrate, with a CTE_{th} nearly three times the CTE_{th} of the BF33 and CTE_{exp} nearly twice that of the BF33. This difference in the thermal expansion of various glass substrates as well as their different content in alkali elements may have an effect on the adhesion properties of the subsequent Mo and CIGS layers. This is studied in the following section.

3.3 Molybdenum deposition and adhesion properties

3.3.1 Mo deposition conditions

Mo is the most common choice for CIGS back contact due to its low resistivity, thermal and mechanical stability and typically good adhesion between the glass and the Mo thin film [42]. However the Mo properties which are closely related to the deposition parameters affect the characteristics of CIGS absorbers and the resulting device performance. Specifically, the Mo layer directly influences the Na out-diffusion from the substrate and the formation of $MoSe_2$ during the selenisation stage [74][129]. Mo is typically deposited by magnetron sputtering as this approach provides benefits of high deposition rate and uniformity over large area deposition [130]. However it is important to find the optimum sputtering conditions in order to obtain Mo thin films with suitable characteristics for the application in solution-processed CIGS solar cells.

In this work, Mo thin film deposition was carried out using a Nordiko DC magnetron sputtering system with a 30 cm x 10 cm Mo target, positioned vertically at a distance of approximately 10 cm from the substrate. The 5 cm x 5 cm cleaned glass substrates were mounted in a sample holder and rotated during deposition at a constant rate of 3 rpm. Argon was used as the working gas and the flow rate was controlled using a mass flow controller with a flow range of 2-100 sccm. Prior to deposition, the vacuum chamber was evacuated to a base pressure of less than 3.0×10^{-6} Torr and the target was pre-cleaned by sputtering for 5 min. The deposition could only be performed at room temperature, however for longer depositions using high powers the temperature inside the chamber rose progressively.

Good adherence and low resistivity of the Mo layer are essential for high efficiency CIGS solar cells [131]. When Mo is deposited by DC sputtering, the electrical and

structural properties of the film are strongly influenced by the deposition parameters such as working gas pressure and power supplied by the sputtering system [130]. Each sputtering system is different and the scale for high and low pressures/powers is determined by the particular sputtering chamber design, mass flow controller and target geometry. The Mo thin film deposition conditions used in this work, in particular working pressure and power density, were optimised for the particular sputtering system used. The optimisation consisted first in varying the sputtering power from 0.6 - 2.4 kW, corresponding to a power density of 2-8 W/cm^2, while keeping the Ar gas flow constant. Subsequently, the working pressure was varied by gradually increasing the Ar flow rate from 2 – 100 sccm. For both experiments, the deposition was 10 min long and film thickness and sheet resistance were measured using an Ambios XP2 stylus profilometer and a four-point probe respectively. Mo thin film deposition parameters and measured characteristics are summarised in Table 3.3.

Table 3.3 Deposition and characterisation of Mo thin films deposited with varying sputtering power density and pressure

Power density (W/cm^2)	**Ar flow rate** (sccm)	**Pressure** (mTorr)	**Deposition time** (min)	**Thickness** (nm)	**Sheet resistance** (Ω/sq)
4	2	1.2	10	190	2.1
4	10	2.3	10	230	2.3
4	30	3.6	10	240	4.2
4	50	4.9	10	250	5.3
4	80	14.0	10	290	18.5
4	100	30.0	10	300	44.8
2	2	1.2	10	130	3.9
4	2	1.2	10	190	2.1
6	2	1.2	10	270	1.3
8	2	1.2	10	360	1.2

Figure 3.3 shows the deposition rate as a function of sputtering power density and pressure. The deposition rate increased linearly with increasing power density. This is caused by increased kinetic energy of the Ar ions bombarding the Mo target and transferring that kinetic energy to the Mo particles [130]. With a higher sputtering pressure controlled by increasing the Ar flow rate, the deposition rate increased

slightly. At higher pressures, the number of Ar ions increased as well, however the increased scattering of Mo atoms compensates for the deposition rate [132].

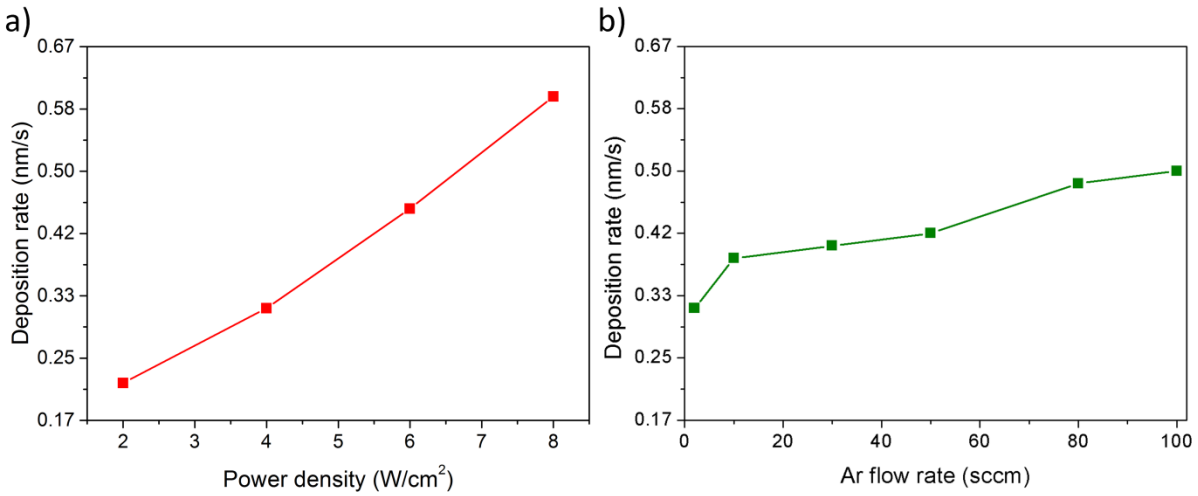

Figure 3.3 Mo deposition rate as a function of sputtering power density (a) and Ar flow rate which is directly related to the sputtering pressure (b).

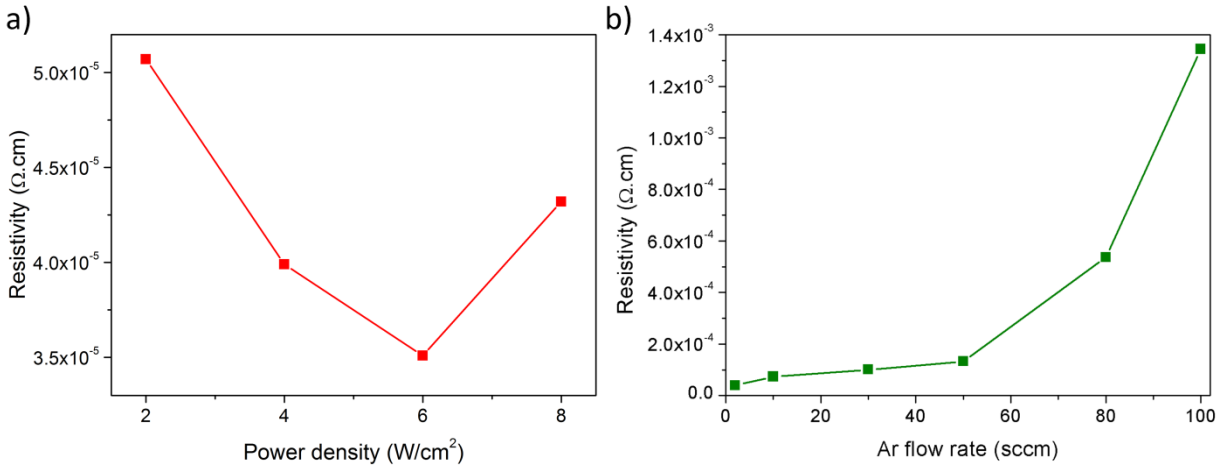

Figure 3.4 Mo film resistivity as a function of sputtering power density (a) and Ar flow rate (b).

Figure 3.4 shows Mo thin film resistivity as a function of sputtering power density and Ar flow rate. The resistivity is a product of thin film sheet resistance and its thickness. The resistivity of the Mo film is strongly influenced by the sputtering pressure, which is controlled by Ar flow rate. The sputtering power has much less influence. The resistivity increased exponentially with the increase in Ar flow rate. On the other hand, the resistivity is inversely proportional to the sputtering power density, up to 6 W/cm^2. At low pressures, the scattering of sputtered particles decreases resulting in more densely packed, well crystallised and less resistive films [133][134]. At low power density, the Mo particles have little energy to recrystallise on the surface of

the substrate resulting in more resistive films [130]. For a power density of 8 W/cm^2, the thickness increased dramatically whereas the sheet resistance reduced only slightly, causing a higher overall resistivity.

Mo film morphology as a function of deposition power density and pressure was studied by SEM. Figure 3.5 shows the SEM images of the Mo surface deposited at various Ar flow rates and sputtering power densities. At low sputtering pressures (≤ 5 mTorr, corresponding to an Ar flow rate ≤ 50 sccm) the Mo film morphology consists of long, fish-like grains. The lower the deposition pressure (Ar flow rate), the more densely packed the film morphology. As the deposition pressure increased (≥ 13 mTorr, Ar flow rate ≥ 80 sccm), the film grain structure changed. The grains became smaller and more spherical, and more voids were observed around their edges. This change in film morphology might explain the dramatic increase in film resistivity measured at higher Ar flow rates (≥ 80 sccm) observed in Figure 3.4 b). With increased sputtering power density, more energy was transferred to Mo particles resulting in more crystalline films with well-defined grain structures.

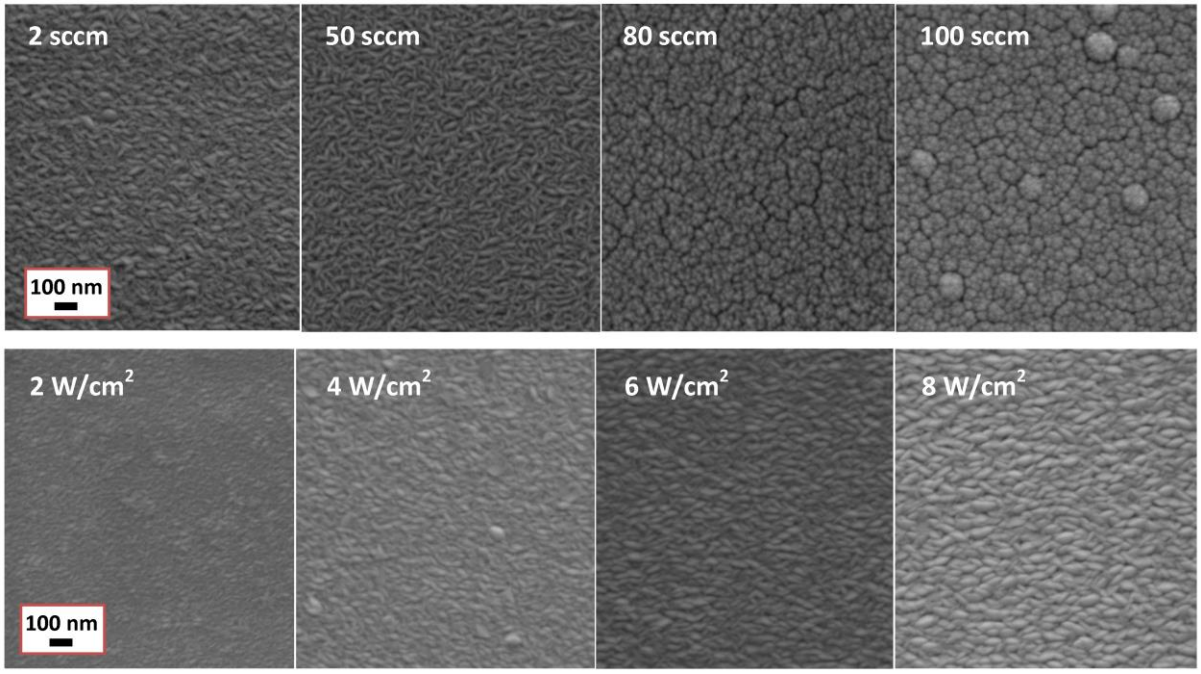

Figure 3.5 SEM surface images of Mo films deposited with increased Ar flow rates at power density of 4 W/cm^2 (top) and increased sputtering power densities at Ar flow rate of 2 sccm (bottom).

Mo SEM cross-sections are shown in Figure 3.6. Mo grains look identical from this observation direction for all the deposition pressures and power densities (not shown

here). The only difference is in the film thickness. Mo grows on the substrate in columnar grains perpendicular to the plane of the surface. For all the deposition conditions, Mo has the same preferential growth direction, which is typically observed for sputtered films [135].

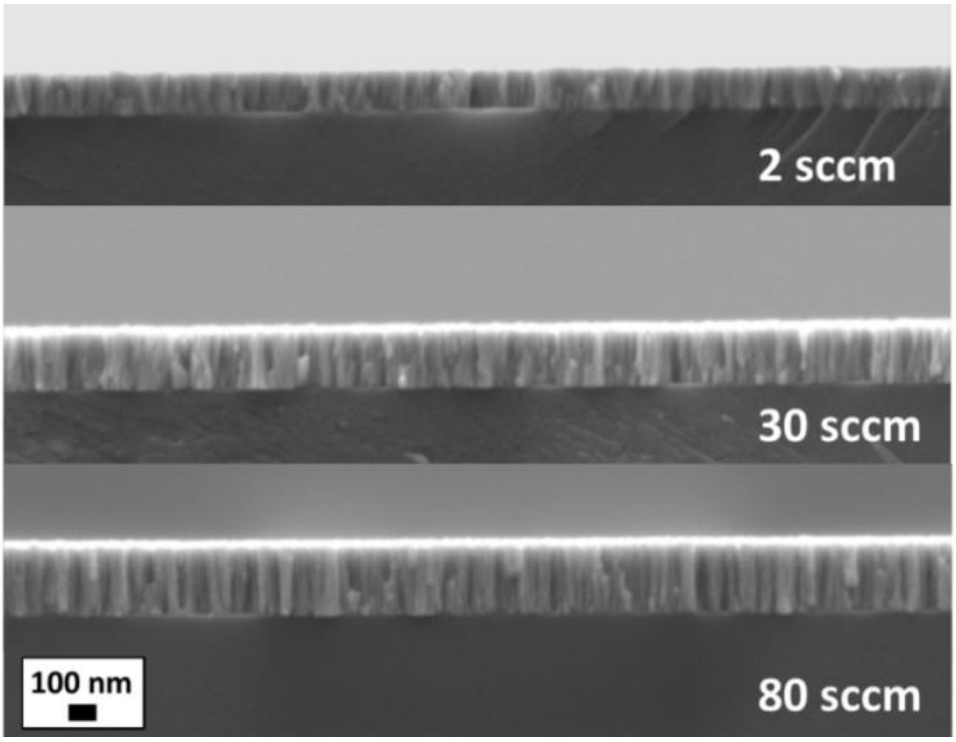

Figure 3.6 SEM cross-section images for Mo films deposited with different Ar flow rates.

The preferential growth orientation and crystal quality of the Mo films prepared using different sputtering conditions were studied using XRD. Figure 3.7 shows XRD patterns of Mo films deposited at different Ar flow rates and sputtering power densities. For all deposition conditions, the most intense XRD peak is observed at diffraction angles of $2\theta = 40.5°$ corresponding to the (110) preferred orientation in the Mo cubic crystal structure (JCPDS 3-065-7442). In addition, Mo peaks at $2\theta \sim 73°$ and 87° were observed which correspond to the (211) and (220) planes of the cubic Mo phase respectively. Hence, the crystallographic orientation is not influenced by the deposition conditions. A single preferred growth direction is typically observed in sputtered films and is also consistent with the similar-looking SEM cross-sections in Figure 3.6. Table 3.4 summarises the full width half maximum (FWHM) obtained by a Gaussian peak fitting routine of the XRD spectra and the intensity of the dominant (110) Mo peak.

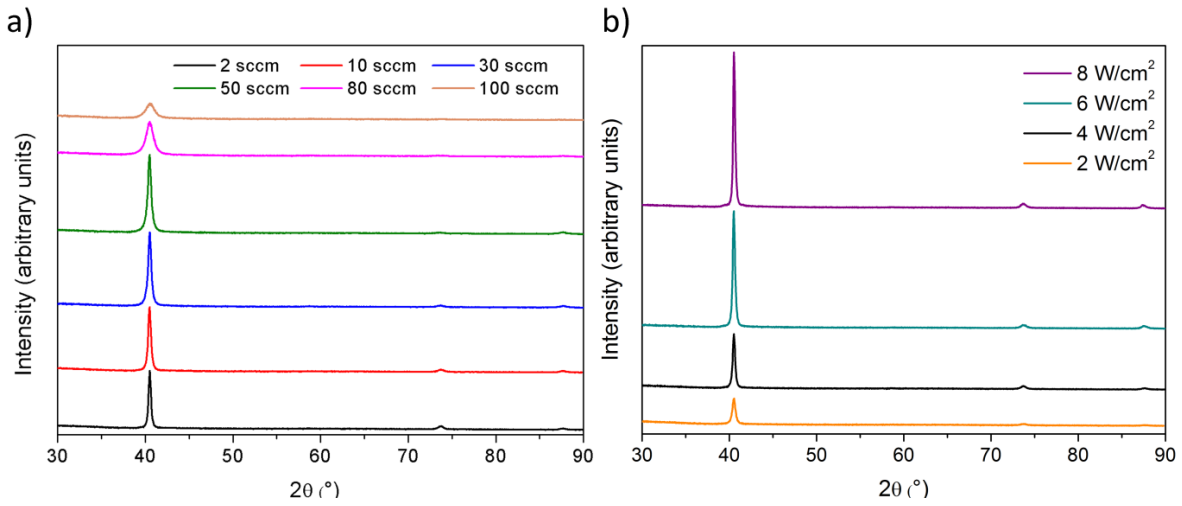

Figure 3.7 XRD spectra of Mo films deposited with varying Ar flow rates (a) and sputtering power densities (b).

Table 3.4 FWHM and intensity of the dominant Mo (110) peak extracted from the XRD patterns

Conditions	**FWHM** (°)	**Peak intensity** (arb. units)
2 sccm	0.371	4100.5
10 sccm	0.435	4520.1
30 sccm	0.512	5097.4
50 sccm	0.564	5274.8
80 sccm	1.173	2293.2
100 sccm	1.410	1008.9
2 W/cm^2	0.456	1862.4
4 W/cm^2	0.371	4100.5
6 W/cm^2	0.355	8925.5
8 W/cm^2	0.299	12091.7

The FWHM of the dominant Mo peak decreased (i.e. the peak became sharper) with the increase in sputtering power. The peak intensity also increased dramatically. Both of these indicate an improved crystal structure quality with increased sputtering power. This is in agreement with the decrease in sheet resistance and apparent improved crystallinity observed for these films. Small and broad Mo (110) peaks were obtained at Ar flow rates ≥ 80 sccm indicating a poor crystal quality of these films. Although the peak intensity increased for Ar flows from 2 to 50 sccm, the FWHM is the lowest for 2 sccm. Therefore a better crystal quality and more densely packed microstructures are obtained with the lowest sputtering pressures introducing 2 sccm of Ar into the chamber. This film was also the most conductive.

3.3.2 Mo bilayer for CIGS application

Delamination is a common issue observed during CIGS solar cell fabrication, especially for solution-processed material. The high temperature selenisation causes various layers to expand differently, introducing internal stresses. Delamination due to different expansion coefficients, Na out-diffusion from the glass and excessive $MoSe_2$ formation have been reported in the literature [136][114][76]. Figure 3.8 shows photographs depicting the film delamination from the glass substrate observed in this work. It typically occurs after the selenisation of Mo/CIGS films using a graphite box.

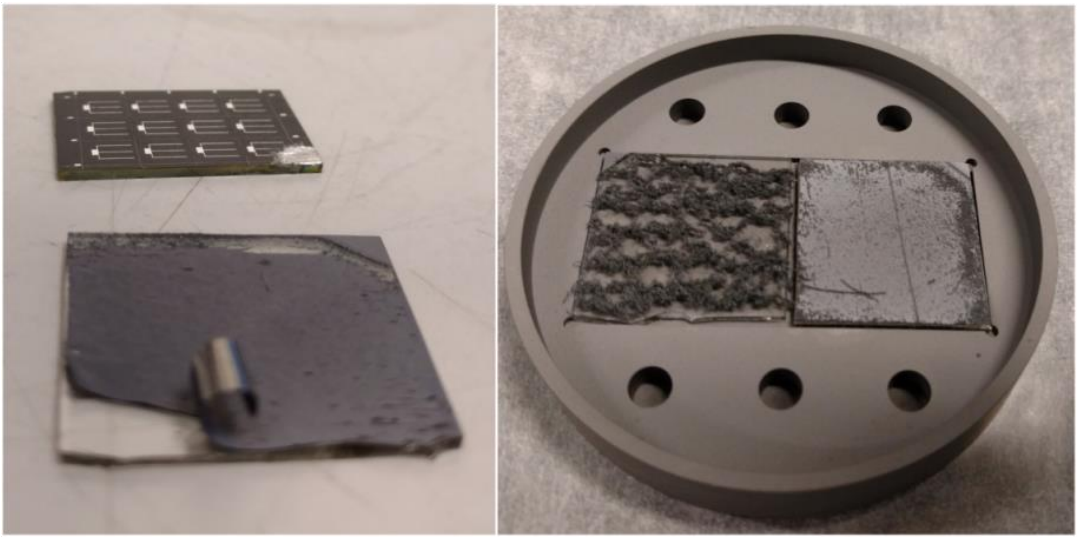

Figure 3.8 Delamination of the Mo/CIGS from the glass substrate after selenisation.

Good Mo adhesion was reported for Mo films deposited at high Ar pressures and low powers when the film is subjected to tensile stress. These films have high resistivity however. Conductive, but poorly adhesive films were obtained at low Ar pressures, when the film is under compressive stress [131][133][137]. Consequently, a film sputtered at a single pressure does not fulfil the requirements for a good quality back contact Mo for CIGS solar cells: highly conductive and well adhesive at the same time. To cope with this problem, Schofield *et al*. suggested depositing a Mo bilayer consisting of a thin first layer deposited at high Ar pressure to assure good film adhesion on the substrate, followed by a thicker conductive second layer deposited at low Ar pressure for a good quality contact to the CIGS absorber [133]. The bilayer approach was generally accepted as a standard procedure for Mo back contact deposition in CIGS solar cells [138][139][140].

The Mo bilayer approach was implemented in this work. The conductive top layer was deposited at the lowest Ar flow rate of 2 sccm and power density of 6 W/cm^2 which previously showed the lowest film resistivity and good crystal quality. However the choice of sputtering conditions for the underlying Mo layer for good adhesion was less straightforward. To determine the optimum conditions, several Mo bilayers were deposited whilst varying the deposition pressure by varying the Ar flow rate of the 1st Mo layer from 30 to 100 sccm while keeping the sputtering power density at 4 W/cm^2. A 5 min deposition of this layer resulted in a thickness of ~100 nm. The subsequent conductive layer using an Ar flow rate of 2 sccm was sputtered for 30 min, resulting in layer thickness of ~800 nm. In order to avoid any delamination caused due to excessive $MoSe_2$ formation, a Mo-N diffusion barrier layer followed by a 'sacrificial' Mo layer were deposited on top of the Mo adhesive/conductive bilayer. The sheet resistance of the final multilayer was ~0.4 Ω/sq., regardless of the conditions used to deposit the 1st Mo layer. The resistivity of the final film was therefore largely dominated by the thick conductive layer.

Immediately after the Mo deposition, the films did not show any signs of delamination. However, different behaviour was observed after their selenisation. Mo/Mo-N/Mo multilayers were selenised at 540°C for 90 min inside a graphite box. After the selenisation, films on three different glass substrates (SLG, BF33 and Eagle glass) with varied conditions for the 1st Mo layer were visually inspected for any signs of delamination. Table 3.5 summarises the conclusions on the adhesion of these Mo films post-selenisation. Figure 3.9 shows photographs of the films with various degrees of delamination.

Table 3.5 Adhesion properties of Mo after selenisation with 1st Mo layer deposited using power density of 4 W/cm^2 and varied Ar flow rate onto three different glass substrates

Conditions 1st layer		**30 sccm, 3.6 mTorr**	**50 sccm, 4.9 mTorr**	**80 sccm, 14 mTorr**	**100 sccm, 30 mTorr**
Conditions 2nd layer		**2 sccm, 1.2 mTorr**			
Peeling ?	*SLG*	yes	yes	partially	partially
	BF33	partially	partially	no	no
	Eagle	no	no	no	no

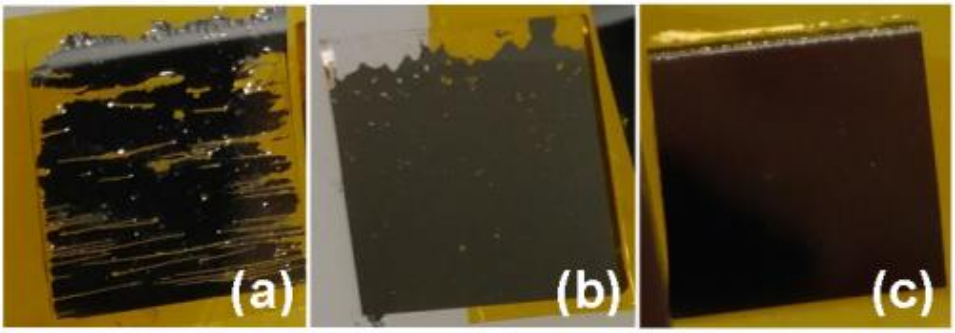

Figure 3.9 Delamination of the Mo films after being subjected to selenisation. Film peeling of the substrate was observed for SLG substrates with Mo 1st layer deposited at lower pressures (a). Partial peeling was seen for SLG at high pressures and BF33 at low pressures for the 1st Mo layer (b). No delamination was observed for Eagle glass at all Mo 1st layer pressures and BF33 with Mo at high pressures (c).

Delamination from SLG substrates was the most severe and persisted even at the highest pressures for the 1st Mo layer. The Mo on BF33 substrate delaminated partially at Ar flow rates of 30 and 50 sccm for the Mo 1st layer, but remained intact for higher Ar flow rates. The Mo film on Eagle glass was unaffected for all Mo deposition conditions. These observations are most likely related to the considerable difference in the expansion coefficient between these three glass substrates as well as their chemical compositions. Eagle glass, with the lowest CTE among the substrates, shows the best adhesion properties. However, it also contains no alkali elements. The delamination induced by sodium will be discussed in greater depth in Chapter 6. Additionally, higher Ar pressure (≥ 14 mTorr) during the deposition of the bottom Mo layer also improves the adhesion properties on the Mo/glass interface. However, with the sputtering system and mass flow controller used in this work, it remained challenging if not impossible to deposit a suitable Mo bilayer that would withstand the selenisation conditions necessary to crystallise the solution-processed absorber on SLG substrates. Consequently, in the following sections, Eagle glass substrates were used when the Mo back contact was deposited using this sputtering setup. In addition, commercial Mo-coated SLG substrates were purchased from M-Solv Ltd.

3.4 Mo-N back contact diffusion barrier layer

3.4.1 $MoSe_2$ formation

During selenisation, selenium reacts with Mo to form $MoSe_2$ at the CIGS/Mo interface. A thin $MoSe_2$ layer contributes to the formation of a quasi-ohmic contact,

and due to a wider bandgap than CIGS (1.4 eV) $MoSe_2$ forms a back surface field reducing back contact recombination [141]. However too thick a $MoSe_2$ layer plays a detrimental role in device performance due to its high resistivity (10^1-10^4 Ω.cm) limiting current collection at the back electrode and occasionally causing delamination [75][142]. Therefore control of the $MoSe_2$ layer formation is vital for the CIGS solar cell formation and performance. Figure 3.10 shows delamination due to excessively thick $MoSe_2$ formed after selenisation of the solution-processed CIGS absorber.

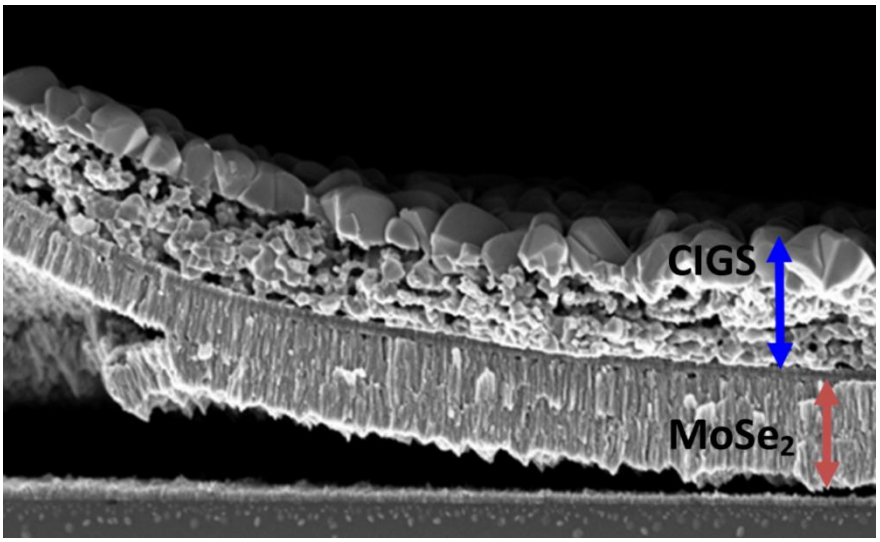

Figure 3.10 Delamination from the Mo due to excessively thick $MoSe_2$.

The hexagonal structure of $MoSe_2$ grains consists of Se-Mo-Se sheets perpendicular to the c-axis connected between each other by weak van der Waals (vdW) forces. The force within each sheet is of a strong, covalent type. The adhesion of $MoSe_2$ is much stronger and less resistive if its c-axis is parallel to the Mo surface. Moreover, the growth rate of the $MoSe_2$ layer is larger due to increased diffusion of Se vapor through the natural channels between the sheets [73]. The $MoSe_2$ c-axis orientation depends on selenisation conditions such as temperature, the amount of Se supplied and the state of the Mo prior to selenisation [73][142][143]. It was observed that with increased selenisation temperature, the orientation of the $MoSe_2$ c-axis changed to become parallel to the Mo surface due to different thermal expansion coefficients between Mo and $MoSe_2$ [73]. Additionally, the higher amount of Se supplied induced formation of a thicker $MoSe_2$ layer [75]. Other parameters such as CIGS growth recipe, the deposition technique, Mo properties and the presence of Na, Ga, Cu and O also play a role in the $MoSe_2$ formation. Witte *et al*. observed that Ga content in

the CIGS absorber affects the $MoSe_2$ formation [144]. Wada *et al*. demonstrated that $MoSe_2$ does not form under Cu-rich conditions [74]. Zhu *et al.* found that the physical properties of Mo such as density, stress and orientation can greatly influence $MoSe_2$ formation [145]. Na diffusion from SLG is regarded as a catalyst for $MoSe_2$ growth [141]. In another report, the oxygen content in the Mo was found to have an effect on the $MoSe_2$ layer thickness [146]. Excessive $MoSe_2$ layer formation is often an issue in solution-processed CIGS/CZTS solar cells. This is attributed to the porous as-deposited absorber microstructure providing little protection to the underlying Mo layer which is directly exposed to Se vapours.

To cope with the delamination and high resistivity of the back contact caused by excessive $MoSe_2$ formation, various back contact diffusion barriers, including metal oxides and nitrides, have been studied in order to prevent Se diffusion to the back contact of the CIGS/CZTS solar cell. These include ZnO, Ag, TiN, TiB_4, Mo-N and MoO_2 [77][78][79][147][148][149]. Suitable barrier layer candidates in addition to preventing Se diffusion should also be sufficiently conductive to allow low resistivity back contacts and be mechanically and chemically stable. Among previously studied layers, ZnO and Ag could diffuse to the absorber and have secondary effects [147][148][149]. TiN is stable but its deposition would require an additional step and material cost [79][149]. MoO_2 and Mo-N have the advantage of deposition using the same sputtering chamber and Mo target as for Mo deposition, with simply tuning the sputtering gas ratio. It was suggested however, that Mo oxides might also act as diffusion barrier for alkali metals diffusing from soda-lime glass (SLG) [150]. $Mo/MoN_x/Mo$ multilayers employed by Jeon *et al.* were shown to effectively control the $MoSe_2$ thickness [77]. However, resulting CZTS devices had significantly lower performance than devices without the barrier layer, presenting a roll-over behaviour in the J-V curve [151]. In this work, a Mo-N barrier layer was successfully applied at the back contact of the CIGS devices and allowed for longer selenisation times and hence better absorber crystallinity and overall device performance.

3.4.2 Mo-N barrier layer deposition and optimisation

Mo-N/Mo bilayers were deposited by DC magnetron sputtering in the same sputtering system as described for the Mo deposition. To optimise the Mo-N deposition conditions, films were first prepared by introducing different Ar/N_2 gas

proportions while keeping the deposition pressure constant at 2.3 mTorr (total gas flow rate of 15 sccm). Subsequently, the pressure was varied by introducing more gas into the chamber (10, 15, 30 and 60 sccm) with fixed Ar/N_2 ratio (67% N_2). The deposition was conducted for 4 min (Mo-N) and 2 min (Mo) using a power density of 6 W/cm^2 with the substrate rotating at 3 rpm. The top Mo layer deposited at Ar flow rate of 2 sccm is also called 'sacrificial' as this Mo layer only will be converted into $MoSe_2$ after selenisation. Table 3.6 summarises the deposition conditions and properties of Mo-N thin films deposited on SLG substrate with varied Ar/N_2 ratio (no. 1-4) and sputtering pressure (no. 5-8).

Table 3.6 Mo-N deposition parameters and film properties. The sheet resistance was measured on a Mo-N/Mo bilayer

	N_2 content (%)	**Dep. pressure** (mTorr)	**Flow rate** (sccm)	**Sheet resistance** (Ω/sq)
1	33	2.3	15	9.2
2	50	2.3	15	8.5
3	67	2.3	15	9.5
4	83	2.3	15	8.9
5	67	2.0	10	7.2
6=3	67	2.3	15	9.5
7	67	3.6	30	11
8	67	5.7	60	14

For all deposition conditions, the Mo-N and sacrificial Mo layer thickness was approximately 100 nm and 50 nm respectively. Therefore the deposition rate is estimated to be ~25 nm/min. The sheet resistance of the bilayer increased with increasing the sputtering pressure, while it remained relatively constant with varying nitrogen content of the Mo-N layer. The sheet resistance of the sputtered Mo is highly dependent on the sputtering pressure, as shown in Table 3.3.

The chemical bonds formed between Mo and N atoms and the nitrogen content of the film with varied deposition conditions were analysed using XPS depth profiles. Figures 3.11 a-b) show at% of N1s and Mo3d5 peaks found in the XPS analysis of the Mo-N/Mo bilayers prepared using various N_2 contents and gas flow rates. The first ~400 s of etch time correspond to the Mo layer. Approximately 95% of this layer consists of metallic Mo quantified from the Mo3d5 double peak found at binding energy of 228.2 eV (main peak). Reaching the Mo-N layer at etch time > 400 s, the

Mo3d5 peak shifts from 228.2 eV to slightly higher binding energies. This peak shift is clearly visible on a colour map representing the Mo3d5 double peak for one of the Mo-N/Mo samples in Figure 3.11 e). It corresponds to the change in chemical bonding from metallic Mo to a Mo-N phase.

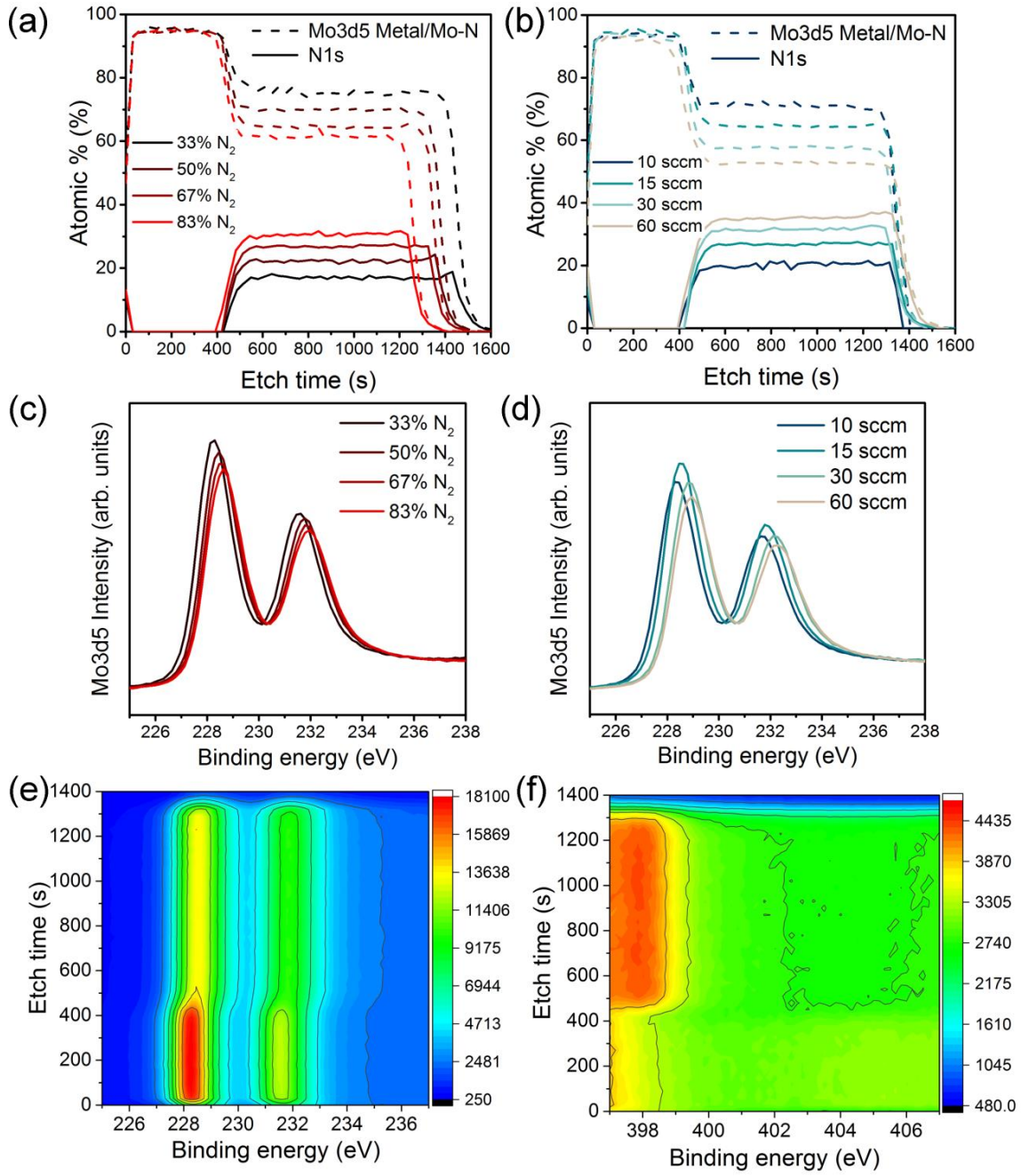

Figure 3.11 XPS analysis of the Mo-N/Mo: depth profile showing at% of Mo and N through the bilayer with Mo-N at varied Ar/N_2 ratio at 15 sccm (a) at varied gas flow/pressure with N_2 = 67% (b) Mo3d5 peak at etch time of 990 s for Mo-N films with varied Ar/N_2 ratio (c) and at varied gas flow/pressure (d) colour map of Mo3d5 (e) and N1s peak (f) at all etching levels for Mo-N at 15 sccm, 67% N_2. The colour scale represents peak intensity with arbitrary units.

The N1s peak was observed at binding energy of 398 eV as shown in Figure 3.11 f). As expected, with decreased Ar/N_2 gas proportions during the deposition, the actual N_2 content in the film increased from 17 to 30% (Figure 3.11 a)). Interestingly, with increasing sputtering pressure (by increasing the total gas flow), the N_2 content in the Mo-N layer also increased from 20 to 37% (Figure 3.11 b)). At higher pressures more Ar and N ions are available and scattering of sputtered particles increased. Both of these contribute to the formation of a Mo-N film richer in nitrogen. A small, constant amount of oxygen (5 at%) is present throughout the bilayer. It is uncertain whether the oxygen contamination comes from the measurement or deposition.

It can be observed that the etching rate through the Mo-N layer with lower nitrogen content decreased (longer etching time). This can be caused by a slight change in the Mo-N layer thickness or hardness. With high Ar/N_2 ratio, more Ar ions are available to bombard the Mo target which would result in a higher deposition rate and thickness of a Mo-N film with low N_2 content. Films deposited at lower N_2 partial pressures have higher hardness [152]. A combination of the thicker films and high hardness for Mo-N with increasing Ar/N_2 gas ratio during sputtering would explain the longer XPS etching time seen in Figure 3.11 a). However, for the films deposited at higher gas flows/pressures, the effects of higher deposition rate and consequently film thickness (from increased sputtering gas ionisation), and lower hardness (increase in N_2 partial pressure) might compensate each other resulting in similar XPS etch time (Figure 3.11 b)). These small thickness variations could not be detected by the profilometer.

Finally, Figures 3.11 c-d) show the Mo3d5 peak intensity collected at etch time of 990 s (Mo-N layer) for samples with different N_2 content and sputter gas flow/pressure. There is a clear peak shift with varied nitrogen content suggesting a possible change in Mo-N chemical state. In reactive sputtering of Mo-N, different phases including MoN and Mo_2N can be observed depending on the sputtering pressure [77][152]. The XPS main Mo3d5 peak positions together with the XRD peak positions for all Mo-N films are summarised in Table 3.7. XRD analysis was performed on all of these samples to investigate changes in crystal structure and chemical bonds of Mo-N phases with the deposition parameters. Figure 3.12 shows the XRD patterns of Mo-N/Mo bilayers with varied Ar/N_2 gas ratio and gas flow.

Table 3.7 XPS Mo3d5 peak positions and XRD peak positions corresponding to Mo-N

	XPS Binding energy (eV)	**XRD 2θ** (°)
1	228.3	37.7
2	228.5	37.3
3	228.6	37.1
4	228.7	36.8
5	228.4	37.1
6=3	228.6	37.1
7	228.9	36.9
8	229.0	36.8

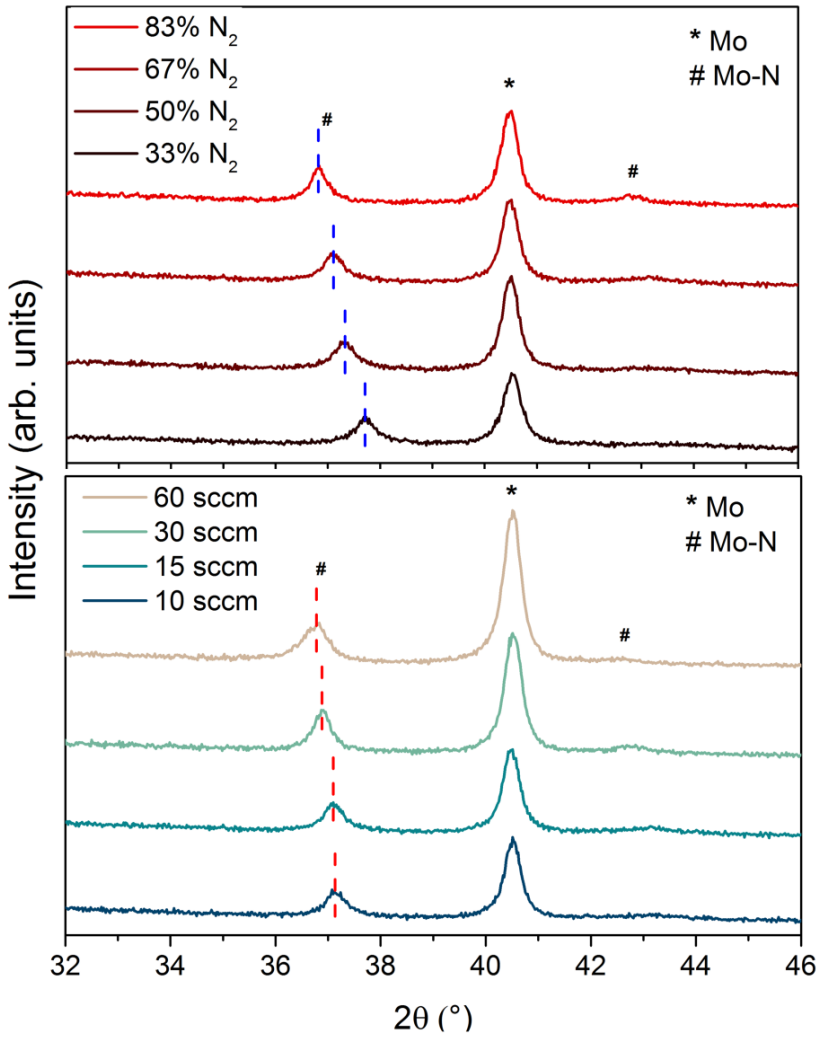

Figure 3.12 XRD patterns of Mo-N/Mo bilayer with Mo-N deposited with different Ar/N_2 ratios at 15 sccm (a) and sputtering pressures/gas flows with 67% N_2 (b). The dotted lines are showing the Mo-N peak shift from 2θ = 36.8° to 37.7° (a) and from 2θ = 36.8° to 37.1° (b).

The main peak observed at 2θ equal to 40.5° corresponds to the cubic phase of Mo (110) (JCPDS 42-1120). The second most pronounced peak is observed at 2θ ranging from 36.8° to 37.7°. This peak corresponds to the Mo-N phase and its exact position depends on the deposition conditions (Table 3.7). The peak is shifted to lower diffraction angles with increased sputtering pressure (gas flow) and to higher diffraction angles with increased Ar/N_2 ratio. This observation together with the small shift in the Mo3d5 peak position seen in the XPS implies that the crystallographic structure of the Mo-N layer might have been affected by the reactive sputtering conditions. With decreasing Ar/N_2 gas proportions during sputtering, the Mo-N becomes richer in N_2 and the crystal structure changes from tetragonal Mo_2N (112) for N_2 = 33% (JCPDS 25-1368) to cubic Mo_2N (111) or cubic Mo_3N_2 (111) for N_2 = 50% (JCPDS 25-1366 and 65-4278) to hexagonal MoN (102) for N_2 = 83% (JCPDS 74-4266), all performed at 15 sccm. When the gas flow was increased keeping the N_2 content to 67% the peak shift was smaller. From all the available crystallographic data, these films are closest to the hexagonal MoN phase. XRD analysis confirms the Mo-N phase change with varied N_2 content of the film presumed from the XPS and identifies the Mo-N crystallographic structure of each film.

3.4.3 Mo-N functionality as a diffusion barrier

In this section, Mo-N/Mo bilayer was deposited onto bare Mo-coated SLG using the following conditions: total gas flow of 15 sccm with 67% N_2, 2.3 mTorr sputtering pressure. These conditions were chosen based on the analysis above as a compromise between a sufficient film hardness and N_2 content. The sheet resistance of the bare Mo measured by four-point probe was found to be 0.28 Ω/sq and remained almost unchanged with the introduction of Mo-N/Mo bilayer, 0.27 Ω/sq. In order to test the barrier layer function as a diffusion barrier against selenium, the stack of Mo/Mo-N/Mo was selenised at 540°C for 50 min. After selenisation, TEM cross-section of the multilayer was performed and EDX mapping was used to identify the composition of each layer observed. Figure 3.13 shows the TEM/EDX analysis of the selenised Mo/Mo-N/Mo multilayer.

Columnar grains perpendicular to the substrate corresponding to Mo and $MoSe_2$ can be identified. The Mo-N layer is not clearly visible in the high angle annular dark field scanning TEM (HAADF-STEM) image, perhaps due to growing epitaxially onto the

Mo layer, as well as little change in Z-contrast and morphology between the layers. Its effect as a diffusion barrier against selenium is evident however. After selenisation, almost the entire initial Mo layer stays intact. Some channels along the columnar Mo grains where Se could penetrate under the Mo-N barrier can be observed. Only the top sacrificial Mo, deposited as a Mo-N/Mo bilayer was converted into approximately 340 nm thick $MoSe_2$. The $MoSe_2$ formation is therefore controllable by adjusting the thickness of the sacrificial Mo layer.

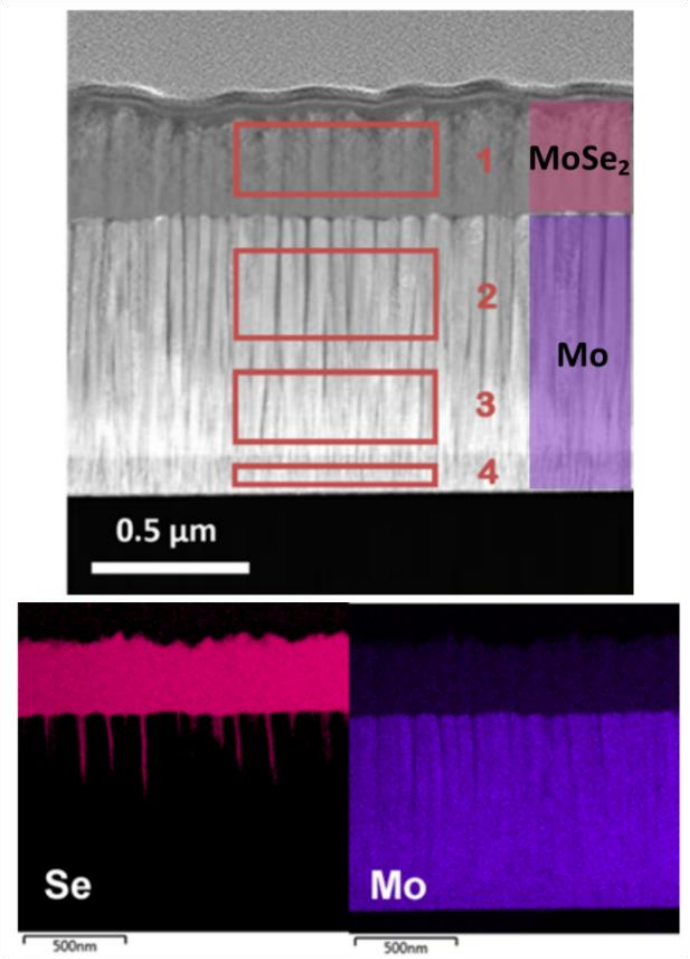

Figure 3.13 TEM/EDX analysis of selenised Mo/Mo-N/Mo multilayer. Areas 1-4 are quantified in Table 3.8.

Table 3.8 Elemental composition of the 4 areas from Figure 3.13 through the depth of the selenised back contact multilayer

	Mo (at%)	**Se** (at%)
Area 1	29.7	70.3
Area 2	98.3	1.7
Area 3	100	0.0
Area 4	100	0.0

Table 3.8 quantifies the composition of 4 areas at different depths through the selenised multilayer using EDX. These areas are indicated by a red rectangle in Figure 3.13. Area 4 corresponds to the thin, adhesive Mo layer deposited at Ar flow rate of 50 sccm. Areas 2 and 3 belong to the conductive Mo layer deposited at low working pressure achieved with 2 sccm of Ar. Area 1 corresponds to the $MoSe_2$ layer formed on top of the Mo-N barrier. 1.7 at% of Se diffused through the barrier layer into Area 2, just below the Mo-N. Hence, the Mo-N effectively worked as a Se diffusion barrier protecting the underlying Mo layer from being converted into $MoSe_2$.

In the following step, the Mo-N barrier layer was applied into complete CIGS devices. The Mo-N barrier layer thickness effect was investigated by varying the deposition time from 2 to 10 min, corresponding to a thickness range of 50 - 250 nm. Figure 3.14 shows the SEM cross-sections of selenised Mo/Mo-N/Mo/CIGS layers with varied Mo-N layer thickness. It can be observed that performing only 2 min long deposition, the Mo-N layer thickness was insufficient to prevent the selenium diffusion completely. Most of the underlying Mo layer was converted into $MoSe_2$, but no delamination occurred. However, 4 min deposition time (corresponding to ~100 nm) is already sufficient to provide full coverage of the Mo layer and prevent it from being converted into $MoSe_2$. Increasing the Mo-N deposition time does not increase the back contact resistivity (back contact sheet resistance remained the same) or affect the absorber crystallisation.

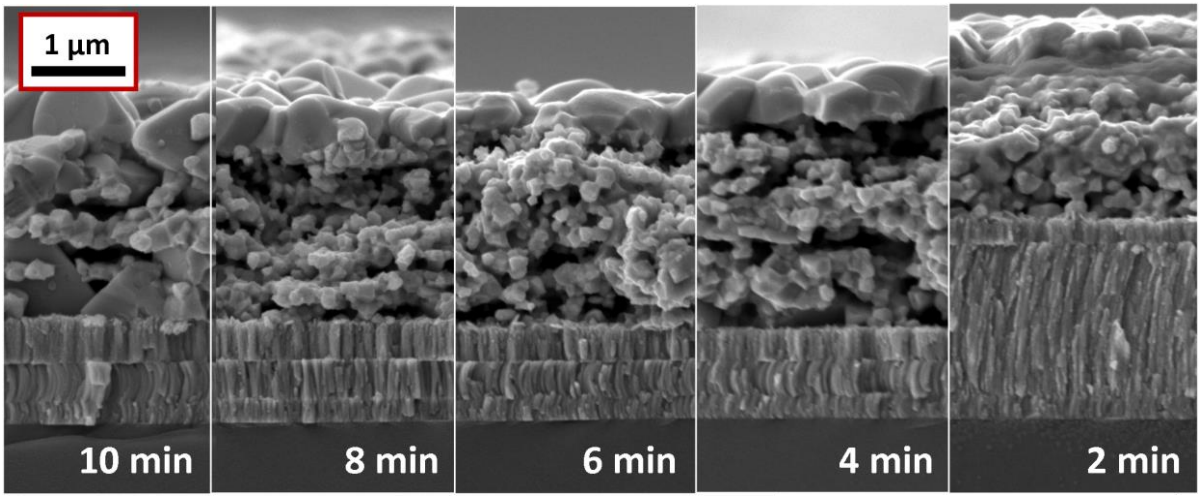

Figure 3.14 SEM cross-sections of Mo/Mo-N/Mo/CIGS layers after selenisation for 90 min. Mo-N layer thickness was varied by varying the deposition time from 10 to 2 min.

Figure 3.15 shows the XRD patterns of the selenised absorbers on Mo/Mo-N/Mo for varied Mo-N deposition time. A dominant Mo peak is observed at 2θ = 40.5° corresponding to the cubic molybdenum (110) phase (JCPDS 42-1120) and $MoSe_2$ (100) peak at 2θ ~ 31.8° (JCPDS 29-0914). Table 3.9 summarises the Mo(110)/$MoSe_2$(100) peak intensity ratio. This ratio increased with increased Mo-N deposition time. The other XRD peaks correspond to the chalcopyrite structure of the $CuIn_{0.5}Ga_{0.5}Se_2$ (JCPDS 40-1488). The dominant CIGS (112) peak is found at 2θ ~ 27.0° and smaller peaks corresponding to (220)/(204) and (312)/(116) planes of tetragonal CIGS phase are found at 2θ ~ 45.0° and 54.0° respectively. The Mo-N peak seen at 2θ ~ 37.0° in Figure 3.12 would overlap with the low intensity CIGS (211) peak.

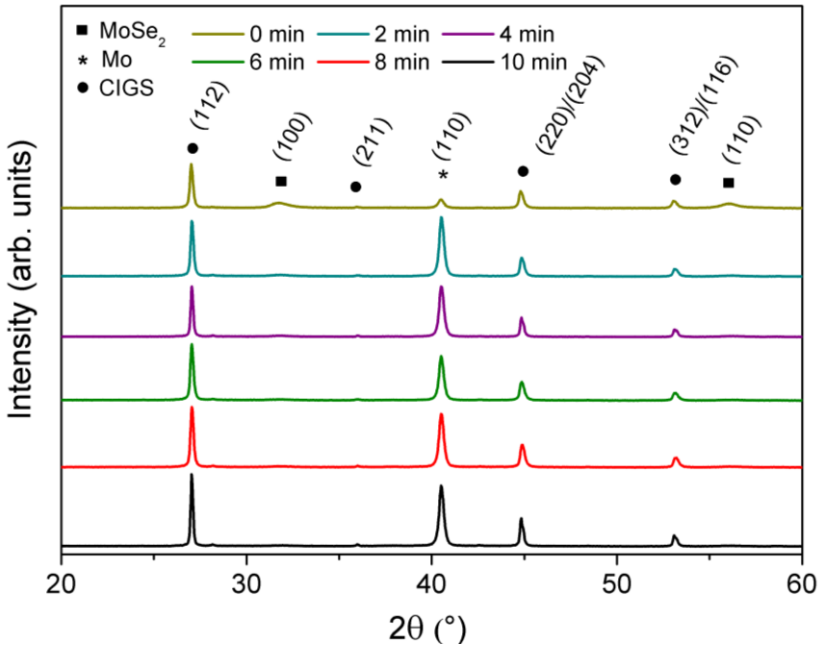

Figure 3.15 XRD patterns of the Mo/Mo-N/Mo/CIGS films for different Mo-N barrier deposition durations.

Table 3.9 XRD peak intensity ratio for selenised Mo/Mo-N/Mo/CIGS films with varied Mo-N layer deposition duration

Deposition time (min)	**Approx. Mo-N thickness** (μm)	**Mo/$MoSe_2$ intensity ratio**
0	0	1.73
2	0.05	55.25
4	0.1	64.03
6	0.15	70.89
8	0.2	76.49
10	0.25	126.83

Alkali dopants such as Na, were found to promote grain growth of CIGS and CZTS absorber layers [153][154]. It is reported that incorporation of Na involves a formation of liquid Na-Se phases during selenisation. The reactive selenium provided via Na-Se phases reacts with the metal containing precursors resulting in greatly enhanced grain growth [154]. The most common source of Na for CIGS is SLG from which Na migrates to the CIGS absorber during high temperature selenisation. However some back contact barrier layers, such as MoO_2 can also block Na diffusion from SLG to the absorber [150]. In order to study the presence of a small quantity (order of few at%) of light elements (such as Na) in the CIGS absorber, SIMS measurements were performed. The two SIMS depth profiles shown in Figure 3.16 compare relative quantities of Cu, In, Ga, Se, Mo and Na in CIGS and Mo layers for samples with and without Mo-N barrier layers at the back contact. For this experiment, the Mo-N barrier layer was deposited for 10 min and the absorber was selenised for 90 min. This is an uncalibrated measurement and therefore the data is only relative and not absolute. The inset of Figure 3.16 shows the SEM cross-section of the Mo/CIGS layers analysed. From these it is clear that rough and porous films were measured resulting in profiles with broader interfaces. Moreover any partial delamination of the layers in the measurement area would exacerbate this effect and potentially explain the different slope in the Mo signal for both samples.

The profiles of Ga and In are very closely matching within the two samples. The barrier-free sample contains a considerable amount of cracked and partially delaminated $MoSe_2$. Se is present and constant through the absorber and back contact in the barrier-free sample indicating an even distribution of Se through CIGS and $MoSe_2$. The sputtering through the $MoSe_2$ layer was not finished at the end of the 3000 s of analysis time. In comparison, in the Mo-N containing sample Se started to decrease from 2000 s along with In, Ga and Cu profiles implying that the CIGS/Mo interface was reached. Interestingly, in the barrier-free sample, the Cu signal does not decrease along with In and Ga profiles in the $MoSe_2$ layer. The Cu signal is reduced but constantly present in the $MoSe_2$ layer. Copper is a fast diffusing element and has migrated and segregated in the back contact $MoSe_2$ layer, consequently reducing the CGI ratio in the CIGS absorber. Cu diffusion into MoS_2 and $MoSe_2$ has been previously reported in several studies [119][155][156].

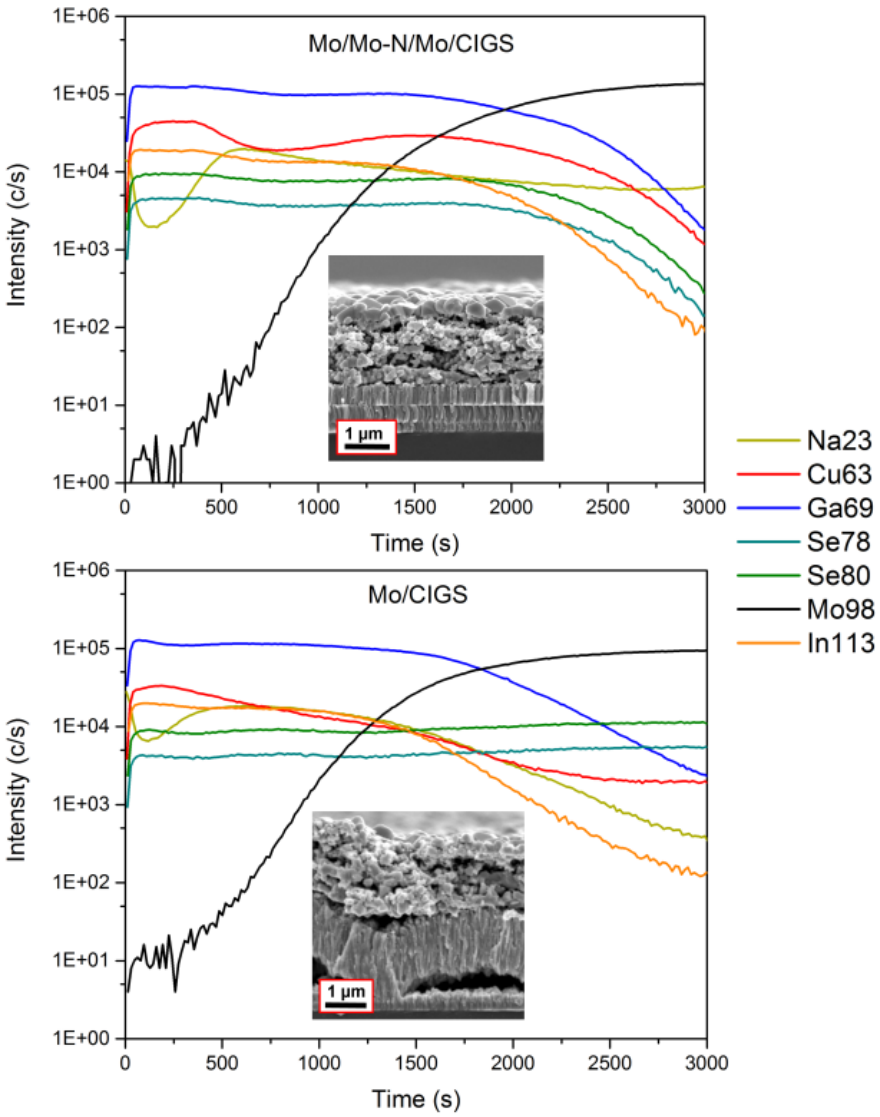

Figure 3.16 SIMS depth profiles showing the elemental line scans through the absorber deposited on Mo/Mo-N/Mo back contact (top) and on bare Mo (bottom). Inset: SEM cross-section through the analysed samples.

High Cu content is essential for good CIGS crystal growth [157]. The lower apparent Cu quantity throughout the absorber of the barrier-free sample relative to the barrier containing sample could cause reduced grain growth and lower J_{SC}. Sodium is present in the bulk of both CIGS absorbers. The surface of the absorber appears to be Na-deficient relative to the bulk however, and similar trends can be observed for both samples. In the barrier-free device, the Na signal shows smaller local minimum near the surface relative to Na signal in the Mo-N sample. This might be related to the grain size of the crystallised top absorber layer. The grain size is much smaller in the barrier-free absorber. Na is known to passivate grain boundaries and there are more GBs present in the less crystallised barrier-free absorber. Similar SIMS Na

signal shapes are common in the literature [43]. SIMS analysis showed that Na diffusion from the SLG was not hindered by the presence of Mo-N barrier layer at the back contact. Moreover, owing to the barrier layer, Cu diffusion from the absorber to the $MoSe_2$ back contact was significantly reduced.

3.4.4 Mo-N barrier layer application in CIGS devices

To study the effect of the Mo-N barrier layer on the device performance, two types of devices were prepared: on a bare Mo-coated substrate and on a Mo/Mo-N/Mo multilayer-coated substrate. Figure 3.17 shows a cross-section of CIGS absorbers and back contacts with (highlighted 'B' in images) and without Mo-N barrier after selenisation for 50 and 90 min.

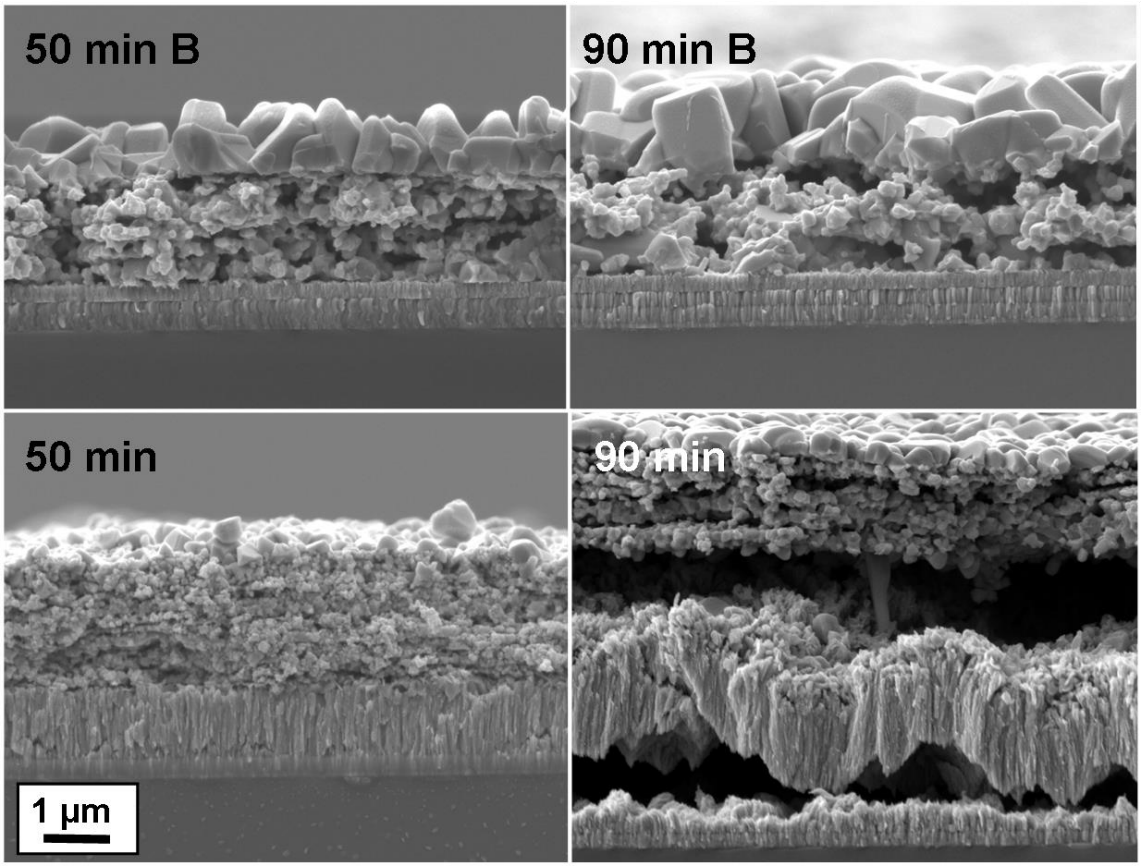

Figure 3.17 SEM cross-sections through the CIGS absorber and back contact for 50 and 90 min selenised samples with (B) and without Mo-N barrier.

Without using the barrier layer, over 1 µm thick $MoSe_2$ forms at the Mo/CIGS interface after a 50 min selenisation. After a 90 min selenisation, the Mo almost completely reacts with Se vapour to form $MoSe_2$ and delamination is observed. Additionally, since more selenium is incorporated into the back contact, the absorber

remains poorly crystallised. On the other hand, when a barrier layer acts as Se diffusion barrier, there is more Se available for the absorber recrystallisation. High Cu content and high Se partial pressure are two of the main conditions to achieve a good CIGS crystal growth. Higher Cu content in the absorber on modified Mo/Mo-N/Mo back contact was evidenced by SIMS analysis of the absorbers (Figure 3.16). In addition, more Se was available for the whole annealing time to create higher Se partial pressure owing to the lower reaction with Mo to form $MoSe_2$ (Figure 3.17). As a result, significantly larger grains are formed at the surface of the absorber, with the largest grains observed after longer selenisation.

The four types of samples were completed into CIGS devices. Figure 3.18 shows box plots of PV performance parameters such as V_{OC}, J_{SC}, FF and PCE measured on more than 14 cells for each selenisation (50 and 90 min) and back contact (B: barrier, or bare Mo) configuration.

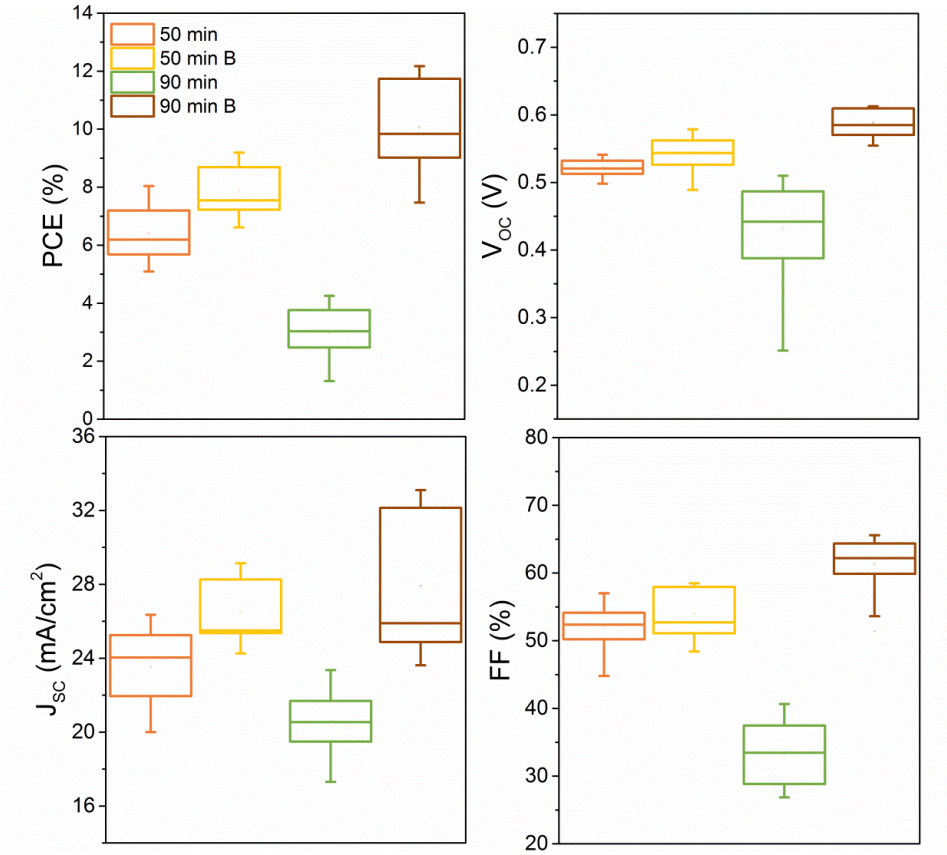

Figure 3.18 Box plots showing the distribution of PV parameters measured from more than 14 solar cells obtained from minimum two distinct devices for each sample.

As expected from the cross-section SEM image (Figure 3.17), the performance of the delaminated (90 min selenised) device on bare Mo is poor

with all parameters significantly lower than for the other samples. Its low FF results from the highly resistive and delaminated back contact. Lower J_{SC} and V_{OC} can be attributed to the poor crystallinity of the CIGS absorber containing more GBs. Introducing the back contact barrier (B), the solar cell performance increased from an average 6.5 to 8% with mainly a gain in J_{SC} by an average of over 3 mA/cm^2 after 50 min selenisation. A non-negligible gain in V_{OC} is also observed. After a longer (90 min) selenisation, the device performance was further increased from an average of 8 to 10%, with an additional gain in V_{OC} (an average of 40 mV) and in FF which increased (in average) from 55 to 63%. The J_{SC} was also increased; however the distribution of the values is much larger implying lateral inhomogeneity of the grain crystallisation.

It is anticipated that the improved crystallinity is largely responsible for the remarkable performance improvement. The modified back contact containing only a thin $MoSe_2$ layer likely caused the reduction in the device series resistance (R_S) resulting in higher FF, as the $MoSe_2$ is very resistive. The improved device characteristics when the Mo-N barrier was applied, is also reflected in lower diode ideality factor (n) and dark saturation current density (J_0). These values along with the typical PV performance parameters are reported in Table 3.10 for a representative device from each configuration.

Table 3.10 PV characteristics of a representative solar cell for the four selenisation/back contact configurations. These cells were measured using a different solar simulator (Wacom, Japan) following the accredited measurement procedure at CREST Photovoltaic Measurement and Calibration Laboratory (CPVMCL).

	PCE (%)	**V_{OC}** (V)	**J_{SC}** (mA/cm^2)	**FF** (%)	**R_S** (Ω.cm^2)	**R_{SH}** (Ω.cm^2)	**n**	**J_0** (mA/cm^2)
90 min B	12.05	0.622	28.67	67.53	0.967	331.0	1.79	3.94×10^{-5}
50 min B	8.26	0.591	23.08	60.64	0.365	305.6	2.71	4.61×10^{-3}
50 min	6.54	0.553	19.85	59.68	1.116	350.9	2.52	3.76×10^{-3}
90 min	4.23	0.510	21.39	38.79	7.202	119.74	3.28	4.58×10^{-2}

3.5 Conclusions

This chapter presented the choice, deposition and optimisation of the substrate and back contact for CIGS solar cells. Various glass substrates differ in their thermal expansion and content of alkali elements which were found to have an effect on film

delamination after selenisation. When SLG was used as substrate, the delamination was severe. SLG has the highest expansion coefficient among the studied glass substrates and contains a non-negligible amount of Na, which becomes mobile at elevated temperatures and its presence in CIGS absorber is widely recognised as beneficial for device performance.

Mo was deposited onto glass substrates in form of an adhesive/conductive bilayer. The adhesive layer was deposited at high sputtering pressure controlled by Ar flow rate and low power as opposed to the conductive layer at low pressure, high power. The adhesion improved with increasing the pressure for the 1st Mo layer up to 30 mTorr. The conductivity of the entire Mo stack wasn't affected as this layer was very thin compared to the 2nd, conductive Mo layer.

Delamination due to excessively thick $MoSe_2$ formation at the Mo/CIGS interface was effectively prevented by introducing Mo-N diffusion barrier layer at the back contact. A relatively simple deposition process performed in the same sputtering chamber as Mo and tunability of the Mo-N thin film characteristics (N_2 content and crystallographic phase) were demonstrated. The functionality as a barrier layer against Se diffusion was shown and resulted in controllable $MoSe_2$ layer thickness. The Mo-N application at the back contact of CIGS solar cells resulted in devices with considerably improved performance. FF was improved due to lower R_S as the resistive $MoSe_2$ layer thickness was significantly reduced. The increase in device J_{SC} and V_{OC} resulted from the improved CIGS crystal quality as more Se and Cu were available during selenisation of the absorber containing the barrier layer. Finally, the Mo-N application and consequent improvement of the back contact quality allows focusing on the improvement of the solution-processed absorbers without being limited by the back contact resistivity and delamination.

CHAPTER 4

CIGS/CdS junction properties

4.1 Scope

It was experimentally observed that device performance was often variable with limited degree of reproducibility despite no change was made in the fabrication process. Process conditions including temperature, pressure and duration of each CIGS solar cell fabrication step are typically well controlled except for the last fabrication step: the thermal evaporation of the metal grid. The metal evaporator is an in-house bell-jar vacuum system with a power supply delivering current to a tungsten evaporation boat containing silver pellets. Evaporated thickness is measured using a quartz crystal microbalance and a thermocouple gives an indication of substrate temperature during the process. Despite performing the evaporation using repeatedly the same conditions (base pressure and current), the evaporation process was typically very variable with deposition durations and final temperatures changing from run to run. This behaviour is most likely influenced by the state of the tungsten boat and the terminals of the system, which are prone to oxidise and be less conductive.

Device performance and in particular the V_{OC}, was remarkably increased when finished devices were subjected to higher temperatures during the evaporation. An often mentioned in the literature, but rarely explicitly described step in CIGS device fabrication, is the air-annealing of the heterojunction. This is typically performed at temperatures above 100°C directly after the CdS CBD [158][159][160][161][162]. The effects of air-annealing on the electronic properties of the solution-processed CIGS devices were studied in order to achieve a stable and reproducible process yielding higher efficiencies. The importance of the CdS layer deposition directly after the absorber selenisation was evidenced by a TRPL study of the minority carrier lifetime decay with air-exposure.

4.2 Buffer layer

4.2.1 CdS properties, deposition and alternatives

CdS is the most commonly used buffer layer for CIGS solar cells satisfying most of the requirements for a suitable n-type layer for the p-type CIGS absorber. It has a suitable conduction band alignment to the CIGS and i-ZnO, beneficial interface defect chemistry and suitable bandgap of 2.4 eV [41] The major drawback is the presence of Cd, which is an issue for the commercial production of CIGS modules and their decommissioning [8]. Hence, an extensive research has been carried out to find a suitable Cd-free alternative with similar beneficial properties that CdS has. Solar Frontier is currently producing modules with CBD grown Zn(S,O,OH) [26]. It has even larger bandgap (tunable by varying S/O ratio) limiting the parasitic absorption losses in the buffer layer, but it has a stronger light soaking metastability than the CdS [41].

Chemical bath deposition (CBD) gives currently the best performing and most reliable solar cells. The chemical bath is typically made of an alkaline aqueous solution (pH ~11) containing ammonium hydroxide (NH_4OH), thiourea as sulfur source and Cd salts as cadmium precursors. Ammonia in the bath serves as a complexing agent, however it also etches the CIGS surface removing Na- and O-containing impurities from the surface prior to the CdS nucleation. The recipe and experimental procedures of the CdS CBD used in this work were described in Chapter 2. The general chemical reaction of the process is [41]:

$$Cd(NH_3)_4^{2+} + SC(NH_2)_2 + 2OH^- \rightarrow CdS + CN_2H_2 + 4NH_3 + 2H_2O \qquad [4.1]$$

The actual reaction scheme behind the Equation [4.1] is still debated however; in particular whether the growth is preferentially homogeneous (through formation of surface intermediate products such as $Cd(OH)_2$) or heterogeneous (precipitation of CdS particles formed in the solution) [41]. The deposition rate is controlled via the concentration of thiourea in the bath. To avoid rough and porous films, the deposition should be terminated before reaching the saturation point where the solution is depleted from non-reacted Cd-species. During the CBD Cd^{2+} diffusion into the absorber close-to-surface region filling Cu vacancies was observed to take place [163].The presence of a buffer layer in CIGS device is attenuating the difference in refractive index of the window and absorber layers, thus causing an optical gain due to reduced window reflection. However large buffer layer thickness causes collection

losses due to absorption of photons in this layer. An optimum buffer layer thickness up to which the optical gain compensates for the collection loss has to be found. This is dependent on the specific optical parameters of the absorber, buffer and window layers. The optimum CdS thickness for the high-efficiency co-evaporated CIGS devices is ~50 nm.

4.2.2 Interface recombination and junction passivation by air-annealing

CdS has been shown to electronically passivate the absorber surface and preserve high carrier lifetime in the absorber measurable by the TRPL decay. CIGS films capped with the CdS buffer layer are stable and can be stored for weeks, as opposed to bare absorbers [41]. The absorber material degrades with time from the point of being exposed to air and this degradation is strongly visible on the rapid reduction of the minority carrier lifetime, already within minutes from the film preparation [164].

Charge carrier recombination at the interfaces is a limiting factor of the heterojunction solar cells such as CIGS and becomes even more significant as the bulk material properties improve. Recombination is triggered by the presence of interface defects acting as recombination centres for electron-hole pairs, which arise from the lattice mismatch between the two junction partners or were introduced during the junction fabrication process. Devices with severe interface recombination suffer mainly from poor V_{OC} which is a consequence of increased dark saturation current density (J_0). An approach to mitigate the interface recombination is to carefully engineer the device parameters that affect it, such as band alignment at the CIGS/CdS interface and CdS doping and thickness. In addition the energetic location and defect type of the interface states have also an effect on the recombination rate [165]. A small, positive conduction band offset ($0.1\ eV \leq \Delta E_C \leq 0.3\ eV$), also called a ‘spike’ introduces greater band bending and consequently a larger hole barrier adjacent to the interface that supresses the interface recombination. High doping ratio between CdS and absorber creates a strong absorber surface inversion and consequently the p-n junction is located within the absorber (buried junction). Minority carriers in the bulk become majority carriers at the interface, thus reducing the interface recombination [41]. In addition, an increase in CdS thickness reduces the band bending of the absorber surface, increasing the hole density. As a result

cells with thin and highly doped CdS and a spike offset can maintain high conversion efficiency despite the presence of interface defects (high interface recombination velocity). Finally, the acceptor-type interface defects located near the mid-gap cause more severe performance loss than donor-type defects with energies near a band edge [165].

The post-deposition air-annealing of the heterojunction interface, its underlying physics and effect on the device performance have been previously studied [94][96][161]. A generally accepted conclusion is that the air-annealing step is important in order to achieve high efficiency CIGS devices with increased V_{OC} due to reduced recombination, however its duration is critical [166]. Rau *et al.* observed a decrease in device capacitance with air-annealing of Cd-free devices and attributed it to the Cu diffusion deep into the bulk and acting as compensating donors. This resulted in significantly reduced bulk doping density and an increase in absorber SCR width [94]. Hence the Cu-diffusion is limiting the effective air-annealing duration. No effect of the air-annealing on the bare absorbers observed suggests that the build-in electrical field in presence of the junction is the driving force to the migration of the positively charged Cu ions into the bulk [96].

The use of CdS as a buffer has an additional benefit: it allows Cd diffusion into the close-to-surface region of the CIGS absorber, where it forms a positively charged substitutional defect Cd_{Cu}. Carefully designed Cd diffusion can help to optimise the junction and device properties by contributing to the absorber surface inversion and adjusting the field profile in the SCR [163]. According to the model of Cahen and Noufi, the beneficial effects of air-annealing consist in the passivation of the surface dangling bonds related to the Se vacancies (V_{Se}) at GBs and absorber surface by oxygen atoms [167]. The positively charges V_{Se} donor defects are detrimental to the device performance as they act as recombination centres for photo-generated electrons. Moreover the positive GB surface charge creates a depletion region within each grain and forms a potential barrier reducing the effective p-type doping and impeding the inter-grain transport of photo-generated electrons [94]. The oxygen filling V_{Se} creates a charge neutral O_{Se}, which is thought to cancel both of these detrimental effects. Removing the positive charge form the heterojunction interface would reduce the band bending and enhance interface recombination, however. Hence, an important but not always recognised role of the CdS buffer is to restore

the interface band bending by reintroduction of positively charged defect states at the interface, likely through Cd occupying empty Cu sites [94].

4.3 Air-annealing of the junction

The positive effects of oxygenation on the CIGS/CdS junction properties and their origin have been discussed. Considering diverse and often confusing trends obtained after the evaporation of silver grids, the annealing in presence of oxygen was thought to have an effect on the performance of the solution-processed absorbers studied in this work. Although the evaporation is carried out under vacuum, a small amount of oxygen may have remained in the relatively porous atmospherically-processed absorber or come from the front contact TCO. Various annealing conditions as well as diverse effects on the device electronic properties have been reported in the literature. The air-annealing experiments conducted in this work were performed on the CIGS samples with base-line $Cu_{0.9}In_{0.7}Ga_{0.3}Se_2$ composition prepared by spray-coating onto Mo/Mo-N/Mo-coated SLG substrates followed by selenisation at 540°C. The CdS was deposited by CBD onto the selenised absorbers. An air-annealing step was performed at three different stages of the cell fabrication: directly after selenisation, after CdS CBD and after TCO and grid deposition (finished device). The air-circulating furnace was preheated at 180°C and the samples were annealed for various durations from 5 to 60 min. A non-annealed sample was used as a reference. The metal grid evaporation was performed at higher current ultimately reaching lower temperatures (< 60°C) to avoid cumulative annealing of the sample.

4.3.1 Annealing after selenisation

The devices presented in this section were prepared from CIGS absorbers subjected to air-annealing for various durations. PV performance parameters including V_{OC}, J_{SC}, FF and PCE extracted from the J-V measurements of approximately 15 cells for each annealing duration are summarised in the form of box plots in Figure 4.1. Device performance became gradually worse with longer annealing durations. The progressive decrease in efficiency with annealing time is primarily caused by the progressive decay of the device FF. In addition, the V_{OC} dropped by more than 100 mV on average after the first 15 min of air-annealing. On the other hand, the J_{SC} shows the opposite trend with the highest value reached for 30 min long annealing.

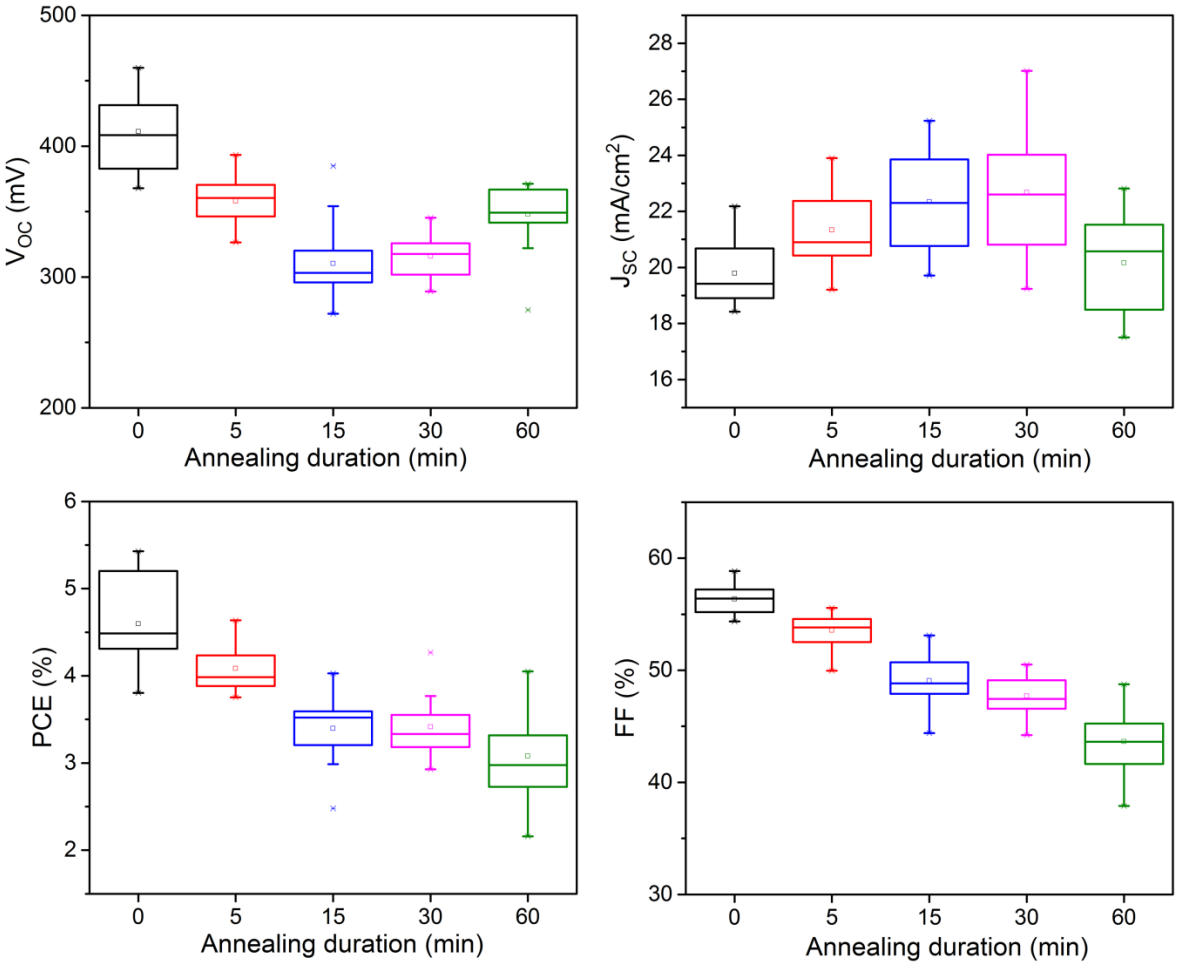

Figure 4.1 Box plots of PV indicators of CIGS cells when air-annealing was performed after selenisation of the bare absorber.

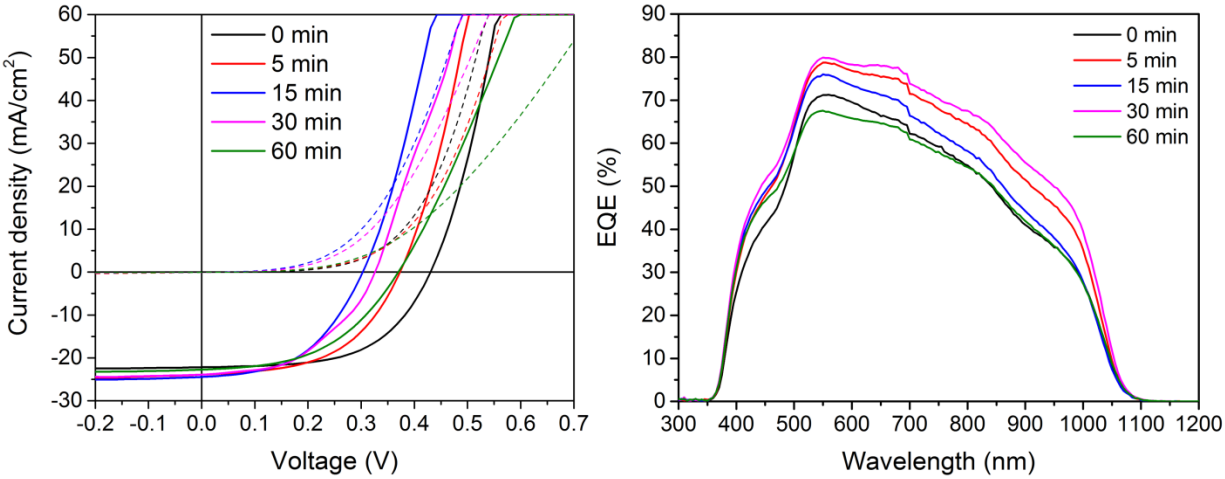

Figure 4.2 J-V (left) and EQE (right) graphs of a representative device for each annealing.

J-V and EQE measurements were performed on a representative device for each annealing duration. The J-V and EQE curves are presented in Figure 4.2. A

significant improvement in the EQE signal at all wavelengths is observed with air-annealing up to 30 min. The V_{OC} loss after annealing is observed from the J-V curves. The deterioration of the device performance with annealing of the absorber surface prior to CdS CBD indicates that the oxygenation of the bare absorber surface is detrimental. The air-annealing of the uncoated CIGS surface is most likely accelerating the absorber degradation with air-exposure studied using TRPL in section 4.4 and reported in various other studies [164][168]. It was suggested that CIGS surface degradation may be caused by the reaction of Na with O_2 or H_2O in air [169]. Shin *et al.* found however that compositional changes (Cu decrease and Ga increase) associated with the air-annealing of the free CIGS surface resulted in the increase of V_{OC} and FF [166]. In the experiments conducted here, device performance decreased with air-annealing and as a result no further study to analyse the origin of the performance degradation was performed.

4.3.2 Annealing after CdS CBD

To confirm the importance of the junction presence during the air-annealing, the annealing was performed this time directly after the CdS CBD. The box plots of the PV performance indicators for each type of device are shown in Figure 4.3. An increase in PCE was achieved with increasing the annealing time up to 30 min. Longer annealing (60 min) resulted in more scattered PCEs with no overall improvement from the 30 min annealing. A small decrease in device FF was observed however, indicating the beginning performance degradation.

Figure 4.4 compares J-V curves of the champion cells for each annealing duration. All key performance indicators corresponding to the curves in Figure 4.4 are summarised in Table 4.1. It is observed that air-annealing for as short as 5 min starts to improve all device parameters and after 15 min a significant improvement in the device performance can be seen with PCE escalating from an initial 5.4% to above 9%. This remarkable improvement in the device performance originates primarily from a remarkable increase in V_{OC} by over 130 mV from 0 to 30 min of air-annealing. Improvements in J_{SC} are also non-negligible; however FF starts to decrease slowly after 15 min of air-annealing.

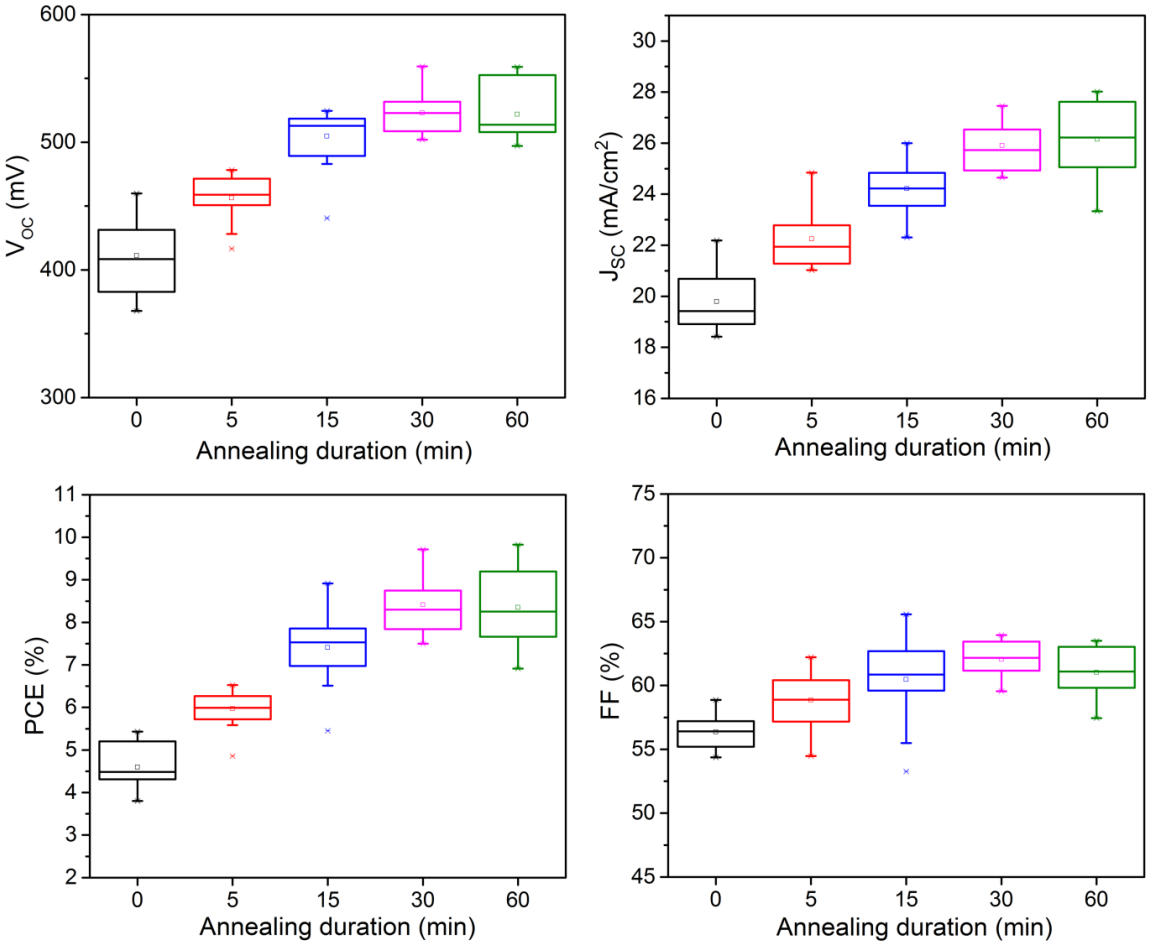

Figure 4.3 Box plots of PV indicators of CIGS cells when air-annealing was performed after CdS CBD for various durations.

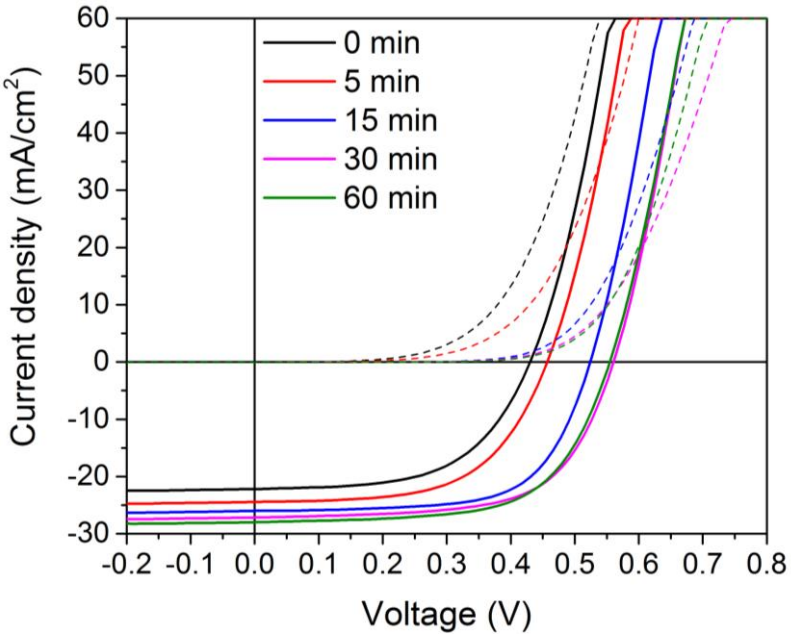

Figure 4.4 Light and dark J-V curves of the champion cell for each air-annealing duration.

Table 4.1 PV parameters of the champion cell for each CIGS/CdS air-annealing duration

	V_{OC} (V)	J_{SC} (mA/cm^2)	FF (%)	PCE (%)
0 min	429.0	22.2	57.1	5.4
5 min	455.8	24.4	58.6	6.5
15 min	523.1	26.0	65.6	8.9
30 min	559.4	27.2	63.9	9.7
60 min	553.5	28.0	63.5	9.8

To study the material quality across the entire cell area, EL images of the champion cell for each type of device were performed under a current load of ~J_{SC} with acquisition time of 10 min. The EL images (Figure 4.5) map the electronic quality of the absorber across the entire active area of the solar cell.

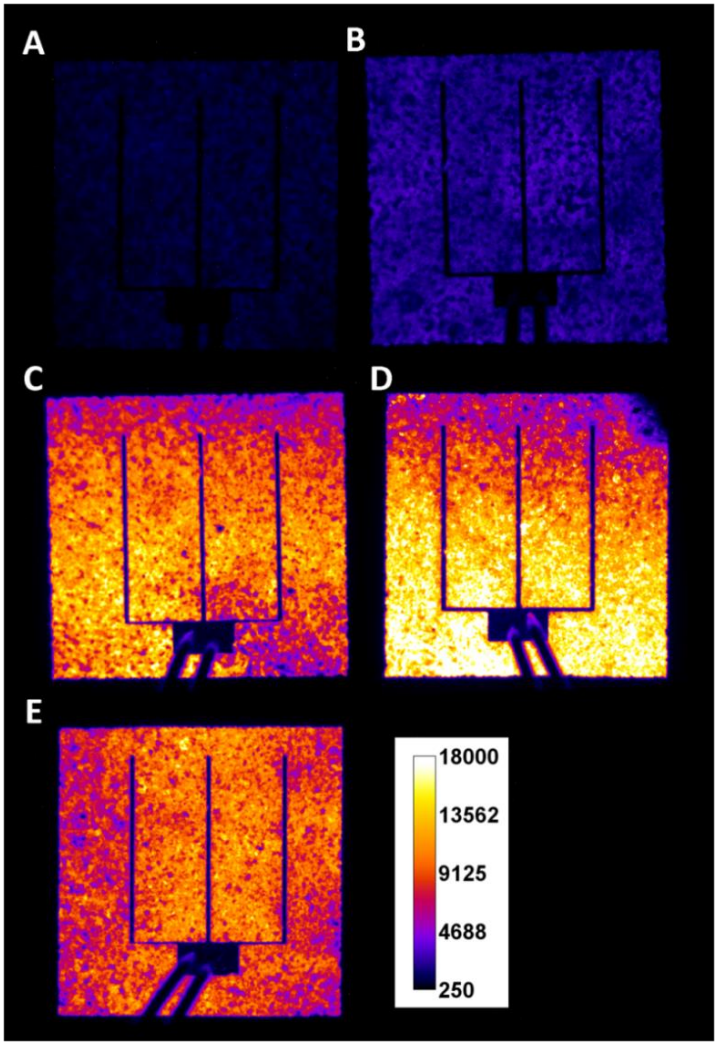

Figure 4.5 EL images of devices with air-annealed CIGS/CdS for 0 min (A), 5 min (B), 15 min (C), 30 min (D) and 60 min (E). The colour scale is in arbitrary units.

The uneven signal over the cell area can originate from the non-identical PV properties of all CIGS grains amplified by their solution-based nature and presence of local shunts and grain boundary (GB) recombination. It can be seen that the signal is significantly stronger in cells annealed for longer than 15 min and is the highest for the 30 min long anneal, which is consistent with the V_{OC} values of these cells reported in Table 4.1. The voltage improvement can most likely be attributed to oxygen passivation of the surface and GB defects such as Se vacancies, as well as Cd incorporation and consequent n-type doping of the absorber close-to-surface region reducing both GB and interface recombination. After 60 min of air-annealing the EL signal weakened. During air-annealing, Cd diffusion from the buffer layer to the absorber surface is beneficial to adjust field profile in the SCR. Further migration damages junction stability and reduces carrier density of the CIGS material however [92][163]. In addition, oxygen was found to promote Cu liberation from the near-surface region and migration towards the back, where it acts as compensating donor, decreasing the net doping density and increasing the absorber SCR width [94]. This results in an increase in R_S and consequently a drop in FF, which was observed experimentally.

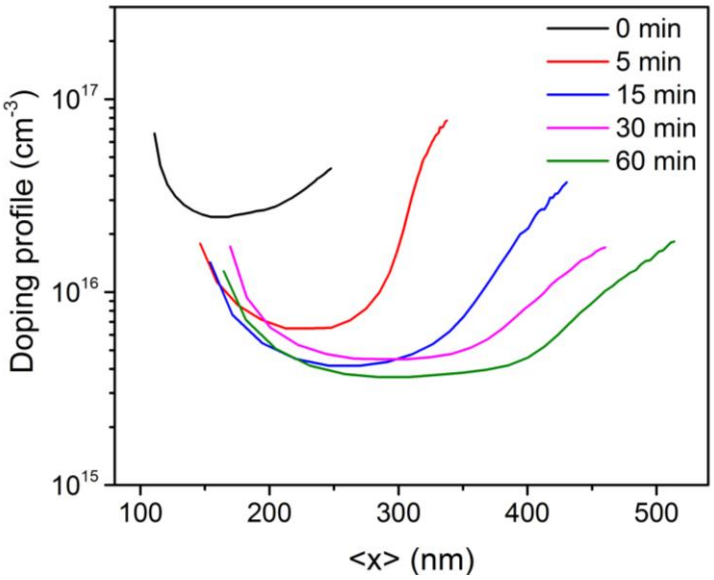

Figure 4.6 Carrier density profiles extracted from C-V measurements at RT for various air-annealing durations of CIGS/CdS films.

To evaluate the doping density of the CIGS absorber, carrier density profiles displayed in Figure 4.6 were extracted from the C-V measurements at room temperature. Longer annealing times resulted in a drop in the apparent carrier

density. The absorber acceptor density decreased by almost one order of magnitude from $2.5x10^{16}$ cm^{-3} (non-annealed) to $3.6x10^{15}$ cm^{-3} (60 min annealed). Interface states may contribute to the capacitance signal and therefore C-V measurement can give ambiguous values. Although not performed here, DLCP would be a better method of estimating the free carrier concentration due to its insensitivity to the response from interface or near-interface states [170]. Additionally, the depletion region width (*W)* at 0V bias increased with the annealing duration (Table 4.2). This is consistent with the findings in the literature suggesting Cu^{+} release from the surface and migration deeper into the bulk decreasing the absorber doping density either by direct compensation or by eliminating the negatively charged Cu vacancies [94].

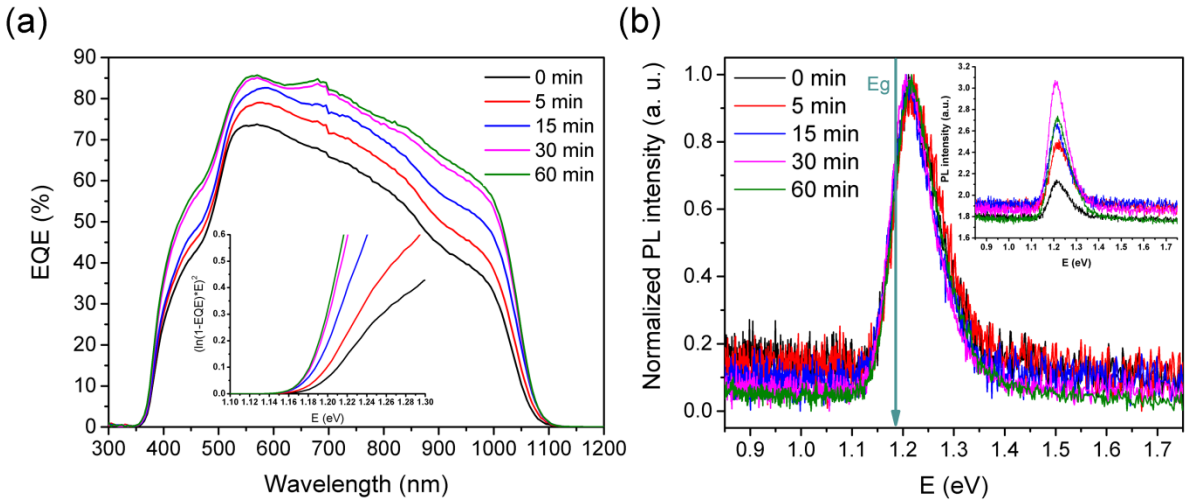

Figure 4.7 EQE spectra with inset: plot of ln((1-EQE)*E)^2 vs. E used to extract the material bandgap (a) and normalised PL spectra with the inset showing PL intensity of each signal (b) for the different annealing durations.

From the EQE spectra in Figure 4.7 a), an increase in carrier collection from 0 to 60 min annealing is observed at all wavelengths, agreeing with the gradual increase in J_{SC}. The increase in carrier collection with annealing can result from elimination of interface defects or from larger depletion width. Moreover the increase of the optical transition through the CdS can also add to the value of J_{SC}, as the EQE signal at low wavelengths (~400 nm) is progressively shifted towards higher values with the increase of annealing time. An increase in CIGS solar cell efficiency, mainly due to an increase in the device J_{SC} was observed in the literature and was attributed to the elimination of the recombination centres at the p-n junction and increase of the optical transmittance of the CdS [171]. All the EQE curves show a lack of long wavelength response however. This can be attributed to a porous and poorly

crystallised absorber near the back contact resulting in a weak minority carrier-collection and low carrier lifetimes in this part of the absorber. EQE spectra were used to determine the bandgap (E_g) of the absorber material by fitting a plot of $[\ln(1-EQE)*E]^2$ vs. E, as displayed in the inset of Figure 4.7 a).

Table 4.2 Summary of the bandgap, activation energy of the dominant recombination mechanism (E_A), voltage deficit, doping density, depletion width (*W*) and activation energy of shallow defects (E_{A-AS})

	E_g (eV)	E_A (eV)	$E_g/q - V_{OC}$ (V)	N_{C-V} ($x10^{15}$ cm^{-3})	*W* at 0V *(nm)*	E_{A-AS} (meV)
0 min	1.189	1.092	0.76	24.5	161	70
5 min	1.185	1.240	0.73	6.49	275	222
15 min	1.182	1.282	0.66	4.16	340	244
30 min	1.182	1.278	0.62	4.49	341	298
60 min	1.182	1.259	0.63	3.63	368	273

The bandgaps for all air-annealing durations are summarised in Table 4.2, along with the calculated open-circuit voltage deficit ($E_g/q - V_{OC}$) where q is the electron charge. A slight decrease in E_g from 1.189 eV to 1.185 eV after 5 min annealing and to 1.182 eV above 15 min annealing is observed. This relatively small E_g reduction upon annealing could originate from compositional variation through the depth of the absorber due to atom migration and redistribution. No shift in the PL peak position was observed for any anneal duration however. PL spectra shown in Figure 4.7 b), exhibited a dominant peak at 1.21 eV. All PL peaks are shifted to higher energies with respect to their bandgap energy E_g (~20 meV). This shift can be caused by using a fixed laser wavelength (640 nm) for the measurement as a result of which the PL spectra would not show any compositional variation through the absorber depth. The laser light would be totally absorbed in the first few hundred nanometers of the absorber thickness. Alternatively, the shift in the PL peak relative to the E_g obtained from the EQE plots could also suggest that the absorber surface is slightly richer in Ga compared to the bulk. The inset of Figure 4.7 b) shows that PL intensity was enhanced with annealing duration up to 30 min and decreased for 60 min of annealing.

The voltage difference between V_{OC} and E_g/q, also called voltage deficit, is nominally close to 0.5 V for high quality CIGS solar cells [172]. The voltage deficit is larger than

0.6 V for all the devices presented here, and this difference becomes even larger with shorter annealing times. To examine the cause of the V_{OC} deficiency, temperature-dependent measurements were performed to find the dominant recombination mechanism and defect energy levels. Admittance and J-V-T measurements were performed within a temperature range of 315-105 K. The activation energy for the dominant recombination mechanism (E_A) can be extracted from the J-V-T by plotting a graph of V_{OC} vs. temperature (Figure 4.8 a)).

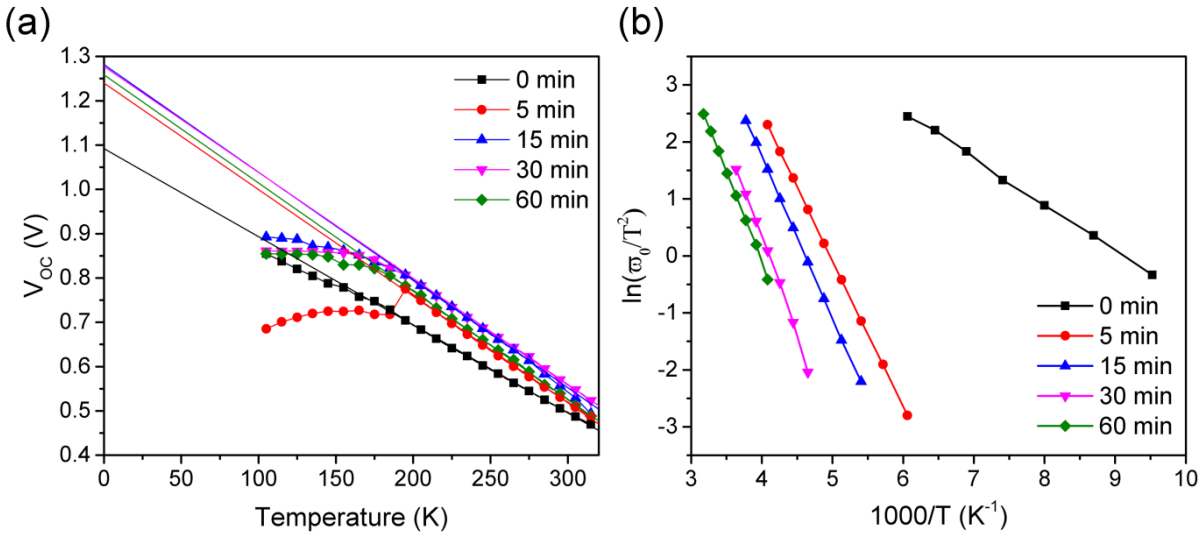

Figure 4.8 V_{OC} vs. temperature from J-V-T measurement (a). The intercept of the linear extrapolation at T = 0 K is equal to E_A/q. Arrhenius plot of the admittance spectroscopy data (b). The slope of the curves gives the activation energies of these transitions, $E_{A\text{-}AS}$.

Extrapolation of the linear part of the curves to T = 0 K gives an intercept equal to E_A/q. E_A values for each annealing duration are summarised and compared to the respective bandgaps in Table 4.2. The activation energy is equal to or close to the bandgap for all annealed samples, indicating that the Shockley-Read-Hall (SRH) recombination in the bulk is the dominant recombination mechanism in the annealed samples. E_A is lower than the bandgap for the non-annealed CIGS cell however, suggesting that recombination is primarily occurring at the heterojunction interface [173]. Therefore, annealing of the CIGS/CdS is reducing recombination at this interface. Interface recombination in the non-annealed device can be a result of the presence of surface traps such as selenium vacancies, which are effectively passivated by oxygen during annealing.

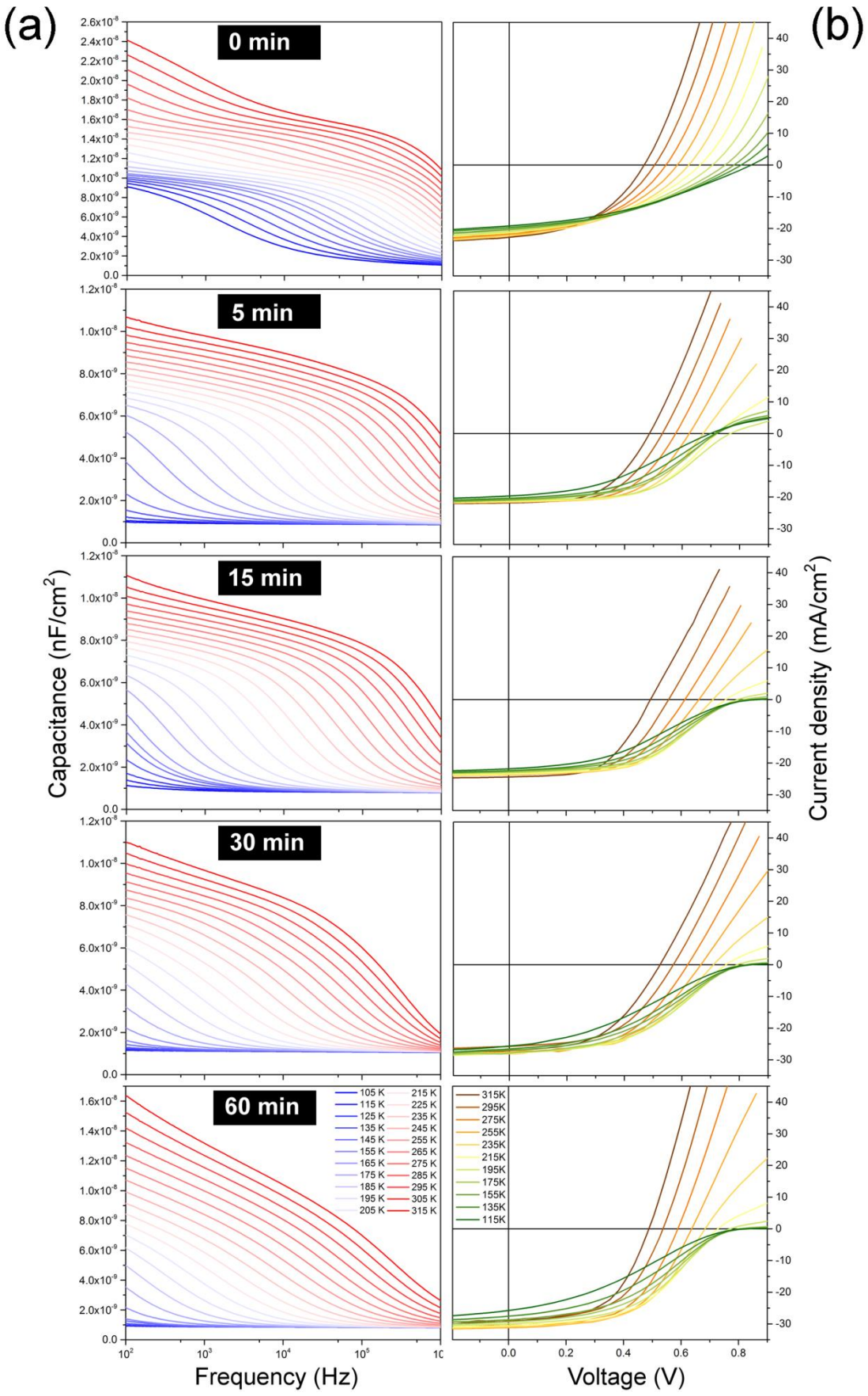

Figure 4.9 Admittance spectra in the dark at 0 V bias (a) and J-V-T curves (b) of CIGS devices with junction annealed in air for various durations.

To analyse the energetic position of the defects within the p-n junction, admittance spectroscopy was conducted in equilibrium conditions (no bias applied). This involved measuring capacitance as a function of frequency and temperature. Capacitance-frequency (C(f)) curves (Figure 4.9 a)) feature a capacitance step from low to high frequencies. At low temperatures (105 – 165 K) the curve of the non-annealed device features a capacitance step which is often associated with a discrete shallow interface state N1, with the activation energy typically in the range of 50-200 meV. There is no capacitance step observed at low temperatures for any annealed sample. A step is present in the mid to high temperature range (165 – 315 K) for all annealed samples however. A high temperature capacitance step is generally identified as a bulk acceptor defect N2 with the activation energy of about 300 meV [174]. To calculate activation energies associated with these transitions, $\ln(\omega_0/T^2)$ vs. 1000/T was plotted (Figure 4.8 b)), where $\omega_0 = 2\pi f_0$ with f_0 (transition frequency) corresponding to the inflection points of the C(f) curves. The inflection points were obtained from the peak values of the G(f) spectra, where G is the conductance.

Using the Arrhenius equation, activation energies of these transitions were extracted from the slope of the curves in Figure 4.8 b) and are summarised in Table 4.2 under the abbreviation $E_{A\text{-}AS}$. An admittance response with activation energy of about 70 meV was obtained in the non-annealed sample, close to the energy level of V_{Cu} defect. Shifts in the positions of N1 and N2 defects as compared to the literature may be related to the particular precursor solution chemistry or selenisation process used [174]. In all annealed devices, shallow defects at low temperatures possibly attributed to V_{Se} or V_{Cu} are not present. The shallow interface states observed in the non-annealed sample seemed to sink into deeper energy levels with annealing however. These transitions were found at energy levels of 222, 244, 298 and 273 meV for annealing times of 5, 15, 30 and 60 min respectively. Once more the suggestions of GB passivation of Se vacancies by oxygen atoms, Cd diffusion into V_{Cu} at absorber surface and Cu migration deep into the absorber creating deep traps are plausible also from the energetic point of view of these defects [94].

J-V-T curves displayed in Figure 4.9 b) reveal that efficiencies collapse towards lower temperatures, primarily due to the collapse of the FF. This can in turn be related to a dramatic increase in series resistance that quenches the FF. Another

feature observed from the J-V-T curves is the presence of a rollover at low temperatures, which appears in all the annealed samples. Rollover and crossover between light and dark J-V can be indicative of a presence of a blocking back contact at the Mo/CIGS interface which perhaps becomes more severe with longer annealing times [174].

The effect of air-annealing on the electrical properties of solution-processed CIGS/CdS films was studied. The devices with annealed CIGS/CdS junction exhibited an increase in all PV indicators up to 30 min of annealing. Further annealing was no longer beneficial to the device performance with mainly reduction in device FF. It was suggested that the interface states such as Se vacancies were effectively passivated by oxygen atoms removing shallow defects located at or near the CIGS/CdS heterointerface. Driven by the junction field, mobile Cu ions diffused deeper into the absorber however, reducing the absorber apparent doping density and created deep traps. Cd diffusion to the near the junction region of the absorber helped to adjust the charge and the field in the SCR having beneficial effect on the reduction of interface recombination. The electrical performance of CIGS solar cells is heavily influenced by the presence of deep level defects in the bulk and at the heterojunction interface, which are greatly affected by the junction air-annealing. Defect measurement techniques such as admittance spectroscopy, capacitance profiling and phenomena such as rollover seen in the presented air-annealed CIGS devices are sensitive to specific assumptions about material properties and therefore very difficult to interpret. Understanding the electrical characterisation is nonetheless a necessary step for further improvement of these amine/thiol-based solution-processed CIGS solar cells.

4.3.3 Annealing of a finished device

The beneficial effects of junction air-annealing were presented, however they do not explain the inconsistent performance of non-annealed devices typically observed after variable metal evaporation runs. Therefore an experiment of annealing of a finished device was conducted using the same annealing conditions (180°C for 5 - 60 min). The box plots summarising the performance of all five devices are presented in Figure 4.10.

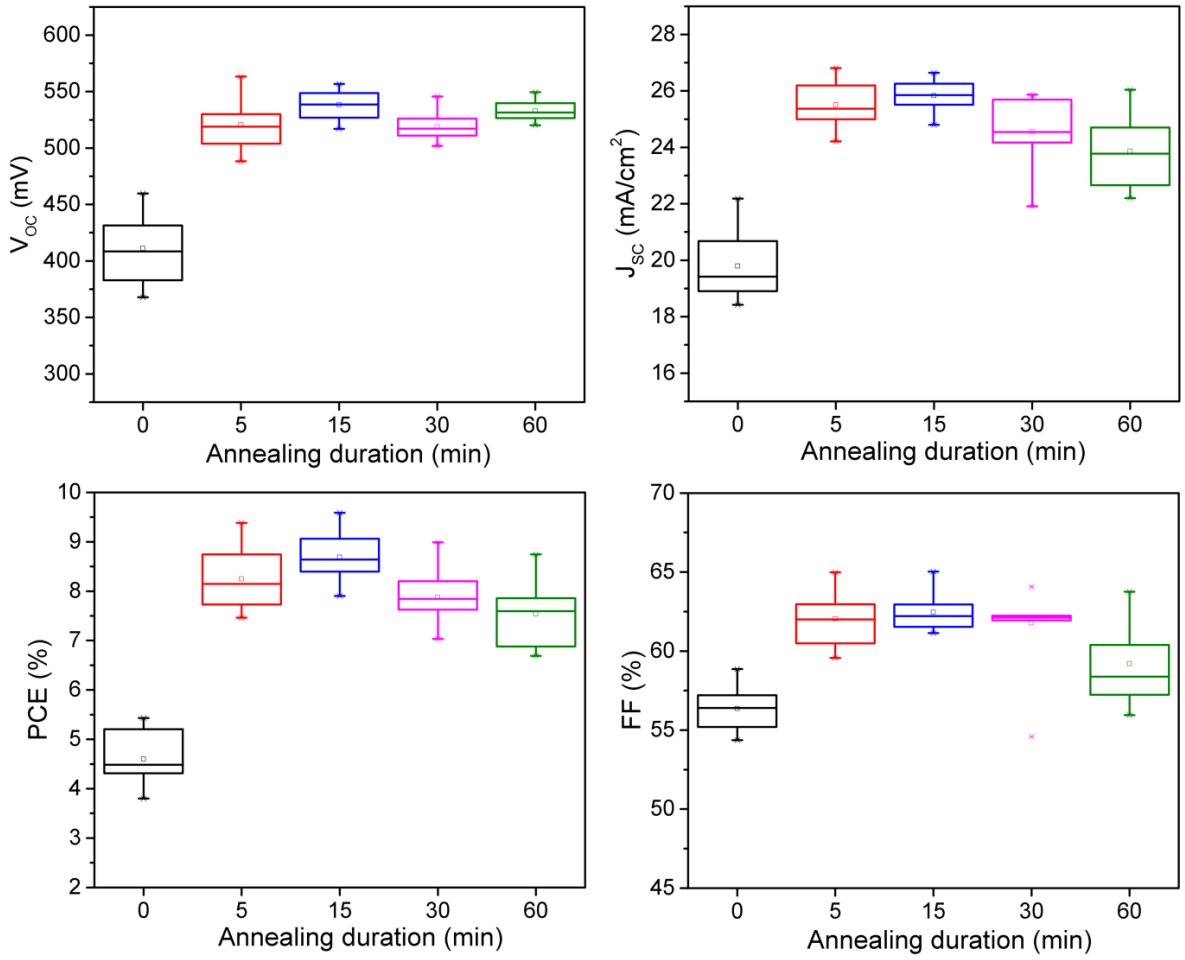

Figure 4.10 Box plots of PV indicators of CIGS cells when air-annealing was performed on a finished device (Mo/CIGS/CdS/i-ZnO/AZO/Ag).

In first 5 min of annealing, the performance increased remarkably, from 4.5 to 8.5% on average. The annealing significantly improved all performance indicators. Annealing for 15 min improved the performance even further, but to a smaller extent, from 8.5% to 9% on average. Annealing the devices for longer (30 min and above) resulted in performance degradation, with main performance losses in the device J_{SC} and FF. The reduction of J_{SC} was not observed previously in the annealing of absorber surface or junction. Hence, it is probable that the air-annealing of the full device has negative effects on the TCO causing the J_{SC} to decrease. Sputtered Al-doped ZnO was deposited at RT, but depositing AZO films at slightly higher than RT (100°C) was shown to have beneficial effects on the conductivity and overall crystallinity of this TCO [175]. Annealing AZO in air can cause the resistivity to increase by two orders of magnitude however [176]. The exposure of the AZO to humidity and atmospheric species such as O_2 and CO_2 was shown to degrade the

AZO film quality. This could cause an increase in series resistance of CIGS devices reducing the FF as well as to reduce the J_{SC} by formation of shunt paths [177].

Figure 4.11 shows the J-V and EQE curves of the best device for each annealing duration. Table 4.3 summarises the performance parameters. A remarkable shift in the J-V and EQE curves towards higher values was observed for all the annealed devices relative to the non-annealed reference device. There is a decrease in the EQE signal at wavelengths > 550 nm and an increase of the EQE signal in the absorption region of the CdS for the samples annealed for ≥ 30 min. This indicates that the transmission through the CdS improved with the annealing time, however the overall collection at all wavelengths corresponding to the absorption in the absorber layer was reduced.

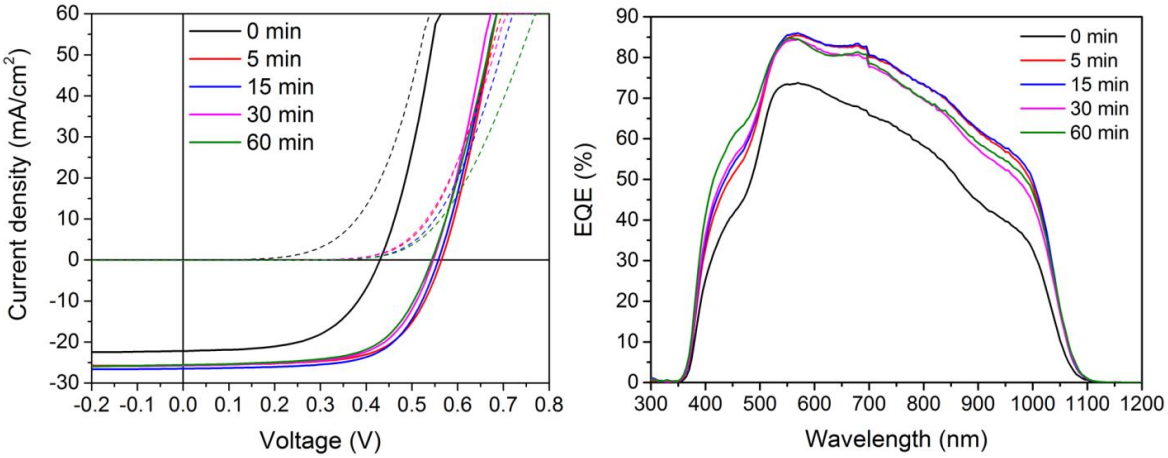

Figure 4.11 J-V (left) and EQE (right) curves of the best device for each annealing duration.

Table 4.3 PV parameters of the champion cell for different annealing durations of the complete device

	V_{OC} (V)	**J_{SC}** (mA/cm^2)	**FF** (%)	**PCE** (%)
0 min	429.0	22.2	57.1	5.4
5 min	563.3	25.6	65.0	9.4
15 min	556.7	26.5	65.0	9.6
30 min	545.8	25.7	64.0	9.0
60 min	542.4	25.6	63.0	8.7

Hence, annealing of a finished device is also possible and brings the advantage of adjusting the annealing time by measuring the device before and after annealing. On

the other hand, the annealing time of finished devices is limited by the stability of the TCO, which will start to reduce device FF and J_{SC} fast, after only few minutes of annealing in air.

4.4 TRPL study of CIGS free surface degradation by prolonged air-exposure

TRPL studies of the high efficiency vacuum-based CIGS solar cells discovered that the minority carrier lifetime can decrease by two orders of magnitude when the films were exposed to air for as short as several hours. However after the CdS deposition, lifetime did not change and the samples were more stable in air [178][179]. As different processing steps in the fabrication of solution-processed solar cells have different throughputs and the samples are handled in air between various stages, it is important to study the atmospherically-induced degradation of these absorbers. This study consisted in measuring device minority carrier lifetime decay using TRPL at various times of sample being exposed to ambient air. In the experiment, a selenised CIGS absorber was fractured in three pieces. A sample referred to as “CIGS” was measured directly after being removed from the selenisation furnace. The other two samples were coated with the CdS buffer layer and one of them was in addition subjected to a thermal annealing in air for 30 min at 180°C. These were named as “CIGS/CdS” and “CIGS/CdS+air-anneal” respectively.

The carrier lifetime of all the samples was measured using TRPL at different times after being exposed to air. Figure 4.12 shows TRPL decay curves of the bare CIGS film several minutes, hours or even days or weeks after being removed from the selenisation furnace and brought to the measurement system. The TRPL decay curves shown in Figure 4.12 a) were measured on the same spot of the sample and the laser beam was blocked between the measurements. In Figure 4.12 b), the laser was moved to another spot on the sample. The minority carrier lifetimes were extracted fitting a double-exponential function:

$$I_{PL}(t) = I_0 + A_1 e^{-(t-t_0)/\tau_1} + A_2 e^{-(t-t_0)/\tau_2} \qquad [4.2]$$

where I_{PL} is the PL intensity as a function of time after a fast laser pulse excites carriers in the sample, I_0, A_1, A_2 are coefficients and τ_1, τ_2 are decay times corresponding to initial (fast) and final (slow) sections of the decay curves [164]. The

minority carrier lifetimes after different absorber air-exposure times are summarised in Table 4.4.

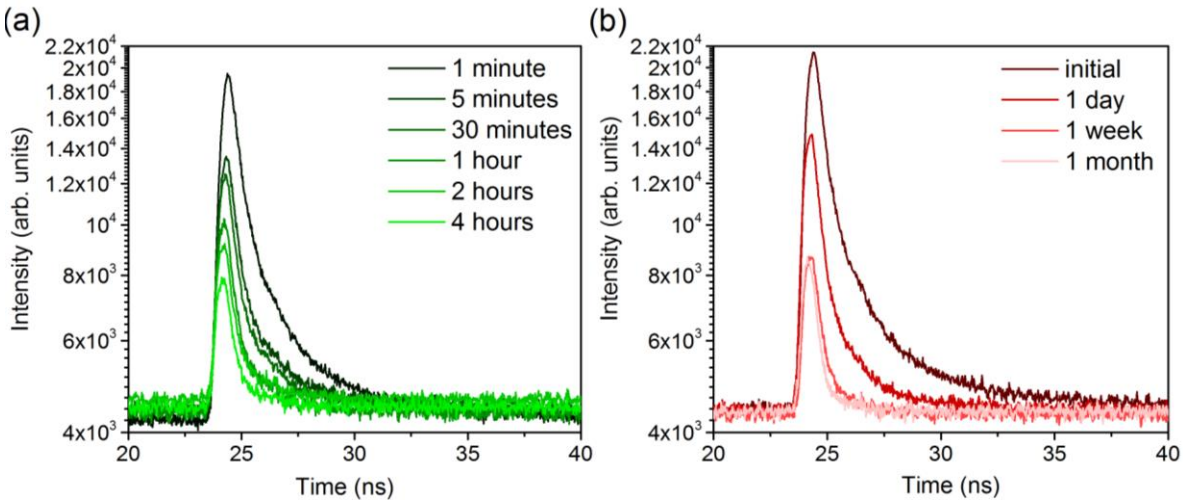

Figure 4.12 TRPL decay curves measured at 1040 nm on the uncoated CIGS absorber: on the same spot (degradation accelerated by the exposure to the laser beam) (a) and on different spots of the sample surface after prolonged exposure to air for several days (b).

Table 4.4 Minority carrier lifetimes as a function of the air-exposure time for the uncoated CIGS absorber extracted from the TRPL decay curves

	Time exposed to air	**Lifetime (τ_2)** (ns)
On the same spot: effect of the high-intensity laser beam	initial	2.80
	5 min	2.82
	30 min	2.65
	1 h	2.28
	2 h	1.95
	4h	1.90
Different spots: effect of air-exposure only	1 day	1.86
	1 week	1.70
	1 month	1.42

The bare absorbers were found to degrade rapidly after being exposed to ambient conditions. After just one day of air-exposure the lifetime decreased from 2.80 ns to 1.86 ns. The lifetime further decreased after 1 week to 1.70 ns and after 1 month to 1.42 ns. The TRPL signal intensity decreased spectacularly as well. The lifetime degradation after bare absorber air-exposure was previously observed by Metzger *et al.* and Shirakata *et al.* [178][179]. However the lifetime degradation is not as spectacular for these devices as for the high efficiency co-evaporated CIGS, where

the lifetime of 250 ns decreased to only 1 ns after 1 day of air-exposure [178]. Figure 4.12 a) shows that the laser light itself accelerates the film degradation, which was also observed in the literature [164].

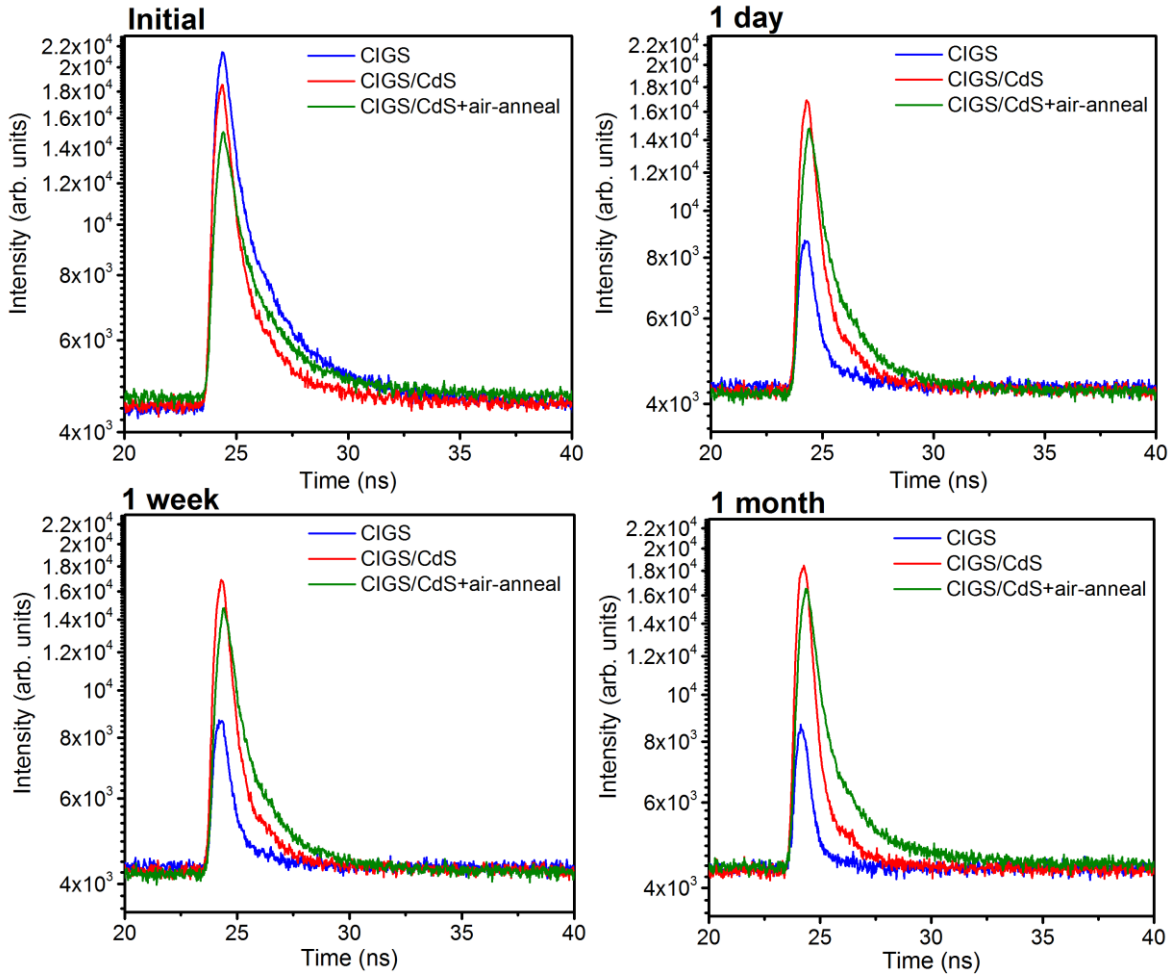

Figure 4.13 TRPL decay curves measured at 1040 nm on the uncoated CIGS absorber, CIGS/CdS and CIGS/CdS sample treated with air-annealing for 30 min at 180°C. The TRPL was measured straight after the deposition, 1 day, 1 week and 1 month later.

A method to avoid the degradation by air-exposure is to deposit the CdS buffer layer as fast as possible. Figure 4.13 shows the TRPL decay curves of bare absorbers and CIGS/CdS films with and without the junction air-annealing after being exposed to air for different times. Table 4.5 summarises the measured carrier lifetimes for the three samples. The lifetime and the TRPL signal intensity strongly decreased with prolonged air-exposure of the uncoated CIGS. In contrast, the CIGS/CdS samples were observed to be relatively stable, keeping the lifetime above 2 ns even after 1 month of air-exposure. The lifetime measured after the CdS deposition was not higher than the lifetime of the uncoated CIGS initially, therefore it is thought that the

CdS does not passivate the absorber surface, but its role consists in protecting the exposed CIGS surface from the air-induced degradation.

Table 4.5 Carrier lifetimes of uncoated CIGS film, CIGS/CdS and CIGS/CdS after air-annealing as a function of air-exposure time

Lifetime (τ_2) (ns)	CIGS	CIGS/CdS	CIGS/CdS + air-annealing
initial	2.80	2.21	2.35
1 day	1.86	2.22	2.13
1 week	1.70	2.01	2.24
1 month	1.42	2.00	2.38

The lifetimes of the air-annealed CIGS/CdS appear to be slightly higher than those of the non-annealed CIGS/CdS, and show no signs of degradation even after 1 month of air-exposure. The values for the measured lifetimes fluctuate between 2.1-2.4 ns for the four different measurements which can be interpreted by a small change in material properties of different points measured on the sample rather than an increase of the carrier lifetime with air-exposure.

The lifetime degradation was strongly correlated with the degradation of the opto-electronic properties of the CIGS films and consequently device performance. No devices were made from these films, however Metzger *et al.* observed a degradation of efficiency from 16% (lifetime of 40 ns after air-exposure of 10 min) down to 5% (lifetime of 0.3 ns after air-exposure of 21h) [164]. The studied solution-processed devices have a clearly different material quality and properties than the vacuum-processed devices, resulting in much lower initial lifetimes and a different degradation rate. However the importance of coating the CIGS absorbers quickly with CdS was emphasised in this study. The origins of the lifetime degradation with air-exposure are not yet fully understood. The chemical bath would remove surface features such as metal oxides or selenides that would form on the surface and induce strong surface recombination [180]. Consequently these are not directly responsible for the observed lifetime degradation [164]. A possibility of Na reaction with O_2 and H_2O from air was also suggested [169].

4.5 Conclusions

The air-annealing experiments were performed at various stages of device fabrication: after absorber selenisation, after CdS junction formation and annealing of a finished device. It was concluded that the air-annealing has beneficial effects on device performance, however the junction has to be formed first. The annealing of the bare absorber accelerated the absorber degradation associated with rapid drop of the minority carrier lifetime when exposed to air. The absorber degradation was related to the affinity between Na with the ambient species such as H_2O and O_2 rather than formation of oxide and selenide related traps at the absorber surface. The immediate capping of the CIGS absorber with CdS buffer was found to be vital to preserve high device efficiencies.

The annealing of the CIGS/CdS junction in air caused an increase in all PV parameters up to 30 min of annealing at 180°C. The most spectacular was the increase in V_{OC}, which was attributed to the passivation of interface and GB defects such as Se vacancies by oxygen atoms. In addition, oxygen helped to liberate Cu atoms from near-surface region and their redistribution in the absorber. The formed Cu vacancies near the CdS heterojunction were filled with the Cd^{2+} ions diffusing from the CdS which is thought to be beneficial to restore the interface charge and adjust the field profile in the SCR. Positive effects of the interdiffusion resulted in higher J_{SC} due to better junction quality, increase in SCR width and improved transmission through CdS layer. Too long annealing caused reduction of the doping density and creation of deep trap states in the absorber, attributed to the excessive Cu diffusion deeper into the bulk. The FF of the device started to collapse due to increased series resistance.

Annealing of the full CIGS device is also beneficial; however prolonged air-annealing of the front contact TCO degrades its quality, resulting in an increase in R_S and decrease in J_{SC} with annealing for longer than 15 min. Consequently, the annealing duration of a CIGS/CdS interface is limited by the Cu diffusion deeper to the absorber, whereas the annealing duration of a finished CIGS device is limited by the stability of the front contact AZO, which is prone to degrade in humid and hot ambient conditions. The annealing duration has to be therefore carefully optimised as it is strongly dependent on the specific material electronic quality and fabrication processes employed.

CHAPTER 5

Development of selenisation process and compositional variation

5.1 Scope

During selenisation, the precursor layers are converted into the chalcopyrite-structured Cu(In,Ga)Se_2 phase. This is a critical step as it involves high temperatures and determines the final morphology of the CIGS absorber. The choice of selenisation configuration and conditions has to be carefully optimised to achieve the best quality absorber material. The aim of this chapter is to study the effects of different selenisation parameters on the morphological, structural and compositional properties of CIGS absorber layers and solar cells prepared by spray-coating. The copper content was found to have a strong effect on film and finished solar cell properties. Film Cu content variation is discussed in the last section of this chapter.

5.2 Comparison of selenisation configurations using a two-zone tube furnace

In the course of this work, several selenisation configurations and reactor types were employed with the aim of identifying the optimum absorber crystallisation conditions. CIS and CIGS absorbers with base-line $Cu_{0.8}InSe_2$ and $Cu_{0.9}In_{0.7}Ga_{0.3}Se_2$ compositions were prepared by spray deposition as described in Chapter 2. Unless stated otherwise, SLG substrates were used to provide alkali doping of the absorbers. For each selenisation configuration, the sample is compared to a reference sample selenised in the tube furnace using a standard process, involving the use of a graphite box and a closed reactor vessel.

5.2.1 Development of a standard selenisation process using graphite box

The tube furnace used in this approach allows for independent temperature control of two heating zones; although only one zone was used for selenisation of the precursor. The as-deposited precursor of 2.5 x 5 cm^2 is placed inside a porous graphite box. Selenium pellets are placed into holes inside the box surrounding the sample. The box is then sealed with a lid and placed in the middle of the left-hand heating zone of the tube furnace. The lid has a small - 1 mm diameter - hole in the centre allowing for pressure equilibration; hence the box is only partially closed. The graphite box is shown in Figure 5.1. The temperature is measured with a thermocouple which is placed under the graphite box. The selenisation process takes place in a tube sealed at both ends, allowing for higher Se partial pressure. The tube is first purged with N_2 several times to remove all the oxygen from the deposition atmosphere. The starting pressure was set to 450 Torr. Due to the temperature increase in the tube, the working pressure increased during selenisation and typically reached around 750 Torr at the end of the process. The nominal selenisation temperature was 540°C with a ramping rate of approximately 35°C/min, but the actual temperature read by the thermocouple was typically only 525°C. The relatively high starting pressure delays the selenium evaporation. This is important in order to avoid evaporation of all of the selenium too early in the process such as during the ramping stage, which lasts for about 15 minutes. The temperature and pressure profiles are displayed in Figure 5.1 b). Depending on the back contact design (whether or not a Mo-N diffusion barrier is included) selenisation took 50-90 minutes including ramping.

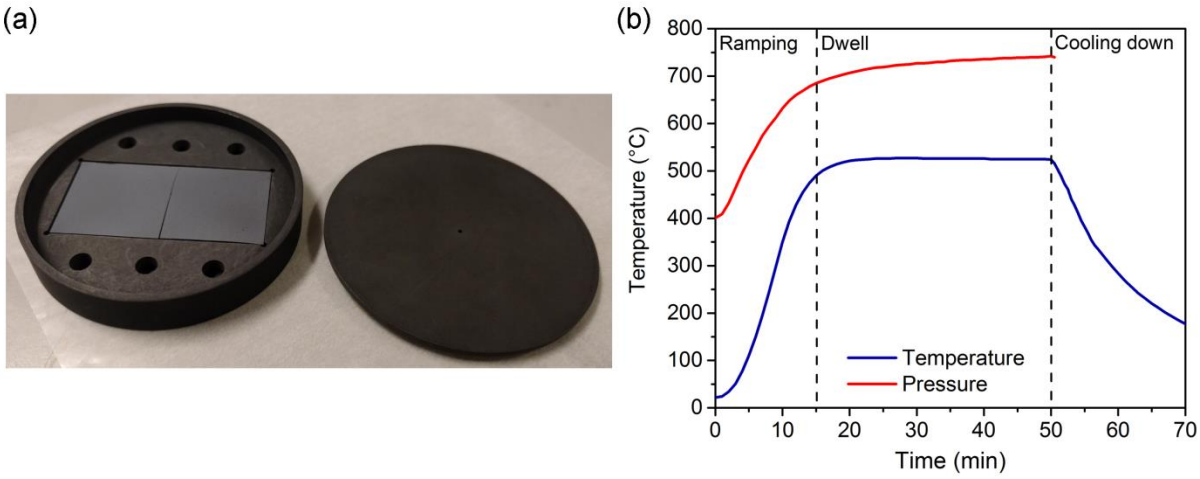

Figure 5.1 Snapshot of the selenisation graphite box (a) and temperature/pressure profiles as a function of selenisation duration (b).

Typical film morphology after selenisation using this configuration and parameter set is shown in Figure 5.2. CIS films exhibit slightly larger grains than CIGS even after a shorter selenisation time. It was observed that CIGS absorbers are more difficult to recrystallise due to their more complex chemical structure involving an additional element. However CIGS solar cells benefit from improved electrical properties as the material absorption curve is slightly better tailored to AM1.5G spectrum and the possibility of optional bandgap grading. Both CIS and CIGS absorbers have a bilayer morphology consisting of large grains at the surface and smaller grains underneath. Similar bilayer absorber morphologies have previously been obtained from solution-processing of CIGS and CZTS absorbers [59][181]. The CIGS grains do not extend through the entire depth of the film; however the fine-grained layer provides adequate electrical contacting allowing the device to function. The bilayer morphology has often been attributed to the presence of impurities introduced from the starting materials, a large carbon and oxygen content, insufficient Se partial pressure during selenisation or incomplete selenisation leaving unreacted cations behind [86][181][182][183]. The existence of the underlying fine-grained layer has previously been explained as a result of material rejection from the growing film as cations diffuse to the reaction front [181].

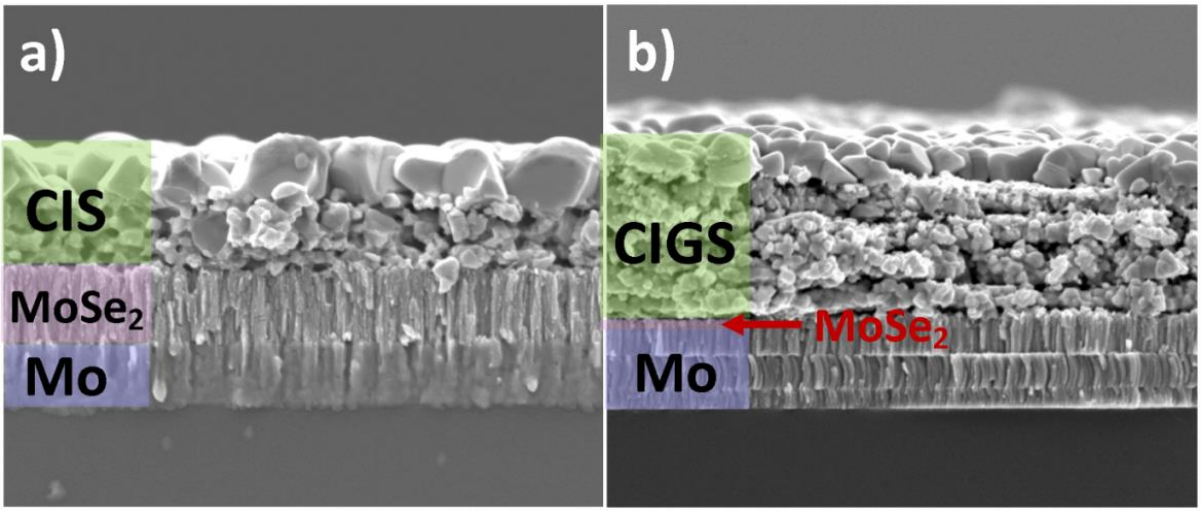

Figure 5.2 SEM cross-section of CIS absorber on bare Mo selenised for 50 min (a) and CIGS absorber on Mo/Mo-N/Mo selenised for 90 min (b).

The device efficiency is largely dependent on the thickness of the large-grain layer [182]. In the work presented here, the use of metal chalcogenides minimises the impurities introduced from the precursors, and any carbon in the films comes from the coating solvents. The presence of oxygen is a consequence of the deposition

being carried out in air; however this is something that cannot be avoided using the process described in this work. Moreover, oxygen atoms are displaced by selenium during selenisation [184]. Consequently, in the following sub-sections, the selenisation configuration and conditions were modified in order to achieve an improved crystal growth.

5.2.2 Two-zone selenisation approach

Selenium plays a crucial role in the growth of CIGS films and the film quality depends on the selenisation technique, Se compounds and overall reaction kinetics. When elemental selenium is thermally evaporated, the selenium molecules are arranged into large molecular chains, typically Se_x with $x > 5$. These have low chemical activity resulting in low selenium incorporation into the film [185]. Moreover, the physisorption of large Se molecules leads to increases in point defects resulting in three-dimensional growth with rough surfaces and small grain sizes [186]. In_2Se and Ga_2Se gaseous phases form locally, creating non-uniformity in the film stoichiometry and causing crystal structure deterioration within the film [187]. Using more reactive H_2Se vapours instead of Se vapours would increase the level of Se incorporation into the sample resulting in superior morphological features and in-depth compositional uniformity [188]. However H_2Se is the most toxic selenium compound making this selenisation technique very hazardous. Several groups report using thermal cracking of selenium to decompose selenium clusters into smaller and more highly reactive molecules [185][186][187]. The selenium cracking was achieved using an RF plasma discharge chamber or by thermal cracking using a high temperature cracking unit [186][187]. Cracked selenium used for selenisation of CIGS films was shown to result in smooth and dense films containing large grains [186].

Following the ideology of the selenium cracking and its beneficial effects on the crystallisation and compositional uniformity of the absorber, the two zones of the selenisation furnace were used to decouple the selenium source from the substrate. The two zones were heated separately, the sample at 540°C and the crucible containing Se pellets at 800°C to attempt selenium thermal cracking. The selenium source heating was delayed for 20 min allowing for the substrate to reach the dwell temperature first. The selenisation was 80 min long, including both ramping up

(~35°C/min) and the delay time. The heating profiles as set by the controller for both heating zones are shown in Figure 5.3.

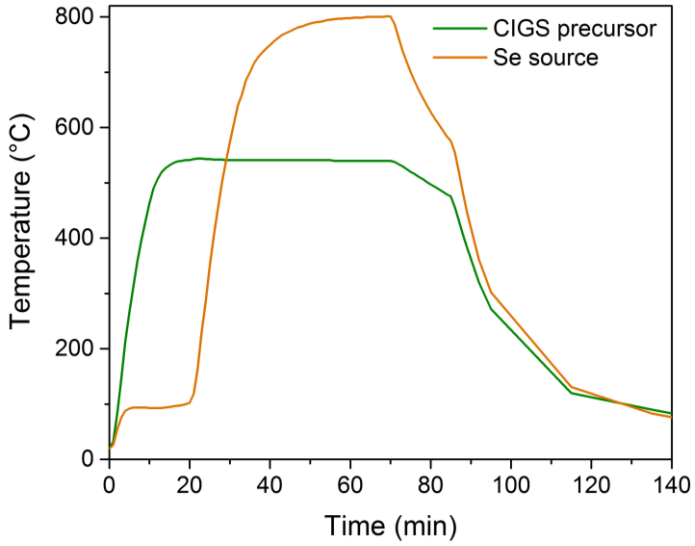

Figure 5.3 Heating profiles of the two zones set by the furnace temperature controller.

The tube was purged with nitrogen and then sealed at both ends so as to prevent any gas flow within the system. The selenium flux was transported towards the substrate solely by thermal convection due to the temperature gradient across the tube. Figure 5.4 shows a diagram comparing this selenisation configuration with the standard selenisation where samples contained together with selenium pellets are heated in one zone of the furnace.

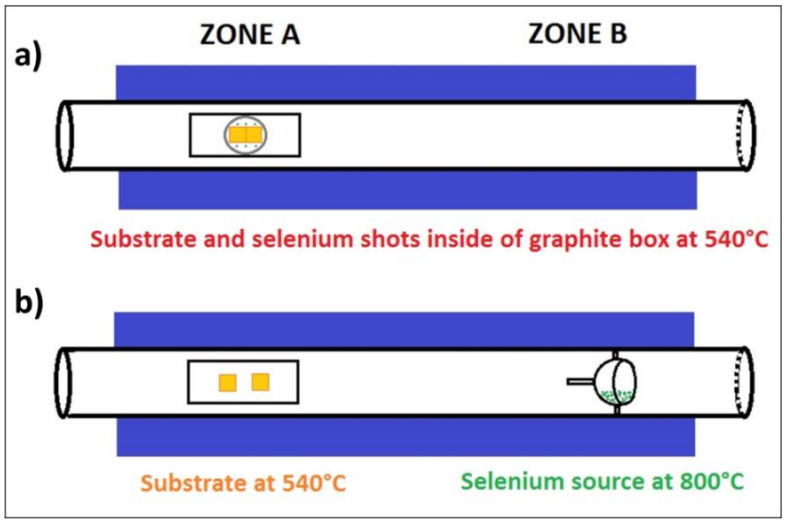

Figure 5.4 Selenisation configurations: base-line selenisation using graphite box (a) and two-zone selenisation (b).

The CIS precursor films were selenised at three different starting pressures, 50, 150 and 300 Torr. At the end of the process, the pressure inside the tube was raised to

240, 360 and 780 Torr respectively. 600 mg of Se in the form of pellets was placed inside the quartz crucible at the right-hand side of the heating zone (Zone B). At the end of the process no remaining selenium was present in the crucible.

Figure 5.5 shows SEM cross-section images of the selenised absorbers. The absorber morphologies are very different from those selenised using the graphite box (Figure 5.2), having larger grains near the back contact with decreasing pressures. Despite the large grains present, especially for the sample selenised at 50 Torr, the absorbers seem to contain secondary phases in addition to the chalcopyrite-structured CIS phase.

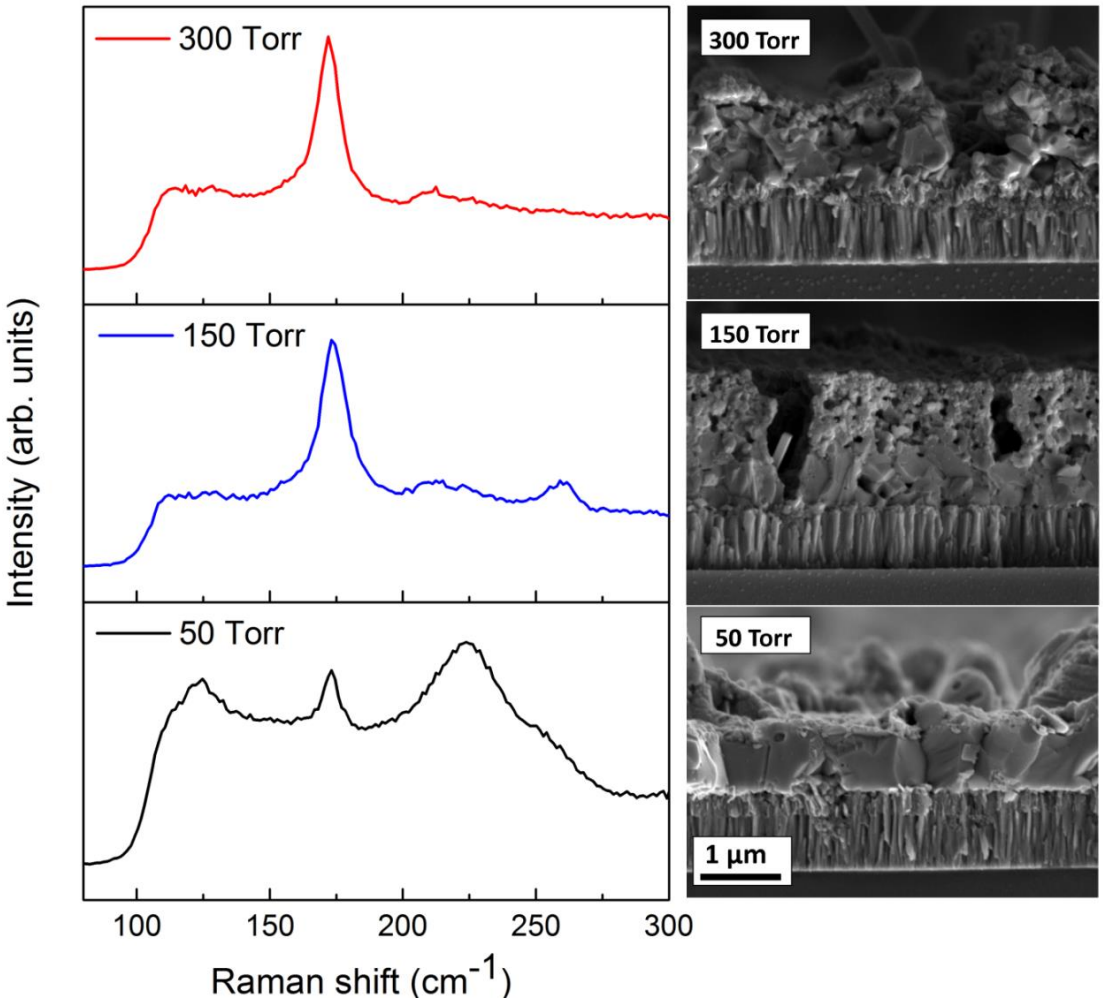

Figure 5.5 Raman spectra and SEM cross-sections of CIS films selenised by two-zone approach at three different starting pressures.

Raman analysis (Figure 5.5) confirms the formation of a $CuInSe_2$ phase (Raman A1 peak identified at 172 cm^{-1}) for all samples. The small peak at ~ 210 cm^{-1} seen in the 150 and 300 Torr samples corresponds to the B2/E signal of the $CuInSe_2$ phase.

Raman spectra of the sample selenised at 150 Torr also contain a peak at 260 cm^{-1} corresponding to the Cu_xSe secondary phase. The absorber selenised at 50 Torr with the largest grains has a very different Raman spectrum, with two dominant peaks at ~ 121 and 225 cm^{-1}. These might be a result of In-Se phases being present in the film [189].

None of the absorber layers presented above gave a working solar cell, probably due to the presence of secondary phases. As the tube is relatively long (more than 1m) and with a volume of approximately 4.3 L, the selenium partial pressure over the sample is likely to be much lower than inside a closed graphite box. Subsequently, significantly more selenium (2g) was added into the crucible. The absorber layer morphology after selenisation at a starting pressure of 100 Torr is shown in Figure 5.6 as compared with two absorbers selenised using a graphite box.

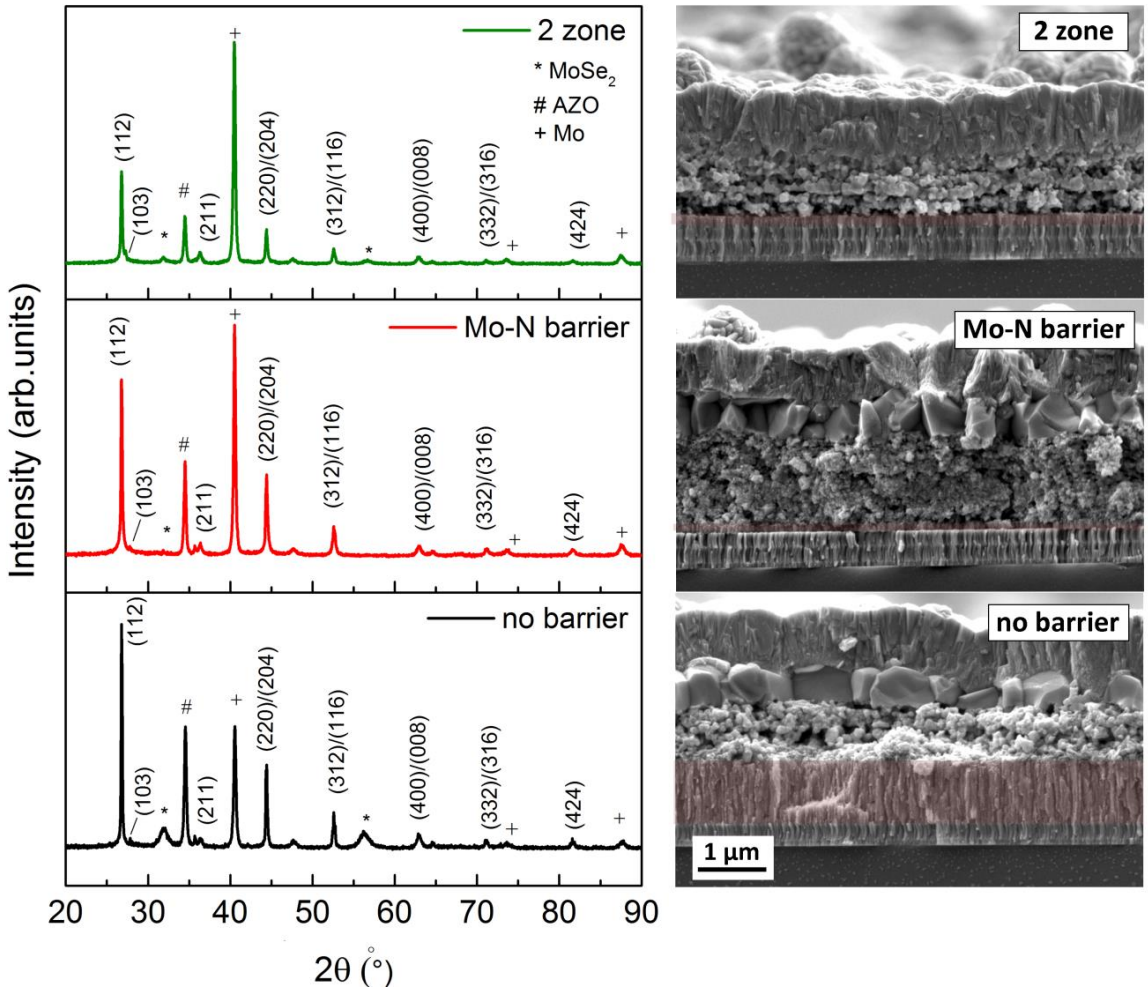

Figure 5.6 XRD patterns and SEM cross-section of $CuIn(S,Se)_2$ devices selenised by two-zone approach and using the graphite box with and without Mo-N barrier layer at the back contact. $MoSe_2$ layer is highlighted in red.

The SEM images in Figure 5.6 show the cross-section through the full CIGS device with AZO as a front contact. These are prepared on bare Mo and on a modified Mo/Mo-N/Mo back contact, and as a consequence contain a thick and thin $MoSe_2$ layer respectively. The absorber selenised using the two-zone approach was prepared on bare Mo. Its morphology is similar to the absorber morphology of the samples selenised in the graphite box. However despite not using the Mo-N barrier layer at the back contact, only a thin $MoSe_2$ layer was formed. The XRD patterns in Figure 5.6 show peaks corresponding to the chalcopyrite structure of the tetragonal $CuIn(S,Se)_2$ phase (JCPDS 31-1311). Table 5.1 summarises the FWHM of the CIS (112) dominant peak at ~ 27° and the Mo(110)/$MoSe_2$(100) peak intensity ratio extracted from the XRD scans.

Table 5.1 FWHM of the dominant (112) CIS peak and the Mo (110)/$MoSe_2$ (110) peak intensity ratio

	FWHM $CuInSe_2$ (112) (°)	**Mo (110)/$MoSe_2$ (100) intensity ratio**
Two-zone	0.228	22.57
Mo-N barrier	0.207	30.12
No barrier	0.164	5.11

The intensity of the most pronounced $MoSe_2$ (100) peak at $2\theta \approx 32°$ as compared to the main Mo (110) peak at $2\theta \approx 41°$ was substantially reduced when the two-zone selenisation was employed and was almost non-existent when the barrier layer was present. The FWHM of the dominant (112) peak of the CuInSSe phase gives an indication of the crystal quality of the absorber. The FWHM is lowest for the "no barrier" sample, 0.164° as compared to 0.207° and 0.228° for the 'Mo-N barrier' and 'Two-zone' samples respectively. This is indicative of a slightly better crystal quality for the absorber selenised using the graphite box. This may be attributable to the lack of large-grained layer typically formed at the absorber surface during the two-zone selenisation. Improved absorber quality in the device without the Mo-N barrier relative to the device with a Mo-N layer is contradictory to what was demonstrated in Chapter 3 regarding the positive role of Mo-N not only in preventing excessive $MoSe_2$ formation but also in enabling improved absorber crystallisation. In this case, the inferior absorber quality of the 'Mo-N barrier' sample as suggested by the XRD might be caused by an increased absorber thickness, with a 75% thicker fine-grained

layer. From the SEM cross-sections, the large-grained/fine-grained absorber bilayer structure is clearly seen in the devices selenised using the graphite box. Although the size of the large grains on the surface of the absorber is approximately the same (~500 nm) in both cases, the poorly crystallised layer varies in thickness due to the manual nature of the deposition technique. The large grains are not observed on the absorber surface after the two-zone selenisation, hence the FWHM is highest for the sample selenised using this process. Figure 5.7 shows J-V curves for these three samples. Table 5.2 summarises the PV performance parameters for each of the curves.

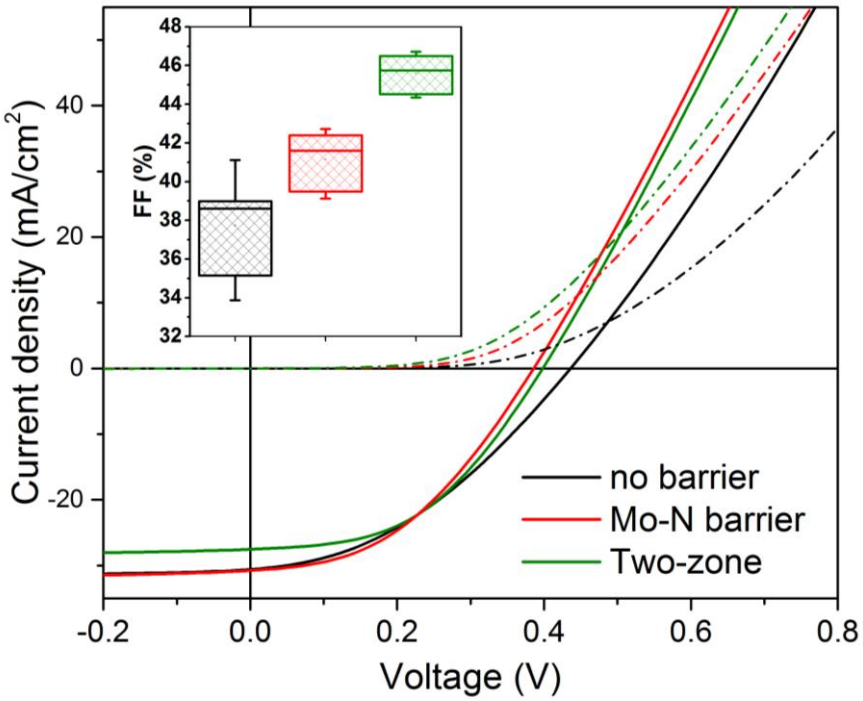

Figure 5.7 Light and dark J-V curves for the representative cell of the three devices: 'Two-zone', 'Mo-N barrier' and 'no barrier'. The inset shows the box plot of the FF from 6 cells for each device.

Table 5.2 PV performance parameters for curves in Figure 5.7

	V_{OC} (V)	**J_{SC}** (mA/cm^2)	**FF** (%)	**PCE** (%)
Two-zone	0.398	27.5	46.7	5.12
Mo-N barrier	0.386	30.7	42.7	5.07
No barrier	0.436	30.6	38.5	5.13

All three devices yielded very similar performance with efficiencies of approximately 5%. It should be noted that these were CIS devices prepared at the very early stages

of this work. CIS devices generally have inferior efficiencies due to lower, less optimum bandgaps than CIGS, which result in a lower V_{OC}. The sample with the Mo-N barrier layer was one of the first samples containing this modified back contact and its deposition process had not been fully optimised. The samples do not contain Ag grids and were not subjected to any junction annealing treatments. The J_{SC} of the samples selenised using the graphite box is ~3 mA/cm^2 greater than that of the sample selenised using the two-zone approach. This is consistent with the inferior structural features of the two-zone selenised absorber such as the absence of the large-grained surface layer. V_{OC} is highest for the 'no barrier' device, and is ~50 mV higher than the identically selenised device containing the Mo-N barrier. This last sample had a much thicker fine-grained layer and hence a larger density of grain boundaries. These act as recombination centres and are probably responsible for the lower V_{OC} in the sample with substantially thicker absorber layer.

Finally, the FF (inset of Figure 5.7) improved with the implementation of the Mo-N barrier layer at the back contact, and was highest for the 'two-zone' device. The improved FF can be attributed to the reduction of $MoSe_2$ formation through either implementation of the Mo-N barrier or through using the two-zone selenisation process. $MoSe_2$ is very resistive and causes increased R_S of the back contact. The improvement of the FF using the two-zone selenisation may also be the result of different absorber grain growth. In this approach, the large-grained/fine-grained morphology is not present, and instead grains of an intermediate size are observed throughout the entire absorber layer thickness. This might result in lower R_S due to the absence of the resistive fine-grained layer near the back contact.

Smaller $MoSe_2$ layer formation and inferior absorber layer quality without large grains at the surface suggest either that in the two-zone selenisation approach selenium failed to become more reactive or its supply towards the sample was insufficient to recrystallise the absorber. The selenisation tube is over 1 m long with exposed (cold) ends. Selenium vapour spreads in the whole tube and it is likely that Se partial pressure over the sample is lower than when the sample is enclosed in a graphite box. For the formation of large grains during selenisation, the smallest possible reaction vessels, such as ampoules have typically been shown to be the most efficient [190]. In addition, it was observed that selenisation was significantly

affected by the tube aging and few results could be reliably reproduced. Consequently, the two-zone selenisation approach was not studied further and it was concluded that the use of graphite box for selenisation was necessary to achieve high selenium partial pressures and consequently better absorber crystallinity.

5.2.3 Multiple and longer selenisation using graphite box

Multiple selenisation has been suggested as a means to improve overall absorber quality and device reproducibility [191]. The concept consists of depositing thinner precursor layers followed by their selenisation and repeating the deposition/selenisation process steps several times until sufficient absorber thickness is achieved. As a result, a more compact absorber morphology without presence of holes, cracks and multilayer structures was achieved [191]. In this work, a double selenisation was performed using the sprayed amine/thiol-based CIGS precursors. Instead of spraying the absorber in 6 layers, a thinner film (3 layers) was deposited and subsequently selenised. This spraying/selenising step was then repeated. Both selenisations were 50 min long including the temperature ramping time. As the total duration of this selenisation is 100 min, the device performance and absorber morphology were compared to devices selenised for different durations. It is important to highlight that longer or multiple selenisations were possible owing to the application of the Mo-N diffusion barrier layer against selenium at the back contact. Without the use of the barrier layer, the $MoSe_2$ resulting from selenisation durations above 50 min was too thick, causing films to delaminate and drastically reducing device performance. The SEM cross-section and surface images of the CIGS absorbers for selenisation times ranging between 50 and 90 min as well as of the double-selenised absorber are shown in Figure 5.8.

From the SEM images it is clear that the grain size in the top crystallised absorber layer increased progressively with longer selenisation times, from 50 to 90 min. However in all of these the fine-grained layer is still present, meaning that the precursor was not fully converted into large CIGS grains. The surface grains in the double (50 + 50 min) selenised absorber were actually smaller, similar to the single-selenised top layer after 50 min. Larger grains, similar in size to the surface grains, are present in the bulk of the double-selenised sample. A small gap separating the two sprayed/selenised stacks can be observed in the middle of the absorber.

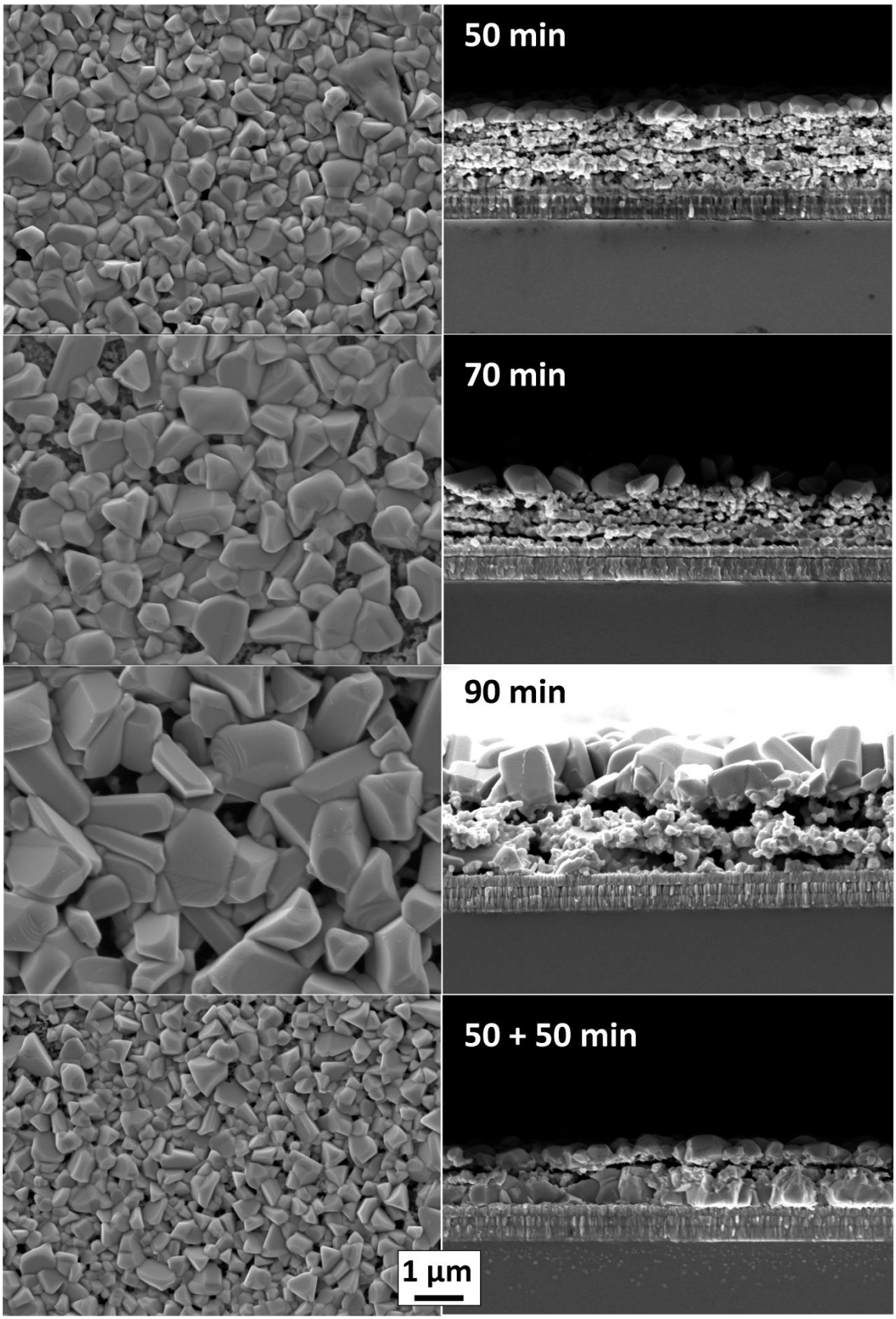

Figure 5.8 SEM images for different selenisation durations of CIGS absorbers.

XRD patterns of these films are presented in Figure 5.9. Distinct peaks corresponding to the chalcopyrite structure of $CuIn_{0.5}Ga_{0.5}(S,Se)_2$ (JCPDS 40-1488) are identified along with the reflections of Mo and $MoSe_2$ at the back contact. The intensity of the $MoSe_2$ (100) peak at 2θ ~32° is very small confirming that the Mo-N barrier effectively reduced $MoSe_2$ formation. The extracted FWHM of the dominant (112) CIGS peak gives an indication of the crystal growth during selenisation. The values for all selenisation conditions are summarised in Table 5.3. The FWHM decreased by almost half from 0.254° to 0.134° with increased selenisation time from 50 to 90 min. This confirms the observations from the SEM images regarding increased crystal sizes resulting from longer selenisations. The FWHM value for the double-selenised sample is 0.162°, implying a relative crystal quality between those of the 70 and 90 min selenised absorbers. This can be attributed to the larger grains present not only at the absorber surface, but also near the back contact.

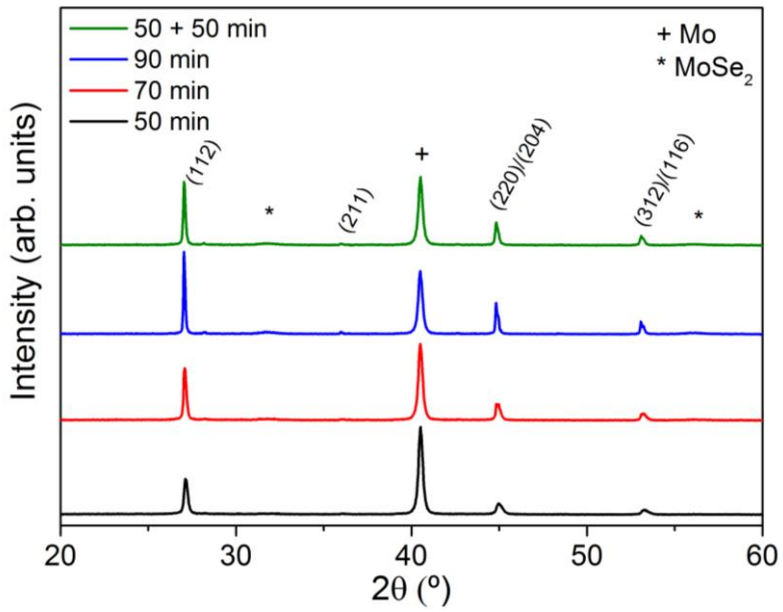

Figure 5.9 XRD patterns of Mo/CIGS layers selenised for different durations.

Table 5.3 FWHM and intensity of the dominant CIGS (112) peak giving an indication of the absorber crystal quality

	FWHM CIGS (112) (°)	**Intensity** (arb. units)
50 min	0.254	2137
70 min	0.193	3198
90 min	0.134	4705
50 + 50 min	0.162	3659

The box plots of PV parameters and light and dark J-V characteristics of the champion cell for each selenisation process are displayed in Figure 5.10. The key performance indicators corresponding to each of the J-V curves are summarised in Table 5.4. As suggested from SEM and XRD analysis, the best performing device consists of the CIGS absorber selenised for 90 min. From the box plots, the 90 min selenised device has the highest J_{SC} (an average of 33 mA/cm^2), which is on average 4 mA/cm^2 higher than the sample with the second highest J_{SC} after 70 min of absorber selenisation. The J_{SC} follows the same trend as the absorber surface crystal size. The J_{SC} is surprisingly low in the double-selenised sample (~25 mA/cm^2 on average), which might be due to the presence of the gap between the two large-grained layers, and consequent reduced carrier transport between the individual grains.

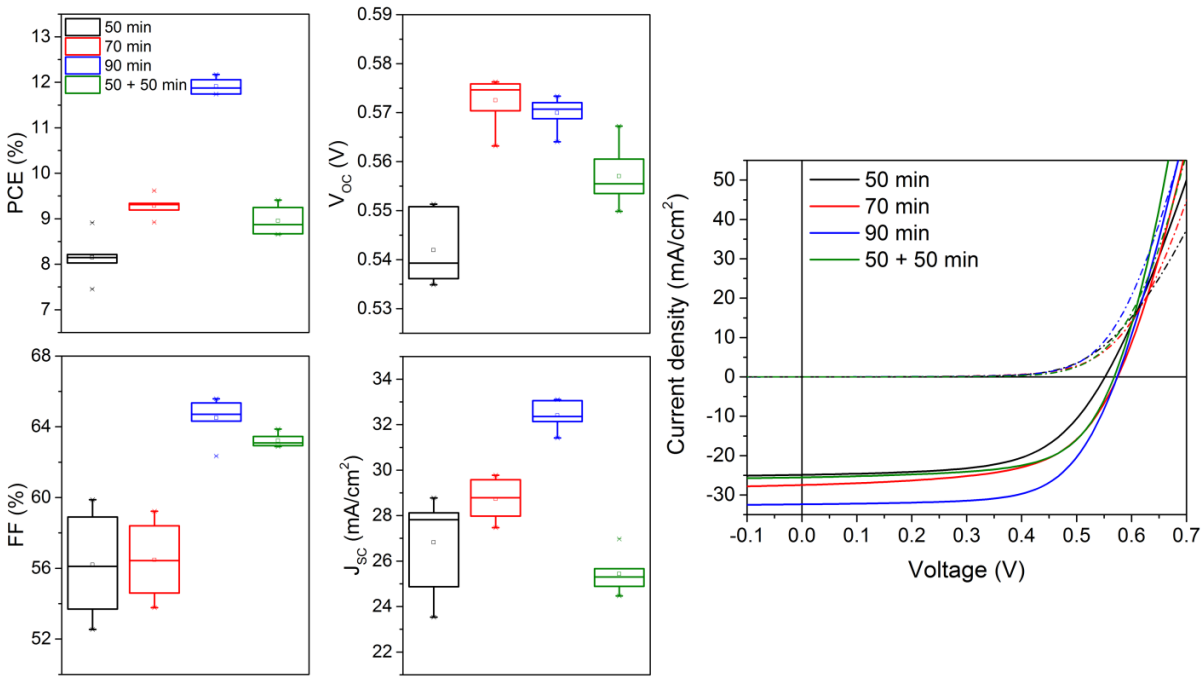

Figure 5.10 Box plots formed of 6 devices for each selenisation duration and J-V curves of a representative CIGS cell with PV parameters summarised in Table 5.4.

The increase in FF for the double-selenised sample is most likely associated with the improved crystallisation in the bulk of the absorber. This sample has the lowest R_S as a consequence of the lack of the porous fine-grained layer seen in the other samples. The champion device (90 min selenisation time) does not exhibit the best values for the parasitic resistances R_S and R_{SH}, but it does have the smallest ideality factor (*n*) and dark saturation current density (J_0) and highest FF (Table 5.4). The unintentional thickness variation due to the manual deposition method can also

affect the relative solar cell performances and consequently the scatter of the J-V parameter data (Figure 5.10). The poorest performance was achieved for the CIGS cell selenised for only 50 min, having the highest values for *n* and J_0, as well as highest R_S. The absorber in this device had the lowest degree of crystallinity, largely reflected in the device performance, especially in the J_{SC} and R_S values.

Table 5.4 PV performance indicators of the representative cell for each selenisation duration

	PCE (%)	**FF** (%)	**V_{OC}** (V)	**J_{SC}** (mA/cm^2)	**R_S** (Ω/cm^2)	**R_{SH}** (Ω/cm^2)	**n**	**J_0** (mA/cm^2)
50 min	8.2	59.9	0.551	24.9	1.554	502.4	2.48	4.56×10^{-3}
70 min	9.3	59.2	0.574	27.5	1.007	161.3	2.17	8.92×10^{-4}
90 min	12.2	65.6	0.573	32.4	1.206	419.9	1.78	1.19×10^{-4}
50 + 50 min	9.4	62.9	0.575	25.9	0.942	227.5	1.91	2.12×10^{-4}

The results presented here underline the necessity of long selenisations for these amine/thiol and metal chalcogenide-based precursors in order to achieve better absorber crystallinity and consequent device performance. Further electrical characterisation was performed on these devices, especially on the champion 12.2% efficient cell in order to identify their performance losses. Figure 5.11 b) shows the extracted doping profiles from the C-V measurements at 300 K. The doping densities were estimated from the minima of these curves. The net doping density is the lowest for the 50 min selenised device. This sample has a typical U-shape profile. The doping profiles of all other samples have an unusual shape presenting a local maximum and two minima. It seems reasonable to assume that the unusual doping density profile is connected to the large-grained/small-grained structure of the devices. It could represent either a genuine doping profile or an artefact caused by the roughness and incomplete coverage of the large crystal layer. The SEM cross-sections (Figure 5.8) indicate that the devices which display this double dip characteristic have a much larger top crystal region (~500nm) compared to the 50 min selenised device (< 200 nm). This can be interpreted as the large crystal region being fully depleted in the devices with short selenisation times, whereas for the long and double selenisations the depletion width crosses the interface between the large and small layers during the voltage sweep. This is not consistent with the measured profile depth <x> as this measure is strongly affected by deep defects and interface states, which could have artificially lowered its value [111].

The EQE spectra of these devices are shown in Figure 5.11 a). The 90 min selenised device has a much higher EQE signal at all wavelengths. The carrier collection is mostly improved in longer wavelengths, where the gradual decay of the EQE is less severe than for the other devices. The small decay below 530 nm is due to the absorption in the CdS layer. The inset of Figure 5.11 a) shows the extracted bandgaps (E_g) from the band edge of the EQE curves. The bandgap values as well as the absorber net doping densities ($N_{C\text{-}V}$) for each sample are summarised in Table 5.5.

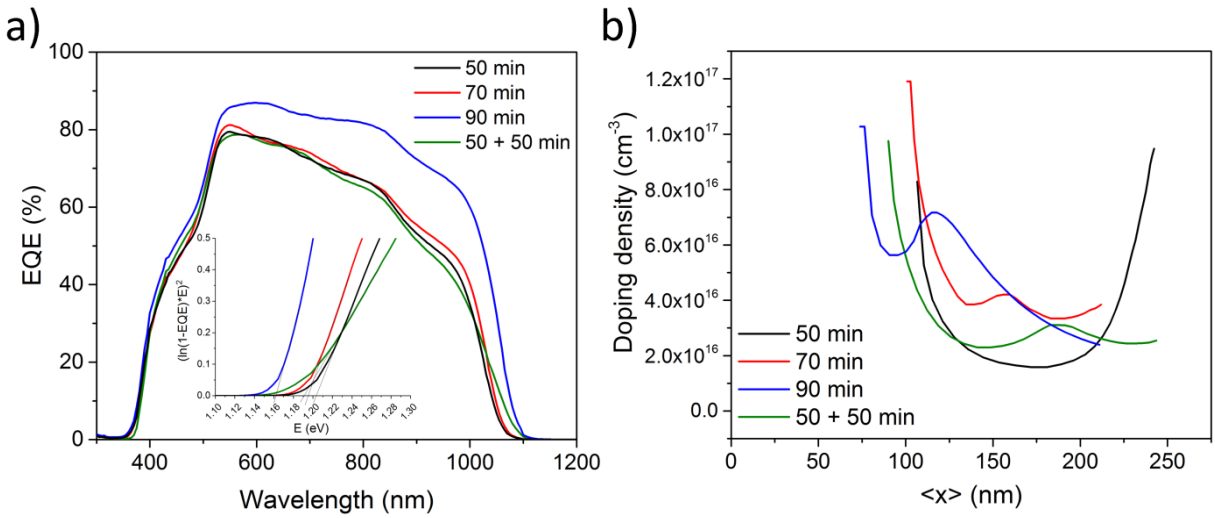

Figure 5.11 EQE curves (a) and doping profile extracted from C-V measurement at RT.

Table 5.5 Bandgap and doping density $N_{C\text{-}V}$ from C-V performed at RT. The $N_{C\text{-}V}$ values were obtained from the minima of the doping density profiles

	E_g (eV)	$N_{C\text{-}V}$ (cm^{-3})
50 min	1.2	1.58×10^{16}
70 min	1.19	3.10×10^{16}
90 min	1.16	5.63×10^{16}
50 + 50 min	1.19	2.30×10^{16}

The small apparent reduction in bandgap with increasing selenisation duration is most likely related to low-level Ga loss from the absorber during annealing. To evaluate whether the Ga loss from the film occurs, EDX analysis was performed and the calculated CGI and GGI ratios are summarised in Table 5.6. The EDX compositional analysis confirms that there is a small loss in Ga and Cu from the film subjected to 90 min long selenisation as compared to the other films.

Table 5.6 CGI and GGI ratios of the different CIGS films calculated from the compositional analysis of the absorber films using EDX

	Targeted	50 min	70 min	90 min	50 + 50 min
CGI	0.9	0.87	0.84	0.8	0.84
GGI	0.3	0.3	0.3	0.27	0.29

Temperature dependent current density – voltage (J-V-T) measurements are useful for determining the dominant recombination path of the CIGS solar cell. By plotting V_{OC} vs. temperature (Figure 5.12 a)), the activation energy for recombination (E_A) can be extracted through linear extrapolation of the plot to T = 0 K. The activation energy was found to be 1.12 eV and 1.18 eV for the 90 and 50 min selenised devices respectively. Activation energy equal to the bandgap would indicate that the major recombination mechanism is the Schottky-Read–Hall (SRH) recombination in the bulk, which is the usual mechanism in high-performance CIGS cells [172]. However in this case, the E_A is lower than the bandgap for both devices which indicates interface recombination is taking place. Therefore further improvement of the CIGS/CdS junction as outlined in Chapter 4 might be beneficial for further improvement of device performance.

To investigate the absorption properties of both 50 and 90 min selenised devices in greater depth, a multi wavelength-laser-beam induced current (LBIC) measurement was performed on a cell of each sample type. Six independent lasers covering the wavelength range from 405 to 1060 nm were swept across the cell. The output in the form of the absorber's EQE signal at each wavelength of the light sources was collected from the whole cell area with a resolution of greater than 2200 pt/mm^2. The EQE maps for the two studied absorbers are displayed in Figure 5.12 b). The lowest wavelength laser at 405 nm shows the absorption in the CdS layer. At 532 nm, absorption occurs in the CIGS absorber in the near-surface region. The absorption at this wavelength is highest for both devices and corresponds to absorption in the large-grained layer. At higher wavelengths the absorption falls off, especially for the 50 min selenised sample. This is caused by the presence of the underlying lower quality fine-grained layer. In the 90 min selenised absorber, attenuation of the LBIC signal is much slower. The 530 nm and 690 nm lasers gave similar output, showing that the large-grained layer extended much deeper into the absorber. 980 nm laser excitation gives an indication of the EQE near the back contact of the absorber. 1060

nm laser excitation is close to or slightly above absorber bandgap and consequently there is limited absorption at this wavelength.

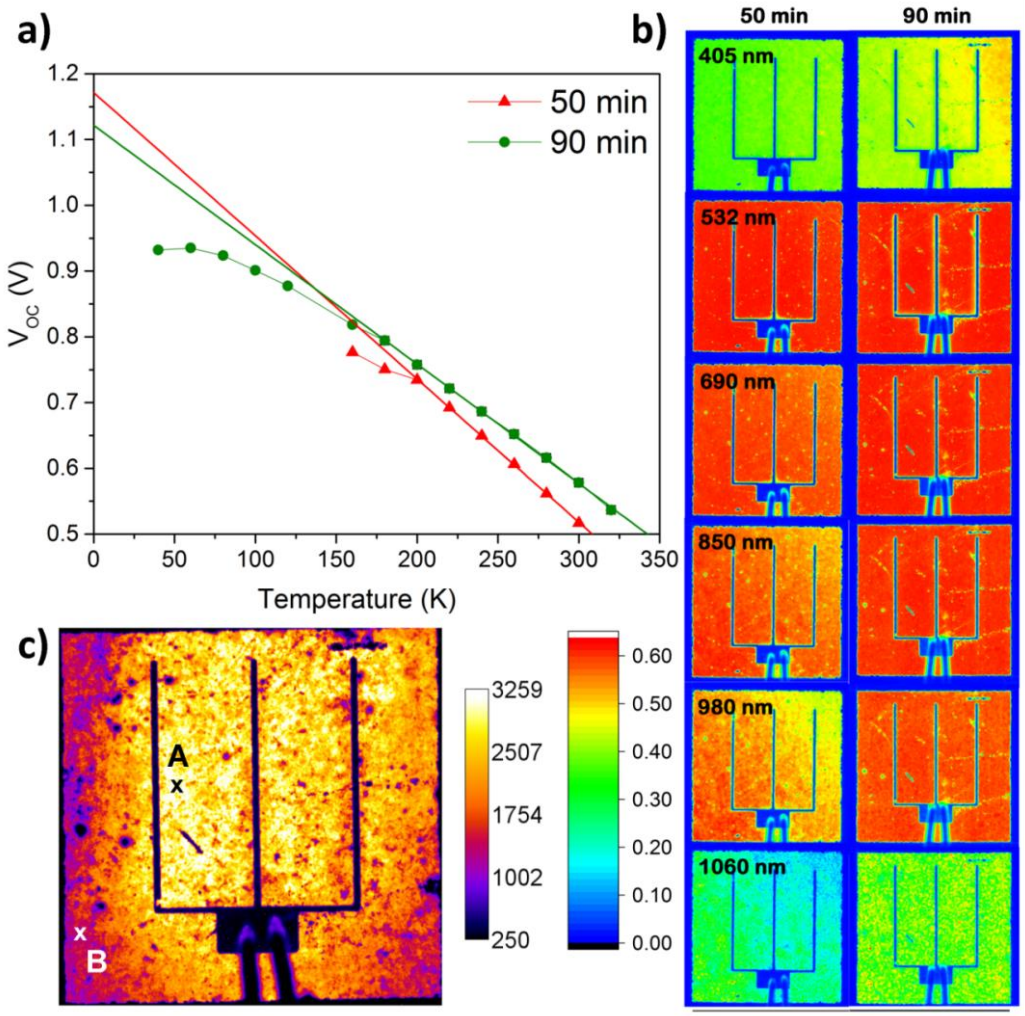

Figure 5.12 V_{OC} vs. *T* obtained from J-V-T measurement (a), EQE maps extracted from LBIC measurement across the cell using 6 lasers of different wavelengths (b) for 50 and 90 min selenised CIGS and EL image of the 90 min cell under current load of ~J_{SC} and acquisition time of 10 min (c). The EL and LBIC maps have arbitrary units.

An EL image of the 12.2% efficient cell, selenised for 90 min, is displayed in Figure 5.12 c). This shows a spatial inhomogeneity of the cell voltage output under an injected current of ~J_{SC}. To find out the origin of this disparity, a TEM cross-section was performed at two different points on the cell shown in Figure 5.13 a). Image A corresponds to point A on the EL map (Figure 5.12 c)) with a high EL signal, and image B corresponds to point B with a much lower EL signal. Both TEM cross-sections show significant voids through the absorber depth, which limits the performance. Image A shows slightly larger grains and smaller voids than Image B, which can explain the better EL signal from this area.

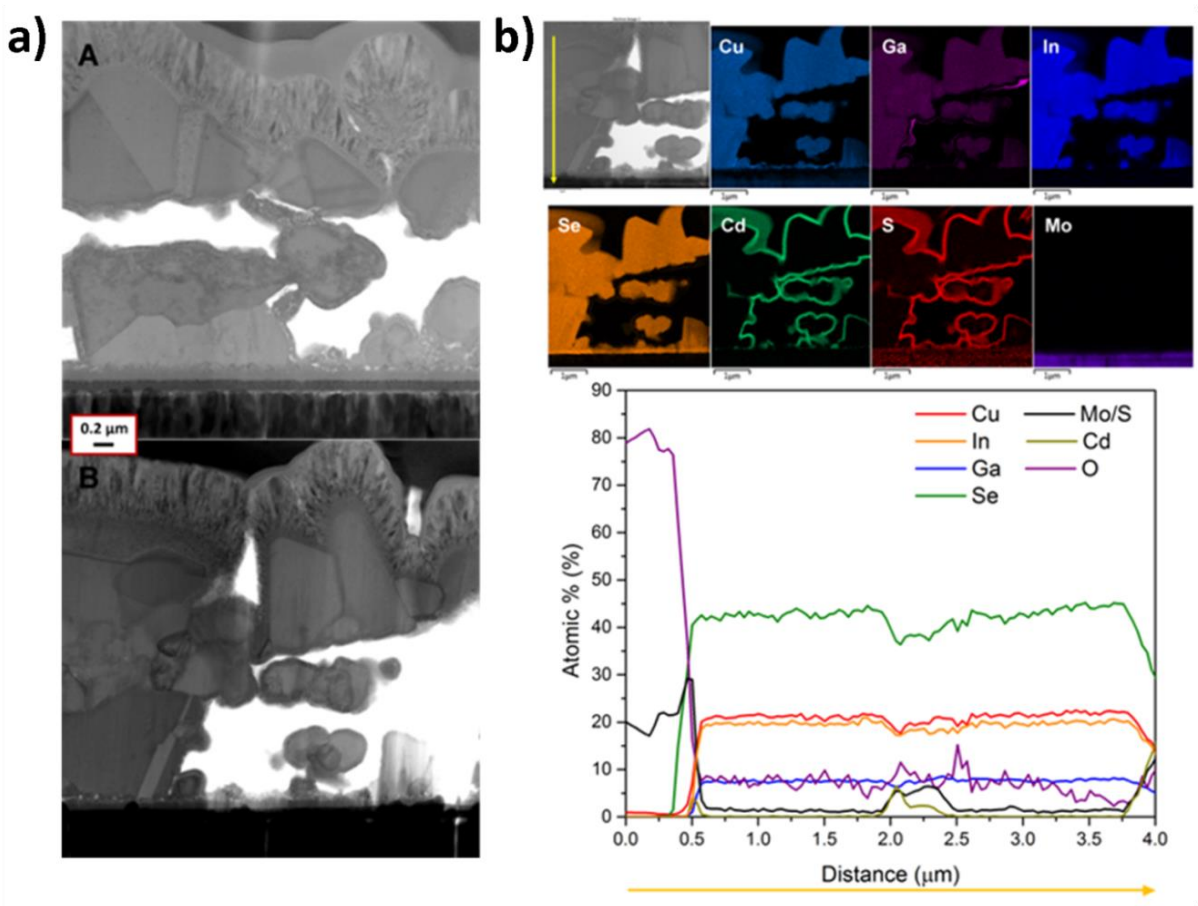

Figure 5.13 TEM cross-sections in 2 points of the 12% CIGS cell selenised for 90 min with high (A) and low (B) EL signal (a) and EDS mapping and line scan (b). The yellow arrow indicates the direction of the EDX line scan starting in the TCO and ending in the back contact.

An EDX line scan and elemental maps were performed through the absorber depth as shown in Figure 5.13 b), area B. Due to the presence of extensive voids, the CdS grown by chemical bath deposition envelops each grain separately and therefore is present in the bulk of the absorber rather than just on the surface. Ga also sometimes segregates into points of higher concentration located at grain boundaries. Ga was previously reported to react with oxygen to form gallium oxide which would not participate in the formation of the CIGS phase [58]. The relatively high oxygen concentration observed in the EDX line scan may be a consequence of storage of the FIB cross-section in air between its preparation and the TEM analysis. Therefore this value is unlikely to represent the actual content of oxygen in the CIGS absorber. The composition of the CIGS absorber through its depth is relatively constant, with overall CGI and GGI ratios of approximately 0.8 and 0.27 respectively. The observed CGI ratio in the film is lower than the intended CGI of 0.9 from the

solution, even though Cu is no longer migrating into the back contact. Cu is a fast migrating element and its high concentration is crucial for a well crystallised CIGS absorber [192]. Consequently an investigation of the origin of the Cu deficiency in the absorber and careful adjustment of the CGI ratio is still necessary.

5.3 Graphite box choice

The graphite box plays an important role during the selenisation and has a pronounced effect on the film crystallisation. The semi-closed box forms a contained environment for the selenium evaporation, creating a higher selenium partial pressure than if the sample was simply placed in the tube as in the two-zone selenisation approach. The graphite is however a porous material and selenium sinks into the box (Figure 5.14 a)). Additionally impurities such as Na can become intercalated by the graphite and consequently delivered to a sample during subsequent selenisations in an uncontrolled manner. Cleaning of the box was performed by heating to high temperature and evaporating the stored selenium; however after cleaning subsequent devices suffered from poorer absorber crystallisation and reduced performances. In order to induce better absorber crystallisation and reproducibility of the selenisation step, other graphite box designs were proposed. Photographs of the graphite boxes are displayed in Figure 5.14.

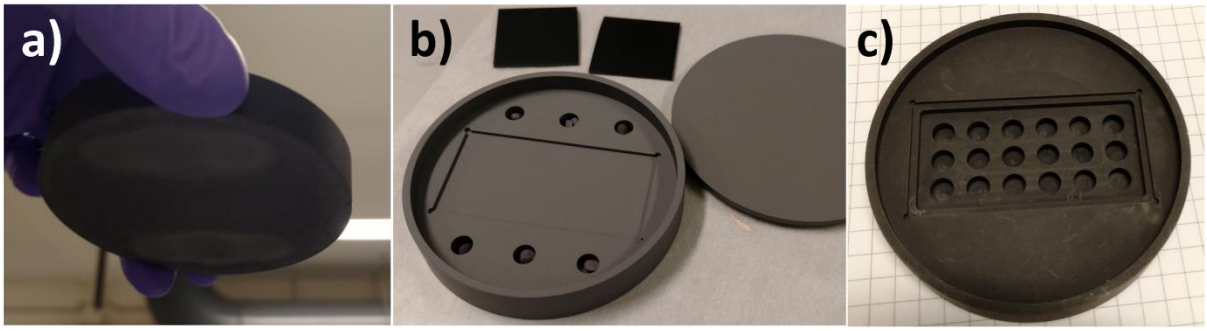

Figure 5.14 Graphite box designs: porous graphite box, same as in Figure 5.1 (a), silicon carbide coated box (b) and porous 'upside-down' graphite box (c).

5.3.1 'Upside down' graphite box design

The graphite box in Figure 5.14 b) was coated in SiC, preventing the graphite from intercalating selenium and other elements and redelivering them to another sample in a following run. This is supposed to provide improved control to the selenisation process. Otherwise the design was the same as for the simple graphite box used previously, with space for two 2.5 x 2.5 cm^2 samples facing up and 6 holes for

selenium pellets. Unlike the original uncoated box, the SiC-coated box lid was now redesigned to be fully closed in order to maintain even higher selenium partial pressures. The graphite box shown in Figure 5.14 c) is uncoated and has a different design. The holes for selenium pellets are located under the sample, with the film facing the pellets. This design was meant to deliver more Se to the sample as the vapours would be in direct contact with the precursor film prior escaping out of the box. In addition, the smaller distance between the film and Se source would potentially result in even higher Se partial pressure in the immediate film proximity. Figure 5.15 shows a photograph and SEM surface and cross-section images of the absorber films after selenisation for 50 min using the 'upside down' graphite box design.

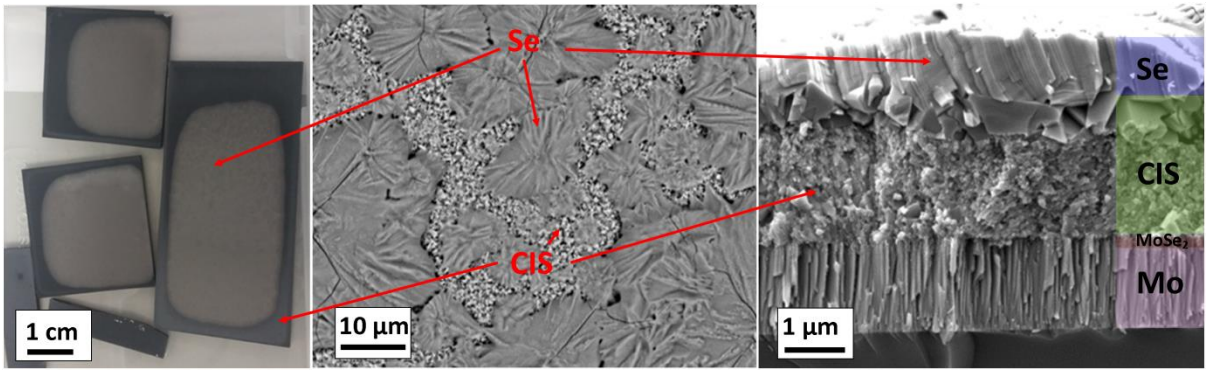

Figure 5.15 Photograph and SEM images of the selenised CIS absorbers using the 'upside down' graphite box

After selenisation, the absorber is unevenly covered with a layer identified by EDX as elemental selenium. Selenium condensed on the absorber surface forming a layer of thickness up to 1 µm. The selenium layer was present even after selenisations of more than 50 min long and using fewer Se pellets. As shown in the SEM cross-section, the absorber layer underneath consists of a large/fine-grained bilayer, similar to absorbers typically obtained after selenisation using the initial graphite box design (Figure 5.1 a)). The suggested improvement of absorber crystallisation did not appear to take place and the Se surface layer has to be removed with an additional annealing step. The distance between the film and Se source was ultimately too small to be beneficial. The selenium layer was evaporated from the surface of the absorber by an annealing step in the tube furnace. The best performing CIS device achieved using this graphite box design was 3.9% efficient. Its SEM cross-section and J-V characteristics are shown in Figure 5.16.

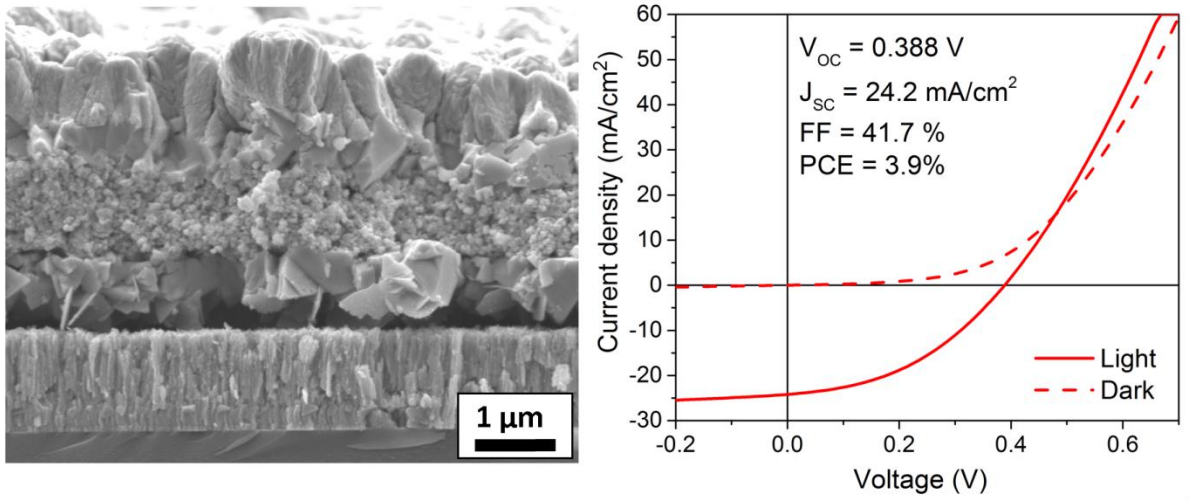

Figure 5.16 SEM cross-section and light and dark J-V curves of a CIS device after absorber selenisation in the 'upside down' graphite box for 50 min and evaporation of the selenium surface layer for 30 min.

The absorber consists of large grains at the top and bottom, near the CdS and $MoSe_2$ interface respectively. The fine-grained layer is still present, sandwiched in between the two more crystallised layers. However, the degree of absorber crystallinity was also variable across the entire sample area. The device has a lower J_{SC} and V_{OC} compared to the 'no barrier' CIS device selenised in the original graphite box and whose characteristics were shown in Table 5.2. Due to the poor selenisation uniformity, the necessity of an additional processing step (Se layer evaporation) and low performance, this graphite box was not used any further.

5.3.2 SiC-coated graphite box

This section focuses on the comparison of the uncoated graphite box and SiC-coated graphite box. The role of the SiC coating consists in preventing intercalation of Se and other impurities into the porous graphite. This would not only enable higher Se partial pressure inside the box but also improve the selenisation reproducibility as the amount of Se is much more controllable. It would also reduce the presence of additional impurities such as Na. The electrical and morphological characterisation of devices selenised in each box was used to identify and discuss the differences between the two methods.

Figure 5.17 a) shows the SEM absorber cross-section and surface images. Both CIGS absorbers present similar morphological features through their depth; however

the absorber selenised in the SiC-coated box has slightly larger surface grains. This is also reflected in a lower FWHM of its dominant (112) XRD peak (Figure 17 b)).

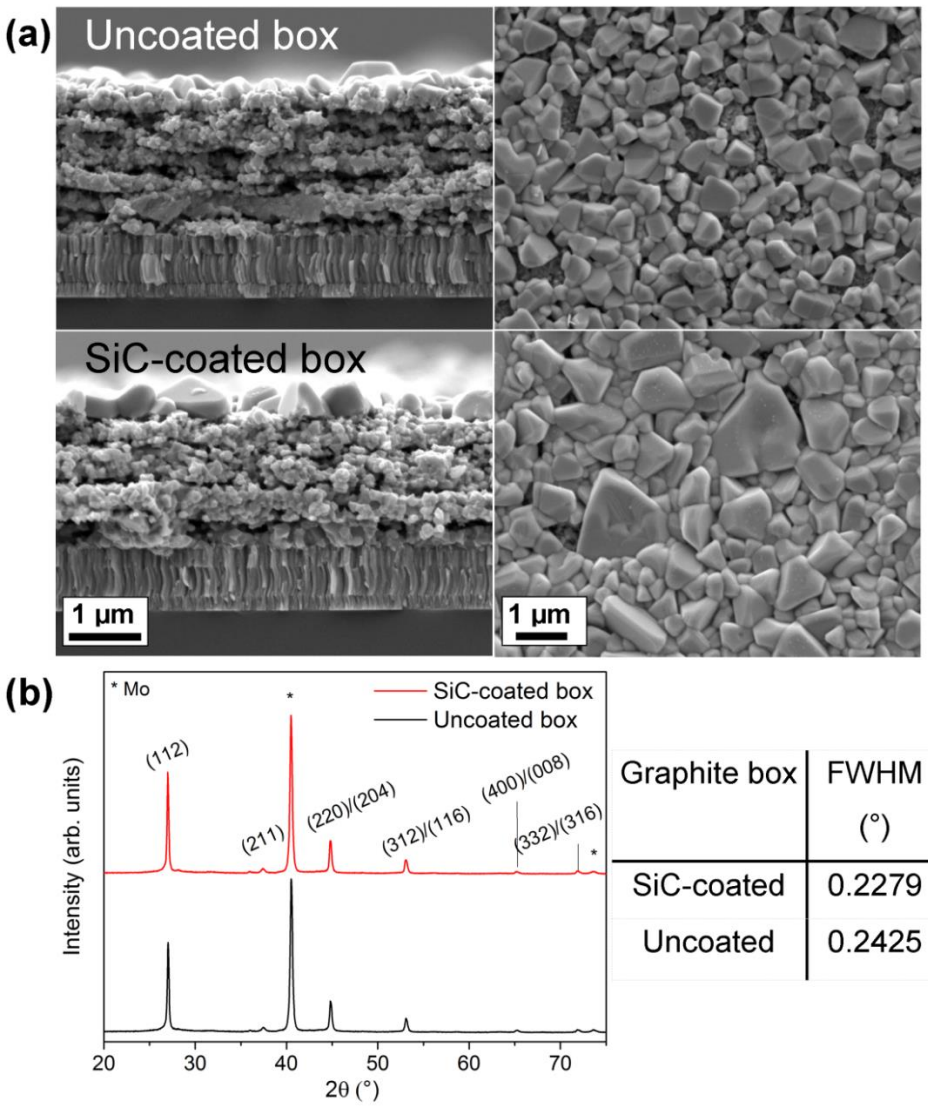

Graphite box	FWHM (°)
SiC-coated	0.2279
Uncoated	0.2425

Figure 5.17 SEM cross-section and surface images of CIGS absorbers selenised using the uncoated and SiC-coated graphite box (a) and XRD spectra of the two films with a table summarising the FWHM of the dominant (112) peak corresponding to the CIGS phase (b).

The V_{OC}, FF, J_{SC} and efficiency are presented in the form of box plots consisting of the data from 12 cells for each sample (Figure 5.18 a)). All the PV parameters of the CIGS sample selenised in the uncoated box are higher, with the best device showing 9.3% efficiency (Figure 5.18 b)). This is in direct contradiction to the improved absorber morphology of the samples selenised using the SiC-coated box, which yielded a maximum device efficiency of 5.0%. The reason for the improved performances of solar cells selenised in the uncoated box can be related to different

sodium doping levels of the absorber. The uncoated graphite box is soaked with selenium, as seen in Figure 5.14 a). Sodium coming from the SLG substrate reacts with Se to form volatile Na-Se phases and is thought to be intercalated together with Se in the porous uncoated graphite box. At elevated temperatures small quantities of Na can therefore be redelivered to the absorber in the following annealing run. As little as 0.1 at% of Na can significantly improve the absorber V_{OC} and FF, which was also observed here. The box plots of PV parameters for the coated box present a much narrower distribution, which confirms the improvement of process uniformity. Consequently the coated box approach is very promising in order to achieve precise control over the process and composition. The selenisation parameters when using the coated box however need to be re-optimised and perhaps a different and controllable approach for absorber sodium doping could be employed in order to achieve sufficient doping and higher efficiencies.

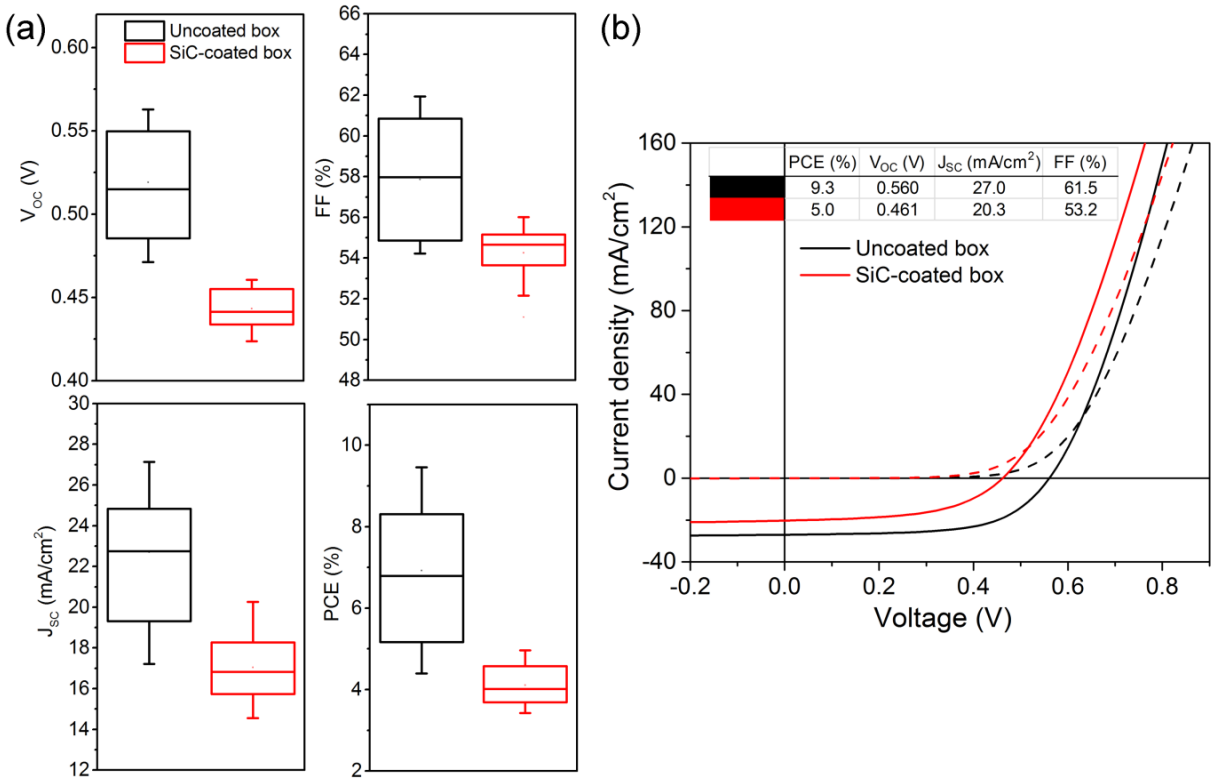

Figure 5.18 Box plots containing 12 cells for each sample (a) and J-V curves of the best cell of each sample selenised using coated and uncoated graphite box (b).

5.4 RTP selenisation

In the following section, the RTP was used in combination with the SiC-coated graphite box. The coated box allows for control of the Se amount and reduces the

risk of accidental doping or impurity incorporation into the film. The RTP has an advantage over the tube furnace as the heating rate of the furnace is extremely quick. In several seconds it can get to the dwell temperature of 550ºC. It doesn't have exposed ends and consequently higher Se quantities are available for selenisation. The combination of the RTP and the coated box is thought to improve CIGS absorber crystallisation and process reproducibility as well as allowing for intentional absorber doping.

5.4.1 Study of the intermediate selenisation dwell

This section examines the influence of the selenisation temperature profile. Initially, a profile with an intermediate dwell at 300°C was employed prior to rapid ramping to the final selenisation temperature of 550°C. The ramp rates in this profile are very fast, at 5°C/s to the first and 4.2°C/s to the second temperature dwell point. The reasons for the use of the intermediate lower temperature annealing stage are attributed to the beneficial effects of the formation of secondary Cu_xSe phases ($x<2$) acting as fluxing agents during absorber sintering and consequently promoting grain growth [193]. The importance of the intermediate stage was studied by comparing the morphological and structural characteristics of the solution-processed CIGS absorbers selenised with and without the intermediate annealing step. Figure 5.19 shows the CIGS absorber morphology, when selenisation was interrupted during the intermediate dwell at 300ºC after various times.

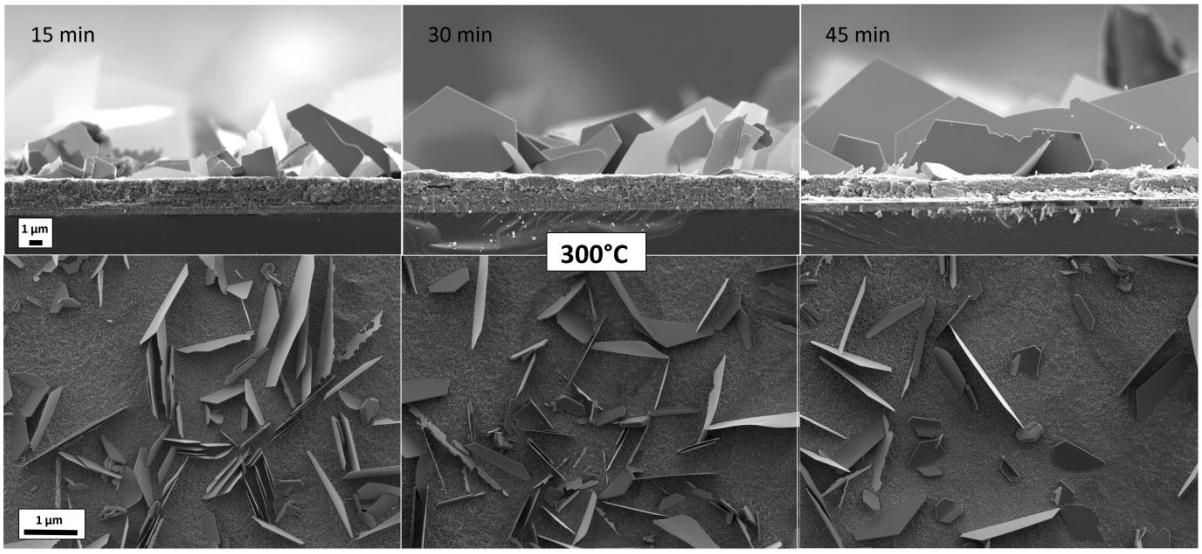

Figure 5.19 SEM images of the CIGS absorbers when the intermediate dwell at 300ºC was interrupted at different durations.

The SEM images show the presence of Cu_xSe hexagonal sheets sticking out of the CIGS absorber surface for all annealing durations. The distribution of the Cu_xSe grains on the absorber surface is however very irregular and a large variation of the grain sizes can be observed even after 45 min dwell time. The grain size of the underlying $Cu(In,Ga)(S,Se)_2$ film doesn't seem to be affected at this stage. The influence of this intermediate dwell on the final absorber morphology was studied by comparison of the SEM surface images with a reference sample selenised at 550°C which was not subjected to the intermediate dwell at 300°C. Figure 5.20 presents the SEM surface images of the absorbers at the end of the selenisation (50 min at 550°C) including various intermediate dwell times.

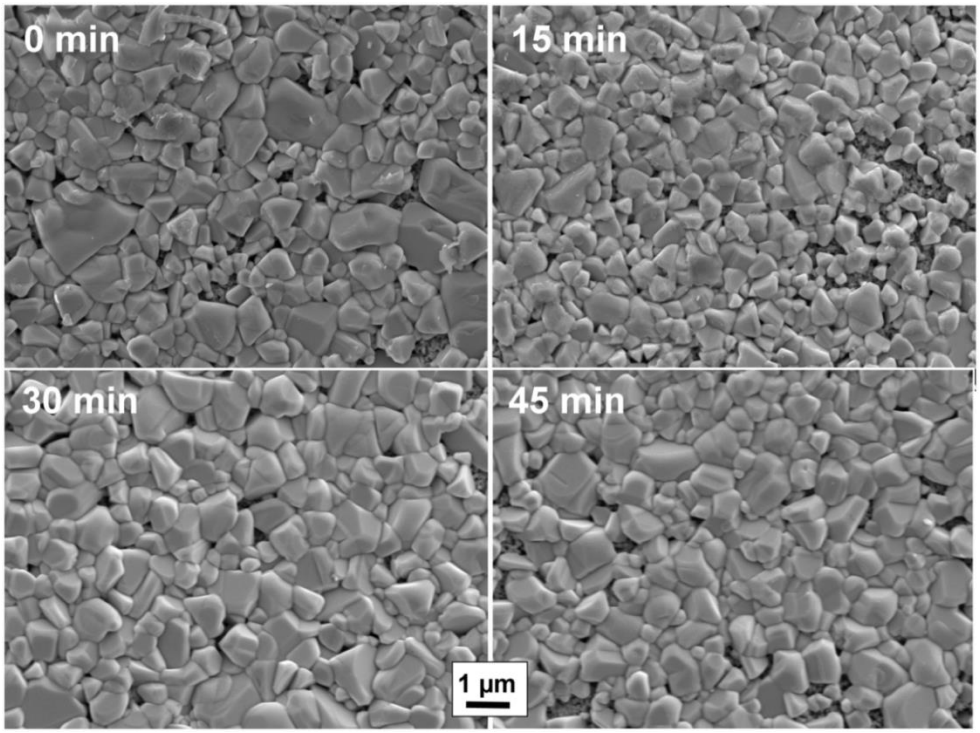

Figure 5.20 SEM images of the CIGS absorbers after selenisation for 50 min at 550°C with varied duration of the intermediate dwell at 300ºC.

The CIGS absorbers were formed of the typical coarse/fine-grained morphology. The size of the surface grains is very similar regardless the intermediate dwell duration. Slightly better grain growth is observed for the absorber selenised using the 30 min long intermediate dwell step. The SEM images however only show ~ 15 x 11 μm^2 of the sample area, therefore XRD was performed to confirm the crystal quality of the absorbers. XRD patterns corresponding to the four films are presented in Figure 5.21. The extracted FWHM of the dominant CIGS (112) XRD peak (Figure 5.21) is very similar for all the films with values between 0.20-0.24°. The lowest FWHM value was

found for the 30 min intermediate dwell time confirming the slightly larger grain growth of this film implied by the SEM images.

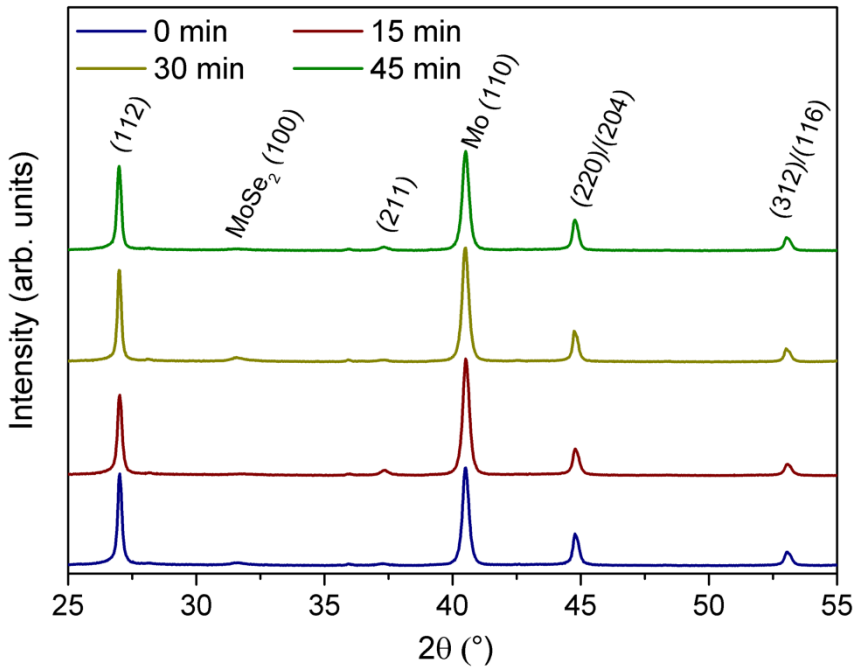

Dwell time (min)	FWHM CIGS(112) (°)
0	0.2251
15	0.2421
30	0.2011
45	0.2240

Figure 5.21 XRD spectra of the films selenised with intermediate dwell at 300°C for various durations. The table summarises the FWHM of the dominant (112) CIGS peak.

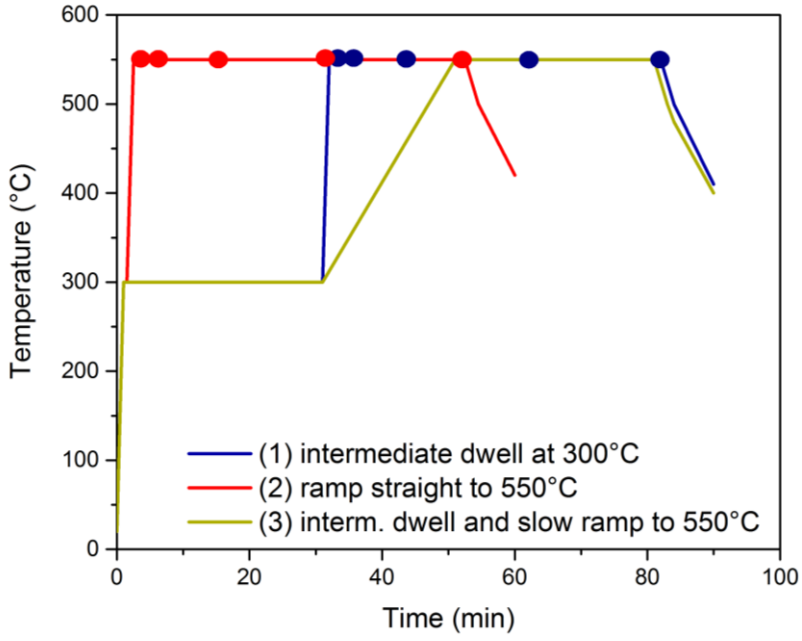

Figure 5.22 RTP temperature profiles: with fast temperature ramping rate (~4°C/s): (1) including an intermediate dwell at 300°C and (2) omitting the intermediate dwell and ramping straight to the selenisation temperature of 550°C; and slow ramping rate (12.5°C/min): (3) including intermediate dwell at 300°C. The circles represent points where the process was interrupted to analyse the absorber morphology after cooling down of the sample.

Figure 5.22 shows three selenisation profiles combining the presence of a 30 min intermediate dwell step with fast and slow ramping rates. The influence of the selenisation profiles (1) and (2) - with and without including the intermediate temperature dwell step - on the absorber morphology is compared by interrupting the process at different times from the start of the final temperature dwell stage at 550°C: 30 s, 5 min, 15 min, 30 min, 50 min and 70 min. Morphologies of the resulting films are displayed in Figure 5.23. The starting pressure was set to 200 Torr and ~ 600 mg of Se was placed in the SiC-coated box together with the sample.

The sample subjected to the intermediate dwell step at 300°C underwent a phase where Cu_xSe crystals were formed (Figure 5.19). These are still present after 30 sec from the ramp to 550ºC, but they disappeared after as little as 5 min of annealing at the final temperature. The sample that was ramped straight from 20ºC to 550ºC did not appear to exhibit any Cu_xSe phase formation at the surface after 30 sec of the dwell step, however some non-identified surface features were nevertheless present at the absorber surface after 5 min of selenisation. These subsequently disappeared after 15 min. The Cu_xSe phase formation at the absorber surface believed to be responsible for CIGS grain growth was either circumvented by the rapid ramp rate or was very short-lived (< 5 min) for this profile. Despite the different initial growth of the samples subjected to different RTP temperature profiles, the absorber morphology at times of ≥ 15 min are very similar, with no evident grain size enlargement in the absorbers subjected to the Cu_xSe-rich intermediate stage. However longer selenisation time increases the grain size of the top CIGS layer for both profiles, up to 50 min selenisation. At this duration, the 600 mg of Se were completely consumed from the graphite box, and additional heating of the sample without the presence of a chalcogen atmosphere was no longer beneficial for crystal growth. Moreover the insufficient supply of Se towards the end of the process can lead to selenium surface depletion [194].

XRD spectra of the absorbers subjected to selenisation profile (1) with various selenisation durations are displayed in Figure 5.24. The lowest FWHM was found for the sample selenised for 50 min, which also exhibited the largest grains under SEM (Figure 5.23).

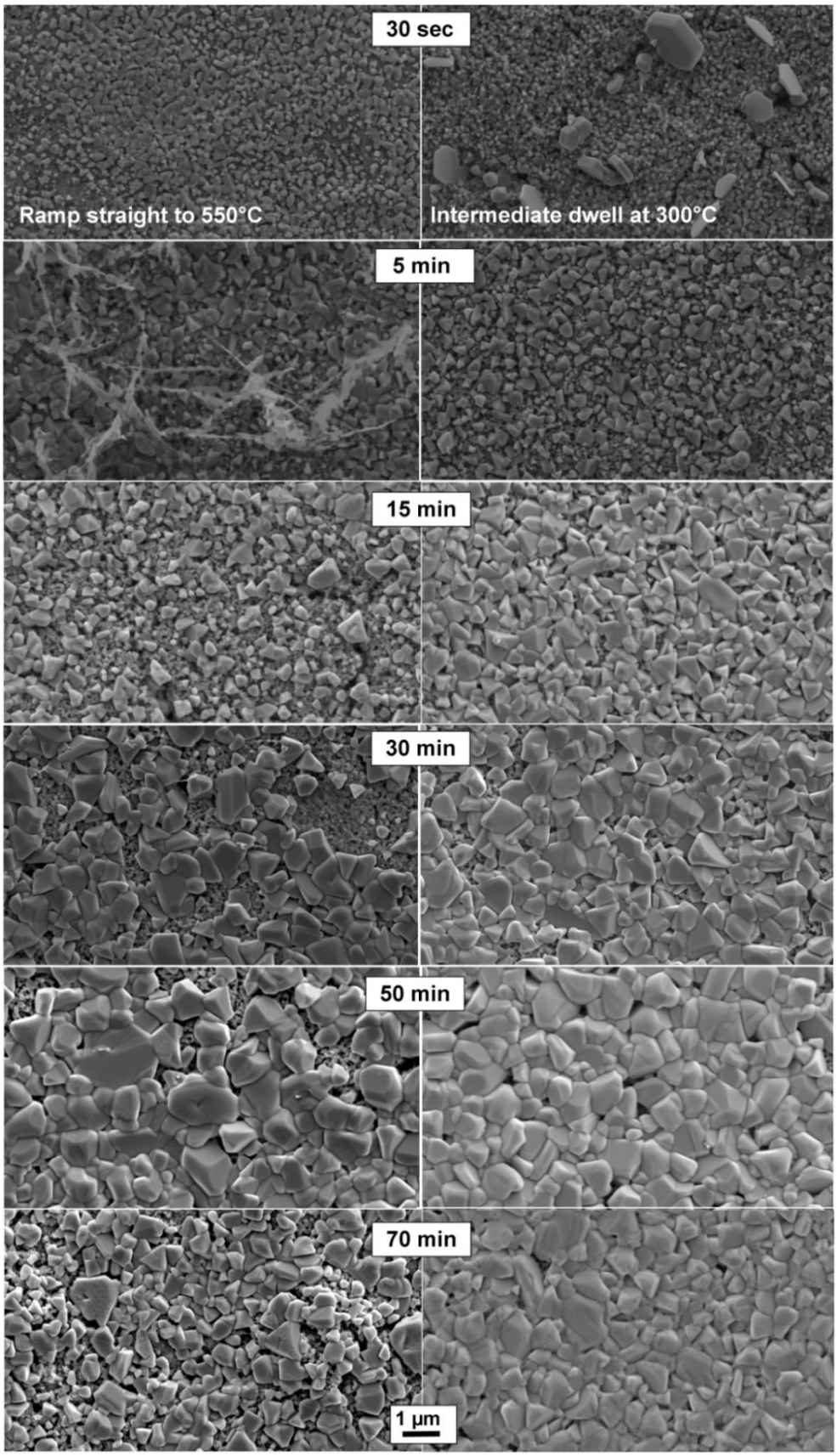

Figure 5.23 SEM images of the CIGS absorbers after various selenisation durations at 550ºC. The absorbers on the left were ramped straight to 550ºC, whereas on the right the absorbers were subjected to a preliminary dwell at 300ºC for 30 min.

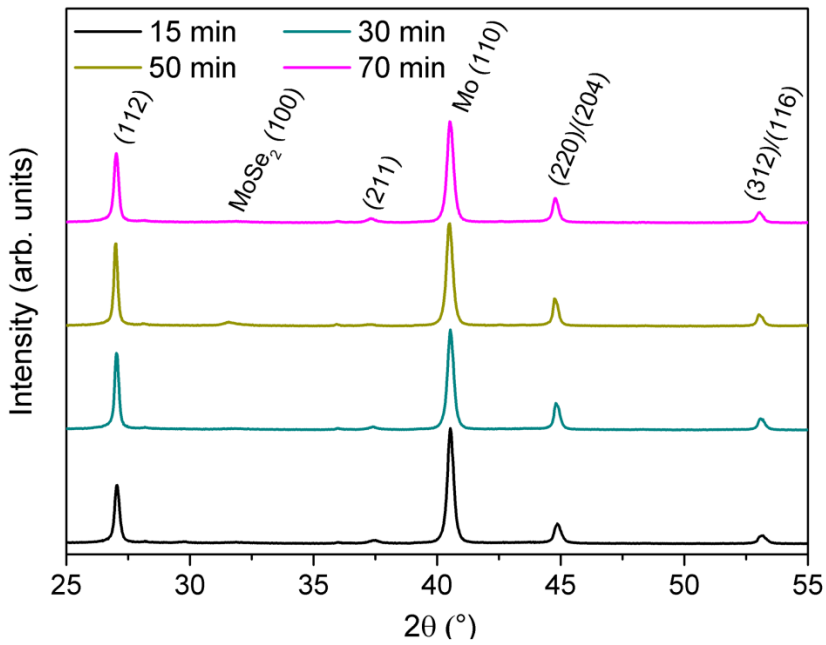

Selenisation time (min)	FWHM CIGS (112) (°)
15	0.2586
30	0.2184
50	0.2011
70	0.2499

Figure 5.24 XRD spectra of CIGS films selenised for various durations following an intermediate dwell at 300°C for 30 min. The table shows the FWHM of the dominant (112) XRD reflection giving an indication of the absorber crystal quality.

Finally, two conclusions can be drawn from these morphological and structural studies. The amount of selenium in the box might have a key influence and could allow for even longer than 50 min selenisation times, thereby further improving the absorber crystal growth. Secondly, in selenisation profile (1), whilst the formation of secondary Cu_xSe phases occurred, the melting point of this phase may not have been reached at this temperature. Meanwhile the high ramping rate to 550°C may have meant that it was consumed very rapidly, without being able to participate in the CIGS grain growth mechanism [195]. This would explain the similarity of the final absorber morphologies after following both selenisation profiles (1) and (2). Consequently slower ramping rates such as in profile (3) would allow for Cu_xSe melting and its progressive consumption. Coarse CIGS grains are expected to grow from the liquid Cu_xSe phase wetting the CIGS surface. This was previously observed to happen at temperatures below 500°C and was strongly affected by the amount of Na present in the absorber [193].

5.4.2 Influence of selenium quantity

In the following section, the amount of Se required to replace sulphur in the precursor and supply a sufficient Se partial pressure to recrystallise the absorber was studied experimentally. A series of selenisations were performed varying the

number of Se pellets introduced into the coated graphite box. The morphology of the absorber layers obtained from selenisation with increasing Se are shown in Figure 5.25.

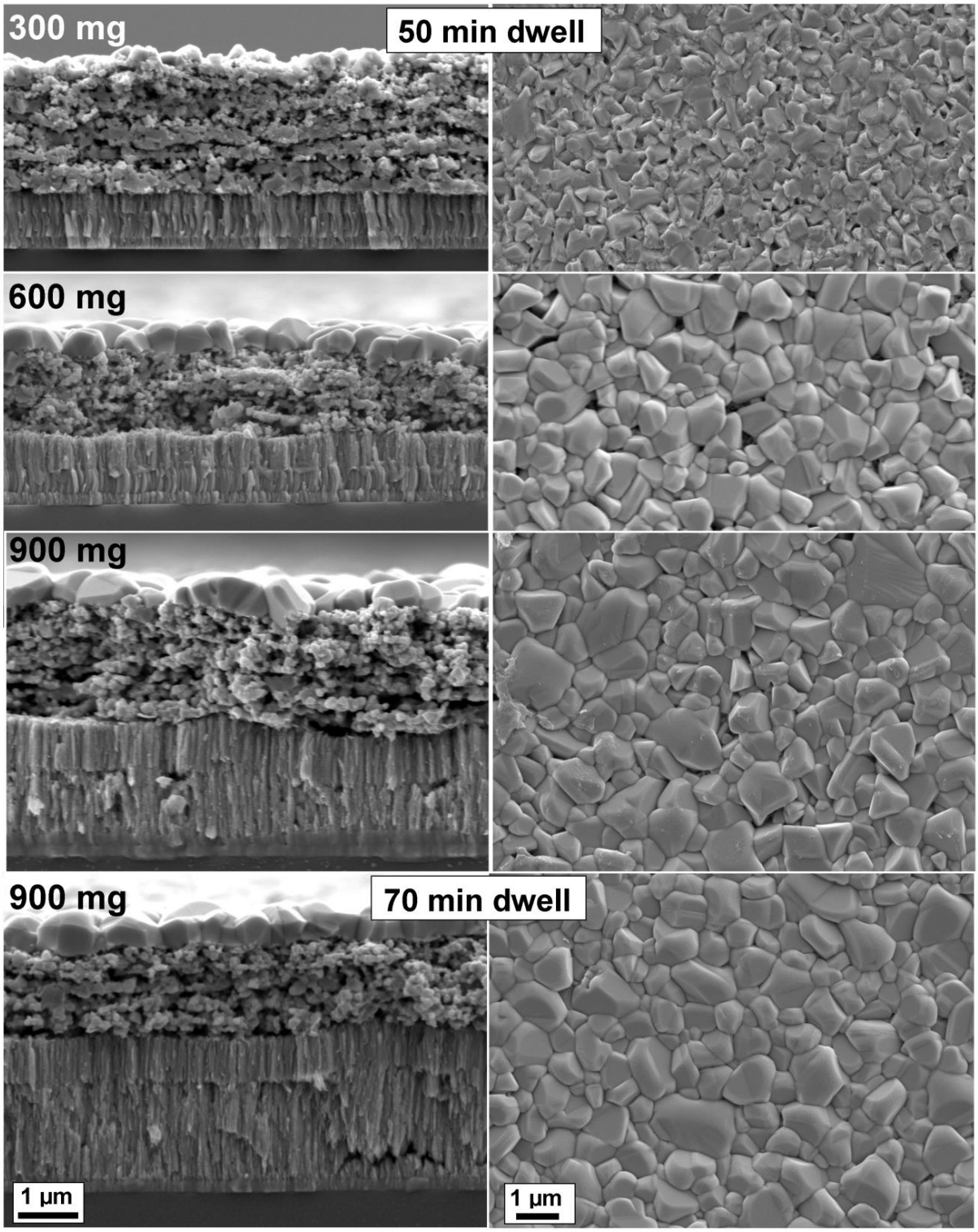

Figure 5.25 SEM cross-section and top view images of the samples with 300, 600 and 900 mg of Se introduced in the graphite box for 50 min long (top three) and 70 min long (bottom) selenisation.

CIGS grains, especially at the absorber surface, increased in size and prominence with increasing Se. Laterally some grains reached up to 2 µm when the greatest amount of Se was used, but the coarse-grained layer is only ~700 nm thick. Longer selenisation times (70 min instead of 50 min) did not result in significantly different grain sizes, however the large-grained surface layer is denser. Larger amounts of Se also affected the $MoSe_2$ formation. With 900 mg of Se, the Mo-N barrier layer was not able to resist the high Se pressure and consequently the underlying Mo was converted into a substantial ~2 µm thick $MoSe_2$ layer. XRD spectra (Figure 5.26) show Mo and CIGS peaks corresponding to the four samples. From the table in Figure 5.26 it is clear that the crystal quality of the CIGS absorber improves with addition of Se, as the FWHM decreases, but the back contact deteriorates with a decreasing Mo/$MoSe_2$ peak intensity ratio. Consequently a compromise between absorber and back contact quality has to be made and 900 mg of Se is therefore considered as excessive. It is also likely to have a negative impact on the device R_S and FF.

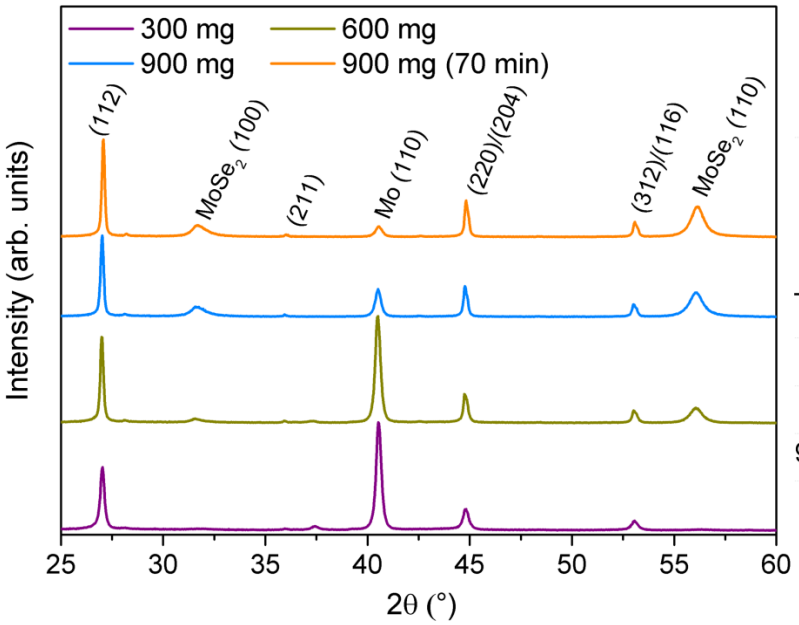

Se amount (mg)	FWHM CIGS(112) (°)	Intensity Mo(110)/ $MoSe_2$ (110)
300	0.2781	51.7
600	0.2011	6.50
900	0.2002	1.14
900 (70min)	0.1844	0.371

Figure 5.26 XRD spectra of CIGS absorbers selenised for 50 min with 300, 600 and 900 mg of Se and selenised for 70 min with 900 mg Se. The table summarises extracted values for FWHM of the dominant CIGS (112) peak and intensity ratio of the most pronounced Mo (110) to $MoSe_2$ (110) peaks.

5.4.3 Influence of the temperature ramping rate

Selenisation profile (3) in Figure 5.22 was employed with three different ramp rates (250°C/min, 25°C/min and 12.5°C/min) and final selenisation dwell step at 550°C for

50 min. The SEM cross-section and top view images of the three absorber morphologies are shown in Figure 5.27.

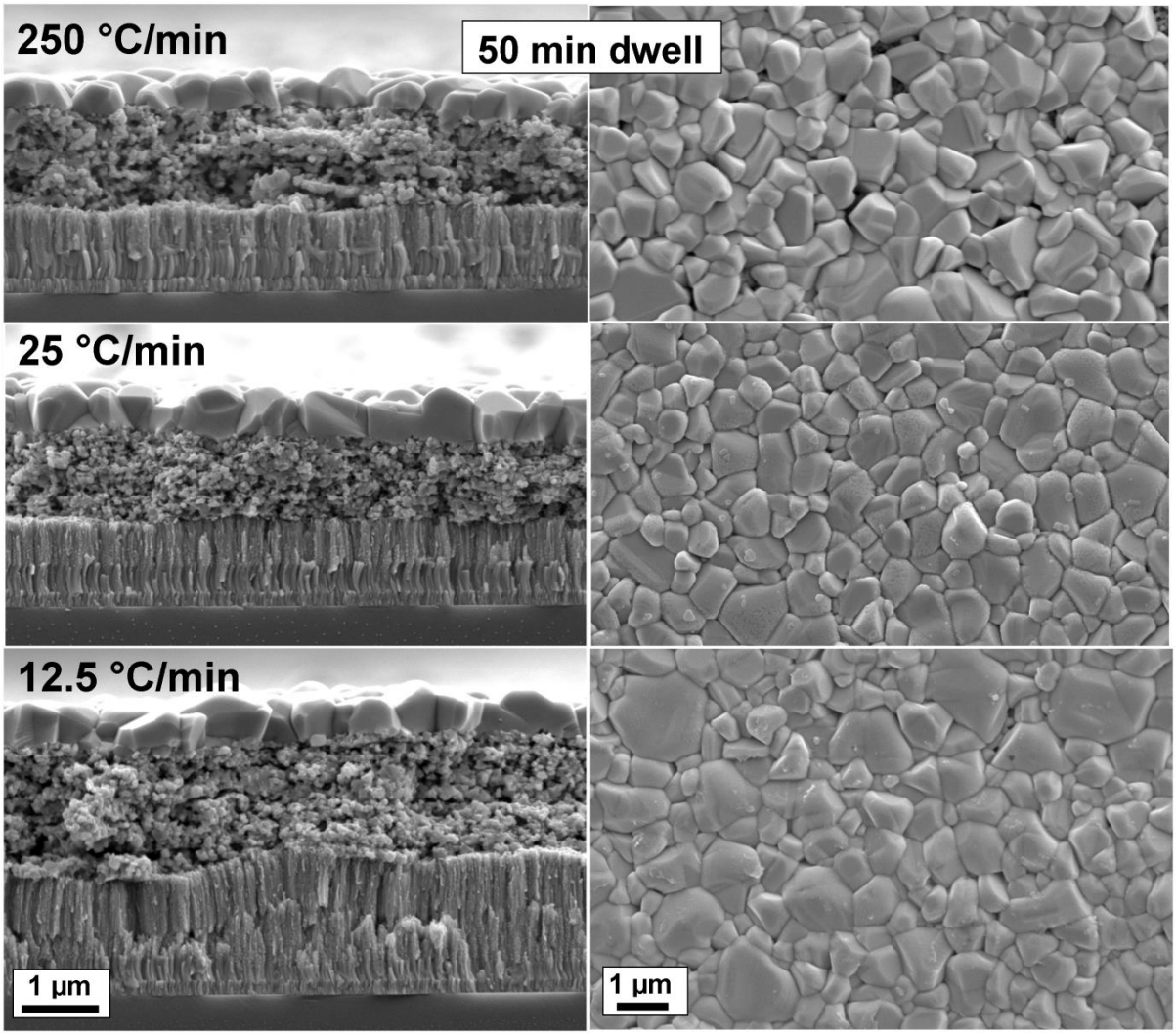

Figure 5.27 SEM cross-section and top view images of CIGS absorbers selenised varying the ramping rate from 300 to 550°C.

A slower ramping rate results in denser large-grained material at the absorber surface. The slowest ramping rate (20 min from 300 to 550°C) also resulted in increased $MoSe_2$ formation. The porous fine-grained layer is present for all conditions tested. XRD patterns corresponding to the three films are shown in Figure 5.28. The extracted FWHM of the CIGS (112) peak confirms that the crystallinity was barely affected when decreasing the ramp rate from 300 to 550°C. The increased consumption of Mo to form $MoSe_2$ with slower ramp is reflected in reduced Mo/$MoSe_2$ peak intensity ratio. Considering the similar bilayer absorber morphologies for all conditions, one may speculate that the selenisation conditions

used, particularly the relatively high working pressure, are producing limited or no Cu_xSe phase melting which results in limited grain growth.

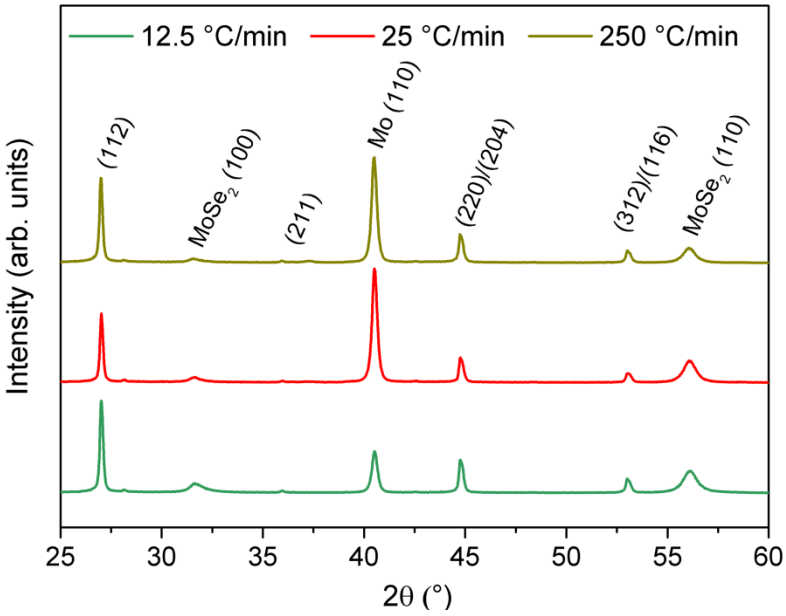

Ramp rate	FWHM CIGS(112) (°)	Intensity Mo(110)/ $MoSe_2$ (110)
250°C/min	0.2011	6.50
25°C/min	0.1941	4.96
12.5°C/min	0.2049	1.84

Figure 5.28 XRD spectra of CIGS absorbers selenised using different temperature ramping rates when passing from 300 to 550°C. The table summarises extracted values for FWHM of the dominant CIGS (112) peak and intensity ratio of the most pronounced Mo (110) to $MoSe_2$ (110) peaks.

5.4.4 Optimisation of RTP selenisation: conclusions

In summary, it was shown that the RTP selenisation in combination with the coated graphite box is a more reliable alternative to the tube furnace selenisation using the uncoated graphite box. Selenisation in the RTP provides a more controllable process with lower losses of Se due to non-exposed tube ends and tunable heating profile. The coated box in addition eliminates the unintentional absorber contamination with impurities intercalated in the box material from previous selenisation runs and allows for precise control over the Se quantity. The selenisation using the coated box needed to be reoptimised in order to achieve the best absorber morphology and crystal quality possible whilst maintaining an unaffected back contact. It was shown that the Se amount and selenisation duration are the factors that affect the crystallisation the most, while temperature ramp rate and intermediate dwell seemed to have less effect. Changing the process parameters failed to result in elimination of the fine-grained layer in the absorber. After optimisation, a CIGS solar cell on a SLG substrate with an efficiency of 9.1% was achieved using this selenisation approach. The J-V curve of this device is displayed in Figure 2.29, and corresponds to

selenisation profile (1) in Figure 5.22 with 30 min intermediate dwell step at 300°C and a ramping rate of 250°C/min to 550°C followed by a dwell time at this temperature of 70 min in the presence of 900 mg of Se.

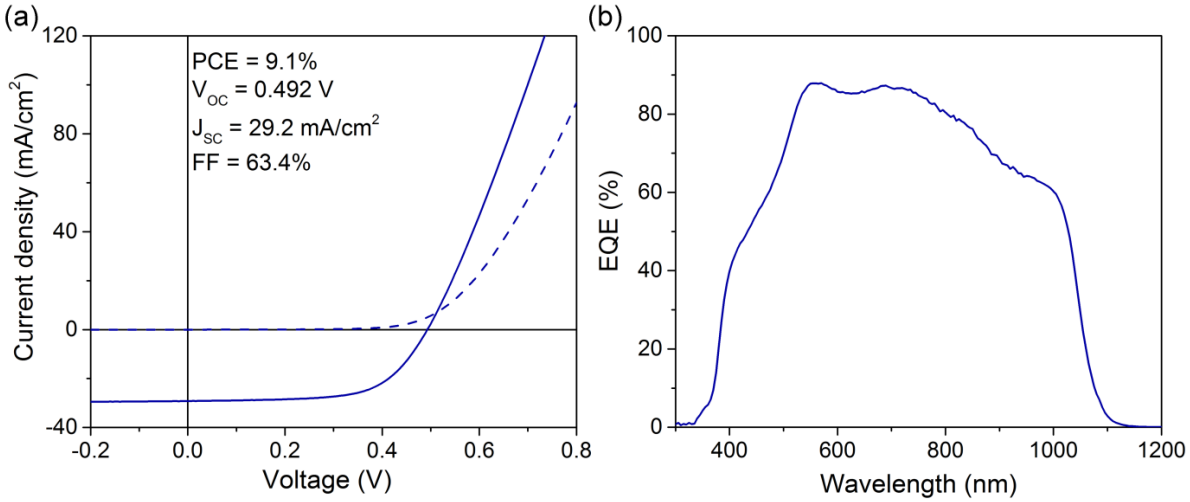

Figure 5.29 J-V (a) and EQE (b) curves of the champion device resulting from the RTP/SiC-coated graphite box selenisation optimisation. The absorber of this cell was selenised with the following profile: intermediate dwell at 300°C for 30 min followed by ramping to 550°C at 250°C/min and finally selenisation at 550°C for 70 min with 900 mg of Se initially introduced into the graphite box.

Despite the excessive $MoSe_2$ formation at the back contact of the device, these selenisation conditions resulted in best device performance. The performance is still slightly behind the performances obtained using the selenisation tube furnace and uncoated graphite box. However as discussed above, this is thought to be a consequence of unintentional doping of the absorber from release of Na intercalated in the box material. An investigation into the intentional absorber doping will be shown in the following chapter and the coated box was essential for performing this study with controllable addition of alkaline impurities.

5.5 Copper composition variation

Following the minor improvement in absorber morphology resulting from selenisation optimisation, the effects of absorber composition were investigated. Changing the absorber composition away from the nominal stoichiometry introduces native defects into the absorber that will have an effect on the electrical behaviour of the material. Moreover, it was shown that the amount of Cu in the absorber material strongly influences the morphology and structure of the absorber film [196]. It was found that

the presence of Cu_xSe (x<2) has a crucial role in the recrystallisation mechanism and quality of the final absorber material. Films grown under Cu-rich conditions exhibit much larger grain sizes (2-5 µm) as opposed to films grown under Cu-poor conditions (1-2 µm) [196]. However Cu-rich films typically suffer from segregation of secondary Cu_xSe phases, preferentially at film surfaces and grain boundaries. Cu_xSe are degenerate p-type semiconductors with bulk resistivities of ~10^{-3} Ω.cm and absorption greater than 10^4 cm^{-1}, therefore dominating the surface and opto-electronic properties of the device [196]. Secondary phases can be removed from the surface by etching with KCN to restore the film photovoltaic activity. However the use of such material for photovoltaic applications might be limited due to high doping densities of the Cu-rich material (10^{18} cm^{-3}) [159].

The secondary copper-chalcogenide phases are of particular importance during the growth of the absorber and this is typically taken advantage of in the multistage co-evaporation process. The success of the early-stage BOEING recipe was based on the recognition that single-layer absorbers do not result in optimum cell performances. In this approach a bilayer deposition process was implemented, consisting of a Cu-poor layer deposited on top of a Cu-rich layer, but with an overall Cu-poor composition [197]. This implies that the top layer inherits the preferred orientation and will also grow in the form of large crystallites. Moreover a compositional equilibrium reaction takes place during the process and results in removal of the secondary phases from the bottom layer. The growth model proposed by Klenk *et al.* suggests the presence of a low temperature liquid Cu-Se phase aiding the growth of the CIGS grains by the means of a vapour-liquid-solid mechanism (VLS) [195]. In this mechanism the vapour species condense at the surface of the liquid binary phase covering the grains. They are then transferred to the interface between the binary/CIGS phases where the crystallites are growing.

To follow the success of the BOEING bilayer approach, subsequently implemented by several other groups, single-layer and bilayer solution-processed CIGS absorbers of various Cu compositions were prepared and studied. Figure 5.30 presents CIGS single-layer absorber morphologies with CGI ratios from 0.9 to 1.05. As expected, absorbers with stoichiometric or slightly Cu-rich compositions show much larger crystallites at the surface, however there are hexagonal Cu_xSe inclusions sticking out from the GBs and film surface. The absorber is not fully crystalline for any of the

studied Cu compositions. The CIGS grains appear to grow laterally rather than through the film depth, reaching up to 4.5 µm in length for a CGI ≥ 1.0, as opposed to only approximately 1 µm for Cu poor compositions. The large grains go only approximately 0.5 µm down into the absorber. The single-layer CIGS approach is therefore not compatible with obtaining a large-grained CIGS morphology as the presence of Cu_xSe phases would result in shunting of the devices.

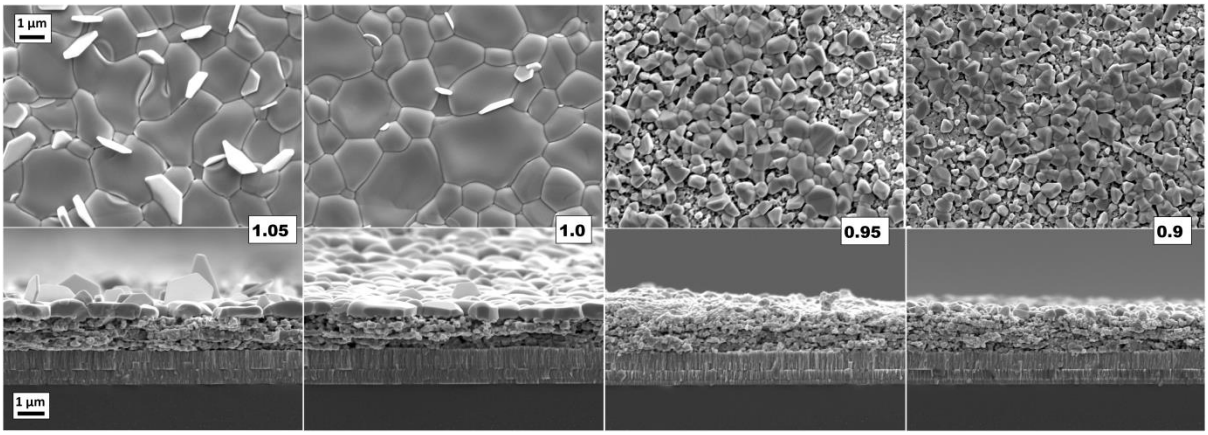

Figure 5.30 SEM images of CIGS films with varied CGI ratio from 0.9 to 1.05.

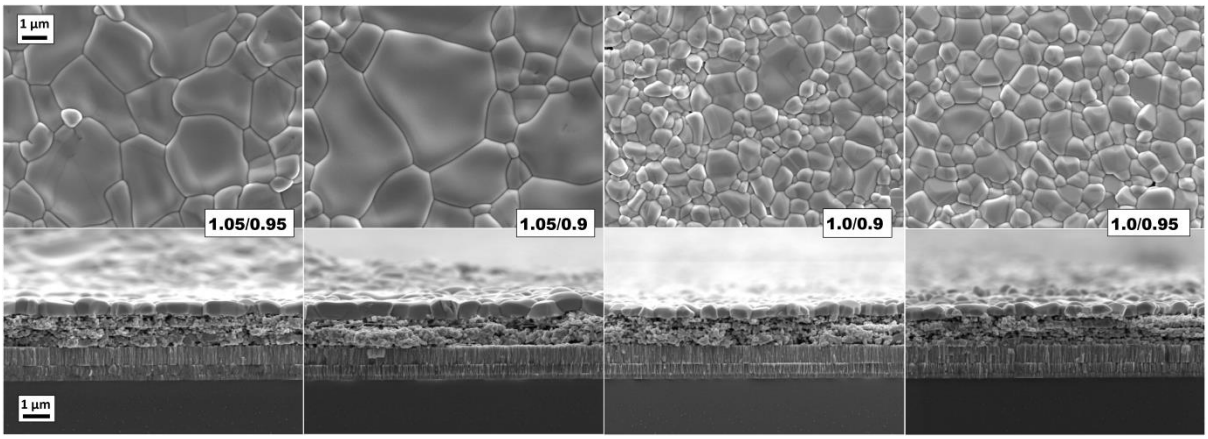

Figure 5.31 SEM images of CIGS films formed of double-layers with different CGI ratio for the top and bottom layers (Cu-rich back and Cu-poor top).

Figure 5.31 shows the SEM absorber morphologies when the absorber was deposited in the form of a Cu-rich/Cu-poor bilayer. Various compositions for the top and bottom layer were compared. The surface images show that the CIGS grains are laterally largest when the bottom layer had the composition of CGI = 1.05, with grains larger than for a single-layer of this composition. In addition, no Cu_xSe phases are present at the surface of any of these bilayer absorbers. As for the single-layers, the porous fine-grain bottom layer wasn't eliminated and was approximately of the

same thickness for all compared compositions. Therefore full absorber recrystallisation was not achieved by varying the Cu composition throughout the absorber. On the other hand, the absorber surface is very flat providing good coverage and likely be beneficial for junction formation.

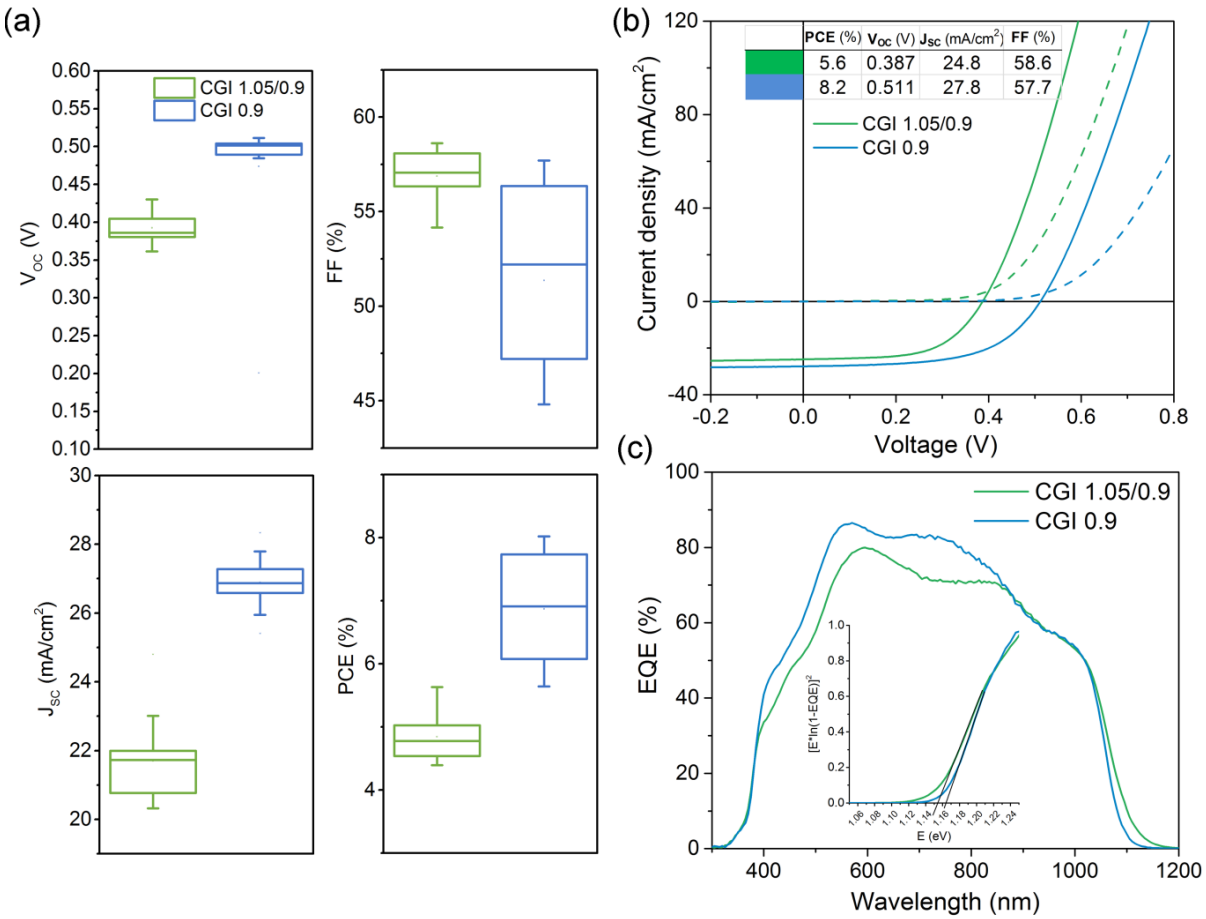

Figure 5.32 Box plots containing 13 cells for each sample (a), J-V (b) and EQE curves (c) of the best cell from the double CGI layer (1.05/0.9) and single CGI layer (0.9).

The device performance of the single-layer and bilayer absorbers was compared by performing J-V and EQE measurements. Here the single-layer absorber had CGI ratio of 0.9 and the bilayer a ratio of 1.05/0.9. The bilayer absorber was prepared by spraying two times three layers of solutions with different Cu compositions. Both absorbers were selenised identically, using selenisation profile (3) in Figure 5.22 with a 30 min intermediate dwell step at 300°C before ramping to 550°C at 25°C/min and 50 min selenisation in the presence of 600 mg of Se. This profile gave the second best performance during the RTP optimisation and didn't compromise the back contact quality by excessive $MoSe_2$ formation. Figure 5.32 a-b) shows the box plots of PV parameters and J-V curves of a representative device for both compositions.

Despite the promising absorber morphology from the bilayer approach, the performance is drastically lower than that of the single-layer. The presence of larger CIGS grains and resulting better absorber crystal quality did not lead to the expected improvement in device J_{SC}; rather the J_{SC} reduced on average by 6 mA/cm^2. Similarly the V_{OC} is lower by 100 mV on average. Figure 5.32 c) shows a lower EQE signal at all wavelengths. The extracted bandgap from a plot of [ln(1-EQE)*E]^2 in the inset shows a bandgap shift in the two samples. The single-layer CIGS solar cell with CGI of 0.9 has a bandgap of 1.165 eV, whereas the bandgap of the double-layer absorber with CGI 1.05/0.9 is lower, at 1.155 eV. The reason for the small bandgap shift is not known, but may be related to compositional changes in the absorber.

The relatively low double-layer device performance is probably a consequence of the modified absorber composition rather than crystal quality. The CIGS process window with respect to Cu composition is astonishingly large, especially if the samples contain sodium. The presence of Na in the absorber widens the range over which the chalcopyrite α phase can exist towards more Cu-poor compositions [41]. CGI ratios in the range of 0.56-0.92 can be tolerated under these conditions [159]. The compositional analysis of the samples was performed using EDX at a low acceleration voltage (5 keV) to minimise the interaction volume. Elemental quantification was performed by mapping two rectangular areas on the SEM cross-section corresponding to the fine-grained layer at the bottom and coarse-grained layer at absorber surface. The elemental composition of these layers as well as of the entire absorber are summarised in Table 5.7.

Table 5.7 Compositional analysis of the double- and single-layer absorbers through their cross-sections using EDX

	Double-layer *Intended CGI = 1.05/0.9*			**Single-layer** *Intended CGI = 0.9*		
	Fine-grain	*Large-grain*	*Whole*	*Fine-grain*	*Large-grain*	*Whole*
Se	50.7	43.2	52.3	48.2	39.5	48.4
In	18.6	26.3	19.2	22.9	30.8	24.4
Cu	25.0	25.5	23.9	23.4	24.5	22.1
Ga	5.7	5.0	4.6	5.5	5.2	5.1
CGI	1.02	0.817	1.0	0.824	0.68	0.748
GGI	0.235	0.16	0.194	0.193	0.144	0.174

For both single- and double-layer absorbers it can be observed that the large-grained surface layer is largely indium rich and selenium poor relative to the absorber as a whole. The same trend is also observed for both absorbers in terms of Cu and Ga compositions, accounting for the slightly Cu-rich and Ga-poor large-grained layer. This compositional variation through the depth of the absorbers results in CGI and GGI grading with overall lower CGI and GGI near the absorber surface. The GGI ratio is overall substantially below the intended 0.3 however. As explained previously, Ga loss from the absorber is possible through the formation of Ga oxides. Quantification by EDX in SEM also has to be regarded critically and used mostly as a comparative tool between samples. Despite the Cu-poor surface, the overall composition of the double-layer absorber is stoichiometric which is probably the cause of the electrical losses, most likely due to a high doping density [159]. High absorber doping density results in a narrow depletion width, which negatively affects device J_{SC} and V_{OC}. The double-layer absorber processing is a promising path; however it requires adjustment of the Cu and Ga quantities in the two layers to obtain an acceptable compositional profile.

5.6 Conclusions

In this chapter, the selenisation process for solution-based CIGS absorbers was developed and optimised. Various selenisation approaches were compared using a two-zone tube furnace. A 12% efficient CIGS solar cell was achieved by selenisation of the amine/thiol-processed absorbers in one zone of the tube furnace inside an uncoated partially closed graphite box. Due to low repeatability of the process, this selenisation approach was substituted with RTP selenisation using a SiC-coated graphite box. This approach provides better process uniformity due to the controllability of the amount of Se and elimination of impurities introduced into the film. Moreover the RTP, having smaller volume with no exposed tube ends, results in higher Se partial pressures during the process. Despite the careful optimisation of the selenisation in the RTP, the device performances are lagging behind those obtained previously using the tube furnace. It is thought that unintentional alkali doping of the absorber might be responsible for better performances achieved previously. Highly volatile Na-Se has most likely accumulated in the uncoated box through intercalation in the graphite over a period of time and has been re-

evaporated in the following runs. This would explain the improved electronic properties whilst having a lower crystal quality absorber material.

Finally, the absorber composition was evaluated after an intentional Cu variation was introduced through the absorber depth. It was found that a Cu-rich/Cu-poor bilayer results in improved absorber morphologies without the presence of secondary phases as compared to single-layer absorbers. Despite the large lateral grain growth and smooth, dense surfaces, the performance of devices constructed using the bilayer absorbers was substantially lower than that of single-layer cells, with losses in both V_{OC} and J_{SC}. The limited performances of these bilayer cells were attributed to a high Cu content relative to In and Ga, as the film was found to be stoichiometric rather than Cu-poor. The coarse-grained and fine-grained layers presented very different compositions in both types of samples according to the EDX. Understanding the compositional grading in the final absorber can help in further adjustment of the precursor compositions in order to achieve device performance improvement.

CHAPTER 6

Alkaline doping of CIGS absorbers from a NaCl source

6.1 Scope

Poor crystallinity, rough surfaces and the presence of voids are the main drawbacks of solution processed CIGS absorbers [32]. A large number of grain boundaries acting as recombination centres are responsible for low V_{OC}. Therefore, control of grain growth is key to further improve solar cell efficiencies. Enhanced grain growth can be achieved through optimisation of selenisation conditions, or by creating liquid copper-rich selenide phases acting as fluxing agents [75][195][198]. An alternative option is to use impurity elements such as Na, Sb, K, Li, Cs and Rb to promote crystallisation [153][199][200][201]. The presence of alkaline elements, especially sodium, is generally recognised as indispensable for high efficiency CIGS solar cells. Sodium is the most commonly studied alkaline element due to its presence in SLG, a common substrate for CIGS, from which it diffuses into the CIGS absorber layer during growth [117]. Sodium was found to have beneficial effects on the opto-electronic properties of CIGS devices. It can also substantially improve the reactive selenisation of solution-based absorbers, resulting in improved grain growth [154]. However, precise control of the sodium quantity in the absorber is necessary in order to achieve the optimum doping level for enhanced device performance.

This chapter studies possible approaches of Na incorporation into the solution-based CIGS absorber. The motivation of experimental work detailed in this chapter was to achieve a controlled grain growth of the solution-processed CIGS absorber, leading to further efficiency improvements.

6.2 Effects of alkali metals on CIGS material and electrical properties

6.2.1 Na effects

In 1993, Hedstrom *et al*. were the first to notice the importance of Na on electrical properties and absorber morphology of CIGS solar cells by comparing devices constructed on SLG and borosilicate glass [194]. Holz *et al.* demonstrated that Na can be supplied not only from the substrates but also externally, and that the concentration of Na atoms in the absorber is crucial [202]. The typical optimum concentration of Na in CIGS is believed to be only ~0.1 at% [203]. It is widely accepted that the beneficial effects of sodium include:

- enlargement of grain size [121][204][205] ,
- a strong dominant (112) crystal orientation [121][194][202][205][206],
- increased free carrier concentration and p-type conductivity [207][208][209][210],
- hindering of In/Ga elemental intermixing [43][205][206].

Sometimes contradictory findings are reported, especially regarding the absorber morphology and preferentially oriented growth [115]. The Na effects are strongly dependent on the CIGS growth process and method of Na incorporation. CIGS is a largely intrinsically doped material and the material growth method itself greatly influences the electrical and morphological properties of the absorber [115]. The exact physical mechanism of how sodium increases the p-type conductivity of the absorber is still highly debated [211]. Sodium is often found to accumulate at surfaces and grain boundaries [153][212]. However, atom-probe tomography measurements have revealed a small amount of Na present in CIGS grain interiors as well [213]. Even a dilute Na concentration in the bulk may modify the overall electronic properties of the material, since improved p-type doping was also reported from single-crystal epitaxial CIGS films doped with Na [207]. Finally, the influence of Na on $MoSe_2$ formation and its affinity with oxidised compounds have also been reported [73][118][153][214][215][216]. The detrimental effects caused by excess Na have been less extensively explored than the beneficial effects. Speculation includes the elimination of V_{Cu} acceptor states, the formation of competing phases, and the creation of additional recombination centres leading to overall degradation of device performance [160][217].

6.2.2 Possible mechanism of Na action

The mechanism of how Na affects CIGS p-type conductivity through various point defects has been a subject of intense discussion with no clear consensus. A variety of scenarios have been presented with the conclusion that Na influences the material in multiple ways [159]. Na behaviour in the bulk should be understood before studying its effect on the more complicated GBs. The incorporation of Na into the CIGS lattice creates point defects which can either be substitutional or interstitial. Na was found to go preferentially onto vacant copper sites (V_{Cu}), since Na_{Cu} has the lowest formation energy among the considered point defects. Substituting Cu with a single Na atom does not change the valency of the site; however, Na_{Cu} is charge-neutral and electrically passive, hence does not change the doping of the material [211][217]. Na can enter various sites in the chalcopyrite lattice as interstitial Na_i; however, this has a much higher formation energy than Na_{Cu}. Therefore under copper poor conditions, Na_i would be transferred to a vacant copper site. In any case, neither of these sites create deep states in the bandgap [211].

It has been suggested that Na could populate not only vacant Cu sites, but also those occupied by In [217]. Replacing donor-type In_{Cu} antisites with electrically passive Na_{Cu} defects would decrease charge compensation. However, this is not favourable due to In_{Cu} stability and formation kinetics, therefore their overall concentration in the material is unlikely to be affected by Na [218]. Na occupying the In (or Ga) sites, creating an acceptor-type defect has also been suggested [203]; however, Na_{In} is not among the energetically preferred defects according to density functional theory (DFT). Therefore its concentration would also remain negligible [211].

As there is no direct evidence of how Na-related point defects change the p-type conductivity of the CIGS material, Oikkonen *et al.* suggest a mechanism, where Na influences the doping in a more indirect way: by modifying the point defect mobility. Charge neutral and electrically passive Na_{Cu} defects can capture copper vacancies to form Na_{Cu}-V_{Cu} complex and consequently hinder the Cu migration in the material. The reduced amount of available V_{Cu} will in turn also affect the defect cluster formation and distribution in the material, such as In_{Cu}-$2V_{Cu}$ and V_{Se}-V_{Cu} [211].

It has been suggested that the majority of Na resides at grain boundaries, with Na passivating GB defects [219]. It was found by numerical modelling that potential

barriers at grain boundaries decreased with addition of Na resulting in an increase of hole concentration. It was attributed to the removal of donor interface states located at GBs. The resulting degree of change in hole concentration however depends on the interface state density, energy position, net acceptor concentration in the bulk and the grain size [220]. If the GBs are in addition positively charged, the downward band bending attracts electrons to the GB and these then recombine. Neutralising these traps by Na can improve the cell efficiency significantly [219]. The primary electrically active defect at GBs is the selenium vacancy (V_{Se}). A model was proposed by Kronik *et al*., where Na catalyses the oxygenation of this defect to form electrically neutral O_{Se}. [221]. However, the Na incorporation reversibility observed by Forest *et al.* disagrees with this hypothesis, suggesting that removing O from GBs to reform V_{Se} is thermodynamically unfavourable as O forms a very stable bond with In and Ga. Instead, they favour a mechanism involving the formation of Na_{Cu} by replacing In_{Cu} defects. The high solubility of Na compounds would allow for reversibility of this mechanism [222].

The mechanism of sodium action on the CIGS grain growth was also studied in the literature. Sodium is believed to influence the CIGS grain growth by its interaction with Se during the selenisation process due to high affinity between these two elements [153]. Sutter-Fella *et al*. proposed a Na_2Se_x mediated mechanism to explain the massive grain growth in the presence of sodium they observed in CZTS devices with an evaporated layer of NaF. This starts with chemisorption of Se vapours at the surface of the NaF layer, followed by the formation of liquid polyselenide phases at the precursor surface and finally crystallisation of the absorber by reaction of the reactive Se supplied by Na_2Se_x with the metal containing precursor [154]. Na_2Se_x has a higher sticking coefficient than Se_x, therefore making Se more reactive during the selenisation process [153]. Hergert *et al.* and Braunger *et al.* also consider the formation of sodium polyselenide phases exhibiting a surface and GBs intermediary catalytic behaviour during selenisation [153][223].

Gas-phase alkali doping is also possible, but so far is very little understood about the mechanism involved. It was concluded that alkali gas-phase transport occurs via a number of routes and can be responsible for accidental alkali metal doping during the growth of the semiconductor. The phenomenon of gas-phase doping was first observed by Wieting *et al.* during reactive batch annealing of CIGSe at Shell Solar.

They observed performance improvement of the batch where the CIGS active layer was facing the SLG substrate of another batch. The performance improvement was attributed to increased content of Na in the CIGS layer achieved by formation of Na_2Se after reaction with H_2Se [224]. Colombara *et al*. have shown that alkali-phase doping influences the opto-electronic properties of the CIGS in the same way as other solid-state doping routes. The mechanism proposed originates from the direct alkali source evaporation, alkali monochalcogenide formation and consequent evaporation and releasing of neutral alkali atoms. Alternatively, the monochalcogenide can react with excess chalcogen to form more volatile polychalcogenides [43].

6.2.3 Na incorporation methods

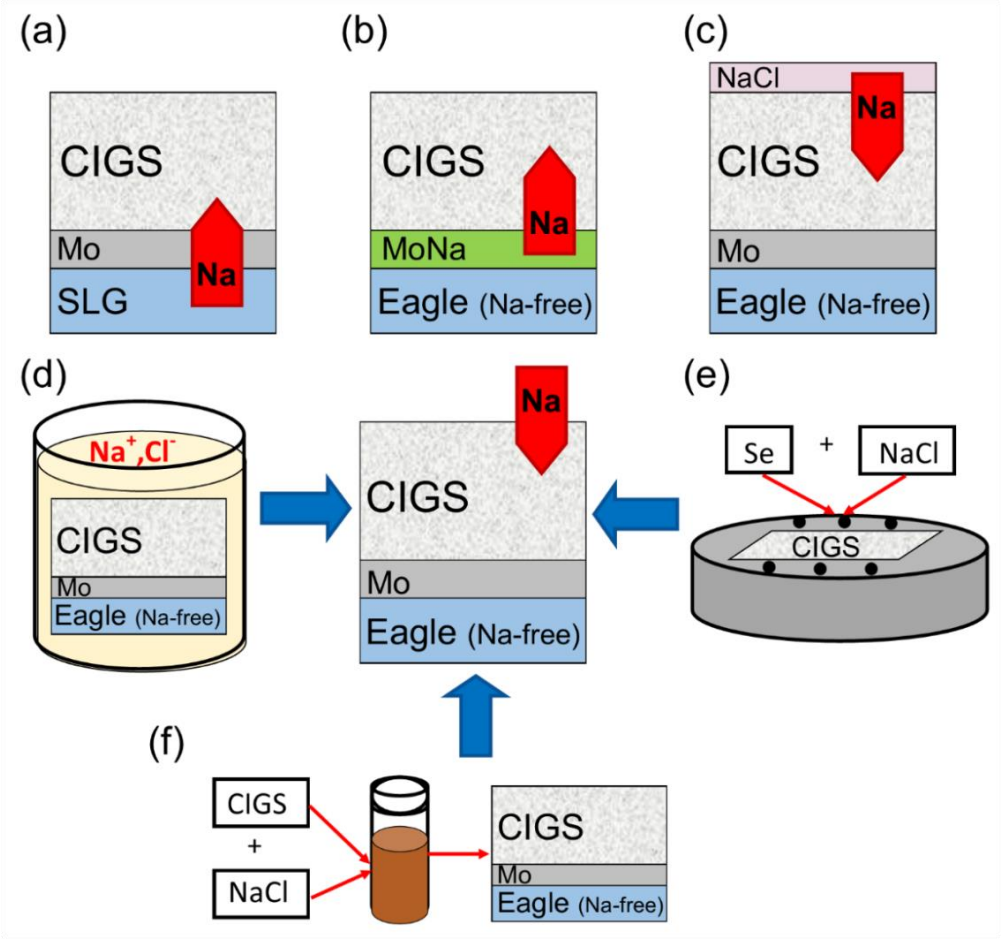

Figure 6.1 Schematic representation of different Na incorporation methods into CIGS absorber: diffusion from SLG substrate (a), diffusion from a Na-doped Mo layer (b), post-deposition diffusion from thermally evaporated NaCl layer (c), absorber soaking in NaCl aqueous solution (d), introduction of NaCl in the gas-phase by mixing NaCl and elemental Se in the selenisation graphite box (e) and addition of NaCl into the precursor solution (f).

Sodium can be supplied before, during or after CIGS growth. Various Na doping approaches are illustrated in Figure 6.1. The most common method of Na incorporation into the CIGS absorber is by out-diffusion from the SLG substrate during a high-temperature annealing [117]. The control over the amount of Na diffusing is difficult: the substrates are never identical; it's strongly dependent on the Mo properties; and it would require exact reproducibility of the substrate temperature during the selenisation step [115][119][225]. Despite this fact, most of the world record CIGS devices were achieved using SLG as a substrate. In order to achieve better control over Na diffusion, an alternative approach involves incorporating Na directly into the Mo layer (MoNa). It was most commonly achieved by sputtering from a Na doped Mo target. These targets are prepared by mixing sodium molybdate (Na_2MoO_x) with Mo powder with typical Na concentration of 2-15 at% [115]. The advantage of this method is that it doesn't require an additional processing step, or extra costs other than any price difference between the Mo and MoNa targets. Mansfield *et al.* demonstrated 16.6% CIGS devices using a 10 at% MoNa target; however, this was still worse than using SLG [226]. The main limitation of this approach was the difficulty of releasing the correct amount of Na to the CIGS layer, as it is strongly influenced by the microstructure of the MoNa layers [227].

The most widely used method of external Na incorporation is by means of thermal evaporation. In this approach, Na can be introduced from various sources including elemental Na, Na_2Se, Na_2S, NaF, NaCl; before, during or after CIGS absorber growth [206][228][229][230][231]. The choice of the Na precursor to be evaporated requires consideration of its toxicity, vapour pressure, the temperature necessary for evaporation and side effects of elements other than Na introduced into CIGS [115]. NaF is the most common choice due to its lower toxicity than Na_2S and Na_2Se, and its higher stability than elemental Na. Another advantage is that it evaporates congruently allowing for better control over the amount of Na, and there is no evidence of negative effects from the fluorine, making this method capable of competing with the well-established SLG route [232]. It was found that evaporation of as little as 10-20 nm of NaF onto the Mo typically provided a sufficient amount of Na for the CIGS absorber [121][233]. Alternatively, Na can also be incorporated after the CIGS growth, through a post-deposition treatment (PDT). This method consists of NaF evaporation after the 3-stage growth of CIGS. This was developed by EMPA for

their low temperature process on polyimide foils [234]. In this approach, a 20-40 nm NaF layer is evaporated onto the finished CIGS absorber at less than 100°C, after which the substrate is heated to 400°C and held there for several minutes to allow the Na to diffuse. The PDT doesn't modify the microstructural properties of the absorber, it only enhances the electrical performance of the devices [235].

These Na incorporation strategies are typically employed in combination with vacuum-based CIGS absorbers [206][226][233]. Sutter-Fella *et al.* have employed NaF evaporation on the top of the solution-processed CZTS absorbers right before the selenisation step [154]. In the same publication, they prove the concept of the beneficial effects of Na on CZTS device properties by spin-coating NaCl on the top of the precursor. Spin-coating of NaCl yielded device performance not far below the device with the optimum NaF thickness. NaCl has been used as precursor for solution-processed CIGS and CZTS solar cells due to its low cost, low-toxicity and high solubility in a number of common solvents including water. Berner *et al.* compared the effects of three different Na salts: NaCl, $NaHCO_2$ and NaSCN on the solution-processed CIGS absorber morphology and cell performance. These Na salts were incorporated directly into the precursor solutions. The devices formed from these solutions performed similarly except for $NaHCO_2$, which was worse. The formate anion in $NaHCO_2$ caused Ga oxidisation and consequently lower Ga incorporation in the final CIGS absorber. After optimisation, 13.3% CIGSe device efficiency was achieved with the addition of 2.5 at% of NaCl [58]. Wang *et al.* used simple dipping of the absorber films into NaCl aqueous solutions for several minutes prior to selenisation. This also resulted in enhanced morphological and electronic properties of the solution-based CIGS solar cells [236]. The gas-phase alkali doping was studied by Colombara *et al.* where the solution-based CIGS precursors were selenised with a mixture of elemental selenium and NaCl [43]. The gas-phase doping strategy has an advantage over the solid-state PDT in that it does not require any additional processing step.

In this work, NaCl was chosen as the Na source because of its low cost, benign nature, high solubility and ease of thermal evaporation. Different doping strategies might result in different effects on absorber morphology and device performance, since the nature of the CIGS precursor material plays an equally important role. Moreover, the ease of execution of various Na doping strategies might vary

depending on the equipment and conditions. Consequently several doping methods were applied to improve the properties of the CIGS cells studied in this work. The CIGS absorbers and solar cells were characterised by various techniques to find the most efficient doping approach. However none of the characterisation techniques used in this chapter allowed for any Na quantification in the films.

6.3 Thermal evaporation of NaCl

Following the success of the NaF post-deposition evaporation doping strategy in vacuum-based as well as solution-based CIGS and CZTS solar cells, the first doping approach studied here was by means of thermal evaporation. This doping strategy is illustrated in Figure 6.1 c). In this experiment, NaCl was thermally evaporated onto the as-deposited CIGS absorber inside the same bell-jar evaporator as used for Ag contacts. The evaporation was performed at a base pressure below $3x10^{-6}$ Torr, applying current of 60 A to a tungsten boat containing NaCl. The substrates were placed directly above the source at distance of 15 cm. NaCl layers of different thicknesses ranging between 15 and 150 nm were evaporated onto the CIGS substrate, as shown in Figure 6.2. Layer thickness during the evaporation was controlled using a quartz crystal microbalance.

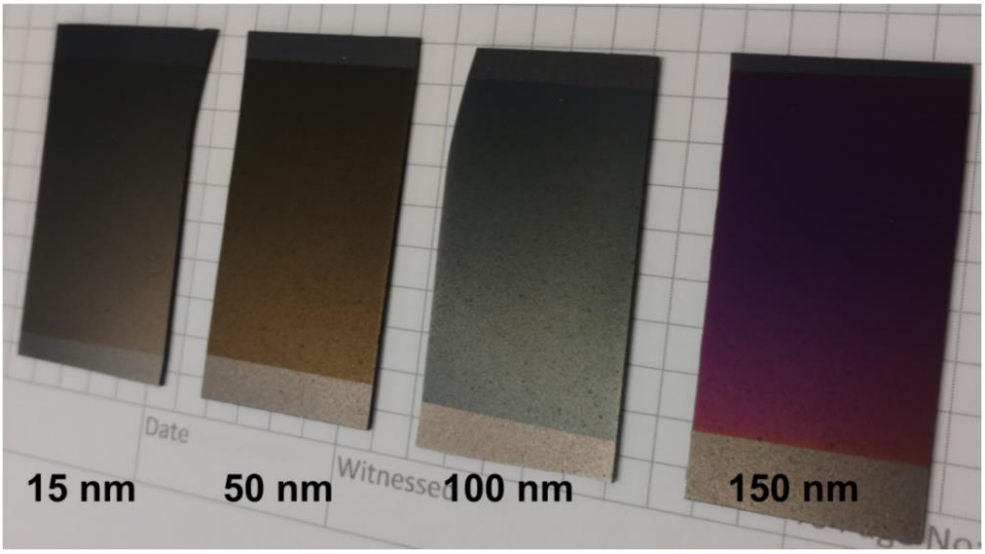

Figure 6.2 Photograph of the CIGS absorber films with thermally evaporated layer of NaCl thick 15-150 nm directly prior the selenisation. The top and bottom parts of each slide have not been coated by NaCl as these have been shaded by the sample holder.

The absorbers were subsequently annealed in a closed SiC-coated graphite box at 550ºC and 200 Torr for 70 min in a selenium atmosphere (900 mg Se) using the RTP.

These conditions were previously found to result in the best absorber crystallisation when deposited on SLG (see Chapter 5). To avoid the cumulative effects of external Na-doping and Na diffusion from SLG substrate, all the CIGS devices were made on alkali-free glass substrate (Corning Eagle XG). In addition, accidental Na-doping might occur by gas-phase transfer from the Na-containing Se residuals accumulated in the annealing apparatus over multiple runs, as emphasized by Colombara *et al.* To minimise any 'accidental' Na-doping, the RTP oven and the graphite box were cleaned by high temperature and low pressure annealing under flowing nitrogen and mechanical scrubbing of the quartz annealing tube to remove residual selenium between each run. CIGS absorbers were prepared with an intended base-line composition ($Cu_{0.9}In_{0.7}Ga_{0.3}(S,Se)_2$) by spray-coating in 6 layers, as described in Chapter 2.

6.3.1 Morphology and composition

Figure 6.3 shows the SEM cross-section and surface images of the CIGS absorbers after being selenised in the presence of the evaporated NaCl layer. The enlarging effect of the intentional Na-doping on the absorber microstructure is evident. Annealing of the CIGS precursor without any NaCl (0 nm NaCl) in the presence of elemental Se vapours resulted in a poorly crystallised, highly porous CIGS absorber. Slightly larger grains on the surface of the absorber are observed with only 15 nm of NaCl being evaporated, however the grain growth improved remarkably with 30 and 50 nm of NaCl. Here, some grains extend to the full absorber thickness, which had never been observed for these absorbers when the Na source was SLG. When thicker NaCl layers were evaporated (100 and 150 nm), the absorber grain size started to decrease slightly. The NaCl layer is still present at the end of the selenisation for these two samples and is clearly visible on the surface SEM of the 150 nm NaCl absorber. EDX surface mapping was performed and confirms the presence of 9.2 at% and 19.4 at% of Cl for 100 nm and 150 nm NaCl-coated absorbers respectively, whereas no Cl was detected for any other sample. Table 6.1 summarises EDX elemental composition of selenised CIGS absorbers and calculated final CGI and GGI ratios for all the films.

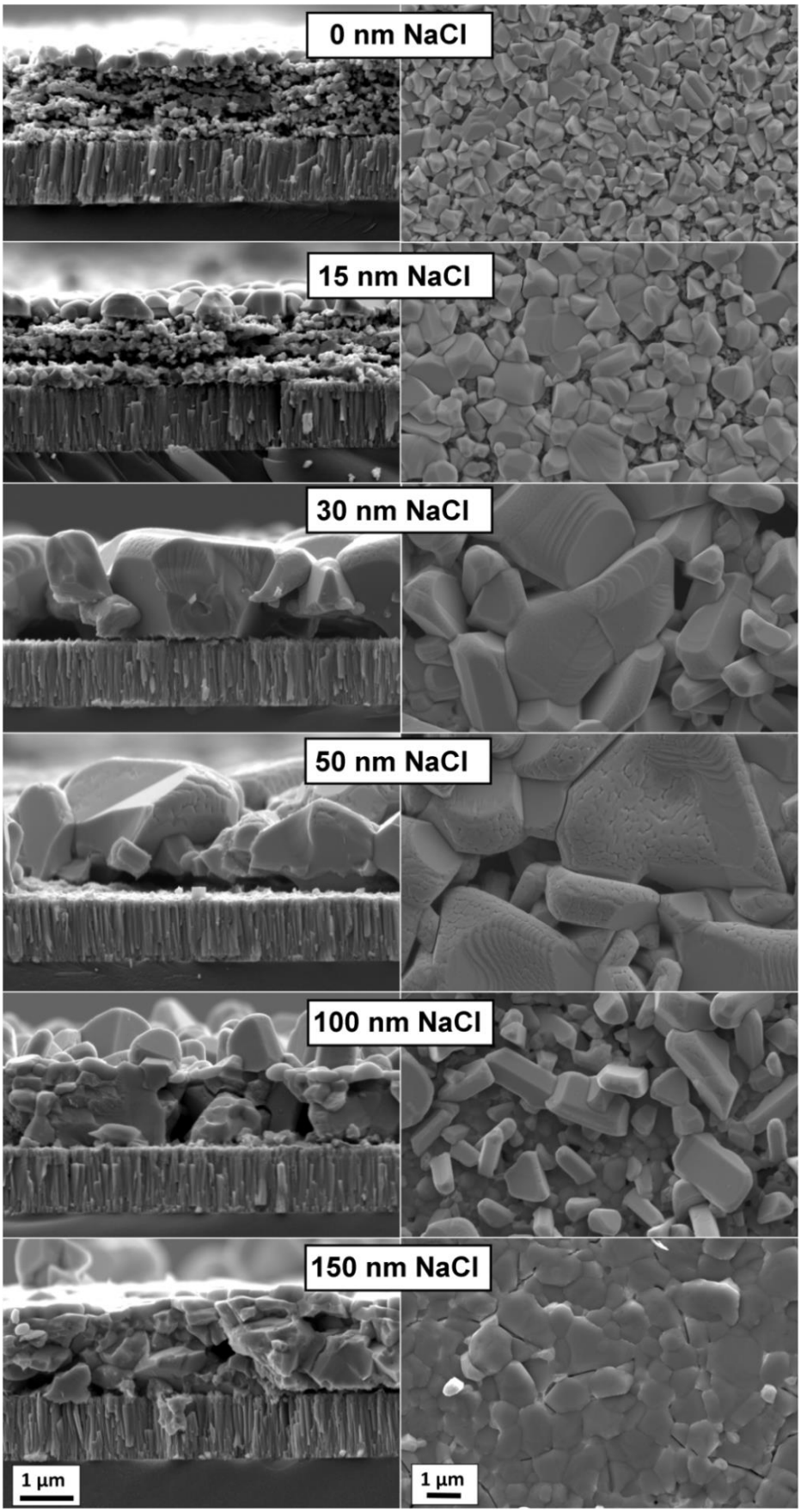

Figure 6.3 SEM surface and cross-section images of the selenised CIGS absorbers processed with evaporated NaCl layer with various thicknesses.

Table 6.1 EDX elemental composition after selenisation of the CIGS absorbers with evaporated NaCl layer with various thicknesses

At%	Cu	In	Ga	Se	Cl	CGI	GGI
0 nm	22.5	17.5	7.0	53.0	0	0.914	0.284
15 nm	19.6	19.0	5.9	55.5	0	0.791	0.237
30 nm	20.5	18.5	6.1	54.9	0	0.831	0.248
50 nm	20.4	18.6	6.0	55.0	0	0.827	0.243
100 nm	19.0	17.1	5.7	49.0	9.2	0.836	0.249
150 nm	16.5	15.8	4.9	43.4	19.4	0.794	0.238

The morphological observations from the SEM images are in agreement with the XRD patterns of the films presented in Figure 6.4. The peak found at 2θ ~31.7º in 100 and 150 nm NaCl samples corresponds to the NaCl (200) XRD reflection. This peak is not present in any other film confirming SEM and EDX observations. The other visible peaks correspond to the diffraction patterns of Mo, Mo-N and CIGS. CIGS has a preferred orientation along the (112) plane of the tetragonal phase and there is no change in dominant crystal orientation when varying the NaCl thickness. The FWHM of the dominant CIGS (112) peak was obtained using a peak fitting routine and is summarised Figure 6.4.

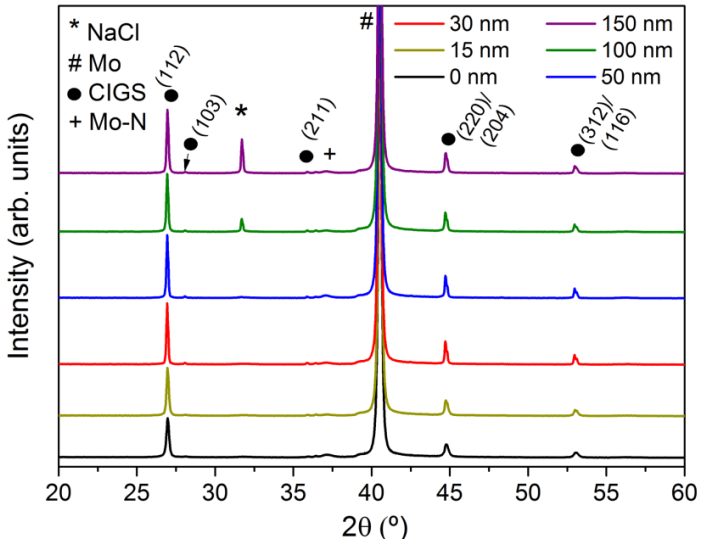

	FWHM CIGS (112) (°)
0 nm	0.219
15 nm	0.184
30 nm	0.142
50 nm	0.144
100 nm	0.151
150 nm	0.154

Figure 6.4 XRD patterns of the selenised CIGS + NaCl films and table summarising the FWHM of the dominant CIGS (112) peak.

The FWHM is the highest for the NaCl-free sample and the lowest for the 30 nm NaCl-containing sample. A lower FWHM (narrowest peak) is indicative of improved crystalline quality and consequently larger grain sizes. The crystalline quality decreases slightly when too much NaCl (≥ 50 nm) was added. Hence, the XRD

measurement is consistent with the SEM images of the CIGS crystals showing the smallest grains for 0 nm NaCl and largest for 30 and 50 nm of NaCl. The presence of residual NaCl phases are thought to be responsible for the lower crystallinity of the absorber, providing a partial shielding effect to the Se vapours and preventing them from coming into contact with the CIGS absorber. However other factors such as compositional changes can also be play a part and have yet to be fully investigated. Several groups have also previously observed a decrease in grain size upon addition of Na [237][81]. Finally, partial delamination was observed for absorbers with 30 and 50 nm NaCl, the absorbers with the largest grains. The delamination of the absorber films with the largest grains was also reported by Sutter-Fella *et al.* where NaF layers of various thickness were evaporated onto CZTS absorbers [154].

6.3.2 PV performance

To study the effect of the NaCl layer on CIGS solar cell performance, the above presented absorber films were made into CIGS devices. The PV performance indicators are summarised in Figure 6.5. In this study, the optimum NaCl thickness for the best device performance was 15 nm. Adding only 15 nm of NaCl substantially improved the V_{OC} and FF by on average 100 mV and 11% respectively. The increase in V_{OC} and FF are typically observed consequences of Na-doping of the CIGS absorbers. Moreover, the optimum thickness of evaporated NaCl of 15 nm is in the range of thicknesses typically used for the evaporation of NaF for high efficiency vacuum-based CIGS solar cells. The increase in J_{SC} with the addition of 15 nm of NaCl from an average of 18 to 26 mA/cm^2 can be attributed to the enhanced grain growth. However the optimum NaCl thickness for the device performance is below the optimum for the CIGS absorber crystallisation at 30 nm. This sample also had the highest J_{SC} among the samples, approximately 29 mA/cm^2 on average. This is also consistent with the smallest FWHM measured for this sample.

The samples with the largest grains show FF and V_{OC} degradation and consequently do not perform as well as CIGS with only 15 nm of NaCl. These samples also suffer from partial delamination, which might be related to the grain size or the high amount of Na incorporated. Sudden improvement in device performance was observed for the sample with 150 nm NaCl. Here, a visible NaCl layer remained after selenisation on the absorber surface, possibly hindering the extensive grain growth (lower J_{SC},

EQE signal and higher FWHM). The V_{OC} and FF values were high, although not as high as for the 15 nm NaCl sample. This suggests that the Na doping was more beneficial than for the samples with 50 and 100 nm of NaCl. The exact origin of this performance improvement and the role of the remaining NaCl layer in the sample with the 150 nm thick NaCl layer need further investigation. The remaining NaCl was probably washed out during the CdS CBD process.

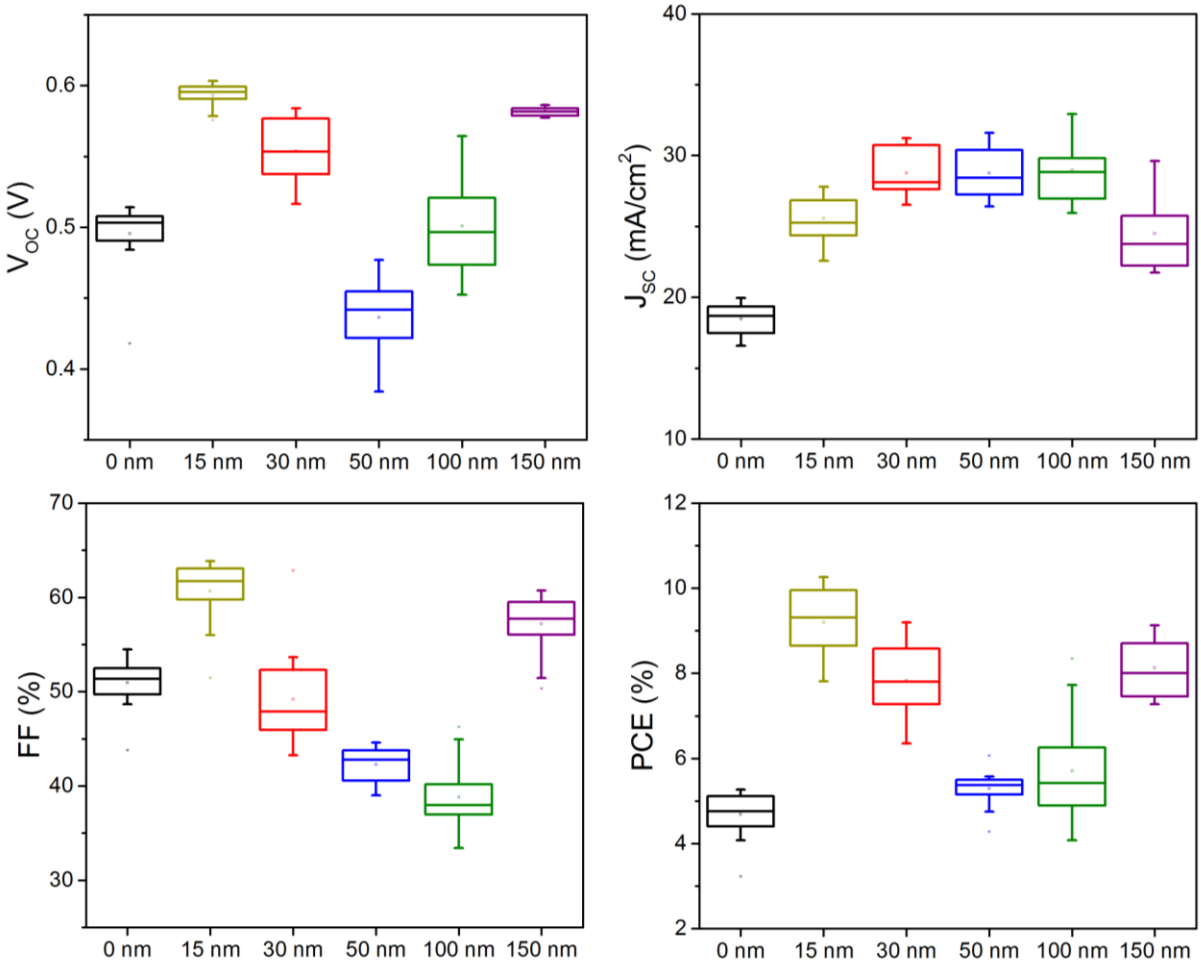

Figure 6.5 Box plots of PV parameters for devices with evaporated NaCl.

Figure 6.6 shows the J-V curves and EQE of a representative device for each NaCl thickness. PV parameters for each curve are summarised in Table 6.2. The bandgap (E_g) was extracted from the peak energy of the derivative of the EQE curves [238]. These bandgap values will be discussed and compared with an alternative bandgap measurement technique in the following sub-section. The EQE curves show improved photocurrent response especially at long wavelengths with the addition of NaCl. The long wavelength decay is the smallest for the samples with the largest grains (NaCl = 30-100 nm), indicating improved carrier collection efficiency. This

might result from reduced GB recombination or longer minority carrier diffusion length. The reduction in GBs due to the increased grain size will almost certainly result in lower GB recombination. Moreover a compositional grading in the absorber created by the lower In/Ga interdiffusion often reported as a consequence of Na doping would create a quasi-electric field increasing the diffusion length of the carriers and enhancing the carrier transfer [239].

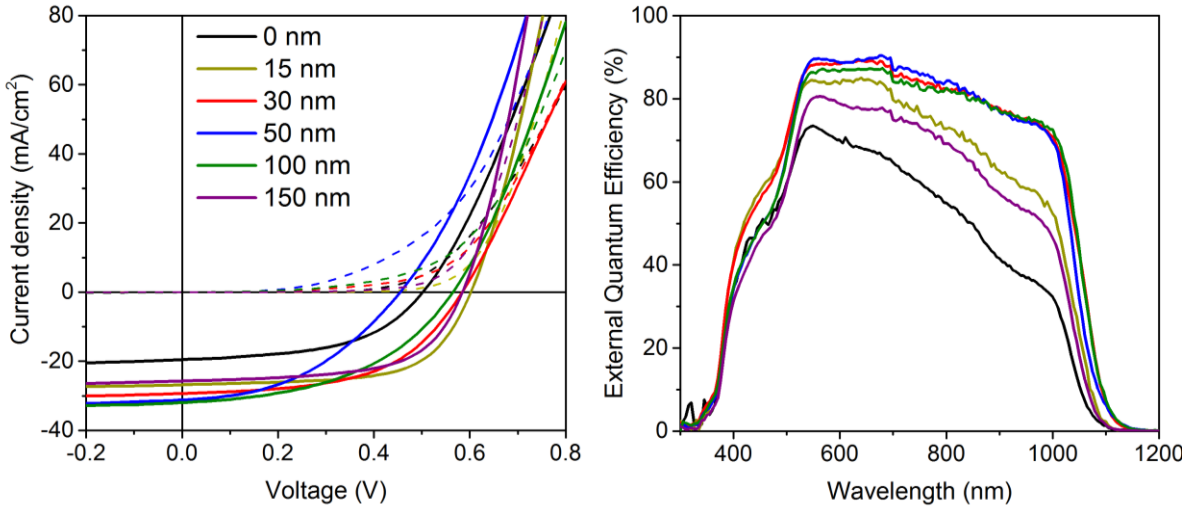

Figure 6.6 Light and dark J-V (left) and EQE (right) of a representative cell for each NaCl layer thickness.

Table 6.2 PV parameters of each J-V curve presented in Figure 6.6

NaCl	PCE (%)	V_{OC} (V)	J_{SC} (mA/cm^2)	FF (%)	R_S (Ω.cm^2)	R_{SH} (Ω.cm^2)	Eg (eV)
0 nm	5.04	0.502	19.6	51.3	1.8	149.3	1.203
15 nm	10.26	0.601	26.8	63.6	0.93	239.5	1.198
30 nm	9.20	0.584	29.4	53.6	2.2	147.0	1.170
50 nm	6.07	0.455	31.2	42.7	1.08	132.0	1.198
100 nm	8.35	0.564	32.0	46.3	1.1	134.5	1.175
150 nm	9.13	0.584	25.7	60.7	0.75	156.3	1.198

6.3.3 Carrier density and lifetime

To better understand the device performance and the role of Na doping, C-V and DLCP measurements at room temperature were performed on these devices. The net acceptor concentration (N_A) was obtained from the minima of the doping profiles shown in Figure 6.7. The C-V measurement and the resulting doping profiles depend on the amount of Na present in the absorber; however it is also affected by the

morphology of the absorbers. The N_A is clearly the lowest for 30 nm of NaCl, ~1x10^{15} cm^{-3}. The highest doping density was measured for the 150 mn NaCl, approximately one order of magnitude higher. The width of the depletion region (*W*) at zero bias was estimated from the C-V measurement and the values are summarised in Table 6.3. *W* at 0 V bias is significantly larger for the 30 nm NaCl sample than for any other studied sample. A larger depletion width improves the long wavelength charge carrier collection, however lower doping density results in a weaker electric field across the SCR.

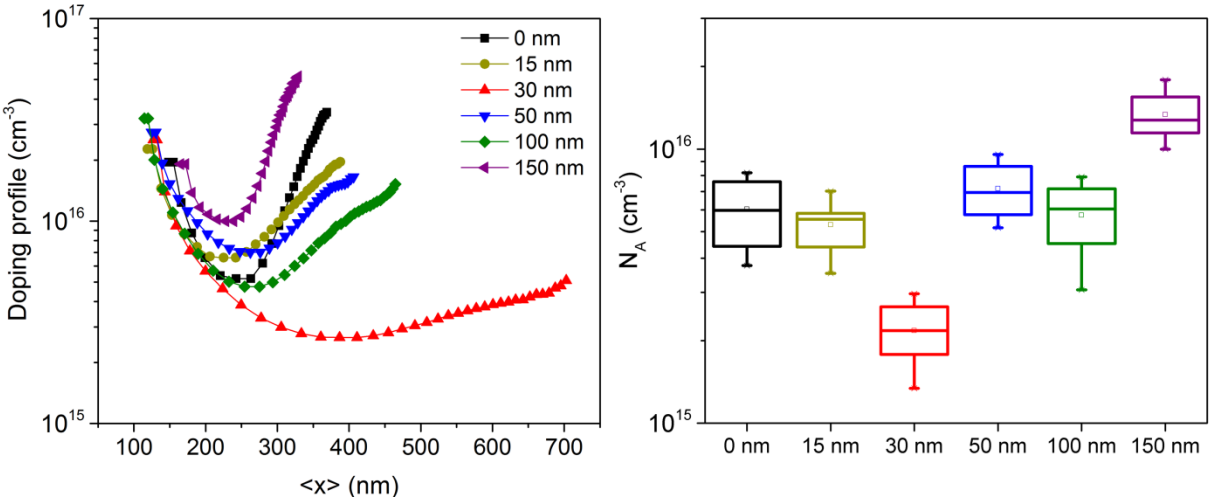

Figure 6.7 Doping profiles of a representative cells and box plots showing the distribution of carrier density from over 10 devices for each NaCl thickness.

As opposed to C-V, the DLCP method is mostly insensitive to the response from interface states. The net acceptor concentrations extracted from these two methods are compared in Figure 6.8. For the undoped and 150 nm NaCl samples, the C-V and DLCP doping profiles are similar, indicating that these two samples are dominated by response from the bulk defect states. For all the other samples DLCP doping profiles are shifted to lower values relative to C-V. For these samples, DLCP is a better method to quantify the net acceptor concentration in the cell, since these cells contain non-negligible interface states [170].

To explain the apparent doping of these morphologically different samples measured using capacitance techniques, some assumptions and speculations must be made. It is suggested that high a concentration of Na accumulates along grain boundaries [235]. Large crystals as seen in the 30 nm NaCl sample cannot host large quantities of Na so it most likely out-diffuses towards the interfaces. Consequently, the sample

with the lowest number of GBs (30 nm NaCl) has the lowest carrier concentration. With thicker NaCl layers, the grains progressively become smaller and at the same time more Na was supplied, hence more Na can be accommodated at the GBs. A similar doping density for the undoped sample and the sample with 15 nm of NaCl may also result from the reduction of the number of GBs in the doped absorber.

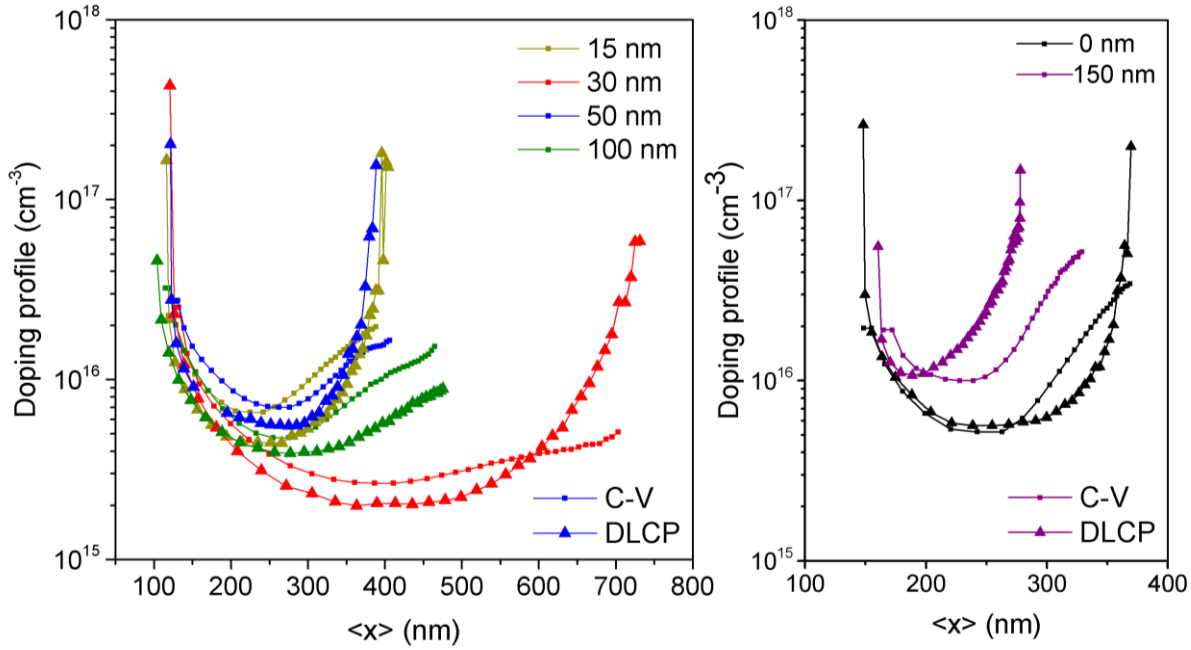

Figure 6.8 Doping profiles extracted from C-V and DLCP measurements at RT. C-V and DLCP minima are shifted (left) and at the same level (right) for these samples.

A study performed by Forest *et al*. regarding the reversibility of the Na incorporation can be used to infer the presence of interface states. In their study, a series of rinse and heat cycles were performed on a Na-doped sample, resulting in the progressive removal of Na from the grain boundaries. Many Na compounds are soluble in water, therefore rinsing the absorber in DI water at 60°C typically removes all the Na salts accumulated at the surface. The heat treatment at 200°C allows oxygen to draw Na from the GBs to the surface, where it is washed out in the next cycle [222]. Although this experiment was not intentionally performed here, the samples are very porous and the CdS bath deposition involves immersing the absorbers in an aqueous solution at 60°C for several minutes before the CdS growth starts. The consequent junction annealing performed in air at 180°C could cause Na to diffuse and create interface states detected by the combination of C-V and DLCP measurements. Whether the NaCl layer in the 150 nm NaCl sample was playing a role in the

protection of the surface or created a smoother and more compact film resulting in lower surface recombination and overall higher doping is unclear.

PL and TRPL measurements were performed and their spectra are displayed in Figure 6.9. PL peaks give another indication of the bandgap of the material. The PL signal from the Na-free sample was so low that it cannot be distinguished from the measurement background noise. PL peaks of all other samples were fitted using a bi-gausian peak fit and the peak position values corresponding to the CIGS bandgap are summarised and compared with the values measured using EQE in Table 6.3. Carrier lifetime was obtained from the TRPL spectra by fitting an exponential decay curve. These values are also shown in Table 6.3.

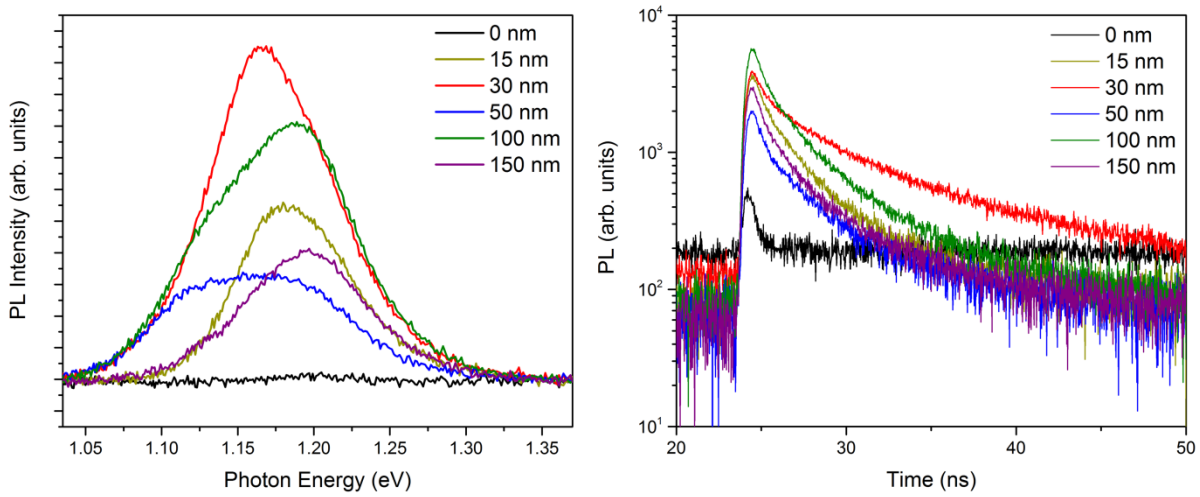

Figure 6.9 Spectrally-resolved PL (left) and TRPL (right) signals of the samples with evaporated NaCl of various thicknesses.

Table 6.3 Summary of the carrier concentration, depletion width, minority carrier lifetime and material bandgap

NaCl	**Eg (EQE)** (eV)	**Eg (PL)** (eV)	τ (ns)	$N_{A(C\text{-}V)}$ ($x10^{15}$ cm^{-3})	$N_{A(DLCP)}$ ($x10^{15}$ cm^{-3})	***W* (at 0V)** (nm)
0 nm	1.203	-	0.50	5.2	5.6	263
15 nm	1.198	1.179	3.48	6.6	4.4	270
30 nm	1.170	1.166	6.04	2.7	2.0	361
50 nm	1.198	1.154	3.93	7.0	5.5	248
100 nm	1.175	1.136/1.187	3.58	4.7	3.9	275
150 nm	1.198	1.139/1.191	3.71	10.0	10.7	266

Carrier lifetime (τ) gives an indication of how fast the minority carriers recombine. τ is therefore directly related to the V_{OC} of the cells. Carrier lifetime is the highest for the 30 nm NaCl sample with largest grains but lowest carrier concentration. Its value, ~6 ns, is almost double the carrier lifetime for the best performing cell from the 15 nm NaCl sample (~3.5 ns). This is due to higher material quality with fewer defects and GBs. Despite the high carrier lifetime and high carrier collection due to large grains in the 30 nm NaCl-doped CIGS, its V_{OC} is lower than that of the 15 nm NaCl sample. The V_{OC} loss is not caused by GB recombination, but its origin is otherwise unknown. Similarly, the sample with the lowest V_{OC} (50 nm NaCl) has large grains and the second highest τ. From the literature, the detrimental effects of an excessive Na incorporation have negative impact on device V_{OC} and FF.

Finally, why the performance of the CIGS solar cells with excessively thick NaCl (> 100 nm) starts to recover owing to a surprising increase in V_{OC} and FF, has yet to be answered. The answer to this question is not evident from any previous characterisation technique or from the literature; however an interesting observation can be made looking at the PL peaks in Figure 6.9. PL signals for 15-50 nm NaCl can be fitted with a single peak, but PL signals corresponding to 100 and 150 nm NaCl are both deformed, fitting two distinct peaks, as shown in Figure 6.10.

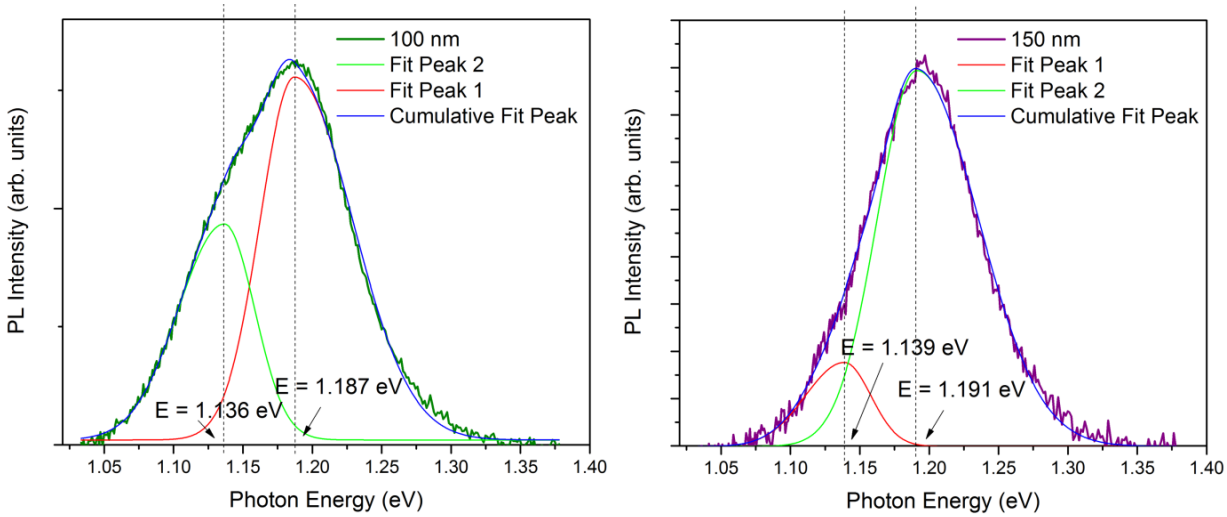

Figure 6.10 Double-peak fitting for the 100 and 150 nm NaCl samples.

Both of these samples still had traces (100 nm) or even a clear layer (150 nm) of NaCl remaining after selenisation. Looking at the PV performance of these two samples, 100 nm NaCl has a large distribution of cell efficiencies ranging from 4.8 to 8.3% due to a large variation in FF and V_{OC}. Therefore half of the cells are similar in

performance to 50 nm NaCl and the other half to 150 nm NaCl. This last sample has relatively improved PCEs reaching up to 9%, with the narrowest distribution of V_{OC} among the samples, at ~580 mV. The two PL peaks indicate a possibility of a compositional gradient in the film, which would involve a bandgap change across the absorber, or perhaps the formation of competing phases. Previously Colombara *et al.* observed a PL peak shift attributed to the formation of Ga-deficient absorber with intentional addition of sodium [43]. Similarly, Rudmann *et al.* reported a [Ga]/[In] concentration ratio change in the first half of the absorber following NaF treatment [206]. In the 100 nm NaCl, sample, the smaller low bandgap peak at ~1.14 eV would correspond to a Ga-poor phase whilst the more pronounced high bandgap peak at ~1.19 eV to a Ga-rich phase. The low E_g peak becomes very small for 150 nm NaCl. Generally, the bandgaps measured by PL are smaller than those measured using EQE spectra with a particularly big discrepancy in the 50 nm NaCl sample. However a general trend of bandgap decreasing from 15 to 50 nm NaCl and then increasing from 50 to 150 nm was observed. This indicates that excess Na causes compositional changes in the absorber involving In/Ga, but perhaps also affecting Cu migration and distribution in the absorber as suggested by Oikkonen *et al*. [211].

6.3.4 Compositional analysis using TEM

To understand the V_{OC} and FF loss in the device with the largest grains, the composition and structure of the device was studied using TEM in combination with EDX elemental mapping. A TEM bright field cross-section through the best performing cell of the 30 nm NaCl sample is shown in Figure 6.11. Different layers of the cell are clearly indicated on the image. The image shows large CIGS grains, however the individual grains are separated by extensive voids. The presence of voids causes the Mo layer to be uncovered at certain places or covered with only small grains. The presence of such extensive voids in the absorber might hinder the photo-generated carrier transport between the grains and limit the carrier collection at the contacts from the grains isolated by the void. Moreover, the CdS deposited by CBD forms not only on the surface of the absorber, but also inside it, which is corroborated by the elemental maps of Cd presented in Figure 6.12. The CdS enveloping each grain separately creates a local p-n junction, leaving the photo-generated carriers trapped inside the grain as they cannot be collected at the

contacts. This is probably the cause of the deterioration of the FF seen in the devices with large grains (30-100 nm NaCl).

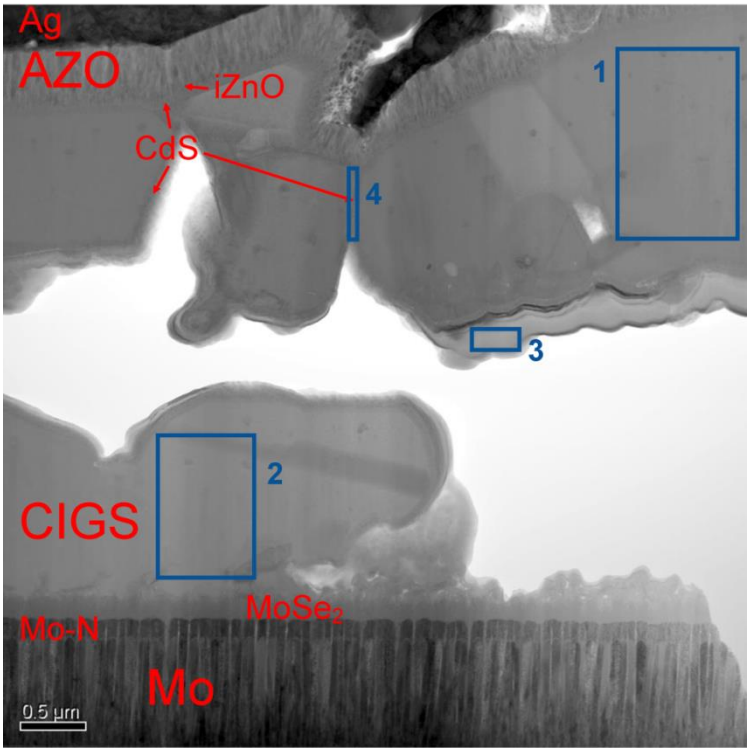

Figure 6.11 Bright field TEM cross-section through the best cell of the device with evaporated 30 nm of NaCl. Heterostructure layers are identified and clearly indicated in red. The blue rectangles indicate 4 areas which were quantified with EDX and summarised in Table 6.4.

The elemental maps (Figure 6.12) show the distributions of the constituent elements of the various layers of the CIGS device. It can be seen that Cd is not only present around each CIGS grain, but also in the Mo back contact. Cd is generally known for diffusing to the surface of CIGS absorbers during the CBD process [163]. Moreover, Cd diffusion into the MoS_2 layer was seen by Gherson *et al.* [119]. Cd diffusion into the absorber and towards the back contact is enabled by the presence of voids in the absorber. However Cd diffusion into the Mo back contact is not typically observed and should not occur in a good quality and dense Mo grain structure. This suggests that the Mo back contact might be of poor quality with GBs allowing for accumulation of Cd and other impurities. The sheet resistance of 0.4 Ω/sq. for ~1.1 µm thick Mo/Mo-N/Mo back contact gives a back contact resistivity of 4.4 x 10^{-5} Ω.cm, which is one order of magnitude higher than a typical Mo resistivity. The Mo-N barrier layer has a similar grain morphology to Mo and if there is the presence of even a small amount of oxygen during the deposition, as suggested in Chapter 3, the oxygenated

columnar GBs would promote $MoSe_2$ formation, which is also accelerated in the presence of Na, and consequent delamination [118]. This phenomenon can be observed in the Se elemental map, where Se is observed to diffuse in the form of channels along GBs into the Mo.

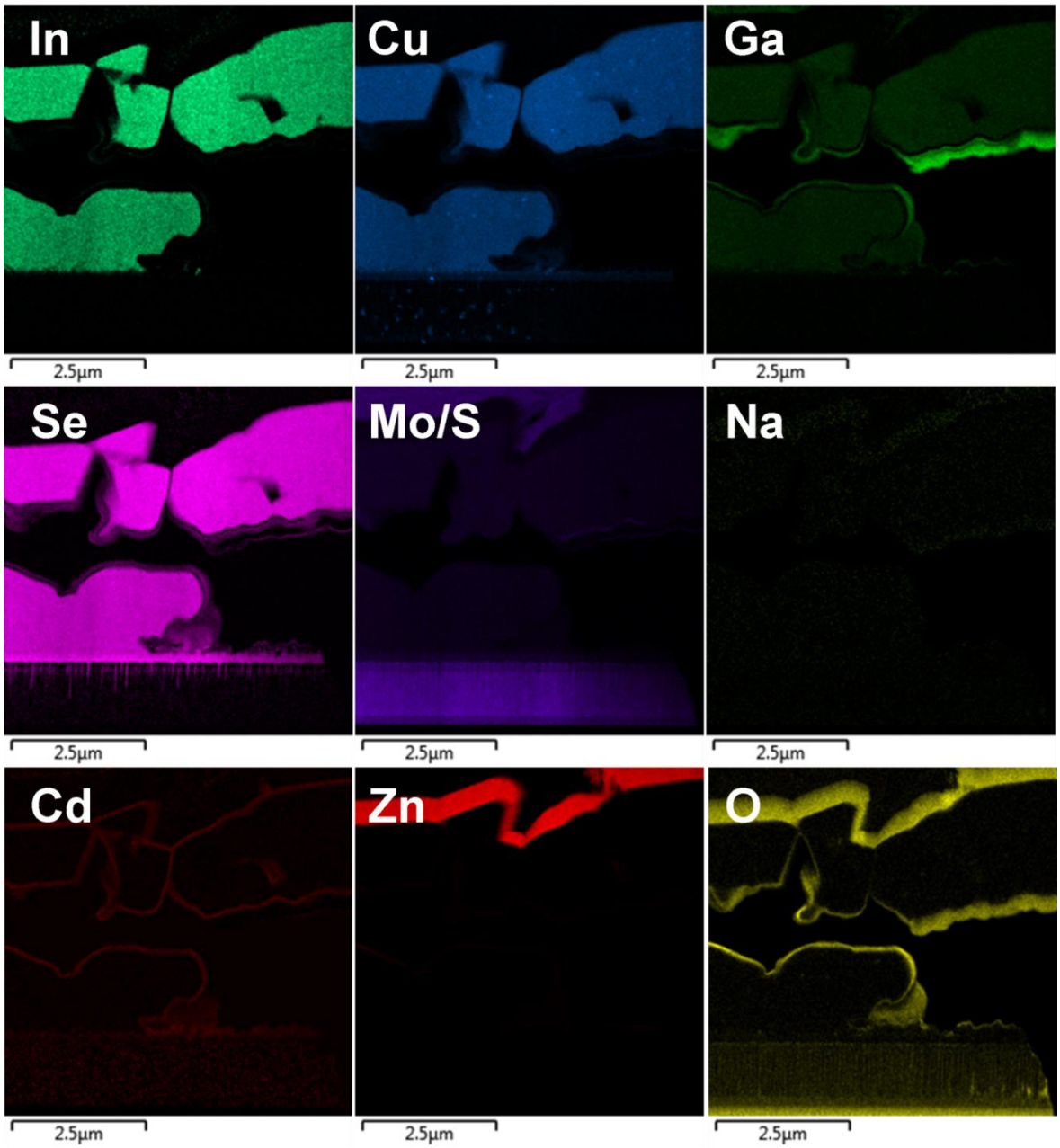

Figure 6.12 TEM-EDX elemental maps of the constituent elements of the CIGS solar cell with 30 nm of NaCl.

Mo and S EDX peaks overlap; therefore there is a combined elemental map for these 2 elements. Its signal in the CIGS absorber indicates that not all the sulphur from the precursors was replaced by Se during the selenisation and consequently the final absorber is not a pure selenide phase but rather a mixed $Cu(In,Ga)(S,Se)_2$

material. The Ga elemental map shows a strong Ga signal around the grains, indicating Ga segregation and consequently a lower GGI ratio in the bulk CIGS. The Na signal is included as well, however Na is a light element and its EDX signal is not trustworthy. But according to this map, the Na signal seems to be stronger where the Ga signal is strong. EDX map also shows presence of oxygen around the grains and its signal is overlapping with the Ga signal. To quantify the device composition, four different areas of the device were analysed, inside the grain, at GBs and in the Ga segregate. The areas are marked by blue rectangles in Figure 6.11 and the composition of each is summarised in Table 6.4.

Table 6.4 EDX compositional analysis at four areas of the CIGS absorber visualised in TEM cross-section of Figure 6.11

At%	Area 1 Top grain	Area 2 Bottom grain	Area 3 Under grain	Area 4 GB
Cu	25.0	24.7	0.6	16.7
In	21.2	21.8	0.3	14.7
Ga	7.4	7.4	25.2	4.6
Se	46.4	46.2	1.1	30.6
O	-	-	50.3	-
Si	-	-	17.1	-
Al	-	-	5.5	-
Cd	-	-	-	16.8
S	-	-	-	16.5
CGI	0.874	0.846	0.024	0.865
GGI	0.259	0.253	0.988	0.238

The EDX compositional analysis reveals lower than intended Ga composition inside the CIGS grains (GGI of ~0.25 instead of 0.3). The Ga loss from the bulk is caused by the accumulation of Ga underneath the grains. In Area 3, Ga is present in an increased quantity, but does not form part of the chalcopyrite phase. Large amounts of oxygen are also present in this region, suggesting possible oxidisation of the gallium. Partial oxidisation and accumulation of Ga was observed by Berner *et al*., when sodium formate was used as the Na precursor. It is claimed that Ga in the form of Ga_2O_3 is no longer available during selenisation as the oxide is very stable [58]. Here, the oxygen can come from the air as the spraying procedure is performed at elevated temperatures in ambient conditions. Dirnstorfer *et al.* observed Ga loss in the chalcopyrite phase due to formation of Ga_2O_3 after annealing the CIGSe

precursor in air at 400°C [240]. Na has a strong affinity for oxygen and Na is typically found at GBs [222]. This can promote the accumulation of the gallium oxide phases around the CIGS grains.

6.3.5 NaCl evaporation: conclusions

The evaporation of NaCl onto CIGS absorbers in order to enhance the morphological and electrical properties of the devices induced by absorber Na doping was successfully achieved. Using NaCl as an evaporation source is a cheap, non-toxic and previously unexplored method of CIGS doping. NaF is typically used as the evaporation source mostly for high efficiency vacuum-based CIGS solar cells. NaCl was also employed as a Na precursor for CIGS, however mostly by direct introduction into the precursor solution in solution-based absorbers. It was shown that NaCl was relatively easy and fast to evaporate under vacuum and its effects on the absorber morphology and performance were similar to those described in the literature for NaF evaporation [154]. It was found that a compromise between the optimum NaCl thickness for CIGS grain growth and the optimum thickness for the improvement of electronic properties of the material had to be made. The large grain growth is accompanied by the creation of extensive voids in the absorber, which has detrimental effects on the device performance and delamination as well as creating shunting paths. The voids are particularly problematic in the successive CdS CBD, where CdS forms not only on the absorber surface as for dense films, but also inside the absorber, resulting in less efficient carrier collection. The reversibility of Na incorporation discussed in the literature suggests that part of the Na incorporated at the GBs can effectively be washed out during the CBD, which may also be facilitated by the presence of voids [222]. The presence of oxygen can drive Na from the GBs to the surface and create surface traps during the post-CBD heat treatments. Finally bandgap changes and segregation of Ga possibly forming gallium oxides in the inter-grain voids were also observed in the presence of various amounts of sodium. All these observations have to be taken into account for the further optimisation of this approach of sodium doping. Overall, this method resulted in a device performance of twice that of the Na-free CIGS solar cells, from PCE of 5 to 10%.

6.4 Other incorporation methods

6.4.1 NaCl added into the graphite box

This doping strategy is illustrated in Figure 6.1 e) and was based on the study performed by Colombara *et al*. showing deliberate gas-phase doping of CIGS by selenising in the presence of elemental Se and NaCl [43]. To perform a similar experiment, NaCl was simply placed in the graphite box together with Se pellets prior the selenisation. The absorbers were selenised at 550ºC for 70 min using the RTP. The graphite box was filled with ~800 mg of Se and 100 mg of NaCl. The selenisation was performed at three different pressures (200 Torr, 50 Torr and 1 Torr) with the aim of triggering a partial NaCl evaporation. Lower pressures are necessary for the NaCl evaporation due to its very high boiling and melting points (1465°C and 801°C respectively under atmospheric conditions). However higher pressures are necessary to slow down the evaporation of selenium and allow its supply progressively, during the whole selenisation process. Since there is not a continuous supply of Se vapour during the process, a compromise in terms of working pressure had to be made.

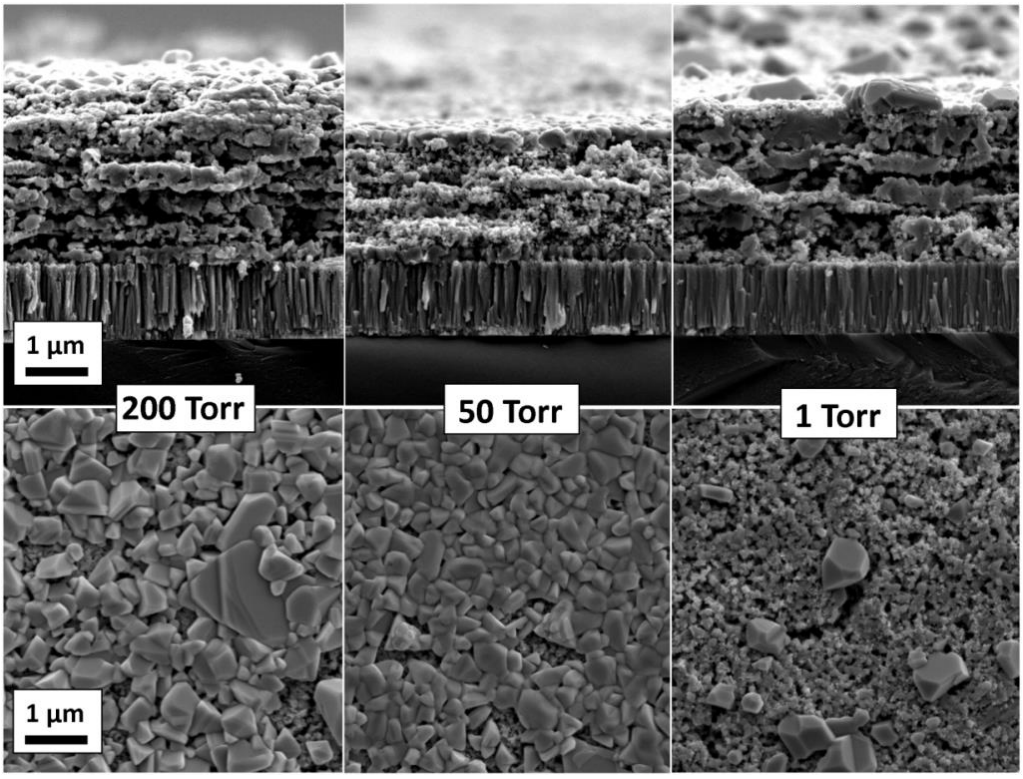

Figure 6.13 SEM cross-section and surface images after selenisation in presence of NaCl in the graphite box at different working pressures.

The SEM cross-sections of the three absorbers selenised at different pressures are shown in Figure 6.13. The SEM images show a lower degree of crystallinity of the absorber at lower working pressures. At the end of each selenisation, all the initially

inserted Se in the box was consumed, however ~100 mg of the NaCl remained. Therefore it is evident that even at the lowest pressure, the evaporation of NaCl did not happen, at least not in any significant quantity. Instead, lower pressures caused Se to evaporate too early in the process, resulting in a less crystalline absorber material. Colombara *et al.* stated that at 550°C, the vapour pressures of alkali chlorides are of the order of 1 mTorr, which is three orders of magnitude lower than the lowest pressure used here [43]. Consequently, the electrical performance of these cells is not expected to be an improvement of that of the undoped CIGS sample presented in the previous section. J-V curves of representative devices are shown in Figure 6.14 and their performance parameters are summarised in Table 6.5.

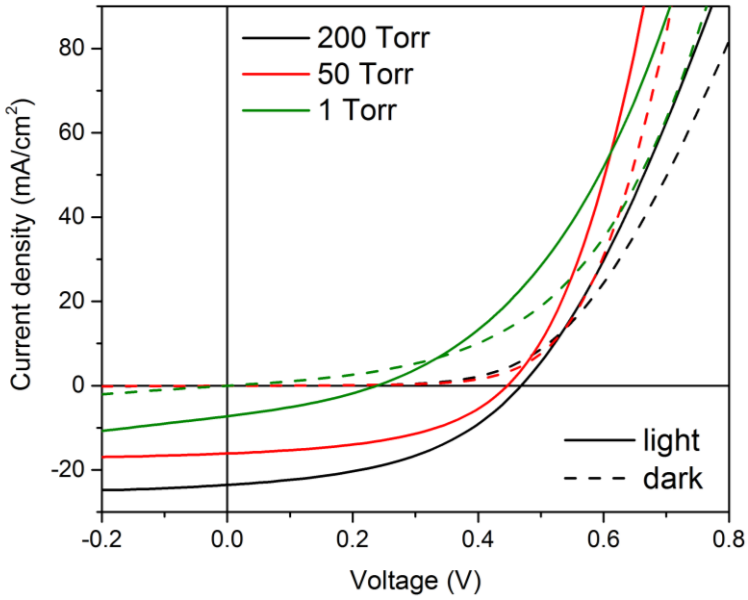

Figure 6.14 Light and dark J-V characteristics of the CIGS devices after selenisation in presence of NaCl in the graphite box at different working pressures.

Table 6.5 PV performance indicators of the J-V curves shown in Figure 6.14

	Working pressure	**PCE** (%)	**V_{oc}** (V)	**J_{sc}** (mA/cm^2)	**FF** (%)
Se + NaCl	**1 Torr**	0.56	0.238	7.3	32.3
	50 Torr	3.43	0.446	16.1	47.8
	200 Torr	4.99	0.468	23.5	45.2
Se	**200 Torr**	5.04	0.502	19.6	51.3

The performance of the device selenised at 200 Torr in presence of NaCl is very similar to the control device with no added NaCl. It confirms that the presence of

NaCl in the selenisation box did not play any major role since the pressure was too high to start its evaporation. Lowering the pressure to 50 Torr caused the efficiency to drop, owing to a significant drop in J_{SC} from 23.5 to 16.1 mA/cm^2. This is consistent with the lower degree of crystallinity of the absorber observed in the SEM images. Lowering the pressure to 1 Torr caused all the PV parameters to decrease dramatically resulting in efficiency of only ~0.6%. These results show that a simultaneous evaporation of Se and NaCl in the experimental setup used here is not achievable and consequently gas-phase alkali doping was not studied any further.

6.4.2 Dipping the absorber into NaCl solution

Another strategy explored for sodium doping was done by dipping of the absorber in NaCl solution (Figure 6.1 d)). This experiment was based on the work done by Wang *et al.* and Guo *et al.* where they achieved an efficiency improvement by dipping the solution-based absorbers into the NaCl aqueous solution for several minutes prior to selenisation [236][52]. Following the methodology used by Wang *et al*., the as-deposited CIGS absorbers were dipped into NaCl solutions of various concentrations for 20 min. The films were then annealed on a hot plate at 300°C to evaporate the excess solvent for 15 min and selenised at 550°C for 70 min. The NaCl solution concentration was varied between 0.02 and 0.2 M. A concentration 0.2 M was found to produce non-uniform drying of the film, leaving traces of NaCl on the surface. Consequently higher concentrations were not tested. The selenisation duration had to be reoptimised for each NaCl solution concentration used due to peeling of the films from the substrate. It was observed that adding NaCl had a negative effect on the absorber and Mo adhesion properties. Figure 6.15 b-c) shows photographs of the extensive pinholes formed after selenisation of Na-doped absorbers. The SEM cross-section in Figure 6.15 a) depicts the origin of the delamination.

The SEM proves that the delamination occurs due to excessive local $MoSe_2$ formation. Adding Na into the absorber prior to selenisation triggers the formation of Na-Se phases during selenisation [154]. The Na-Se flux is more reactive than the pure Se vapour, enhancing the grain growth of the CIGS absorber. However, more reactive Se also has negative effects on the Mo layer, as $MoSe_2$ formation is accelerated. The Mo-N acts as a diffusion barrier against Se, however some Se was

shown to penetrate to the underlying Mo layer following the Mo/Mo-N GBs as the morphology of Mo and Mo-N is similar, with both being columnar.

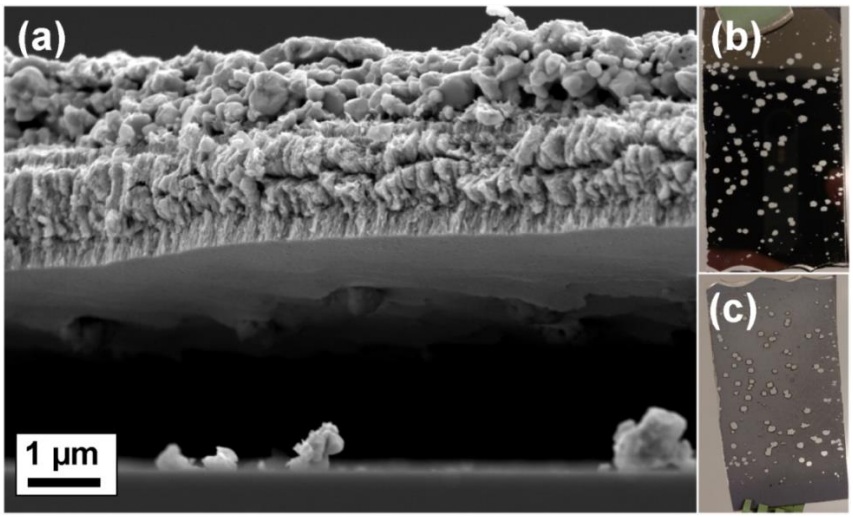

Figure 6.15 SEM cross-section at the points where the delamination occurs (a) and photographs showing the delamination of the thin films from the glass substrate observed from the Mo (b) and CIGS (c) side. The pinholes in the coatings occur after addition of Na in the films and selenisation. The bottom part of the absorber in (c) was not NaCl treated and also does not show any signs of delamination.

Since the delamination occurs locally, in the form of pinholes and since the cross-sections through the absorber away from pinholes (Figure 6.16) show formation of only a thin $MoSe_2$ layer achieved by the functional Mo-N barrier, it is suggested that the pinholes are formed when Se managed to escape through the barrier along the columnar GBs. This diffusion of some Se down the Mo GBs in presence of the Mo-N can be observed in the TEM/EDX maps shown in Figure 6.12. In the case of severe delamination as seen in Figure 6.15, the Se channels reach deeper in the Mo, eventually reaching the substrate. The absorbers with no Na doping do not show any signs of delamination. Higher concentrations of incorporated Na and longer selenisation durations with higher amounts of Se result in increasingly severe Mo delamination.

Longer selenisations are generally better for the solution-processed absorbers studied here, as they were found to produce enhanced absorber grain growth. However long selenisation durations (such as 70 min) in combination with Na doping by dipping into the NaCl aqueous solution resulted in films that were impossible to finish into CIGS devices due to extensive delamination such as shown in Figure 5.15. Figure 6.16 shows SEM images of the absorber films after longer and shorter

selenisation. The Na doping of these films was performed by dipping into the NaCl solution of two different concentrations, 0.02 M and 0.1 M. The absorbers were then selenised for the standard 70 min as well as for shorter times to reduce the delamination effects and ensure a good quality back contact.

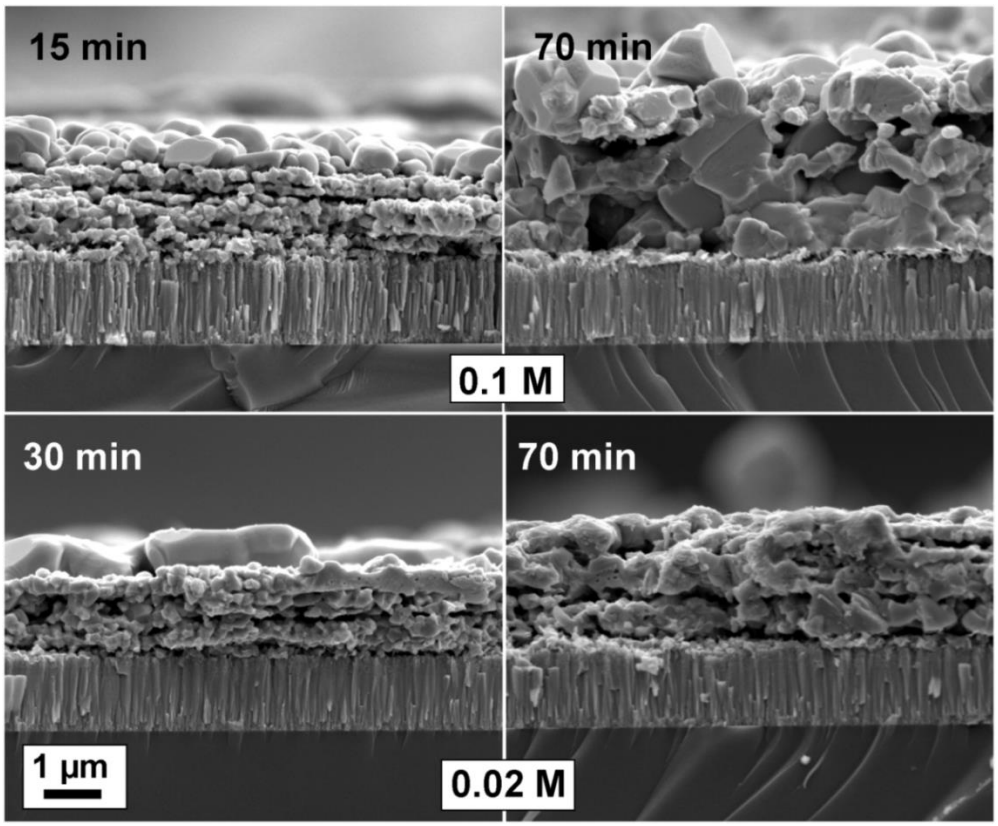

Figure 6.16 SEM cross-sections of the Na doped CIGS absorbers by dipping into NaCl aqueous solution of concentrations of 0.02 M and 0.1 M after selenisation for various durations.

As expected, longer selenisation times had a clear effect on the absorber morphology resulting in larger CIGS grains. Unfortunately the absorber with the largest grain morphology could not be finished into a device due to severe delamination. In addition, the NaCl solution concentration also has an effect on the CIGS grain growth, as larger grains were formed when the absorber was dipped into 0.1 M solution as opposed to 0.02 M. The J-V characteristics of the remaining three CIGS devices are presented in Figure 6.17. This graph contains an additional J-V curve of a sample treated with 0.2 M NaCl solution and selenised for 15 min. The cross-section of this sample was not included in Figure 6.16 as it looks similar to the 0.1 M for the same selenisation time. The J-V curve was added to show that the NaCl solution concentration and consequently the amount of Na incorporated into

the absorber has a key role in determining the device performance. Table 6.6 summarises the key performance indicators of these devices.

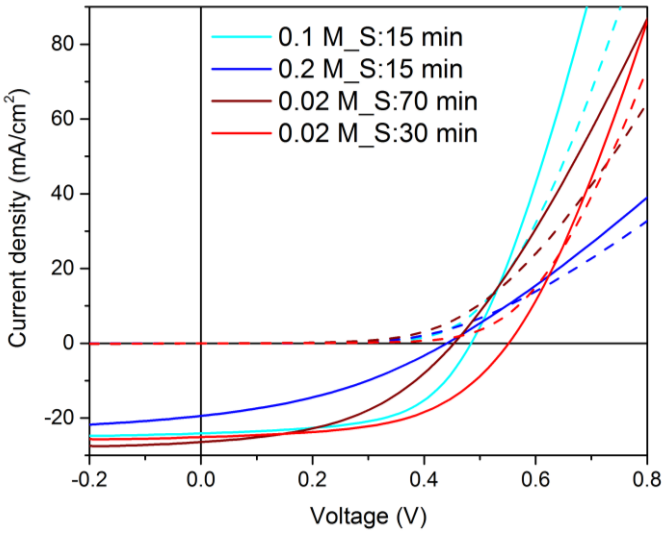

Figure 6.17 Light and dark J-V characteristics of the CIGS devices after dipping in the NaCl solution of concentrations in the range of 0.02-0.2 M. The absorbers have been subsequently selenised for various durations (15-70 min) in order to protect the back contact against delamination accelerated in presence of higher amounts of Na and Se.

Table 6.6 PV performance indicators from the J-V curves in Figure 6.17

Dipping NaCl solution	Selenisation conditions	PCE (%)	V_{OC} (V)	J_{SC} (mA/cm^2)	FF (%)
N/A	**70 min**	5.04	0.502	19.6	51.3
0.02 M	**70 min**	5.39	0.453	26.4	45.0
	30 min	7.42	0.551	25.1	53.6
0.1 M	**15 min**	6.67	0.484	24.1	57.1
0.2 M		3.12	0.441	19.4	36.4

In this approach, a compromise between the NaCl solution concentration and the selenisation length had to be made because of the current limitations of the back contact. It was suggested earlier that the Mo is more resistive than a good quality Mo should be, perhaps due to the presence of a small amount of oxygen. Longer selenisation and higher NaCl solution concentration both improved the grain growth; however they also caused more extensive back contact delamination due to local formation of $MoSe_2$. As opposed to the NaCl evaporation method which implies Na-Se phase formation and supply from the absorber surface, this method incorporates NaCl into the entire absorber and this is further facilitated due to the porous nature of the absorber material. Consequently this approach probably has a more direct effect

on the Mo, which was in several studies reported to act as a sink of Na during CIGS growth [232]. An improvement from the undoped device efficiency of 5% to 7.4% was achieved using this strategy. It is likely that this efficiency could be even higher with a better quality Mo back contact, allowing for higher NaCl solution concentrations and longer selenisation durations. The solution concentration of 0.2 M was found to supply an excessive amount of Na resulting in performance degradation compared to 0.1 M.

6.4.3 NaCl added into the precursor solution

In the last Na doping approach studied in this work, NaCl was added directly into the CIGS solution (Figure 6.1 f)). Berner *et al*. have achieved a 13.3% efficient solution-processed CIGS solar cell by adding 2.5 at% of Na relative to the copper content of the precursor solution [58]. However such a small amount represents adding only 1 mg of NaCl into the 4.4 mL of the CIGS precursor solution, typically prepared for spraying onto two 5 cm x 5 cm substrates. To find the optimum in this case, three different amounts of NaCl were added to the base-line precursor solution. NaCl was not separately dissolved as a fourth constituent solution, instead it was added in solid pieces into the final CIGS precursor solution and left to stir for two hours prior to starting the deposition. The three quantities of NaCl used were approximately 1, 2.5 and 5 mg, corresponding to ~2.5, 6 and 12 at% of Na relative to Cu in the CIGS. Visually all the NaCl was dissolved in the solution after 2h from its addition, and anything which had not dissolved was removed by filtering.

Figure 6.18 shows SEM images of the cross-sections through the finished CIGS devices and absorber surfaces with different amounts of NaCl directly dissolved in the precursor solutions. It appears that there is little, if any, visible change in the CIGS absorber morphology with addition of 2.5 at% and minimal change with 6 at% of Na. This is surprising as 6 at% is more than double the optimum Na concentration found by Berner *et al*. The absorber containing the highest amount of Na (~12 at%) however shows a spectacular change in morphology. The grains are significantly larger than in the other three CIGS absorbers. However, there are grain size differences and significant voids in between the grains. This absorber layer is not as compact and smooth as the absorbers with poorer crystal growth (≤ 6 at% Na),

hence the AZO coverage of the film is very different, less uniform and less smooth, possibly resulting in shunt paths.

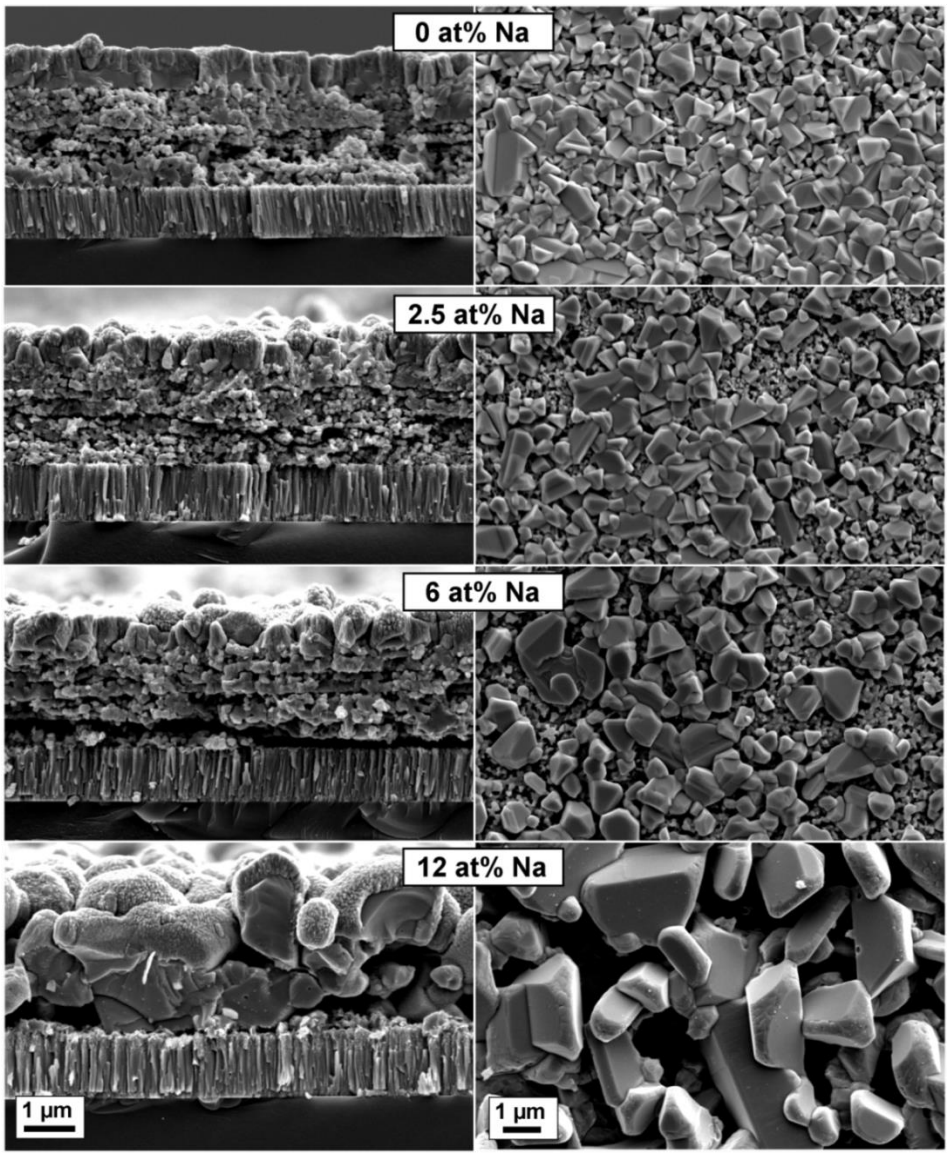

Figure 6.18 SEM cross-section of CIGS devices and SEM surface images of CIGS absorbers doped with different amounts of Na relative to Cu introduced as NaCl directly into the precursor solution prior spray-coating. The at% stated represent the amount of Na intended, not physically present in the film.

The J-V curves of the four devices with the various intended amounts of Na in the absorber are shown in Figure 6.19. Table 6.7 summarises the PV performance indicators of these devices. As suspected from the SEM images, the device with 12 at% of Na added is electrically shunted, probably due to the voids in the absorber and non-conformal TCO growth. The AZO most likely has been sputtered through the voids and made contact with the back contact. The physical contact of the two

conductive electrodes resulted in the formation of a direct shunting path bypassing that of the diode. The extensive voids were created by the enhanced but non-uniform grain growth of the CIGS absorber. As NaCl was dissolved in the precursor solution, it was equally incorporated into the entire absorber. As with the dipping strategy, the grain growth mechanism and kinetics were probably different from those of the surface evaporation technique. The apparently varied grain nucleation resulted in irregular growth without the formation of the coarse large-grained absorber surface typically seen in these devices. The device with 2.5 at% added Na generally exhibited low performance, even lower than that of the undoped control device. This probably does not reflect the Na doping effects but some other problems that might have occurred during its fabrication. Nonetheless, this concentration was most certainly too low to produce any performance improvement. The device with 6 at% Na has a much greater J_{SC}, which is likely caused by the addition of Na improving slightly the absorber grain morphology.

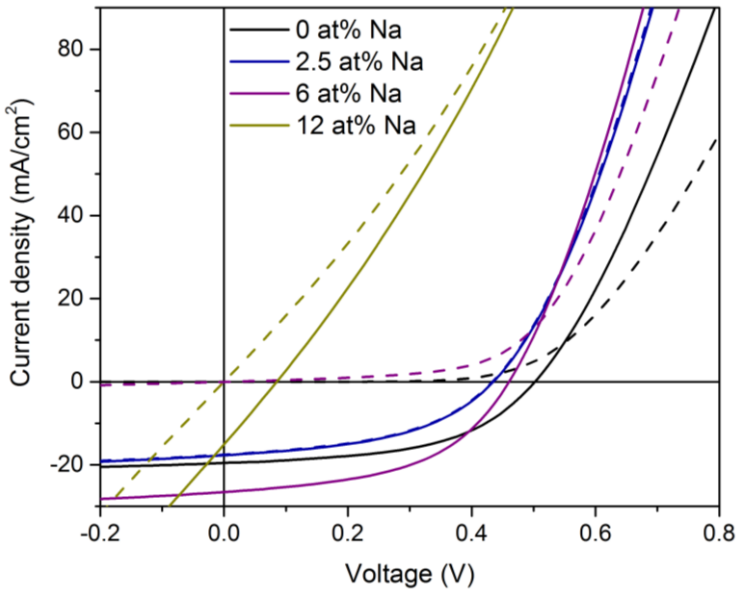

Figure 6.19 Light and dark J-V curves of the CIGS devices prepared from precursor solutions containing NaCl salts.

Table 6.7 PV performance indicators from the J-V curves shown in Figure 6.19

Na concentration (at%)	**PCE** (%)	**V_{OC}** (V)	**J_{SC}** (mA/cm^2)	**FF** (%)
0	5.04	0.502	19.6	51.3
2.5	3.59	0.434	17.7	46.7
6	6.07	0.460	26.6	49.7
12	0.33	0.085	15.1	25.5

This Na doping strategy shows another possible way of doping the solution-processed CIGS absorbers with sodium. Despite only a performance improvement of 1% with the addition of Na into the solution, this method presents a potentially successful method of Na doping with no additional fabrication step. After a further and more precise Na amount optimisation and using a better quality Mo back contact, devices with enhanced morphological and electronic properties are considered to be achievable. It is unlikely that the actual Na content of the absorbers is similar to the quantity added to the solution (i.e. 2.5, 6 and 12 at%). Consequently a more efficient means of NaCl addition could be used, for example dissolving NaCl in a separate solution or forming a single solution containing Cu, In, Ga and Na precursors from the beginning.

6.5 Challenges of Na doping

The beneficial effects of the alkali elements on CIGS device performance are generally known and accepted, however their mechanisms and location of action are not yet precisely understood. Therefore many potential challenges of alkali doping remain, especially in solution-processed CIGS devices. These are fundamentally different in absorber morphology and overall material quality compared to highly efficient vacuum-processed CIGS solar cells.

The first obvious challenge is to select the most appropriate doping strategy taking into account the limitations of the precursor material as well as the processing equipment. In vacuum-processing, NaF PDT is a well-established approach allowing for precise control over Na doping. However in solution-processing, typical Na doping of CIGS devices is achieved by out-diffusion from SLG and consequently intentional methods of Na incorporation into the material are less explored and not unified. Amongst the existing doping strategies, one may be more suitable for a given type of solution-based absorber whilst a different one may be better for another type.

Another challenge is identifying the right Na dosage. The amount of Na found to be beneficial for device performance is very small, in the order of 0.1 at%. This quantity is already too small to be easily detectable with any significant precision. In addition, Na is a light element and very few measurement techniques are able to directly measure it. Those that can work include expensive and rare characterisation

techniques such as atom probe tomography (ATP) and SIMS so long as an appropriate reference sample is provided for quantification. Consequently, no sodium quantification in the films was performed in this work and all the conclusions were based on the relative comparison of the samples and their behaviour.

Na forms a relatively volatile complex with Se, which can accumulate in the selenisation apparatus over several runs. Its re-evaporation can result in background alkali contamination and consequently cause accidental alkali doping of the absorber affecting device performance. The type of reaction chamber, selenisation setup and apparatus cleaning all have a significant impact on accidental absorber doping and need to be taken into consideration to avoid any confusing results and trends. In this work, the selenisation furnace was regularly cleaned by heating and mechanical scrubbing of the accumulated selenium. Moreover a closed-vessel selenisation approach using a SiC-coated graphite box was adopted, thought to minimise accidental alkali contamination.

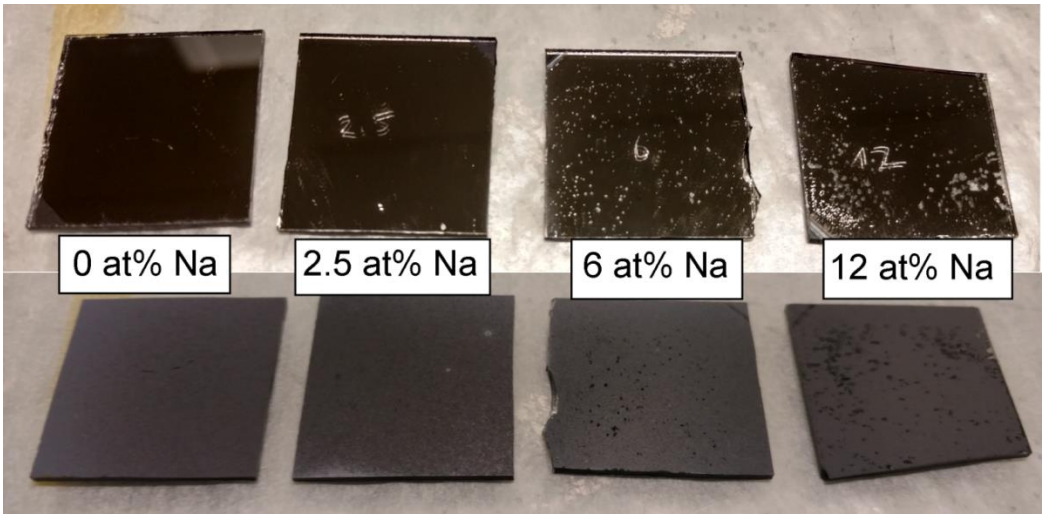

Figure 6.20 Photographs showing the effect of Na concentration in the CIGS film on the delamination properties of the Mo film after selenisation.

Finally another challenge was discovered during the experimental work. Na has an important effect on the quality of the back contact. In the presence of Na, Se becomes more reactive, having a positive impact on the absorber crystallinity, but also promoting excessive $MoSe_2$ formation, as explained in sub-section 6.4.2. Figure 6.20 shows how the increasing amount of Na affects the absorber and the Mo film quality. The oxygenated Mo GBs make the delamination even worse than usual (Figure 6.21). Na_2Se_x has strong affinity for O and H_2O and therefore promotes Na

oxidation [153]. It was concluded that a good quality, low resistivity Mo back contact without any oxygen contamination is essential for any further Na doping studies.

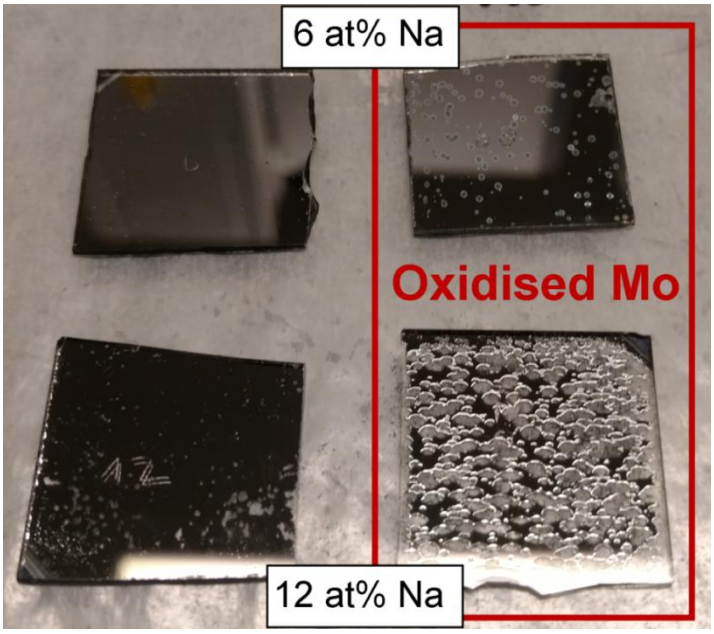

Figure 6.21 Photographs showing the effect of Mo oxidisation on the delamination in presence of Na after selenisation. The Mo film was artificially oxidised by annealing in air.

6.6 Conclusions

Several different doping strategies were applied to provide doping of the amine/thiol-based solution-processed CIGS solar cells studied in this work. The cheap and non-toxic Na precursor NaCl was employed throughout. It was shown that of the four doping methods studied here, different methods are more suitable for particular fabrication processes than others. When NaCl was mixed with elemental selenium during selenisation, the conditions and setup used were not sufficient to provoke NaCl evaporation, or at least not in sufficient quantity to compensate for rapid selenium evaporation and loss. Although this gas-phase alkali doping was successfully applied by others, for instance producing remarkable performance improvement in work published by Colombara *et al.*, small differences in starting materials, equipment design and conditions used can result in very different outcomes [43].

Direct introduction of NaCl into the precursor solution and dipping the absorber into NaCl solution produced a noticeable and encouraging change in absorber morphology and device performance induced by the action of sodium. However

these approaches were found to be less appropriate for the highly porous CIGS absorbers. The NaCl introduced by these methods was distributed equally to the entire absorber prior selenisation rather than on the surface only. This caused more direct action of the Na at the back contact resulting in extensive local delamination. Moreover, the probable different grain growth kinetics created voids in the absorber causing shorting of the device. The delamination produced by more reactive Na-Se fluxes was the primary limiting factor of these devices. The delamination was accelerated by the increased amount of Na and presence of O in the Mo. It is suspected that more efficient, oxygen-free deposition of the Mo back contact would result in more robust devices, where the effects of Na would be easier to separate from the interface issues.

Finally the thermal evaporation of NaCl in this study was found to be a novel and effective way of Na doping of the absorber. It is also a very similar approach to the most successful intentional alkali doping, evaporation of NaF, but using a more benign NaCl precursor. The action of Na in this method occurs through Na-Se phases created at the absorber surface, providing more protection to the back contact. Surprisingly the device with the best absorber morphology did not have the best electrical performance. The significantly larger grains obtained after Na-doping resulted in better absorber material quality reaching higher J_{SC} and minority carrier lifetimes, however the rough surface and presence of voids is thought to have caused interface problems resulting in the reduction of the FF and V_{OC}. Consequently compromises have to be made to improve the CIGS absorber while keeping the interfaces and contacts stable and of sufficient quality. Forming denser CIGS precursor films would most certainly have beneficial effects and allow for more straight forward doping optimisation and consequent efficiency improvements.

Ultimately, NaCl may not be the most suitable Na-precursor material as it introduces the unwanted Cl impurity into the absorber. This was initially attempted to be circumvented by using metal chalcogenides in the original precursor solution. Additionally the presence of Cl^- ions can cause Ga loss in the final film. Cl^- ions can react with Ga^{3+} and form $GaCl_3$ which has a relatively low boiling point (201°C) and can easily leave the film [71]. On the other hand, NaCl is an abundant and non-toxic salt, which has previously been employed for the purposes of CIGS absorber doping with no reported side effects of Cl.

CHAPTER 7

Conclusions and outlook

CIGS solar cells have achieved the highest laboratory efficiencies among all of the thin film technologies. However the market share of this technology is still very limited despite the advantageous material properties of CIGS absorbers. The fabrication processes are not unified and there are many absorber deposition techniques, involving both vacuum and non-vacuum equipment as well as numerous different precursor materials. Consequently there is a very large spectrum of reported CIGS solar cell efficiencies. The highest efficiency deposition methods are currently based on expensive vacuum techniques such as co-evaporation and co-sputtering. Their substitution with atmospheric large-scale deposition methods such as spray-coating or other printing methods could potentially lead to significant cost savings. Before these gains can be realised however, a non-toxic, highly uniform and reproducible non-vacuum absorber deposition method capable of reaching efficiencies close to those achieved by vacuum-based methods must be developed.

In this thesis CIGS absorbers were prepared by spray-coating and high temperature selenisation of a molecular solution formed from an alkahest amine-thiol solvent mixture and metal chalcogenides. The 1,2-ethylenediamine and 1,2-ethanedithiol containing solvent system is able to break the strong covalent bonds of metal chalcogenides, which are impurity-free precursor materials. The relatively environmentally-friendly nature of these solvents in combination with the atmospheric deposition approach employed in this thesis represents a safer and more scalable alternative to the most successful solution-based approach to date, which uses hydrazine as a solvent.

In terms of material quality, solution-processed CIGS absorbers are inferior when compared to those resulting from vacuum-based fabrication. Absorber porosity, non-uniformity, the large number of grain boundaries and presence of impurities are the most common limiting factors. These lead to significant reduction of the device

performance. A number of these negative material properties were observed in the solution-based absorbers prepared in this work, significantly complicating further device efficiency improvement. Moreover, CIGS solar cells are heterojunction devices composed of a number of layers each equally important for the optimum functioning of the cell. Better understanding of the different processing steps, parameters and quantities used and their effects on the device morphological, compositional and electrical properties was a key strategy of this thesis to achieve a more efficient and reproducible deposition process.

The influence of the substrate and back contact on the CIGS devices was studied first. The elemental composition and thermal expansion of the glass substrate was confirmed to have a strong effect on the final absorber morphology and doping as well as the adhesion properties of the Mo and CIGS layers after high temperature selenisation. Due to the porous nature of the sprayed absorber, the underlying Mo has little protection from the selenium vapour during the selenisation process. When bare Mo was used as a back contact, the Se vapour converted most of the underlying Mo into $MoSe_2$. $MoSe_2$ is not only very resistive, but also less cohesive due to weak van der Waals forces binding the molecule. A thick $MoSe_2$ layer caused high series resistance and physical delamination. Moreover $MoSe_2$ was found to act as a sink of mobile elements such as Cu, reducing its quantity in the absorber. A thin $MoSe_2$ ohmic contact between Mo and CIGS was achieved by deposition of a Mo-N/Mo bilayer on the top of the original bare Mo. Mo-N acts as a diffusion barrier against Se, whilst the thin top Mo layer is sacrificial and is converted into $MoSe_2$. As a consequence of application of the Mo/Mo-N/Mo modified back contact, CIGS solar cells with increased efficiencies were achieved owing to lower R_S and improved absorber recrystallisation.

The heterojunction formed by CIGS and CdS is prone to interface recombination which also negatively affects device performance. It was demonstrated that the junction has to be formed as quickly as possible after absorber selenisation because the CIGS surface degrades quickly on exposure to air. CIGS/CdS is stable even after several weeks, but the role of CdS was found solely to protect the CIGS absorber surface rather than to passivate it. The passivation of the CIGS/CdS interface was attributed to the effects of air-annealing. The air-annealing of the junction up to a given time and temperature was found to have beneficial effects on

all PV performance parameters, but particularly on the V_{OC}. This was attributed to the passivation of Se vacancies located at the absorber surface and grain boundaries by oxygen atoms. Cd and Cu diffusion in the near-interface and deep absorber regions respectively were also thought to occur during annealing. This resulted in modification of the junction electric field and absorber doping profile. The heat treatment of the full device is limited by the degradation of AZO in the presence of atmospheric species and humidity.

Identifying and minimising the emitter and back contact limiting factors allowed for greater focus on the main layer of interest: the CIGS absorber. Post-selenisation, CIGS absorbers prepared from metal chalcogenides dissolved in EDA/EDT solvents exhibit a poorly-crystalline morphology typical of solution-processed absorbers. This consists of a number of small grains near the back contact, many GBs and voids, and occurs despite the expected small impurity content. Various approaches were adopted with the aim of improving the absorber crystallisation, which is closely related to device performance. The impact of the selenisation reactor design and conditions used were investigated initially. An improvement in absorber morphology with improved surface grain size was achieved after the optimisation of the selenisation process using a tube furnace. Full absorber crystallisation was however not attained and poor repeatability of the process was often an issue, which was attributed to the graphite box. RTP selenisation in combination with a SiC-coated graphite box was suggested to produce better quality absorbers in a more reproducible manner. This method benefits from the more rapid heating profile of the RTP as well as the smaller volume and non-exposed tube ends. The use of a coated graphite box brings to the process the aspect of controllability of the amount of Se and impurities such as Na introduced into the absorber.

The implemented 2-stage selenisation profile promoted the formation of the Cu_xSe crystals at the absorber surface during the intermediate annealing stage at 300°C. It was suggested in the literature that the presence of Cu-Se phases assists the absorber crystallisation via a vapour-liquid-solid mechanism at the absorber surface. However neither the presence of the intermediate dwell nor slower temperature ramp enabled to promote the liquid Cu-Se phase formation that would result in significant enhancement of absorber crystallinity. More essential for improved CIGS grain growth were the Se quantity and selenisation duration.

The copper content in the final film and during the absorber growth has a strong effect on the film and solar cell properties. CIGS absorbers formed from a single-composition precursor solution often resulted in a lower than intended CGI ratio. To adjust the CGI ratio of the absorber, Cu-rich/Cu-poor bilayer absorbers were prepared by spraying from two separate precursor solutions. This approach promoted CIGS grain growth while keeping the absorber free of undesired secondary phases. EDX compositional analysis of the absorber cross-sections revealed that overall CGI of the bilayer film was 1.0 which is outside of the allowed Cu composition processing window. This resulted in lower PV performance of the devices with a significant drop in V_{OC} and J_{SC} due to likely high absorber doping density. Ga absorber grading was not explicitly studied in this thesis, however a natural Ga grading and also Ga loss were observed during selenisation. Understanding the unintentional compositional profiles formed in the absorber after selenisation can allow for compositional adjustment leading to improved device performance.

Despite the efforts to fully crystallise the solution-based absorber by optimising the selenisation conditions and adjusting the CGI ratio of the absorber, the final morphology was still in the form of a bilayer with large surface grains and a fine-grain underlying layer. Lastly, the effects of alkali treatment on the grain growth and absorber electronic properties were investigated. A strategy to externally introduce sodium in the absorber was developed by thermal evaporation of a thin layer of NaCl onto the absorber directly prior to selenisation. It was found that Na not only influences the grain growth by making Se more reactive during selenisation, but also modifies the electronic properties of CIGS absorbers. The optimum amount of Na, adjusted by varying the NaCl layer thickness was found to be different for optimum grain growth and ideal device performance. The highest efficiency of 10.4% was achieved with 15 nm of NaCl. This efficiency was more than twice that of a sodium-free control device. This sample did not have a fully crystalline absorber layer however, nor did it exhibit larger grains than when SLG substrates were used. The sample with 30 nm of NaCl on the other hand had several grains extending to the full absorber thickness. Despite the improved minority carrier lifetime, J_{SC} and EQE signal at all wavelengths, the efficiency of this cell was lower (9.7%) probably due to large voids and rougher surfaces creating interface problems, reflected in a lower

device FF and V_{OC}. The beneficial effects of Na were attributed to the passivation of defects and recombination states at the CIGS surface, GBs and grain interiors. The limitations can be related to the detrimental recombination at the CIGS/CdS interface, shunting paths due to the presence of extensive voids and back contact delamination due to poor Mo quality and sodium's affinity for oxygen. Other Na incorporation strategies such as dipping the absorber into NaCl solution or NaCl addition into the precursor solutions were also explored; however none of them was as successful as the evaporation approach, which can be partly attributed to the inadequate back contact quality.

The results and conclusions obtained in this thesis can provide some recommendations for further research. First of all, a good quality Mo back contact is necessary for further optimisation of the CIGS absorber. An effective means of $MoSe_2$ control was developed and presented in this thesis; however good adhesive, morphological and electrical properties of the bulk Mo are equally important. The relatively high resistivity of the as-deposited Mo relative to the commercial Mo supplied by M-Solv Ltd., delamination of the Mo from the glass with addition of Na into the samples and XPS analysis through the as-deposited Mo showing that only 95% of the layer corresponds to metallic Mo strongly suggest that a small amount of oxygen might be present in the bulk Mo layer. The sputtering system used to prepare Mo is very old and consists of a large sputtering chamber not equipped with a load lock. The entire chamber is vented each time the samples are to be loaded. This frequent venting can allow water vapour and other atmospheric species to contaminate the chamber walls and serve as oxygen sources during sputtering. Additionally a leak in the mass-flow controller or insufficient pumping capacity can contribute to the incorporation of oxygen into the Mo layer. High quality Mo is therefore crucial, not only to form a conductive back contact to the CIGS absorber but also to prevent delamination, element segregation and to allow for better Na doping control.

Secondly, CIGS solar cells in this thesis were prepared by manual spraying of the precursor solution using glass chromatography atomisers with air as the carrier gas. This deposition has the advantage of being simple, material efficient and clean (glass atomising nozzles are thoroughly cleaned by soaking in aqueous solution containing sodium hypochlorite and sonicating for several hours). On the other hand,

the manual nature of this technique introduces a considerable thickness variation from sample to sample and even within each sample. Furthermore, using air as the carrier gas introduces more oxygen into the film. Oxidation of Ga was shown to be particularly detrimental as gallium oxides formed would not participate in the CIGS phase formation reactions during selenisation, resulting in Ga loss in the final film [58]. The introduction of an inert carrier gas such as nitrogen may also result in a less porous absorber microstructure. An automated spraying stage equipped with a SonoTek ultrasonic spraying nozzle using nitrogen as the carrier gas is being currently implemented and optimised for the deposition of amine/thiol-based CIGS precursor solutions. Ultrasonic spray pyrolysis has a narrower droplet size distribution and the automated stage will allow for more precise thickness control over the spraying area, ensuring improved film uniformity. These changes are likely to give more reproducible films as well as improving the solar cell electronic properties. For absorber selenisation, a setup involving a constant supply of Se vapours would allow for lower selenisation pressures. This may be beneficial for the CIGS grain growth assisted by liquid Cu_xSe phases.

The primary drawback of the CIGS absorbers prepared using this method is the porosity. It was shown that the implemented modifications in the selenisation, absorber composition and doping do not significantly reduce the degree of porosity either before or after selenisation. Instead, small voids in the as-deposited absorbers agglomerate and result in large voids in the selenised absorbers even when improved grain growth is exhibited. The voids create interface problems and compensate for the beneficial effects achieved by an improved grain growth. Methods of porosity reduction could be further investigated, for example through implementation of a soaking step in a cation precursor solution as suggested by Zhao *et al.* or spin-coating of the precursor solution onto the as-deposited absorber with the aim of filling in the voids [71].

Finally, the sodium doping studied in this thesis showed that controlled Na incorporation into the absorber is desirable. However the study presented here only provides a starting point for this research and needs a further optimisation. Various Na sources, doping methods and conditions could be explored. NaCl was used as the sodium source in all the intentional doping strategies tested in this work due to its low toxicity and ready availability. However other precursors such as Na_2Se and

Na_2S may be more suitable for certain doping strategies due to their different melting points and avoidance of the introduction of undesired impurities such as Cl into the absorber. In addition, selenisation and junction annealing conditions, CdS and i-ZnO thicknesses may have to be reoptimised for different absorber morphologies as a result of Na doping of the absorber. It is equally important to obtain a deeper understanding of the action of Na on the electronic properties of the absorber. To achieve this, various quantitative and defect measurements would be very valuable when studying Na effects on solution-processed absorbers.

The suggestions for future work presented above are focusing on research challenges specific for devices fabricated in this work and them similar. In a broader context, CIGS thin film technology developments and industrialisation have greatly advanced in recent years. Although there are still many challenges lying ahead with the ultimate aim of the technology to achieve a balance between high material qualities for high power output keeping manufacturing costs low. The current challenges include precise control over absorber stoichiometry, uniformity and doping over large area and interface optimisation to reduce recombination. New device, material and process designs for CIGS solar cells have been under close examination to overcome these challenges and potentially lead to more robust next generation solar cells.

The largest manufacturer of CIGS thin film modules, Solar Frontier, developed a process creating a double graded band profile introducing S at the surface of CIGS and Ga at the backside. The band bending created by the absorber grading resulted in reduced back and front surface recombination [241]. In terms of back surface passivation, Ga grading creating a back surface field might not be sufficient especially if the thickness of the absorber is reduced. In fully depleted ultrathin absorbers this would cause weaker electric field in the SCR. As a result, rear surface passivation layers using dielectric-based materials such as Al_2O_3, but also less extensively used SiO_2 or TiO_2 with point contact openings are being used in high efficiency CIGS. In combination with light management techniques such as Ag NP metallic mirrors at the back contact and AR coatings allowing for increased amount and optical path length of the light in the absorber, they result in improved device V_{OC} and carrier collection even for significantly reduced absorber thicknesses [242]. As for the rear surface, similar concept of front surface passivation using HfO_x or

GaO_x with point contact openings were found promising [243][244]. Despite sodium being the most effective alkali element, other alkali elements were also found to have beneficial, yet different effects on CIGS solar cell performance. Additional performance gains with better diode quality were shown to be achievable using heavier alkali elements such as Rb and Cs [67]. Full optimisation of these innovations and their application in large area vacuum-free processing is a promising research path for CIGS thin film technology.

Bibliography

[1] D. J. Mackay, *Sustainable Energy - without the hot air*. UIT Cambridge Ltd., 2009.

[2] D. J. Wuebbles and A. K. Jain, “Concerns about climate change and the role of fossil fuel use,” *Fuel Process. Technol.*, vol. 71, pp. 99–119, 2001.

[3] T. F. Stocker, D. Qin, G.-K. Plattner, M. Tignor, S. K. Allen, J. Boschung, A. Nauels, Y. Xia, V. Bex, and P. M. Midgley, *IPCC, 2013: Climate Change 2013: The Physical Science Basis. Contribution of Working Group I to the Fifth Assessment Report of the Intergovernmental Panel on Climate Change*. Cambrigge University Press, 2013.

[4] IEA, *Solar energy perspectives, International Energy Agency Publications*. ISBN 978-92-6412-457-8, 2011.

[5] Renewables 2018, *Global Status Report*. REN21, ISBN 978-3-9818911-3-3, 2018.

[6] J. Ramanujam, A. Verma, B. González-Díaz, R. Guerrero-Lemus, C. Del Cañizo, E. García-Tabarés, I. Rey-Stolle, F. Granek, L. Korte, M. Tucci, J. Rath, U. P. Singh, T. Todorov, O. Gunawan, S. Rubio, J. L. Plaza, E. Diéguez, B. Hoffmann, S. Christiansen, and G. E. Cirlin, “Inorganic photovoltaics - Planar and nanostructured devices,” *Prog. Mater. Sci.*, vol. 82, pp. 294–404, 2016.

[7] T. M. Bruton, “General trends about photovoltaics based on crystalline silicon,” *Sol. Energy Mater. Sol. Cells*, vol. 72, pp. 3–10, 2002.

[8] J. Ramanujam and U. P. Singh, “Copper indium gallium selenide based solar cells - A review,” *Energy Environ. Sci.*, vol. 10, pp. 1306–1319, 2017.

[9] M. A. Green, Y. Hishikawa, E. D. Dunlop, D. H. Levi, J. Hohl-Ebinger, and A. W. Y. Ho-Baillie, “Solar cell efficiency tables (version 51),” *Prog. Photovoltaics Res. Appl.*, vol. 26, pp. 3–12, 2018.

[10] F. S. Johnson, “The solar constant,” *J. Meteorol.*, vol. 11, pp. 431–439, 1954.

[11] M. G. Villalva, J. R. Gazoli, and E. R. Filho, “Comprehensive Approach to Modeling and Simulation of Photovoltaic Arrays,” *IEEE Trans. Power Electron.*, vol. 24, pp. 1198–1208, 2009.

[12] S. S. Hegedus and A. Luque, “Status, Trends, Challenges and the Bright Future of Solar Electricity from Photovoltaics,” in *Handbook of Photovoltaic Science and Engineering*, Wiley and Sons Ltd, 2003.

[13] A. E. Becquerel, “Mémoire sur les effets électriques produits sous l’influence des rayons solaires, Comptes Rendus,” *C.R. Acad. Sci.*, vol. 9, pp. 561–567, 1839.

[14] J.-P. Colinge and C. A. Colinge, *Physics of Semiconductor Devices*. Kluwer Academic Publishers, 2002.

[15] J. L. Gray, “The Physics of the Solar Cell,” in *Handbook of Photovoltaic Science and Engineering*, 2003, pp. 61–112.

[16] H. Azimi, Y. Hou, and C. J. Brabec, “Towards low-cost, environmentally friendly printed chalcopyrite and kesterite solar cells,” *Energy Environ. Sci.*, vol. 7, pp. 1829–1849, 2014.

[17] K. L. Chopra and S. R. Das, *Thin Film Solar Cells*. Plenum Publishing Corporation, 1983.

[18] A. L. Fahrenbruch and R. H. Bube, *Fundamentals of Solar Cells*. Academic Press, 1983.

[19] S. Hegedus, “Thin Film Solar Modules: The Low Cost, High Throughput and Versatile Alternative to Si Wafers,” *Prog. Photovoltaics Res. Appl.*, vol. 14, pp. 393–411, 2006.

[20] H. S. Ullal, “Overview and Challenges of Thin Film Solar Electric Technologies,” *World Renew. Energy Congr. X Exhib.*, 2008.

[21] H. S. Ullal and B. Von Roedern, “Thin Film CIGS and CdTe Photovoltaic Technologies : Commercialization , Critical Issues, and Applications,” *22nd Eur. Photovolt. Sol. Energy Conf. Exhib.*, 2007.

[22] A. Lunque Lopez and V. M. Andreev, *Concentrator Photovoltaics*. Springer, 2007.

[23] W. Li, J. M. R. Tan, S. W. Leow, S. Lie, S. Magdassi, and L. H. Wong, “Recent Progress in Solution Processed Cu-chalcogenide Thin Film Solar Cells,” *Energy Technol.*, vol. 6, pp. 46–59, 2018.

[24] NREL, “PV Research Cell Record Efficiency Chart.” [Online]. Available: https://www.nrel.gov/pv/assets/pdfs/pv-efficiency-chart.20190103.pdf. [Accessed: 05-Feb-2019].

[25] NREL, “Champion Module Efficiencies Chart.” [Online]. Available: https://www.nrel.gov/pv/assets/pdfs/research-module-efficiency-chart.20190128.pdf. [Accessed: 05-Feb-2019].

[26] Solar Frontier, “Solar Frontier Achieves World Record Thin-Film Solar Cell Efficiency of 23.35%.” [Online]. Available: http://www.solar-frontier.com/eng/news/2019/0117_press.html. [Accessed: 05-Feb-2019].

[27] H. Hahn, G. Frank, W. Klingler, A.-D. Meyer, and G. Storger, “Untersuchungen über ternäre Chalkogenide. V. Über einige ternäre Chalkogenide mit Chalkopyritstruktur,” *J. Inorg. Gen. Chem.*, vol. 271, pp. 153–170, 1953.

[28] J. L. Shay, S. Wagner, and H. M. Kasper, “Efficient $CuInSe_2$/CdS solar cells,” *Appl. Phys. Lett.*, vol. 27, pp. 89–90, 1975.

[29] A. M. Gabor, J. R. Tuttle, D. S. Albin, M. A. Contreras, R. Noufi, and A. M. Hermann, “High-efficiency $CuInxGa_{1-x}Se_2$ solar cells made from $(In_x,Ga_{1-x})_2Se_3$ precursor films,” *Appl. Phys. Lett.*, vol. 65, pp. 198–200, 1994.

[30] V. K. Kapur, V. K. Kapur, A. Bansal, and S. Roth, “Roadmap for manufacturing cost

competitive CIGS modules," *37th IEEE Photovolt. Spec. Conf.*, pp. 3343–3348, 2011.

[31] T. Nakada, T. Kume, T. Mise, and A. Kunioka, "Superstrate-Type Cu(In,Ga)Se_2 Thin Film Solar Cells with ZnO Buffer Layers," *Jpn. J. Appl. Phys.*, vol. 37, p. L499, 1998.

[32] T. Todorov and D. B. Mitzi, "Direct Liquid Coating of Chalcopyrite Light-Absorbing Layers for Photovoltaic Devices," *Eur. J. Inorg. Chem.*, pp. 17–28, 2010.

[33] T. Feurer, P. Reinhard, E. Avancini, B. Bissig, J. Löckinger, P. Fuchs, R. Carron, T. P. Weiss, J. Perrenoud, S. Stutterheim, S. Buecheler, and A. N. Tiwari, "Progress in thin film CIGS photovoltaics – Research and development, manufacturing, and applications," *Prog. Photovoltaics Res. Appl.*, vol. 25, pp. 645–667, 2017.

[34] V. K. Kapur, A. Bansal, P. Le, and O. I. Asensio, "Non-vacuum processing of $CuIn_{1-x}Ga_xSe_2$ solar cells on rigid and flexible substrates using nanoparticle precursor inks," *Thin Solid Films*, vol. 431–432, pp. 53–57, 2003.

[35] I. Repins, M. A. Contreras, B. Egaas, C. DeHart, S. Scharf, C. L. Perkins, B. To, and R. Noufi, "19.9%-efficient ZnO/CdS/$CuInGaSe_2$ Solar Cell with 81.2% Fill Factor," *Prog. Photovolt Res. Appl.*, vol. 16, pp. 235–239, 2008.

[36] M. Gloeckler and J. R. Sites, "Band-gap grading in Cu(In,Ga)Se_2 solar cells," *J. Phys. Chem. Solids*, vol. 66, pp. 1891–1894, 2005.

[37] T. Kato, J.-L. Wu, Y. Hirai, H. Sugimoto, and V. Bermudez, "Record Efficiency for Thin-Film Polycrystalline Solar Cells Up to 22.9% Achieved by Cs-Treated Cu(In,Ga)$(Se,S)_2$," *IEEE J. Photovoltaics*, vol. 9, pp. 325–330, 2019.

[38] B. J. Mueller, C. Zimmermann, V. Haug, F. Hergert, T. Koehler, S. Zweigart, and U. Herr, "Influence of different sulfur to selenium ratios on the structural and electronic properties of Cu(In,Ga)$(S,Se)_2$ thin films and solar cells formed by the stacked elemental layer process," *J. Appl. Phys.*, vol. 116, p. 174503, 2014.

[39] E. Ghorbani, J. Kiss, H. Mirhosseini, G. Roma, M. Schmidt, J. Windeln, T. D. Kühne, and C. Felser, "Hybrid-Functional Calculations on the Incorporation of Na and K Impurities into the $CuInSe_2$ and $CuIn_5Se_8$ Solar-Cell Materials," *J. Phys. Chem. C*, vol. 119, pp. 25197–25203, 2015.

[40] B. J. Stanbery, "Copper Indium Selenides and Related Materials for Photovoltaic Devices," *Crit. Rev. Solid State Mater. Sci.*, vol. 27, pp. 73–117, 2002.

[41] R. Scheer and H.-W. Schock, *Chalcogenide Photovoltaics: Physics, Technologies and Thin Film Devices*. WILEY-VCH, 2011.

[42] W. N. Shafarman and L. Stolt, "Cu(InGa)Se_2 Solar Cells," in *Handbook of Photovoltaic Science and Engineering*, 2003.

[43] D. Colombara, U. Berner, A. Ciccioli, J. C. Malaquias, T. Bertram, A. Crossay, M. Schöneich, H. J. Meadows, D. Regesch, S. Delsante, G. Gigli, N. Valle, J. Guillot, B. El Adib, P. Grysan, and P. J. Dale, "Deliberate and Accidental Gas-Phase Alkali Doping of Chalcogenide Semiconductors: Cu(In,Ga)Se_2," *Sci. Rep.*, vol. 7, p. 43266, 2017.

[44] P. Reinhard, B. Bissig, F. Pianezzi, E. Avancini, H. Hagendorfer, D. Keller, P. Fuchs, M. Döbeli, C. Vigo, P. Crivelli, S. Nishiwaki, S. Buecheler, and A. N. Tiwari, “Features of KF and NaF Postdeposition Treatments of Cu(In,Ga)Se_2 Absorbers for High Efficiency Thin Film Solar Cells,” *Chem. Mater.*, vol. 27, pp. 5755–5764, 2015.

[45] D. Albin, J. Carapella, A. Gabor, A. Tennant, J. Tuttle, A. Duda, R. Matson, A. Mason, M. Contreras, and R. Noufi, “Fundamental thermodynamics and experiments in fabricating high efficiency $CuInSe_2$ solar cells by selenization without the use of H_2Se,” *AIP Conf. Proc.*, vol. 268, pp. 108–121, 1992.

[46] A. Chirilă, P. Reinhard, F. Pianezzi, P. Bloesch, A. R. Uhl, C. Fella, L. Kranz, D. Keller, C. Gretener, H. Hagendorfer, D. Jaeger, R. Erni, S. Nishiwaki, S. Buecheler, and A. N. Tiwari, “Potassium-induced surface modification of Cu(In,Ga)Se_2 thin films for high-efficiency solar cells,” *Nat. Mater.*, vol. 12, pp. 1107–1111, 2013.

[47] C. J. Hibberd, E. Chassaing, W. Liu, D. B. Mitzi, D. Lincot, and A. N. Tiwari, “Non-vacuum methods for formation of Cu(In,Ga)(Se,S)$_2$ thin film photovoltaic absorbers,” *Prog. Photovoltaics Res. Appl.*, vol. 18, pp. 434–452, 2010.

[48] D. Lee and K. Yong, “Non-vacuum deposition of CIGS absorber films for low-cost thin film solar cells,” *Korean J. Chem. Eng.*, vol. 30, pp. 1347–1358, 2013.

[49] V. Bermudez, “An overview on electrodeposited Cu(In,Ga)(Se,S)$_2$ thin films for photovoltaic devices,” *Sol. Energy*, vol. 175, pp. 2–8, 2018.

[50] C. Broussillou, C. Viscogliosi, A. Rogee, S. Angle, P. P. Grand, S. Bodnar, C. Debauche, J. L. Allary, B. Bertrand, C. Guillou, L. Parissi, and S. Coletti, “Statistical Process Control for Cu(In,Ga)(S,Se)$_2$ electrodeposition-based manufacturing process of 60×120cm^2 modules up to 14,0% efficiency,” *42nd IEEE Photovolt. Spec. Conf.*, 2015.

[51] H. Azimi, Y. Hou, and C. J. Brabec, “Towards low-cost, environmentally friendly printed chalcopyrite and kesterite solar cells,” *Energy Environ. Sci.*, vol. 7, pp. 1829–1849, 2014.

[52] Q. Guo, G. M. Ford, R. Agrawal, and H. W. Hillhouse, “Ink formulation and low-temperature incorporation of sodium to yield 12% efficient Cu(In,Ga)(S,Se)$_2$ solar cells from sulfide nanocrystal inks,” *Prog. Photovoltaics Res. Appl.*, vol. 21, pp. 64–71, 2013.

[53] G. Brown, P. Stone, J. Woodruff, B. Cardozo, and D. Jackrel, “Device Characteristics of a 17.1% Efficient Solar Cell Deposited by a Non-Vacuum Printing Method on Flexible Foil,” *38th IEEE Photovolt. Spec. Conf.*, pp. 3230–3233, 2012.

[54] Y. Cai, J. C. W. Ho, S. K. Batabyal, W. Liu, Y. Sun, S. G. Mhaisalkar, and L. H. Wong, “Nanoparticle-Induced Grain Growth of Carbon-Free Solution-Processed CuIn(S,Se)$_2$ Solar Cell with 6% Efficiency,” *ACS Appl. Mater. Interfaces*, vol. 5, pp. 1533–1537, 2013.

[55] S. Ahn, C. Kim, J. H. Yun, J. Gwak, S. Jeong, B. H. Ryu, and K. Yoon, “$CuInSe_2$ (CIS) thin film solar cells by direct coating and selenization of solution precursors,” *J. Phys. Chem. C*, vol. 114, pp. 8108–8113, 2010.

[56] W. Zhao, Y. Cui, and D. Pan, “Air-Stable, Low-Toxicity Precursors for $CuIn(SeS)_2$ Solar Cells with 10.1% Efficiency,” *Energy Technol.*, vol. 1, pp. 131–134, 2013.

[57] A. R. Uhl, J. K. Katahara, and H. W. Hillhouse, “Molecular-ink route to 13.0% efficient low-bandgap $CuIn(S,Se)_2$ and 14.7% efficient $Cu(In,Ga)(S,Se)_2$ solar cells,” *Energy Environ. Sci.*, vol. 9, pp. 130–134, 2016.

[58] U. Berner, D. Colombara, J. de Wild, E. V. C. Robert, M. Schutze, F. Hergert, N. Valle, M. Widenmeyer, and P. J. Dale, “13.3% efficient solution deposited $Cu(In,Ga)Se_2$ solar cells processed with different sodium salt sources,” *Prog. Photovoltaics Res. Appl.*, vol. 24, pp. 749–759, 2016.

[59] D. Zhao, Q. Tian, Z. Zhou, G. Wang, Y. Meng, D. Kou, W. Zhou, and S. Wu, “Solution-deposited pure selenide CIGSe solar cells from elemental Cu, In, Ga, and Se,” *J. Mater. Chem. A*, vol. 3, pp. 19263–19267, 2015.

[60] T. Zhang, Y. Yang, D. Liu, S. C. Tse, W. Cao, Z. Feng, S. Chen, and L. Qian, “High efficiency solution-processed thin-film $Cu(In,Ga)(Se,S)_2$ solar cells,” *Energy Environ. Sci.*, vol. 9, pp. 3674–3681, 2016.

[61] M. A. Hossain, T. Zhang, L. K. Keat, X. Li, R. R. Prabhakar, S. K. Batabyal, S. G. Mhaisalkar, and L. H. Wong, “Synthesis of $Cu(In,Ga)(S,Se)_2$ thin films using an aqueous spray-pyrolysis approach, and their solar cell efficiency of 10.5%,” *J. Mater. Chem. A*, vol. 3, pp. 4147–4154, 2015.

[62] W. Septina, M. Kurihara, S. Ikeda, Y. Nakajima, T. Hirano, Y. Kawasaki, T. Harada, and M. Matsumura, “$Cu(In,Ga)(S,Se)_2$ thin film solar cell with 10.7% conversion efficiency obtained by selenization of the Na-doped spray-pyrolyzed sulfide precursor film,” *ACS Appl. Mater. Interfaces*, vol. 7, pp. 6472–6479, 2015.

[63] X. Lin, R. Klenk, L. Wang, T. Köhler, J. Albert, S. Fiechter, A. Ennaoui, and M. C. Lux-Steiner, “11.3% efficiency $Cu(In,Ga)(S,Se)_2$ thin film solar cells via drop-on-demand inkjet printing,” *Energy Environ. Sci.*, vol. 9, pp. 2037–2043, 2016.

[64] T. K. Todorov, O. Gunawan, T. Gokmen, and D. B. Mitzi, “Solution-processed $Cu(In,Ga)(S,Se)_2$ absorber yielding a 15.2% efficient solar cell,” *Prog. Photovoltaics Res. Appl.*, vol. 21, pp. 82–87, 2013.

[65] H. Zhou, C.-J. Hsu, W.-C. Hsu, H.-S. Duan, C.-H. Chung, W. Yang, and Y. Yang, “Non-Hydrazine Solutions in Processing $CuIn(S,Se)_2$ Photovoltaic Devices from Hydrazinium Precursors,” *Adv. Energy Mater.*, vol. 3, pp. 328–336, 2013.

[66] D. H. Webber and R. L. Brutchey, “Alkahest for V_2VI_3 chalcogenides: dissolution of nine bulk semiconductors in a diamine-dithiol solvent mixture,” *J. Am. Chem. Soc.*, vol. 135, pp. 15722–15725, 2013.

[67] P. Jackson, R. Wuerz, D. Hariskos, E. Lotter, W. Witte, and M. Powalla, “Effects of heavy alkali elements in $Cu(In,Ga)Se_2$ solar cells with efficiencies up to 22.6%,” *Phys. Status Solidi RRL*, vol. 10, pp. 583–586, 2016.

[68] S. Uličná, P. Arnou, A. Abbas, M. Togay, L. M. Welch, M. Bliss, A. V. Malkov, J. M. Walls, and J. W. Bowers, “Deposition and application of a Mo–N back contact diffusion barrier yielding a 12.0% efficiency solution-processed CIGS solar cell using

an amine–thiol solvent system," *J. Mater. Chem. A*, vol. 7, pp. 7042–7052, 2019.

[69] P. Arnou, C. S. Cooper, A. V. Malkov, J. W. Bowers, and J. M. Walls, "Solution-processed $CuIn(S,Se)_2$ absorber layers for application in thin film solar cells," *Thin Solid Films*, vol. 582, pp. 31–34, 2014.

[70] P. Arnou, C. S. Cooper, S. Uličná, A. Abbas, A. Eeles, L. D. Wright, A. V. Malkov, J. M. Walls, and J. W. Bowers, "Solution processing of $CuIn(S,Se)_2$ and $Cu(In,Ga)(S,Se)_2$ thin film solar cells using metal chalcogenide precursors," *Thin Solid Films*, vol. 633, pp. 76–80, 2017.

[71] X. Zhao, M. Lu, M. Koeper, and R. Agrawal, "Solution-Processed Sulfur Depleted $Cu(In,Ga)Se_2$ Solar Cells Synthesized from a Monoamine-Dithiol Solvent Mixture," *J. Mater. Chem. A*, vol. 4, pp. 7390–7397, 2016.

[72] C. D. Technologies, "EAGLE XG Slim Glass: Product Information Sheet," 2013. [Online]. Available: https://www.corning.com/media/worldwide/cdt/documents/EAGLE XG ® Slim Glass.pdf. [Accessed: 10-Feb-2019].

[73] D. Abou-Ras, G. Kostorz, D. Bremaud, M. Kalin, F. V Kurdesau, A. N. Tiwari, and M. Dobeli, "Formation and characterisation of $MoSe_2$ for $Cu(In,Ga)Se_2$ based solar cells," *Thin Solid Films*, vol. 480–481, pp. 433–438, 2005.

[74] T. Wada, N. Kohara, S. Nishiwaki, and T. Negami, "Characterization of the $Cu(In,Ga)Se_2$/Mo interface in CIGS solar cells," *Thin Solid Films*, vol. 387, pp. 118–122, 2001.

[75] S. Ahn, K. H. Kim, J. H. Yun, and K. H. Yoon, "Effects of selenization conditions on densification of $Cu(In,Ga)Se_2$ (CIGS) thin films prepared by spray deposition of CIGS nanoparticles," *J. Appl. Phys.*, vol. 105, p. 113533, 2009.

[76] T. B. Harvey, I. Mori, C. J. Stolle, T. D. Bogart, D. P. Ostrowski, M. S. Glaz, J. Du, D. R. Pernik, V. A. Akhavan, H. Kesrouani, D. A. Vanden Bout, and B. A. Korgel, "Copper indium gallium selenide (CIGS) photovoltaic devices made using multistep selenization of nanocrystal films," *ACS Appl. Mater. Interfaces*, vol. 5, pp. 9134–9140, 2013.

[77] C. W. Jeon, T. Cheon, H. Kim, M. S. Kwon, and S. H. Kim, "Controlled formation of $MoSe_2$ by MoN_x thin film as a diffusion barrier against Se during selenization annealing for CIGS solar cell," *J. Alloys Compd.*, vol. 644, pp. 317–323, 2015.

[78] S. Lopez-Marino, M. Espíndola-Rodríguez, Y. Sánchez, X. Alcobé, F. Oliva, H. Xie, M. Neuschitzer, S. Giraldo, M. Placidi, R. Caballero, V. Izquierdo-Roca, A. Pérez-Rodríguez, and E. Saucedo, "The importance of back contact modification in $Cu_2ZnSnSe_4$ solar cells: The role of a thin MoO_2 layer," *Nano Energy*, vol. 26, pp. 708–721, 2016.

[79] B. Shin, Y. Zhu, N. A. Bojarczuk, S. Jay Chey, and S. Guha, "Control of an interfacial $MoSe_2$ layer in $Cu_2ZnSnSe_4$ thin film solar cells: 8.9% power conversion efficiency with a TiN diffusion barrier," *Appl. Phys. Lett.*, vol. 101, p. 53903, 2012.

[80] C. L. McCarthy and R. L. Brutchey, "Solution Processing of Chalcogenide Materials Using Thiol-Amine 'Alkahest' Solvent Systems," *Chem. Commun.*, vol. 53, pp. 4888–

4902, 2017.

[81] M. Kaelin, D. Rudmann, and A. N. Tiwari, “Low cost processing of CIGS thin film solar cells,” *Sol. Energy*, vol. 77, pp. 749–756, 2004.

[82] M. Kemell, M. Ritala, and M. Leskelä, “Effects of post-deposition treatments on the photoactivity of $CuInSe_2$ thin films deposited by the induced co-deposition mechanism,” *J. Mater. Chem.*, vol. 11, pp. 668–672, 2001.

[83] W. Liu, D. B. Mitzi, M. Yuan, A. J. Kellock, S. J. Chey, and O. Gunawan, “12% Efficiency $CuIn(Se,S)_2$ Photovoltaic Device Prepared Using a Hydrazine Solution Process,” *Chem. Mater.*, vol. 22, pp. 1010–1014, 2010.

[84] S. Uličná, P. Arnou, C. S. Cooper, L. D. Wright, A. V Malkov, J. M. Walls, and J. W. Bowers, “Hydrazine-free metal chalcogenide precursor solutions for sprayed $CuIn(S,Se)_2$ thin film solar cells,” *12th Photovolt. Sci. Technol. Conf.*, 2016.

[85] A. H. Jahagirdar, A. A. Kadam, and N. G. Dhere, “Role of i-ZnO in optimizing open circuit voltage of CIGS2 and CIGS thin film solar cells,” *4th World Conf. Photovolt. Energy Conversion, WCPEC-4*, pp. 557–559, 2006.

[86] J. H. Han, S. Rehan, D. G. Moon, A. Cho, J. Gwak, K. H. Yoon, S. K. Ahn, J. H. Yun, Y. J. Eo, and S. Ahn, “Actual partial pressure of Se vapor in a closed selenization system: quantitative estimation and impact on solution-processed chalcogenide thin-film solar cells,” *J. Mater. Chem. A*, vol. 4, pp. 6319–6331, 2016.

[87] K. H. Liao, C. Y. Su, Y. T. Ding, and H. S. Koo, “Microstructural characterization of CIGS formation using different selenization processes,” *Appl. Surf. Sci.*, vol. 270, pp. 139–144, 2013.

[88] T. B. Harvey, F. Bonafé, T. Updegrave, V. R. Voggu, C. Thomas, S. C. Kamarajugadda, C. J. Stolle, D. Pernik, J. Du, and B. A. Korgel, “Uniform Selenization of Crack-Free Films of $Cu(In,Ga)Se_2$ Nanocrystals,” *ACS Appl. Energy Mater.*, vol. 2, pp. 736–742, 2019.

[89] M. A. Contreras, M. J. Romero, B. To, F. Hasoon, R. Noufi, S. Ward, and K. Ramanathan, “Optimization of CBD CdS process in high-efficiency $Cu(In,Ga)Se_2$-based solar cells,” *Thin Solid Films*, vol. 403–404, pp. 204–211, 2002.

[90] I. Kaur, D. K. Pandya, and K. L. Chopra, “Growth Kinetics and Polymorphism of Chemically Deposited CdS Films,” *J. Electrochem. Soc.*, vol. 127, pp. 943–948, 1980.

[91] J. Kessler, K. O. Velthaus, M. Ruckh, R. Laichinger, H. W. Schock, D. Lincot, R. Ortega, and J. Vedel, “Chemical bath deposition of CdS on $CuInSe_2$, etching effects and growth kinetics,” *Proc. 6th Int. Photovolt. Sci. Eng. Conf.*, p. 1005, 1992.

[92] K. Ramanathan, H. Wiesner, S. Asher, D. Niles, R. Bhattacharya, J. Keane, M. A. Contreras, and R. Noufi, “High efficiency $Cu(In,Ga)Se_2$ thin film solar cells without intermediate buffer layers,” in *2nd World Conference on Photovoltaic Energy Conversion*, 1998.

[93] K. Ramanathan, F. S. Hasoon, S. Smith, D. L. Young, M. A. Contreras, P. K. Johnson, A. O. Pudov, and J. R. Sites, “Surface treatment of $CuInGaSe_2$ thin films and its effect

on the photovoltaic properties of solar cells," *J. Phys. Chem. Solids*, vol. 64, pp. 1495–1498, 2003.

[94] U. Rau, D. Braunger, R. Herberholz, H. W. Schock, J.-F. Guillemoles, L. Kronik, and D. Cahen, "Oxygenation and air-annealing effects on the electronic properties of Cu(In,Ga)Se_2 films and devices," *J. Appl. Phys.*, vol. 86, pp. 497–505, 1999.

[95] J. C. Lee, K. H. Kang, S. K. Kim, K. H. Yoon, I. J. Park, and J. Song, "RF sputter deposition of the high-quality intrinsic and n-type ZnO window layers for Cu(In,Ga)Se_2-based solar cell applications," *Sol. Energy Mater. Sol. Cells*, vol. 64, pp. 185–195, 2000.

[96] U. Rau and M. Schmidt, "Electronic properties of ZnO/CdS/Cu(In,Ga)Se_2 solar cells - Aspects of heterojunction formation," *Thin Solid Films*, vol. 387, pp. 141–146, 2001.

[97] Y. Nagoya, B. Sang, Y. Fujiwara, K. Kushiya, and O. Yamase, "Improved performance of Cu(In,Ga)Se_2-based submodules with a stacked structure of ZnO window prepared by sputtering," *Sol. Energy Mater. Sol. Cells*, vol. 75, pp. 163–169, 2003.

[98] U. Malm and M. Edoff, "Influence From Front Contact Sheet Resistance on Extracted Diode Parameters in CIGS Solar Cells," *Prog. Photovolt Res. Appl.*, vol. 16, pp. 113–121, 2008.

[99] W. C. Nixon, "The General Principles of Scanning Electron Microscopy," *Philos. Trans. R. Soc. B Biol. Sci.*, vol. 261, pp. 45–50, 1971.

[100] L. Reimer, *Transmission Electron Microscopy, Physics of Image Formation and Microanalysis*. Berlin: Springer, 1993.

[101] T. Ishitani, H. Tsuboi, and T. Yaguchi, "Transmission Electron Microscope Sample Preparation Using a Focused Ion Beam," *J. Electron Microsc. (Tokyo).*, vol. 326, pp. 322–326, 1994.

[102] D. Abou-Ras, T. Kirchartz, and U. Rau, *Advanced Characterization Techniques for Thin Film Solar Cells*. WILEY-VCH, 2011.

[103] EDAX, "Interactive Periodic Table - Aluminium." [Online]. Available: https://www.edax.com/resources/interactive-periodic-table/aluminum. [Accessed: 11-Feb-2019].

[104] P. J. Statham, "Prospects for improvement in EDX microanalysis," *J. Microsc.*, vol. 130, pp. 165–176, 1983.

[105] W. Bragg, *An Introduction to Crystal Analysis*. London: G. Bell and Sons Ltd, 1928.

[106] M. Klenk, O. Schenker, U. Probst, and E. Bucher, "X-ray fluorescence measurements of thin film chalcopyrite solar cells," *Sol. Energy Mater. Sol. Cells*, vol. 58, pp. 299–319, 1999.

[107] J. F. Watts and J. Wolstenholme, *An introduction to surface analysis by XPS and AES*. UK: Wiley, 2003.

[108] A. Benninghoven, F. G. Rudenauer, and H. W. Werner, *Secondary ion mass spectrometry: basic concepts, instrumental aspects, applications and trends*. United States: Wiley, 1987.

[109] R. L. Hervig, F. K. Mazdab, P. Williams, Y. Guan, G. R. Huss, and L. A. Leshin, "Useful ion yields for Cameca IMS 3f and 6f SIMS: Limits on quantitative analysis," *Chem. Geol.*, vol. 227, pp. 83–99, 2006.

[110] S. M. Sze, *Semiconductor Devices Physics and Technology*. New York: John Wiley & Sons, Inc., 2002.

[111] J. T. Heath, J. D. Cohen, and W. N. Shafarman, "Bulk and metastable defects in $CuIn_{1-x}Ga_xSe_2$ thin films using drive-level capacitance profiling," *J. Appl. Phys.*, vol. 95, pp. 1000–1010, 2004.

[112] A. Eeles, "Performance characterisation of photovoltaic devices: managing the effects of high capacitance and metastability," Loughborough University, 2016.

[113] V. Tsai, C. Potamialis, S. Ulicna, M. Bliss, T. R. Betts, and R. Gottschalg, "Quantifying minority carrier lifetime and collection efficiency of solar cells by combined optical and electrical characterisation techniques," *EU PVSEC 35 Proc.*, pp. 114–121, 2018.

[114] Y. Sun, S. Lin, W. Li, S. Cheng, Y. Zhang, Y. Liu, and W. Liu, "Review on alkali element doping in $Cu(In,Ga)Se_2$ thin films and solar cells," *Engineering*, vol. 3, pp. 452–459, 2017.

[115] P. M. P. Salomé, H. Rodriguez-Alvarez, and S. Sadewasser, "Incorporation of alkali metals in chalcogenide solar cells," *Sol. Energy Mater. Sol. Cells*, vol. 143, pp. 9–20, 2015.

[116] F. V. Natrup, H. Bracht, S. Murugavel, and B. Roling, "Cation diffusion and ionic conductivity in soda-lime silicate glasses," *Phys. Chem. Chem. Phys.*, vol. 7, pp. 2279–2286, 2005.

[117] G. Hanna, S. Bilger, S. G., H.-W. Schock, U. Rau, and J. H. Werner, "Na diffusion in the $Cu(In,Ga)Se_2$/Mo/glass system," *3rd World Conf. Photovolt. Energy Convers.*, pp. 368–371, 2003.

[118] R. V. Forest, E. Eser, B. E. McCandless, R. W. Birkmire, and J. G. Chen, "Understanding the role of oxygen in the segregation of sodium at the surface of molybdenum coaated soda-lime glass," *AIChE*, vol. 60, p. 2365, 2014.

[119] T. Gershon, C. Hamann, M. Hopstaken, Y. S. Lee, B. Shin, and R. Haight, "Chemical consequences of alkali inhomogeneity in Cu_2ZnSnS_4 thin-film solar cells," *Adv. Energy Mater.*, vol. 5, p. 1500922, 2015.

[120] P. T. Erslev, W. N. Shafarman, and J. D. Cohen, "Metastable properties of $Cu(In_{1-x},Ga_x)Se_2$ with and without sodium," *Appl. Phys. Lett.*, vol. 98, p. 62105, 2011.

[121] K. Granath, M. Bodega, and L. Stolt, "The effect of NaF on $Cu(In,Ga)Se_2$ thin film solar cells," *Sol. Energy Mater. Sol. Cells*, vol. 60, pp. 279–293, 2000.

[122] B. Yates, *Thermal expansion*. London-New York: Plentum Press, 1972.

[123] W. L. Konijnendijk and J. M. Stevels, “Linear thermal expansion of borosilicate glasses in relation to their structure,” *Verres Refract.*, vol. 30, 1976.

[124] G. W. Morey, *The properties of glass*. New York: Reinhold Publishing Corp, 1938.

[125] A. Q. Tool, “Relaxation of stresses in annealing glass,” *J. Res. Natl. Bur. Stand. (1934).*, vol. 34, p. 199, 1945.

[126] “ISO 7991: Glass - Determination of coefficient of mean linear thermal expansion,” 1987.

[127] Continental Trade, “Information sheet- Solda-lime glass prpperties.” [Online]. Available: file:///C:/Users/elsu6/Downloads/Karta informacyjna - wlasciwosci szkla sodowo-wapniowego_EN.pdf. [Accessed: 17-Feb-2019].

[128] “Schott borofloat 33.” [Online]. Available: https://psec.uchicago.edu/glass/borofloat_33_e.pdf. [Accessed: 17-Feb-2019].

[129] A. Rockett, M. Bodegard, K. Granath, and L. Stolt, “Na incorporation and diffusion in $CuIn_{1-x}Ga_xSe_2$,” *25th IEEE Photovolt. Spec. Conf.*, pp. 985–987, 1996.

[130] Z. H. Li, E. S. Cho, and S. J. Kwon, “Molybdenum thin film deposited by in-line DC magnetron sputtering as a back contact for $Cu(In,Ga)Se_2$ solar cells,” *Appl. Surf. Sci.*, vol. 257, pp. 9682–9688, 2011.

[131] S. A. Pethe, E. Takahashi, A. Kaul, and N. G. Dhere, “Effect of sputtering process parameters on film properties of molybdenum back contact,” *Sol. Energy Mater. Sol. Cells*, vol. 100, pp. 1–5, 2012.

[132] E. Takahashi, S. A. Pethe, and N. G. Dhere, “Correlation between preparation parameters and properties of molybdenum back contact layer for CIGS thin film solar cell,” *35th IEEE Photovolt. Spec. Conf.*, pp. 2478–2482, 2010.

[133] J. H. Scofield, A. Duda, D. Albin, B. L. Ballard, and P. K. Predecki, “Sputtered molybdenum bilayer back contact for copper indium diselenide-based polycrystalline thin-film solar cells,” *Thin Solid Films*, vol. 260, pp. 26–31, 1995.

[134] M. Theelen, K. Polman, M. Tomassini, N. Barreau, H. Steijvers, J. van Berkum, Z. Vroon, and M. Zeman, “Influence of deposition pressure and selenisation on damp heat degradation of the $Cu(In,Ga)Se_2$ back contact molybdenum,” *Surf. Coatings Technol.*, vol. 252, pp. 157–167, 2014.

[135] D. Zhou, H. Zhu, X. Liang, C. Zhang, Z. Li, Y. Xu, J. Chen, L. Zhang, and Y. Mai, “Sputtered molybdenum thin films and the application in CIGS solar cells,” *Appl. Surf. Sci.*, vol. 362, pp. 202–209, 2015.

[136] S. Niki, M. Contreras, I. Repins, M. Powalla, K. Kushiya, S. Ishizuka, and K. Matsubara, “CIGS absorbers and processes,” *Prog. Photovoltaics Res. Appl.*, vol. 18, pp. 453–466, 2010.

[137] L. Assmann, J. C. Bernède, A. Drici, C. Amory, E. Halgand, and M. Morsli, “Study of the Mo thin films and Mo/CIGS interface properties,” *Appl. Surf. Sci.*, vol. 246, pp. 159–166, 2005.

[138] A. C. Badgujar, S. R. Dhage, and S. V Joshi, “Process parameter impact on properties of sputtered large-area Mo bilayers for CIGS thin film solar cell applications,” *Thin Solid Films*, vol. 589, pp. 79–84, 2015.

[139] P. C. Huang, C. H. Huang, M. Y. Lin, C. Y. Chou, C. Y. Hsu, and C. G. Kuo, “The effect of sputtering parameters on the film properties of molybdenum back contact for CIGS solar cells,” *Int. J. Photoenergy*, vol. 2013, p. 8, 2013.

[140] M. Jubault, L. Ribeaucourt, E. Chassaing, G. Renou, D. Lincot, and F. Donsanti, “Optimization of molybdenum thin films for electrodeposited CIGS solar cells,” *Sol. Energy Mater. Sol. Cells*, vol. 95, pp. S26–S31, 2011.

[141] N. Kohara, S. Nishiwaki, Y. Hashimoto, T. Negami, and T. Wada, “Electrical properties of the Cu(In,Ga)Se_2/$MoSe_2$/Mo structure,” *Sol. Energy Mater. Sol. Cells*, vol. 67, pp. 209–215, 2001.

[142] T. Klinkert, B. Theys, G. Patriarche, M. Jubault, F. Donsanti, J.-F. Guillemoles, and D. Lincot, “New insights into the Mo/Cu(In,Ga)Se_2 interface in thin film solar cells: Formation and properties of the $MoSe_2$ interfacial layer,” *J. Chem. Phys.*, vol. 145, p. 154702, 2016.

[143] S. Lee, J. Koo, S. Kim, S. H. Kim, T. Cheon, J. S. Oh, S. J. Kim, and W. K. Kim, “Characteristics of $MoSe_2$ formation during rapid thermal processing of Mo-coated glass,” *Thin Solid Films*, vol. 535, pp. 206–213, 2013.

[144] W. Witte, R. Kniese, A. Eicke, and M. Powalla, “Influence of the Ga content on the Mo/Cu(In,Ga)Se_2 interface formation,” *4th World Conf. Photovolt. Energy Conf.*, pp. 553–556, 2006.

[145] X. L. Zhu, Z. Zhou, Y. M. Wang, L. Zhang, A. M. Li, and F. Q. Huang, “Determining factor of $MoSe_2$ formation in Cu(In,Ga)Se_2 solar cells,” *Sol. Energy Mater. Sol. Cells*, vol. 101, pp. 57–61, 2012.

[146] J. Palm, V. Probst, A. Brummer, W. Stetter, R. Tolle, T. P. Niesen, S. Visbeck, O. Hernandez, M. Wendl, H. Vogt, H. Calwer, B. Freienstein, and F. Karg, “CIS module pilot processing applying concurrent rapid selenization and sulfurization of large area thin film precursors,” *Thin Solid Films*, vol. 431–432, pp. 514–522, 2003.

[147] W. Li, J. Chen, H. Cui, F. Liu, and X. Hao, “Inhibiting MoS_2 formation by introducing a ZnO intermediate layer for Cu_2ZnSnS_4 solar cells,” *Mater. Lett.*, vol. 130, pp. 87–90, 2014.

[148] H. Cui, X. Liu, F. Liu, X. Hao, N. Song, and C. Yan, “Boosting Cu_2ZnSnS_4 solar cells efficiency by a thin Ag intermediate layer between absorber and back contact,” *Appl. Phys. Lett.*, vol. 104, p. 41115, 2014.

[149] T. Schnabel and E. Ahlswede, “On the interface between kesterite absorber and Mo back contact and its impact on solution-processed thin-film solar cells,” *Sol. Energy Mater. Sol. Cells*, vol. 159, pp. 290–295, 2017.

[150] Y. Kamikawa, J. Nishinaga, S. Ishizuka, H. Shibata, and S. Niki, “Effects of Mo surface oxidation on Cu(In,Ga)Se_2 solar cells fabricated by three-stage process with KF postdeposition treatment,” *Jpn. J. Appl. Phys.*, vol. 55, p. 22304, 2016.

[151] J. Kang, G. Y. Baek, S. Gedi, Y. J. Song, and C.-W. Jeon, “Effects of the MoN diffusion barrier on the CZTSe growth behavior and solar cell performance,” *J. Alloys Compd.*, vol. 748, pp. 188–192, 2018.

[152] H. A. Jehn, J. H. Kim, and S. Hofmann, “Composition and properties of transition metal nitride thin films (ZrN_x, NbN_x, MoN_x),” *Surf. Coatings Technol.*, vol. 36, pp. 715–727, 1988.

[153] D. Braunger, D. Hariskos, G. Bilger, U. Rau, and H. W. Schock, “Influence of sodium on the growth of polycrystalline Cu(In,Ga)Se_2 thin films,” *Thin Solid Films*, vol. 361–362, pp. 161–166, 2000.

[154] C. M. Sutter-Fella, J. a. Stückelberger, H. Hagendorfer, F. La Mattina, L. Kranz, S. Nishiwaki, A. R. Uhl, Y. E. Romanyuk, and A. N. Tiwari, “Sodium assisted sintering of chalcogenides and its application to solution processed $Cu_2ZnSn(S,Se)_4$ thin film solar cells,” *Chem. Mater.*, vol. 26, pp. 1420–1425, 2014.

[155] B. Shin, O. Gunawan, Y. Zhu, N. A. Bojarczuk, S. Jay Chey, and S. Guha, “Thin film solar cell with 8.4% power conversion efficiency using an earth-abundant Cu_2ZnSnS_4 absorber,” *Prog. Photovoltaics Res. Appl.*, vol. 21, pp. 72–76, 2013.

[156] S. Bag, O. Gunawan, T. Gokmen, Y. Zhu, T. K. Todorov, and D. B. Mitzi, “Low band gap liquid-processed CZTSe solar cell with 10.1% efficiency,” *Energy Environ. Sci.*, vol. 5, pp. 7060–7065, 2012.

[157] S. Nishiwaki, S. Siebentritt, M. Giersig, and M. C. Lux-Steiner, “Growth model of $CuGaSe_2$ grains in a Cu-rich/Cu-poor bilayer process,” *J. Appl. Phys.*, vol. 94, pp. 6864–6870, 2003.

[158] R. J. Matson, R. Noufi, R. K. Ahrenkiel, R. C. Powell, and D. Cahen, “EBIC investigations of junction activity and the role of oxygen in CdS/$CuInSe_2$ devices,” *Sol. Cells*, vol. 16, pp. 495–519, 1986.

[159] U. Rau and H. W. Schock, “Electronic properties of Cu(In,Ga)Se_2 heterojunction solar cells-recent achievements, current understanding, and future challenges,” *Appl. Phys. A Mater. Sci. Process.*, vol. 69, pp. 131–147, 1999.

[160] M. Kemell, M. Ritala, and M. Leskelä, “Thin film deposition methods for $CuInSe_2$ solar cells,” *Crit. Rev. Solid State Mater. Sci.*, vol. 30, pp. 1–31, 2005.

[161] E. Moons, D. Gal, and J. Beier, “Effect of air annealing on the electronic properties of CdS/Cu(In,Ga)Se_2 solar cells,” *Sol. Energy Mater. Sol. Cells*, vol. 43, pp. 73–78, 1996.

[162] D. B. Mitzi, M. Yuan, W. Liu, A. J. Kellock, S. J. Chey, L. Gignac, and A. G. Schrott, “Hydrazine-based deposition route for device-quality CIGS films,” *Thin Solid Films*, vol. 517, pp. 2158–2162, 2009.

[163] T. Nakada and A. Kunioka, “Direct evidence of Cd diffusion into Cu(In,Ga)Se_2 thin films during chemical-bath deposition process of CdS films,” *Appl. Phys. Lett.*, vol. 74, p. 2444, 1999.

[164] W. K. Metzger, I. L. Repins, M. Romero, P. Dippo, M. Contreras, R. Noufi, and D. Levi, “Recombination kinetics and stability in polycrystalline Cu(In,Ga)Se_2 solar cells,” *Thin*

Solid Films, vol. 517, pp. 2360–2364, 2009.

[165] T. Song, A. Kanevce, and J. R. Sites, “Emitter/absorber interface of CdTe solar cells,” *J. Appl. Phys.*, vol. 119, p. 233104, 2016.

[166] Y. M. Shin, C. S. Lee, D. H. Shin, H. S. Kwon, B. G. Park, and B. T. Ahn, “Surface modification of CIGS film by annealing and its effect on the band structure and photovoltaic properties of CIGS solar cells,” *Curr. Appl. Phys.*, vol. 15, pp. 18–24, 2015.

[167] D. Cahen and R. Noufi, “Free energies and enthalpies of possible gas phase and surface reactions for preparation of $CuInSe_2$,” *J. Phys. Chem. Solids*, vol. 53, pp. 991–1005, 1992.

[168] S. Shirakata and T. Nakada, “Photoluminescence and time-resolved photoluminescence in $Cu(In,Ga)Se_2$ thin films and solar cells,” *Phys. Status Solidi Curr. Top. Solid State Phys.*, vol. 6, pp. 1059–1062, 2009.

[169] S. Shirakata, H. Ohta, K. Ishihara, T. Takagi, A. Atarashi, and S. Yudate, “Photoluminescence characterization of surface degradation mechanism in $Cu(In,Ga)Se_2$ thin films grown on Mo/soda lime glass substrate,” *Jpn. J. Appl. Phys.*, vol. 53, p. 05FW11, 2014.

[170] J. T. Heath, J. D. Cohen, and W. N. Shafarman, “Distinguishing metastable changes in bulk CIGS defect densities from interface effects,” *Thin Solid Films*, vol. 431–432, pp. 426–430, 2003.

[171] Y. D. Chung, D. H. Cho, N. M. Park, K. S. Lee, and J. Kim, “Effect of annealing on $CdS/Cu(In,Ga)Se_2$ thin-film solar cells,” *Curr. Appl. Phys.*, vol. 11, pp. S65–S67, 2011.

[172] V. Nadenau, U. Rau, A. Jasenek, and H. W. Schock, “Electronic properties of $CuGaSe_2$-based heterojunction solar cells. Part I. Transport analysis,” *J. Appl. Phys.*, vol. 87, pp. 584–593, 2000.

[173] O. Gunawan, T. K. Todorov, and D. B. Mitzi, “Loss mechanisms in hydrazine-processed $Cu_2ZnSn(Se,S)_4$ solar cells,” *Appl. Phys. Lett.*, vol. 97, p. 233506, 2010.

[174] T. Kobayashi, Z. J. L. Kao, and T. Nakada, “Temperature dependent current-voltage and admittance spectroscopy on heat-light soaking effects of $Cu(In,Ga)Se_2$ solar cells with ALD-Zn(O,S) and CBD-ZnS(O,OH) buffer layers,” *Sol. Energy Mater. Sol. Cells*, vol. 143, pp. 159–167, 2015.

[175] Z. Zhang, C. Bao, W. Yao, S. Ma, L. Zhang, and S. Hou, “Influence of deposition temperature on the crystallinity of Al-doped ZnO thin films at glass substrates prepared by RF magnetron sputtering method,” *Superlattices Microstruct.*, vol. 49, pp. 644–653, 2011.

[176] M. Jin, J. Feng, Z. De-heng, M. Hong-lei, and L. Shu-ying, “Optical and electronic properties of transparent conducting ZnO and ZnO:Al films prepared by evaporating method,” *Thin Solid Films*, vol. 357, pp. 98–101, 1999.

[177] M. Theelen, C. Foster, H. Steijvers, N. Barreau, Z. Vroon, and M. Zeman, “The impact of atmospheric species on the degradation of CIGS solar cells,” *Sol. Energy Mater.*

Sol. Cells, vol. 141, pp. 49–56, 2015.

[178] W. K. Metzger, I. L. Repins, and M. A. Contreras, “Long lifetimes in high-efficiency Cu(In,Ga)Se_2 solar cells,” *Appl. Phys. Lett.*, vol. 93, p. 22110, 2008.

[179] S. Shirakata and T. Nakada, “Time-resolved photoluminescence in Cu(In,Ga)Se_2 thin films and solar cells,” *Thin Solid Films*, vol. 515, pp. 6151–6154, 2007.

[180] C. L. Perkins, F. S. Hasoon, H. A. Al-Thani, S. E. Asher, and P. Sheldon, “XPS and UPS investigation of NH_4OH-exposed Cu(In,Ga)Se_2 thin films,” *31st IEEE Photovolt. Spec. Conf.*, pp. 255–258, 2005.

[181] C. J. Hages, M. J. Koeper, C. K. Miskin, K. W. Brew, and R. Agrawal, “Controlled Grain Growth for High Performance Nanoparticle-Based Kesterite Solar Cells,” *Chem. Mater.*, vol. 28, pp. 7703–7714, 2016.

[182] D. Zhao, Q. Fan, Q. Tian, Z. Zhou, Y. Meng, D. Kou, W. Zhou, S. Wu, J. Mater, D. Zhao, A. Qingmiao Fan, A. Qingwen Tian, A. Zhengji Zhou, A. Yuena Meng, A. Dongxing Kou, A. Wenhui Zhou, and S. Wu, “Eliminating Fine-Grained Layer in Cu(In,Ga)$(S,Se)_2$ Thin Films for Solution-Processed High Efficient Solar Cells,” *J. Mater. Chem. A*, vol. 4, pp. 13476–13481, 2016.

[183] W. Wu, Y. Cao, J. V. Caspar, Q. Guo, L. K. Johnson, I. Malajovich, H. D. Rosenfeld, and K. R. Choudhury, “Studies of the fine-grain sub-layer in the printed CZTSSe photovoltaic devices,” *J. Mater. Chem. C*, vol. 2, p. 3777, 2014.

[184] S. López-Marino, M. Placidi, A. Pérez-Tomás, J. Llobet, V. Izquierdo-Roca, X. Fontané, A. Fairbrother, M. Espíndola-Rodríguez, D. Sylla, A. Pérez-Rodríguez, and E. Saucedo, “Inhibiting the absorber/Mo-back contact decomposition reaction in $Cu_2ZnSnSe_4$ solar cells: The role of a ZnO intermediate nanolayer,” *J. Mater. Chem. A*, vol. 1, p. 8338, 2013.

[185] M. Kawamura, T. Fujita, A. Yamada, and M. Konagai, “Cu(In,Ga)Se_2 thin-film solar cells grown with cracked selenium,” *J. Cryst. Growth*, vol. 311, pp. 753–756, 2009.

[186] S. Ishizuka, H. Shibata, A. Yamada, P. Fons, K. Sakurai, K. Matsubara, and S. Niki, “Growth of polycrystalline Cu(In,Ga)Se_2 thin films using a radio frequency-cracked Se-radical beam source and application for photovoltaic devices,” *Appl. Phys. Lett.*, vol. 91, p. 41902, 2007.

[187] G. Li, W. Liu, Y. Liu, S. Lin, Y. Zhang, Z. Zhou, Q. He, and Y. Sun, “The influence of cracked selenium flux on CIGS thin film growth and device performance prepared by two-step selenization processes,” *Sol. Energy Mater. Sol. Cells*, vol. 139, pp. 108–114, 2015.

[188] J. Bekker, V. Alberts, and M. J. Witcomb, “Influence of selenization techniques on the reaction kinetics of chalcopyrite thin films,” *Thin Solid Films*, vol. 387, pp. 40–43, 2001.

[189] O. A. Balitskii, V. P. Savchyn, and V. O. Yukhymchuk, “Raman investigation of InSe and GaSe single-crystals oxidation,” *Semicond. Sci. Technol.*, vol. 17, pp. L1–L4, 2002.

[190] D. S. Albin, J. R. Tuttle, and R. Noufi, “The formation of large-grain $CuInSe_2$ films by

selenization by high-rate Se transport under moderate vacuum conditions," *J. Electron. Mater.*, vol. 24, pp. 351–357, 1995.

[191] M. Neuwirth, H. Zhou, T. Schnabel, E. Ahlswede, H. Kalt, and M. Hetterich, "A multiple-selenization process for enhanced reproducibility of $Cu_2ZnSn(S,Se)_4$ solar cells," *Appl. Phys. Lett.*, vol. 109, p. 233903, 2016.

[192] W. Witte, R. Kniese, and M. Powalla, "Raman investigations of $Cu(In,Ga)Se_2$ thin films with various copper contents," *Thin Solid Films*, vol. 517, pp. 867–869, 2008.

[193] V. Probst, F. Karg, J. Rimmasch, W. Riedl, W. Stetter, H. Harms, and O. Eibl, "Advanced Stacked Elemental Layer Process for $Cu(InGa)Se_2$ Thin Film Photovoltaic Devices," *Mat. Res. Soc. Symp. Proc.*, vol. 426, pp. 165–176, 2011.

[194] J. Hedstrom, H. Ohlsen, M. Bodegbd, A. Kylner, L. Stolt, D. Hariskos, M. Ruckh, and H.-W. Schock, "ZnO/CdS/$Cu(In,Ga)Se_2$ thin film solar cells with improved performance," *23d IEEE Photovolt. Spec. Conf.*, pp. 364–371, 1993.

[195] R. Klenk, T. Walter, H. - W Schock, and D. Cahen, "A model for the successful growth of polycrystalline films of $CuInSe_2$ by multisource physical vacuum evaporation," *Adv. Mater.*, vol. 5, pp. 114–119, 1993.

[196] J. R. Tuttle, D. S. Albin, and R. Noufi, "Thoughts on the microstructure of polycrystalline thin film $CuInSe_2$ and its impact on material and device performance," *Sol. Cells*, vol. 30, pp. 21–38, 1991.

[197] R. A. Mickelsen and W. S. Chen, "Apparatus for forming thin-film heterojunction solar cells employing materials selected fo the class of I-II-VI_2 chalcopyrite compounds," 1983.

[198] D. S. Albin, G. D. Mooney, A. Duda, J. Tuttle, R. Matson, and R. Noufi, "Enhanced grain growth in polycrystalline $CuInSe_2$ using rapid thermal processing," *Sol. Cells*, vol. 30, pp. 47–52, 1991.

[199] G. Altamura, M. Wang, and K. Choy, "Influence of alkali metals (Na, Li, Rb) on the performance of electrostatic spray-assisted vapor deposited $Cu_2ZnSn(S,Se)_4$ solar cells," *Sci. Rep.*, vol. 6, p. 22109, 2016.

[200] M. Yuan, D. B. Mitzi, O. Gunawan, A. J. Kellock, S. J. Chey, and V. R. Deline, "Antimony assisted low-temperature processing of $CuIn_{1-x}Ga_xSe_{2-y}S_y$ solar cells," *Thin Solid Films*, vol. 519, pp. 852–856, 2010.

[201] T. Nakada, Y. Honishi, Y. Yatsushiro, and H. Nakakoba, "Impacts of Sb and Bi incorporations on CIGS thin films and solar cells," *37th IEEE Photovolt. Spec. Conf.*, pp. 3527–3531, 2011.

[202] J. Holz, F. Karg, and H. von Philipsborn, "The effect of substrate impurities on the electronic conductivity in CIS thin films," *12th Eur. Photov. Sol. Energy Conf.*, p. 1592, 1994.

[203] D. W. Niles, K. Ramanathan, F. Hasoon, R. Noufi, B. J. Tielsch, and J. E. Fulghum, "Na impurity chemistry in photovoltaic CIGS thin films: Investigation with x-ray photoelectron spectroscopy," *J. Vac. Sci. Technol. A*, vol. 15, pp. 3044–3049, 1997.

[204] M. Bodegard, L. Stolt, and J. Hedstrom, “The influence of sodium on the grain structure of $CuInSe_2$ films for photovoltaic applications,” *12th Eur. Photov. Sol. Energy Conf.*, pp. 1743–1746, 1994.

[205] S. Ishizuka, A. Yamada, M. M. Islam, H. Shibata, P. Fons, T. Sakurai, K. Akimoto, S. Niki, S. Ishizuka, A. Yamada, M. M. Islam, and H. Shibata, “Na-induced variations in the structural, optical, and electrical properties of $Cu(In,Ga)Se_2$ thin films,” *J. Appl. Phys.*, vol. 106, p. 34908, 2009.

[206] D. Rudmann, G. Bilger, M. Kaelin, F. . J. Haug, H. Zogg, and A. N. Tiwari, “Effects of NaF coevaporation on structural properties of $Cu(In,Ga)Se_2$ thin films,” *Thin Solid Films*, vol. 431–432, pp. 37–40, 2003.

[207] D. J. Schroeder and A. A. Rockett, “Electronic effects of sodium in epitaxial $CuIn_{1-x}Ga_xSe_2$,” *J. Appl. Phys.*, vol. 82, pp. 4982–4985, 1997.

[208] T. Nakada, D. Iga, H. Ohbo, and A. Kunioka, “Effects of sodium on $Cu(In,Ga)Se_2$-based thin films and solar cells,” *Jpn. J. Appl. Phys.*, vol. 36, pp. 732–737, 1997.

[209] U. Rau, M. Schmitt, F. Engelhardt, O. Seifert, J. Parisi, W. Riedl, J. Rimmasch, and F. Karg, “Impact of Na and S incorporation on the electronic transport mechanisms of $Cu(In,Ga)Se_2$ solar cells,” *Solid State Commun.*, vol. 107, pp. 59–63, 1998.

[210] D. Cho, K. Lee, Y. Chung, J. Kim, S. Park, and J. Kim, “Electronic effect of Na on $Cu(In,Ga)Se_2$ solar cells,” *Appl. Phys. Lett.*, vol. 101, p. 23901, 2012.

[211] L. E. Oikkonen, M. G. Ganchenkova, A. P. Seitsonen, and R. M. Nieminen, “Effect of sodium incorporation into $CuInSe_2$ from first principles,” *J. Appl. Phys.*, vol. 114, p. 83503, 2013.

[212] B. J. Stanbery, E. S. Lambers, and T. J. Anderson, “XPS studies of sodium compound formation and surface segregation in CIGS thin films,” *26th IEEE Photovolt. Spec. Conf.*, pp. 499–502, 1997.

[213] A. Laemmle, R. Wuerz, T. Schwarz, O. Cojocaru-Mirédin, P.-P. Choi, and M. Powalla, “Investigation of the diffusion behavior of sodium in $Cu(In,Ga)Se_2$ layers,” *J. Appl. Phys.*, vol. 115, p. 154501, 2014.

[214] J.-H. Yoon, J.-H. Kim, W. M. Kim, J.-K. Park, Y.-J. Balik, T.-Y. Seong, and J. Jeong, “Electrical properties of CIGS/Mo junctions as a function of $MoSe_2$ orientation and Na doping,” *Prog. Photovoltaics Res. Appl.*, vol. 22, pp. 90–96, 2014.

[215] R. Caballero, M. Nichterwitz, A. Steigert, A. Eicke, I. Lauermann, H. W. Schock, and C. A. Kaufmann, “Impact of Na on $MoSe_2$ formation at the CIGSe/Mo interface in thin-film solar cells on polyimide foil at low process temperatures,” *Acta Mater.*, vol. 63, pp. 54–62, 2014.

[216] C. Heske, G. Richter, Z. Chen, R. Fink, E. Umbach, W. Riedl, and F. Karg, “Influence of Na and H_2O on the surface properties of $Cu(In,Ga)Se_2$ thin films,” *J. Appl. Phys.*, vol. 82, pp. 2411–2420, 1997.

[217] S. H. Wei, S. B. Zhang, and A. Zunger, “Effects of Na on the electrical and structural properties of $CuInSe_2$,” *J. Appl. Phys.*, vol. 85, pp. 7214–7218, 1999.

[218] C. Persson, Y.-J. Zhao, S. Lany, and A. Zunger, “n-type doping of $CuInSe_2$ and $CuGaSe_2$,” *Phys. Rev. B*, vol. 72, p. 35211, 2005.

[219] E. S. Mungan, X. Wang, and M. A. Alam, “Modeling the effects of na incorporation on CIGS solar cells,” *IEEE J. Photovoltaics*, vol. 3, pp. 451–456, 2013.

[220] A. Urbaniak, M. Igalson, F. Pianezzi, S. Bücheler, A. Chirilă, P. Reinhard, and A. N. Tiwari, “Effects of Na incorporation on electrical properties of $Cu(In,Ga)Se_2$-based photovoltaic devices on polyimide substrates,” *Sol. Energy Mater. Sol. Cells*, vol. 128, pp. 52–56, 2014.

[221] L. Kronik, D. Cahen, and H. W. Schock, “Effects of Sodium on Polycrystalline $Cu(In,Ga)Se_2$ and Its Solar Cell Performance,” *Adv. Mater.*, vol. 10, pp. 31–36, 1998.

[222] R. V Forest, E. Eser, B. E. Mccandless, J. G. Chen, and R. W. Birkmire, “Reversibility of $(Ag,Cu)(In,Ga)Se_2$ electrical properties with the addition and removal of Na : Role of grain boundaries,” *J. Appl. Phys.*, vol. 117, p. 115102, 2015.

[223] R. Hock, F. Hergert, S. Jost, J. Palm, and M. Purwins, “Formation reactions of chalcopyrite compounds and the role of sodium doping,” *Thin Solid Films*, vol. 515, pp. 5843–5847, 2007.

[224] R. Wieting, R. Gay, H. Nguyen, J. Palm, C. Rischmiller, A. Seapan, D. Tarrant, and D. Willett, “CIS thin film manufacturing at Shell Solar: practical techniques in volume manufacturing,” *IEEE J. Photovoltaics*, pp. 177–182, 2005.

[225] H. A. Al-Thani, F. S. Hasoon, M. Young, S. Asher, J. L. Alleman, M. M. Al-Jassim, and D. L. Williamson, “The effect of Mo back contact on Na out-diffusion and device performance of $Mo/Cu(In,Ga)Se_2/CdS/ZnO$ solar cells,” *29th IEEE Photovolt. Spec. Conf.,* pp. 720–723, 2002.

[226] L. M. Mansfield, I. L. Repins, S. Glynn, M. D. Carducci, D. M. Honecker, J. W. Pankow, M. R. Young, C. Dehart, R. Sundaramoorthy, C. L. Beall, and B. To, “Sodium-doped molybdenum targets for controllable sodium incorporation in CIGS solar cells,” *37th IEEE Photovolt. Spec. Conf.*, pp. 3636–3641, 2011.

[227] C. Roger, G. Altamura, F. Emieux, O. Sicardy, F. Roux, R. Fillon, P. Faucherand, N. Karst, H. Fournier, L. Grenet, F. Ducroquet, A. Brioude, and S. Perraud, “Sodium-doped Mo back contacts for $Cu(In,Ga)Se_2$ solar cells on Ti foils: Growth, morphology, and sodium diffusion,” *J. Renew. Sustain. Energy*, vol. 6, p. 11405, 2014.

[228] M. Lammer, U. Klemm, and M. Powalla, “Sodium co-evaporation for low temperature $Cu(In,Ga)Se_2$ deposition,” *Thin Solid Films*, vol. 387, pp. 33–36, 2001.

[229] Y. M. Shin, D. H. Shin, J. H. Kim, and B. T. Ahn, “Effect of Na doping using Na_2S on the structure and photovoltaic properties of CIGS solar cells,” *Curr. Appl. Phys.*, vol. 11, pp. S59–S64, 2011.

[230] T. Nakada, H. Ohbo, M. Fukuda, and A. Kunioka, “Improved compositional flexibility of $Cu(In,Ga)Se_2$-based thin film solar cells by sodium control technique,” *Sol. Energy Mater. Sol. Cells*, vol. 49, pp. 261–267, 1997.

[231] A. N. Tiwari, M. Krejci, and H. Zogg, “12.8% efficiency $Cu(In,Ga)Se_2$ solar cell on a

flexible polymer sheet," *Prog. Photovoltaics Res. Appl.*, vol. 7, pp. 393–397, 1999.

[232] P. M. P. Salomé, A. Hultqvist, V. Fjallstrom, M. Edoff, B. G. Aitken, K. Zhang, K. Fuller, and C. Kosik Williams, "Incorporation of Na in Cu(In,Ga)Se_2 Thin-Film Solar Cells: A Statistical Comparison Between Na From Soda-Lime Glass and From a Precursor Layer of NaF," *IEEE J. Photovoltaics*, vol. 4, pp. 1659–1664, 2014.

[233] R. Caballero, C. A. Kaufmann, T. Eisenbarth, A. Grimm, I. Lauermann, T. Unold, R. Klenk, and H. W. Schock, "Influence of Na on Cu(In,Ga)Se_2 solar cells grown on polyimide substrates at low temperature: Impact on the Cu(In,Ga)Se_2/Mo interface," *Appl. Phys. Lett.*, vol. 96, p. 92104, 2010.

[234] D. Rudmann, D. Bremaud, A. F. da Cunha, G. Bilger, A. Strohm, M. Kaelin, H. Zogg, and A. N. Tiwari, "Sodium incorporation strategies for CIGS growth at different temperatures," *Thin Solid Films*, vol. 480–481, pp. 55–60, 2005.

[235] D. Rudmann, A. F. da Cunha, M. Kaelin, F. Kurdesau, H. Zogg, A. N. Tiwari, and G. Bilger, "Efficiency enhancement of Cu(In,Ga)Se_2 solar cells due to post-deposition Na incorporation," *Appl. Phys. Lett.*, vol. 84, no. 7, pp. 1129–1131, 2004.

[236] M. Wang, M. A. Hossain, and K. L. Choy, "Effect of Sodium Treatment on the Performance of Electrostatic Spray Assisted Vapour Deposited Copper-poor Cu(In,Ga)$(S,Se)_2$ Solar Cells," *Sci. Rep.*, vol. 7, p. 6788, 2017.

[237] V. Izquierdo-Roca, R. Caballero, X. Fontané, C. A. Kaufmann, J. Álvarez-García, L. Calvo-Barrio, E. Saucedo, A. Pérez-Rodríguez, J. R. Morante, and H. W. Schock, "Raman scattering analysis of Cu-poor Cu(In,Ga)Se_2 cells fabricated on polyimide substrates: Effect of Na content on microstructure and phase structure," *Thin Solid Films*, vol. 519, pp. 7300–7303, 2011.

[238] R. Carron, C. Andres, E. Avancini, T. Feurer, S. Nishiwaki, S. Pisoni, F. Fu, M. Lingg, Y. E. Romanyuk, S. Buecheler, and A. N. Tiwari, "Bandgap of thin film solar cell absorbers: A comparison of various determination methods," *Thin Solid Films*, vol. 669, pp. 482–486, 2018.

[239] O. Lundberg, M. Edoff, and L. Stolt, "The effect of Ga-grading in CIGS thin film solar cells," *Thin Solid Films*, vol. 480–481, pp. 520–525, 2005.

[240] I. Dirnstorfer, W. Burkhardt, W. Kriegseis, I. Österreicher, H. Alves, D. M. Hofmann, O. Ka, A. Polity, B. K. Meyer, and D. Braunger, "Annealing studies on CuIn(Ga)Se_2: the influence of gallium," *Thin Solid Films*, vol. 361–362, pp. 400–405, 2000.

[241] T. Kato, "Cu(In,Ga)$(Se,S)_2$ solar cell research in Solar Frontier: Progress and current status," *Jpn. J. Appl. Phys.*, vol. 56, p. 04CA02, 2017.

[242] G. Birant, J. de Wild, M. Meuris, J. Poortmans, and B. Vermang, "Dielectric-Based Rear Surface Passivation Approaches for Cu(In,Ga)Se_2 Solar Cells—A Review," *Appl. Sci.*, vol. 9, p. 677, 2019.

[243] S. Garud, N. Gampa, T. G. Allen, R. Kotipalli, D. Flandre, M. Batuk, J. Hadermann, M. Meuris, J. Poortmans, A. Smets, and B. Vermang, "Surface Passivation of CIGS Solar Cells Using Gallium Oxide," *Phys. Status Solidi Appl. Mater. Sci.*, vol. 215, no. 7, pp. 1–6, 2018.

[244] J. Löckinger, S. Nishiwaki, B. Bissig, G. Degutis, Y. E. Romanyuk, S. Buecheler, and A. N. Tiwari, “The use of HfO_2 in a point contact concept for front interface passivation of Cu(In,Ga)Se_2 solar cells,” *Sol. Energy Mater. Sol. Cells*, vol. 195, pp. 213–219, 2019.